Biochemical regulation of cell mechanics in C. elegans Embryo

Serena Prigent

Sorbonne Université

Ecole doctorale 515 – Complexité du Vivant

Institut de Biologie Paris-Seine (IBPS)

Laboratoire de Biologie du Développement (UMR7622)

Équipe de François ROBIN

Biochemical Regulation of Cell Mechanics in *C. elegans* Embryo

Régulation biochimique de la mécanique cellulaire dans l'embryon de C. elegans

Par Serena PRIGENT GARCIA

Thèse de doctorat de Biologie

Dirigée par Dr. François ROBIN

Présentée et soutenue publiquement le 15 juin 2021

Devant un jury composé de :

Dr. Nathan GOEHRING	Rapporteur, Chef d'équipe, Francis Crick Institute
Dr. Grégoire MICHAUX	Rapporteur, Directeur de Recherche, Université de Rennes 1, IGDR
Dr. Julie PLASTINO	Présidente, Directrice de Recherche, Sorbonne Université, Institut Curie
Dr. Ana de CARVALHO	Chef d'équipe, Université de Porto
Dr. Antoine JÉGOU	Directeur de Recherche, Université de Paris, IJM
Dr. Magali SUZANNE	Directrice de Recherche, Université Toulouse III-Paul Sabatier, CBI
Dr. François ROBIN	Chargé de Recherche, Sorbonne Université, IBPS

Acknowledgments

This PhD work was made possible because I was surrounded by people who supported me during this journey and without them I could not have made it until the end, without a shadow of a doubt.

First, I want to thank the people in my lab, and first and foremost my PhD advisor: **François**. Thank you for offering me a place in your brand-new team, trusting me with this project, coping with my anxieties and guiding me at every step of the way. Thank you for your patience and your indulgence. Thank you, **Camille**, for being a great colleague, thank you for more coffee breaks that I can count, and thank you for letting me venting when my PhD was a little too much. Thank you, **Vlad**, for all the help with this damn microscope, I know it drove you mad as much as me. Gracias **Karen** por siempre estar de tan buen humor, nunca quejarte de nada, tu alegría es exactamente lo que este laboratorio necesita, voy a echar de menos poder asomarme por tu despacho y hacer que lo sueltes todo para charlar las dos. Thank you, **Loan**, your expertise and your hard-work did wonders for my PhD work and sharing with you all the latest series we were watching was something I always looked forward to do in the morning. Thank you, **Shashi**, for teaching me so much, for being always available for any question, I will always admire your work and dedication. Thank you, **Simon**, your humor was able to change the mood of the whole lab in an instant. Thank you, **Jeff**, for all the cat related talks and the incredible number of private jokes still running in the lab thanks to you. Thank you, **Anaïs**, for accepting to be my intern in times of Covid and to have done it with such enthusiasm, the Arp2/3 work here is as much mine than it is yours. Thank you, **Anne**, for being my co-PhD student in the lab, your strong personality wrapped under your kindness was the perfect match for me in the lab.

I want to thank all the people in Michel Labouesse lab. Thank you, **Michel**, **Flora** and **Teresa**, for always asking the tough questions, my work grew better after each discussion. Thank you, Alicia, for being my friend, for complaining with me every time we needed it to say how PhD student life could suck, for all the talks about Harry Potter and for never being tired of talking about cats, even after the Xth picture of my own cat. Thank you, **Thanh**, **Saurabh** and **Xinyi**, for being such awesome labmates.

Thank you to all the people in the 6th floor, which became friends and offered so many laughs at coffee breaks and lunchs: **Marie-Ange, Cédrine, Viviane, Rodolphe, Claire, Estelle**. Thank you to all my friends from the 5th other floor: **Dilyana, Pénélope, Angélique**. Thank you, **Pauline,** for countless lunches and for lifting my mood at each single one of them.

I also want to thank the members of my jury who kindly accepted to read and correct this work.

Je voudrais remercier tous mes amis qui m'ont soutenue, écoutée, rappelée que la vie en dehors du labo existe et que finalement tout n'est pas si grave : **Floriane, Bryann, Mélanie, Pierre, Solenne, Sebastian** et **Helena.** Je vous promets de rattraper toutes (ou presque) les soirées prises par cette thèse. Je tiendrai ma réputation de bretonne.

Je remercie tout particulièrement mes **parents**, je sais que je n'ai pas toujours été là, que la thèse avançant c'était de moins en moins. J'espère qu'avec ce travail vous verrez où sont passées toutes les heures où je n'étais pas là. Merci d'avoir été là, de m'avoir soutenue,

m’avoir encouragée, de vous être inquiétés aussi je sais. Merci pour tout ce que vous avez fait, de m’avoir fait confiance, vous avez rendu cette thèse possible. Merci à **Cécilia**, tu as toujours été à un coup de téléphone de moi, toujours là pour les moments durs et pour les moments de joie intense. Merci aussi de me remettre en place quand j’en ai besoin, il n’y a que toi qui puisse le faire.

Merci à mon rédacteur en chat, **Nicky**, et mon chassistant, **Vasco**, pour avoir contrôlé chaque jour que ce manuscrit avançait et que j’avais toujours de la compagnie pour le faire, sans vous je n’aurais pas tenu mes nuits blanches.

Merci à **Salim**, pour avoir tenu, toujours avec bonne humeur, pendant cette fin de thèse alors que je n’étais pas toujours ni sympathique ni facile à vivre. Merci d’avoir partagé mes pauses, m’avoir fait rire et avoir été là tous les jours ou presque, je ne me suis jamais sentie seule grâce à toi.

Pour finir je remercie de tout mon cœur **Yacine**, merci de m’avoir soutenue, de m’avoir portée à bout de bras pendant cette thèse et ce Covid. Merci d’avoir essuyé mes larmes, mes nerfs, mes colères, d’avoir fait des litres de thé, acheté des kilos de douceur, d’avoir partagé mes nuits de rédaction malgré ton boulot. Merci d’avoir pris autant soin de moi, d’avoir veillé à ce que j’aille toujours au mieux, d’avoir toujours été de mon côté. Merci de m’avoir motivé, tous les jours, m’avoir poussé, d’avoir cru en moi. Merci.

Les mots ne sont pas suffisants pour exprimer ma gratitude, cette thèse est autant la vôtre que la mienne.

Table of contents

Abstracts
(in English and French)

Abstract in english:

Actin network architecture and dynamics play a central role in cell contractility and tissue morphogenesis. Local modulations of Actomyosin network dynamics depend largely on the activation of the RhoA activation cascade. In my thesis, I combined quantitative microscopy using TIRFM, single-molecule imaging, numerical simulations and simple mathematical modeling, to explore the dynamic network architecture underlying pulsed contractions in a simple model, the *C. elegans* early embryo. Focusing on the Actin elongator Formin, we observed that F-Actin elongation was catalyzed by a specific subpopulation of cortical Formins – termed elongating Formins – that displayed a characteristic ballistic mobility. My results also showed that Formin-mediated F-Actin elongation rate was dependent on the phase of the cell cycle and embryonic stage. We subsequently showed that elongating Formins saturate available barbed ends of Actin filaments, converting a local biochemical gradient of RhoA activity into a polar network architecture. In second study, focusing on the kinetics of the RhoA activation cascade, we developed and functionally challenged a simple numerical model. This model takes advantage of the measurements of the dynamical parameters of the Myosin, downstream effector of the RhoA activation cascade, to predict the temporal evolution of this cascade. I propose that this simple and generic model – which can in essence fit any activation cascade – offers a simple mathematical framework to understand the temporal dynamics of signaling cascades, and the delay and change in the shape of the response which can be observed between the input and the output of a cascade.

Résumé court en français :

L'architecture et la dynamique du cortex d'Actine joue un rôle central dans la contractilité cellulaire et la morphogénèse des tissus. La modulation locale de la dynamique du réseau d'Actomyosine dépend majoritairement de la cascade d'activation de RhoA. Dans ma thèse, j'ai combiné des approches de microscopie quantitative en TIRFM, de l'imagerie en molécule unique, des simulations numériques et de la modélisation mathématique simple pour explorer l'architecture dynamique du réseau sous-jacent aux contractions pulsées dans un modèle simple : le jeune embryon de *C. elegans*. En se concentrant sur la Formine, élongateurs de l'Actine, nous avons observé que l'élongation de la F-Actine était catalysée par une population spécifique de Formines corticales – appelées Formines élongatrices – qui montrent une mobilité de type balistique. Nous avons ensuite montré que les Formines saturent les extrémités barbées disponibles et convertissent un gradient biochimique local de l'activité de RhoA en un réseau d'architecture polaire. Dans une seconde étude, en se concentrant sur la cinétique de la cascade d'activation de RhoA, nous avons développé un modèle numérique simple. Celui-ci tire profit des mesures des paramètres dynamiques de la Myosine, un effecteur terminal de la cascade d'activation de RhoA, pour prédire l'évolution temporelle de cette cascade. Je propose ici que ce modèle simple et générique – qui peut par essence s'adapter à n'importe quelle cascade – offre un cadre mathématique simple pour comprendre la dynamique temporelle des cascades d'activation, et le délai et changement dans la forme de la réponse qui peuvent être observés entre l'entrée et la sortie.

Résumé long en français :

Les cascades d'activation sont définies par une succession séquentielles d'activation de protéines de signalisation. Un stimulus provoque l'émission d'un signal qui est propagé au travers d'une cascade d'activation ce qui déclenche une réponse appropriée de la cellule. Ces stimulus peuvent venir de l'extérieur et répondre par exemple à un stress ou une modification de l'environnement de la cellule ou de l'intérieur et provenir d'une activation programmée de la cascade d'activation ce qui aura pour conséquence la différenciation de la cellule par exemple. L'activation de la cascade mène généralement à l'activation d'un effecteur terminal donnant lieu à l'expression d'un gène ou une modification des propriétés biochimiques ou mécaniques de la cellule. Le signal transmis par la cascade d'activation possède donc des caractéristiques précises pour permettre cette réponse avec une intensité précise et un timing précis, une erreur dans le timing menant généralement à un échec dans la mise en place de la fonction biologique. En particulier une même cascade recevant deux signaux différents peut dans certains cas donner lieu à deux fonctions biologiques différentes. C'est le cas de la cascade MAPK/Erk dans les cellules PC12, où une stimulation soutenue provoque la différentiation tandis qu'une stimulation transitoire de la cascade provoque la prolifération des cellules. Pendant la morphogénèse, le timing est crucial, en effet un échec dans l'activation d'une cascade au moment opportun mènera le plus souvent à des anomalies dans le développement et à la mort de l'embryon.

Ici, nous proposons d'analyser le déroulement d'une cascade simple pendant le développement embryonnaire précoce d'un métazoaire, en utilisant l'exemple canonique de la cascade d'activation de RhoA. Cette activation déclenche le recrutement local et l'activation de la Formine qui catalyse l'élongation les filaments d'Actine aux extrémités barbées. Les Formines sont responsables de la formation d'un réseau composé de longs filaments d'Actine, sans branchements (ceux-ci étant polymérisés par le complexe Arp2/3 à partir de filaments déjà présents) à partir de monomères d'Actine liés à une protéine co-facteur, la Profiline, depuis le cytoplasme. En parallèle, RhoA déclenche le recrutement et l'activation de ROCK qui à son tour active la Myosine. La Myosine est un hexamère composé de deux chaines lourdes, deux chaines légères régulatrices et deux chaines légères essentielles. Celles-ci forment ensemble une protéine dont les têtes globulaires ont une activité motrice dépendante de l'hydrolyse de l'ATP et dont la queue peut se polymériser pour former des mini-filaments

formés de plusieurs dizaines de têtes de Myosine. La Myosine est normalement dans un état inhibé où tête et queue interagissent, la phosphorylation par ROCK des chaines légères régulatrices est suggérée comme étant responsables de la déstabilisation de ces interactions, permettant l'activation de la Myosine, la déphosphorylation et donc l'inactivation étant médiées par la Myosine Phosphatase. Des travaux antérieurs ont montré que le recrutement de l'Actomyosine au cortex cellulaire est essentiel dans une large variété d'événements morphogénétiques comme l'établissement de la polarité ou la gastrulation. La cascade d'activation de RhoA conduit ainsi à une densification locale et transitoire, menant à une contraction de la zone avant relaxation de la contraction pulsée et retour au niveau de densité basale d'Actomyosine corticale. Dans ce contexte, on peut mesurer, à l'endroit de la contraction pulsée, un délai stéréotypé entre l'activation du régulateur en amont, RhoA, et le recrutement et l'activation de l'effecteur en aval, l'Actine ou la Myosine.

Dans mes travaux de thèse, je propose d'utiliser cette cascade d'activation RhoA comme modèle pour mieux comprendre et modéliser la cinétique temporelle observée dans toute cascade d'activation au cours du développement. J'ai réalisé cette étude par l'observation des contractions pulsées au cortex des jeunes embryons de *Caenorhabditis elegans* à l'aide de la microscopie de fluorescence par réflexion totale TIRF, de la molécule unique, de simulations numériques et de modèles mathématiques simples. A l'aide de ces outils, je propose une meilleure compréhension de l'architecture de ces contractions pulsées à différents stades du développement précoce.

Des travaux antérieurs par Michaux, Robin *et al.* ont montré qu'un délai de plusieurs secondes pouvait être observé entre l'activation de RhoA et le recrutement de la Myosine au cortex. Dans mes travaux, j'ai d'abord procédé à une caractérisation fine de la dynamique entre deux étapes consécutives de la cascade. En utilisant la microscopie TIRF, je me suis intéressée aux différentes étapes de la cascade d'activation RhoA, en utilisant la Myosine comme repère pour mesurer le délai dans la cascade au cortex d'embryons précoces de *C. elegans*. J'ai pu mettre en évidence que le délai de 4,5 s que je pouvais observer entre RhoA et la Myosine se retrouvait entre ROCK et la Myosine montrant que toutes les étapes au sein de la cascade d'activation n'étaient pas équivalentes en termes de temps écoulé. J'ai aussi pu montrer que, contre toute attente, l'Actine et la Myosine, les deux effecteurs en aval de la cascade d'activation, n'étaient pas recrutés de façon synchrone mais plutôt que l'Actine était recrutée 0,5 s avant la Myosine, suggérant que la Myosine pouvait être recrutée directement

sur les filaments d'Actine. Mes résultats ont permis de mettre en évidence qu'une variabilité non expliquée par la variabilité dans la mesure du délai pouvait être observée, suggérant que le système travaille dans une gamme de délai plutôt qu'avec un délai strict et est robuste à des changements mineurs dans la valeur du délai entre le recrutement des protéines. En complément, j'ai pu montrer qu'aucun délai significatif ne pouvait être observé entre le recrutement de la chaîne lourde et la chaîne légère régulatrice de la Myosine, suggérant que le complexe est recruté au cortex déjà pré-assemblé à partir du cytoplasme.

Ensuite en utilisant la microscopie en molécule unique, je me suis concentrée sur la dernière étape de la cascade et j'ai mesuré la modulation dynamique du taux d'attachement (K_{on}) et de détachement (k_{off}) de la Myosine en utilisant une souche sur-exprimant en faible quantité la Myosine fusionnée à une GFP. Nous avons émis l'hypothèse que la variation locale du nombre de molécules de Myosine n'était dépendante que de ces deux paramètres et que donc on pouvait exprimer cette variation de la façon suivante :

$$\frac{dN}{dt} = K_{on} - k_{off} * N$$

Cette expression permettant de calculer, à l'équilibre, une valeur d'**objectif de densité** $N^* = \frac{K_{on}}{k_{off}}$. L'observation de cette valeur d'objectif de densité montre que celle-ci ne correspond pas à la valeur réelle moyenne observée pour le nombre de molécules au cortex. De plus, j'ai pu observer qu'un délai entre objectif de densité et valeur réelle moyenne de nombre de molécules pouvait être mesuré et que celui-ci correspondait à ~4,25 s. J'ai pu donc mettre en évidence que le délai observé entre ROCK et la Myosine pouvait être expliqué par la seule observation de la dynamique de la Myosine. A l'aide de simulations numériques, j'ai pu montrer que ROCK avait probablement un effet plus important sur le k_{off} de la Myosine que sur son K_{on}.

J'ai ensuite mis à l'épreuve de façon fonctionnelle ce modèle simple qui tire profit des mesures de K_{on} et de K_{off} pour prédire l'évolution temporelle de cette cascade. J'ai pour cela répéter des mesures de *Kon* et de *koff* de la Myosine dans un contexte où la Myosine Phosphatase était mutée et non fonctionnelle, menant à une absence de déphosphorylation et de désactivation de la Myosine par sa phosphatase. Mes travaux montrent que dans ce cas le délai entre ROCK et Myosine n'est pas affecté mais que l'on peut observer une diminution de la différence d'amplitude entre valeur d'objectif de densité et valeur réelle du nombre de molécules observées, ceci pointant vers l'idée que le système est déjà « à plein régime ». Ces

résultats me permettent de suggérer qu'activation et recrutement de la Myosine sont deux événements séparés, que le premier a lieu dans le cytoplasme avec une régulation globale tandis que le deuxième a lieu au cortex avec une régulation locale.

Afin de confirmer ces résultats je me suis intéressée à la branche « Actine » de la cascade RhoA où RhoA active et recrute la Formine aux extrémités barbées des filaments d'Actine présentes localement, ce qui va promouvoir l'élongation de ces filaments. J'ai pu mesurer un délai équivalent au sein de cette branche par rapport à celui mesuré dans la branche « Myosine ». L'observation de la dynamique de l'Actine en molécule unique de façon similaire à ce décrit plus haut (par la mesure du nombre de molécules présentes au cours du temps, du K_{on}, du k_{off} et le calcul de la valeur d'objectif de densité) m'a permis de conclure que le délai observé dans la branche de la cascade de RhoA lié à l'Actine pouvait aussi être expliqué par notre modèle. A nouveau la perturbation de la dynamique du système, ici par la déplétion de la Cofiline responsable du renouvellement des monomères d'Actine dans les filaments, n'a pas mené à une réduction du délai observé, ce qui suggère à nouveau une robustesse du système contre la perturbation du délai et une potentielle importance biologique du maintien de ce délai à ce stade. Cette dernière hypothèse est aussi soutenue par des simulations numériques supplémentaires que nous avons réalisé et qui montrent qu'il existe un délai optimal pour permettre la meilleure transmission de la tension liée à la contraction pulsée au sein du réseau.

Je propose que ce modèle simple et générique – qui peut par essence s'adapter à n'importe quelle cascade d'activation – offre un cadre mathématique simple pour comprendre la dynamique temporelle des cascades de signalisation, et le délai et le changement dans la forme de la réponse qui peut être observée entre le début et la fin de la cascade.

Afin de mieux caractériser l'architecture d'un réseau d'Actomyosine efficace pendant le développement, j'ai évalué la dynamique de la structure d'une contraction pulsée en suivant le comportement de la Formine. En utilisant la microscopie TIRF en molécule unique, des simulations numériques et des modèles mathématiques simples j'ai ainsi pu mettre en évidence l'existence de deux populations de Formines au cortex caractérisée par une différence de comportement au cortex. J'ai pu observer une population de Formines dont le coefficient de diffusion est significativement réduit (ci-après désignée en tant que population

subdiffusive) et une population au mouvement balistique dont le coefficient de diffusion est significativement augmenté (ci-après désignée en tant que population superdiffusive). Nous suggérons que la population subdiffusive correspond à des Formines *recrutées* au cortex mais non actives et que la population superdiffusive correspond à une population de Formines *élongatrices*, celles-ci étant actives et allongeant les extrémités barbées des filaments d'Actine. Nous avons ensuite pu montrer que les Formines élongatrices, minoritaires, apparaissaient en premier et que seulement ensuite nous pouvions observer au niveau de la contraction pulsée l'émergence des Formines recrutées mais non actives.

Ces résultats suggèrent que les Formines sont recrutées au niveau du pulse, se lient aux extrémités barbées jusqu'à saturation et que les Formines subdiffusives correspondent à des Formines activées n'ayant plus d'extrémités barbées libres accessibles et restant donc recrutées localement au cortex. Nous avons aussi montré que les Formines élongatrices assemblent rapidement les filaments avec les extrémités barbées pointant vers l'extérieur formant un réseau polaire, ceci favorisant une contraction rapide du réseau.

J'ai également montré que la vitesse de polymérisation des filaments d'Actine par les Formines dépend du stade du cycle cellulaire, la vitesse diminuant significativement lors de la cytokinèse. En répétant les mesures sur les vitesses d'élongation de Formine à l'interphase et durant la mitose dans un contexte où la quantité du complexe Arp2/3 est diminuée, j'ai cependant montré que la vitesse d'élongation des filaments n'est pas directement liée à la présence du complexe Arp2/3 dans la cellule.

Pour terminer, j'ai proposé dans cette thèse une estimation de la longueur moyenne des filaments d'Actine pendant l'interphase et pendant la mitose. Cette longueur dépend de la vitesse d'élongation des Formines (v), la durée d'élongation des Formines (t_e) et la dépolymérisation de l'Actine (t_{dep}), suivant l'expression suivante :

$$L = \frac{v}{\frac{1}{t_e} + \frac{1}{t_{dep}}}$$

J'ai pu estimer que les filaments d'Actine avaient une longueur moyenne de ~1,79 µm à l'interphase et ~1,75 µm durant la mitose.

En conclusion, durant ma thèse j'ai pu donner un meilleur aperçu de l'architecture du réseau d'Actomyosine corticale dans le jeune embryon de *C. elegans* à différents stades du développement et à différents moments du cycle cellulaire. En m'intéressant aux contractions pulsées j'ai pu montrer que l'assemblage rapide des filaments d'Actine par les Formines se

faisait de façon polaire avec les extrémités barbées pointant vers l'extérieur du pulse. J'ai montré que la vitesse de l'élongation des filaments est dépendante du stade du cycle cellulaire mais n'est pas montré de différence significative dans cette vitesse en l'absence du complexe Arp2/3.

En conclusion, j'ai pu par ce travail de thèse mieux caractériser l'architecture des contractions pulsées au cortex du jeune embryon de *C. elegans* et que cette architecture est intimement liée à sa composition. En effet, le recrutement des Formines élongatrices promeut une architecture polaire des contractions pulsées où les Formines se lient rapidement et saturent les extrémités barbées, la vitesse de l'élongation étant dépendante du stade du cycle cellulaire. Ce recrutement est dépendant de la cascade d'activation RhoA, cascade dans laquelle j'ai pu observer un délai cinétique entre l'activation des effecteurs en amont et le recrutement et l'activation des effecteurs, l'Actine et la Myosine, en aval. Ce délai est important pour la transmission de la tension produite par la contraction pulsée au sein du réseau et peut être expliqué simplement par la dynamique d'attachement et de détachement de la Myosine. Ce modèle peut être appliqué pour comprendre les délais cinétiques observées dans d'autres cascades d'activation.

Introduction

During development, profusion of activation cascades is activated, ligands bind to receptors, proteins change conformation, signaling pathways are triggered. These complex and interconnected networks of proteins are finely regulated in each cell, so to develop a viable organism. Successful morphogenesis, process by which an organism develops its shape, is dependent on regulations of these activation cascade in time and space. These regulations are diverse and occur at the level of the cell, the tissue and even the whole organism. Yet we simply fail to understand how a finite number of biochemical reaction triggers this large number of complex remodeling of cell biochemical composition, cell shape and overall tissue organization. During my PhD, I aimed at a better understanding the regulation of cell shape changes by simple-looking activation cascade regulation.

In this introduction, I will first describe what is known about information propagation through activation cascade signaling. Then, focus on the Actomyosin cytoskeleton, its related activation cascade and regulatory proteins. Finally, I will discuss the role of Actomyosin cytoskeleton during morphogenesis, focusing on our model organism, the early *C. elegans* embryo.

1 ACTIVATION CASCADES

Activation cascades are a widespread mode of signaling required for cells to tailor an adequate response to a stimulus. They consist in the activation of a protein, which will trigger the sequential activation of several other downstream proteins until a final effector which will have a visible and/or measurable effect on the cell by changing its properties, such as the expression of a set of genes, its biochemical composition, or its mechanical properties. The stimulus can vary in nature and provenance. It can be external and reflect a biochemical or a mechanical change in the environment, and drive cellular adaptation to the stimulus. The stimulus can also be internal and respond to a fated activation of the cascade, triggering the expression of a specific gene required for development or for differentiation, for example. Stimulus perception is particularly important during embryogenesis, where proper spatio-temporal activation and localization of effectors are key for the successful development of the embryo, and failure in activation at the proper time and place of the correct activation cascade or with the incorrect duration or intensity may result in potentially lethal developmental defects.

1.1 ENCODING THE INFORMATION INTO THE SIGNAL

Information is encoded in the signal transmitted through an activation cascade. The stimulus is translated into a signal that will be decoded by the effectors of the activation cascade. In this context, signal is defined by the ensemble of coding features that characterizes the signal and that encodes the stimulus received by the cell. More specifically, the way in which the signal is encoded is the information of the cell's response to the stimulus.

The mitogen-activated protein kinase (MAPK) cascade, a ubiquitous activation cascade, highly conserved from yeast to mammals, is a canonical signaling cascade that plays a fundamental role in the control of common cellular processes, including cell growth and division, migration, differentiation, stress response and apoptosis (Kholodenko and Birtwistle, 2009). It consists in a succession of kinases in which an activated kinase phosphorylates and activates the next kinase in the cascade and so on. Typically, the cascade is composed of three kinases: a MAPK, a MAPK kinase (MAPKK or MAP2K) and a MAPKK kinase (MAPKKK or MAP3K). Kinases are then dephosphorylated by a set of phosphatases. Activation of MAPK cascade can lead to variety of outcome and one of the regulation of this outcome is the way this cascade

is activated. The MAPK/Erk pathway is conserved in vertebrates and extensively studied (Wei et al., 2020). In PC12 cells, exposure to NGF triggers sustained ERK (MAPK) activity which leads to differentiation, whereas these same cells exposed to EGF proliferate in response to a transient activation of ERK (Marshall, 1995). It is the difference in the type of ERK activation (sustained vs transient) that is the key for the regulation of the response. This is supported by recent research using Phy-PIF optogenetic tool to stimulate ERK activity for various duration and frequency. They show that stimulation too short in time (less than 4 min) will be rejected and result in no outcome, but stimulation in broad timescale from 4 min to several hours will be efficiently transmitted. Furthermore, they show difference in outputs between transient (20 min) and sustained (more than an hour) ERK activation, stating that there are pathways set up for 'fast' response which will be triggered in both transient and sustained activation (for example PKC signaling) and 'slow' response only triggered by sustained activation (for example STAT3) (Fig. 1, (Toettcher et al., 2013)). MAPK activation cascade leading to different outcomes is not an isolated example and this underlies the importance of precision in the signal (Behar and Hoffmann, 2010). Hence, activation cascades can have different outcome depending on the time and place they are triggered.

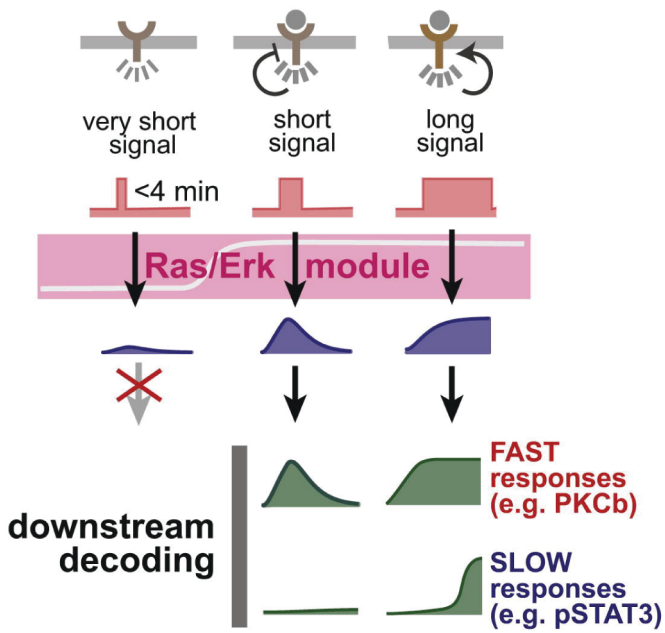

Figure 1. MAPK activation leads to different outcome depending on the stimulation duration. A broad range of dynamics are transmitted through the Ras/MAPK module to Erk activation (representative timecourses shown in blue) and are differentially sensed by "fast" and "slow" downstream decoding modules (representative timecourses shown in green). From (Toettcher et al., 2013).

Therefore, it is important to understand how the information is encoded in order to achieve this diversity in response depending on the stimulus. This is particularly important to be able to manipulate these activation cascades, to precisely affect cells using tools like optogenetics. In this section, I will describe generic strategies that have been observed to encode information into the signal in activation cascade: spatial and temporal segregation of effectors into gradients, modulation in frequency and amplitude of the signal and finally threshold effect response.

1.1.1 Spatial segregation of the effectors

Even inside an individual cell, many physiological events (including during development) rely on the establishment of protein gradient. For a signaling gradient to be established only one condition is required: the spatial segregation of opposing reactions in a shared protein-modification cycle (Kholodenko, 2006). For example, a gradient of a protein that is activated through phosphorylation can be established if its kinase and its phosphatase are not in the same cell compartment. In mitotic cells, Aurora B destabilizes kinetochore-microtubule interaction by phosphorylation of several components of the outer kinetochore. In anaphase, the gradient in phosphorylation is highest on chromatin near the spindle midzone and lowest near the spindle pole. The phosphorylation by Aurora B is counterbalance by PP1-RepoMan phosphatase activity, which is shown to contribute to faithful chromosome segregation. Thus, a balance between opposing kinase and phosphatase activities shapes the spatial gradient of Aurora B-dependent phosphorylation on anaphase chromatin (Fuller et al., 2008; Wurzenberger et al., 2012). Importantly, the size of the gradient is partly determined by the diffusivity (if a protein is emitted from a cell compartment, as the distance from the source increases concentration in this protein decreases) and, if present, by the activity of the enzymes that will take this protein as substrate.

Spatial gradient can last in time (as the gradient of Bicoid in *Drosophila* embryo for example, stable for more than 30 min (Little et al., 2011)) but can also be transient. This is the case for protein of the cell cycle: cyclin-dependent kinase CDK1/CDC2 is activated when cell goes into mitosis and phosphorylates a GEF called RCC1 in the cytoplasm, which then goes and binds to the chromosomes and catalyzes the activation of RanGDP into RanGTP. This leads to an establishment of gradient of active Ran: high concentration of RanGTP near the mitotic

chromosome and low concentration in the surrounding area. Then in G1 phase CDK1/CDC2 activity is low and therefore RCC1 activity drops as well, the gradient is not maintained. Gradient of Ran is therefore dependent of the temporal activation of CDK1/CDC2 (Kholodenko, 2006; Li and Zheng, 2004). Spatial distribution can therefore be intimately linked with temporal distribution and time needs to be taken in account when trying to decipher spatial information from activation cascade.

In conclusion, inside individual cells, with all other conditions being equal, information for cellular processes (like cell cycle) can be regulated in time and space by gradients. Therefore, it is the difference in the cell local intracellular biochemistry which is the signal to the cell and which will trigger difference in cell response. Spatial regulation of signaling proteins is a way of encoding the signal, differentiating different groups of receptors of the signal depending on the position. In the following sections, we will see how the signal itself can be modulated to vary the information it carries.

1.1.2 Amplitude of the activation signal

A signal is characterized by different properties, among which: amplitude, frequency, duration, periodicity. Amplitude of a signal characterizes the maximum value of a signal compared to its average. This means that increasing the amplitude of a signal correspond to increasing the maximum value reached by a signal. For example, in an oscillating system, therefore having a sinusoidal shaped signal variation, increasing the amplitude would correspond to an increase in maximum and equivalent decrease in minimum, thus without changing the average value of this signal. Amplitude is a well-studied way of encoding information in a signal, and is the typical regime when the system is not in a saturated regime. Saturation of a system means that all of one of the components of the system is not available anymore at all time, precisely saturation in an enzyme correspond to the moment where at all time all the enzymes are catalyzing a reaction and therefore increase in the concentration in the substrate will not lead to increase in reaction velocity. In a linear system, increase in signal input correspond in an increase in the cell output. Saturated systems cannot sense variation in the amplitude anymore and will always give the ‘maximum answer’ (Behar and Hoffmann, 2010).

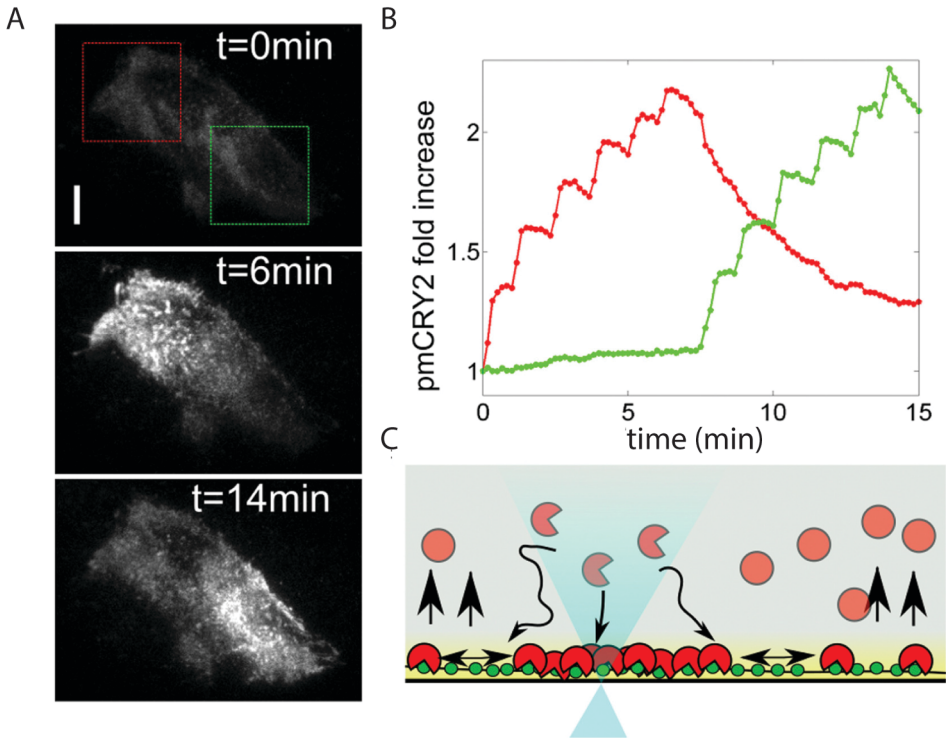

Figure 2. Physical processes responsible for local recruitment of pmCRY2. (A) CRY2-mCherry TIRF images before illumination (*top*) and after six local activations in the indicated red box (*middle*) and after six activations in the indicated green box (*bottom*). **(B)** Quantification of the relative increase of signal in the red and green region over time. **(C)** Scheme of the biophysical processes involved in CRY2-mCherry localization at the plasma membrane. Inactive cytoplasmic CRY2 (*solid red circles*) changes conformation upon illumination into an active state (*open red circle*) that diffuses to the membrane and binds CIBN (*solid green circles*). (*Yellow region*) Evanescent TIRF field. (*Black arrows*) Diffusion-limited membrane recruitment, lateral diffusion, and dimer dissociation altogether representing the cycle of CRY2 in a steady and localized stimulation (*blue cone of light*). From (Valon et al., 2015).

Work by Valon *et al*. provide a valuable quantitative insight on this question (Valon et al., 2015). In this study, the protein CRY2 of the optogenetic system CRY2/CIBN is recruited at the plasma membrane upon blue light illumination (Fig. 2C). With each pulse of illumination, the total quantity of CRY2 recruited at the plasma membrane increases, between pulses the protein concentration decays but with a reduced slope compared to the one of recruitment. The authors observed that, upon sequential laser pulses –specifically pulses of 100 ms spaced out by 80 s– of equal duration, the first pulses lead to a much more potent recruitment of CRY2 at the plasma membrane, the additional increment of recruited CRY2 decreasing with each pulse (Fig. 2A-B). The authors interpret this saturation of the system by postulating that the time elapsing between two consecutive pulses not being sufficient to diffuse or actively release the recruited protein (CRY2/CIBN having a slow dissociation), causing a decrease in the sensitivity of the cascade to a repeated input signal of constant strength.

Amplitude is usually intrinsically linked to the duration of the signal, an easily saturable system will rapidly loose its sensibility to the signal amplitude if the signal duration makes the system unable to lower down below the biological threshold of activation (Behar and Hoffmann, 2010).

1.1.3 Frequency of the activation signal

During development, it is common to observe oscillatory behaviors (periodic activation and recruitment repeated throughout time) in the activation and/or recruitment of a protein. Oscillations in activation and recruitment of cytoskeleton components and signaling proteins have been observed in a large number of cell types and organism. One very well studied example is the MinCDE system in *Escherichia coli* division. Assembly of the Z-ring machinery responsible for cell division is dependent on the establishment of a gradient of negative regulators which inhibits the formation of the Z-ring away from midcell. A gradient of MinC is formed by an oscillatory mechanism that is determined by MinD and MinE. Membrane-bound MinD forms a complex with MinC, which inhibits Z-ring assembly, MinD accumulates at one cell pole, detaches (which is mediated by MinE which triggers MinD ATPase activity), diffuses and accumulates at the opposite pole (Fig. 3, (Halatek et al., 2018; Lutkenhaus, 2007)). These processes can be macroscopically observed as waves of MinD periodically moving to one side of the cell to the other, these oscillations being required for the proper positioning of the Z-ring.

Frequency in the oscillations (meaning the number of pulses per time unit) is another way of encoding information in an activation cascade. In order to properly decode this information, the system must be able to distinguish between an increase in the number of peaks per time unit and an increase in pulse duration (Behar and Hoffmann, 2010). In Valon *et al.* (Valon et al., 2015), they demonstrate that in their system, the steady-state of the system is reached in a shorter time, with fewer pulses, when the system has been previously activated by a round of high-frequency pulses.

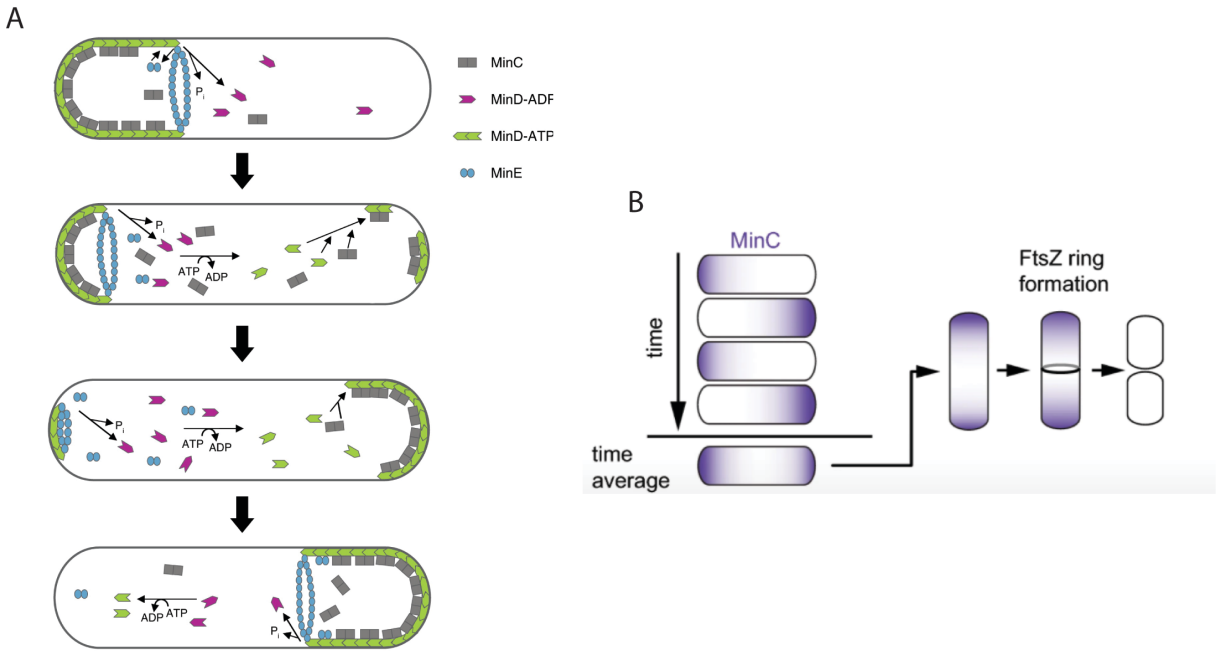

Figure 3. Oscillation of Min proteins in *E. coli*. (A) MinD-ATP binds to the membrane and recruits MinC. MinE displaces MinC and stimulates MinD ATPase, causing release of the proteins from the membrane. MinD diffuses, undergoes nucleotide exchange to regenerate MinD-ATP, eventually binds to the opposite pole and starts again the cycle. From (Lutkenhaus, 2007) **(B)** Oscillations of accumulation of MinC at each pole can be observed and eventually lead to positioning of the Z-ring at midcell. From (Ramm et al., 2019).

Remarkably the composition of a material may also have a direct influence on the oscillatory behavior. High contractility instability might be responsible for oscillatory behavior, as suggested by studies on *Caenorhabditis elegans* embryo cortex where material composed of Myosin motors drives contractile forces through pulsed contractions initiated by oscillatory RhoA (Nishikawa et al., 2017). Although negative feedback loops do not guarantee oscillations, it is thought that all oscillating systems must possess at least one negative feedback loop (Ferrell, 2013).

1.1.4 Threshold effect

Once signal has been integrated through activation cascade until the ultimate effector(s), the system needs to respond accordingly. However, some systems may not display a linear response to change in signal, whether it is in intensity, frequency or duration. During development, junction remodeling is dependent on RhoA activation (Simões et al., 2014). It leads to rapid contractions which drive junction shortening through a ratchet mechanism. Optogenetic activation of RhoA has given evidence that short pulses of RhoA will lead to reversible deformation, meaning that the cell will go back to its original shape after relaxation of the contraction, whereas long pulsed contractions will produce irreversible change in

junction length. This shows that minimal duration is required for adaption of the system to the deformation, epithelial junctions behave elastically to short timescale activations RhoA, irreversible deformation being threshold-dependent (Cavanaugh et al., 2020; Staddon et al., 2019). Here the system is set as to develop a response only once a certain threshold is crossed. This give rise to a filtering in a signal being too weak, potentially not rising above the noise signal.

Additionally, episodic pulses of RhoA activity, separated by periods of rest, can induce greater degree of irreversible change than a prolonged pulse of the same length. Multiple rounds of RhoA activation allows a ratcheting mechanism in junction shrinkage.

Mechanic deformation can, therefore, also be a signal for triggering the activation of a cascade. Similar to a biochemical signal, it needs to be strong enough in order to trigger a response from the cell. Mechanical and biochemical changes in the cell properties can be reversible or irreversible depending on the information encoded in the signal.

Variation in input signal is important to precisely encode information into the signal propagated through activation cascade. Once signal is integrated, the system will modulate its properties according to the received signal. The following section will give an overview of the biochemical and mechanical change that can be observed in a system, reviewing what is known as response: change in equilibrium state, pattern establishment, how these responses can vary to adapt to input signal and finally what is known is kinetic delays in activation cascade.

1.2 Steady-state systems

Biological system are out-of-thermodynamical-equilibrium systems that constantly use energy to establish and maintain their spatial, chemical and physical organization. A system is at steady-state when its properties do not change over time. Perturbations may drive the system out of its steady-state. If the steady-state is stable, small perturbations will not affect the steady-state, while in unstable/meta-stable system, small perturbations may drive the system out of its state. Signal in activation cascade typically drive the cell out of its current steady-state, triggering an adaptive response to the input signal.

1.2.1 ESTABLISHING STEADY-STATES

Biological systems are intrinsically complex, often displaying hundreds of coupled, intertwined reactions. Yet, despite this complexity, their outcome is surprisingly, strikingly robust. Indeed, exploring the dynamics of even mathematically simple systems can already prove daunting and reveal wide ranges of chaotic, unpredictable behaviors. Simple systems can already display a large variety of behaviors depending on how their players interconnect with each other. When considering three nodes, a system can already achieve more than 15 000 different topologies and display complex behaviors such as adaptation. Adaptation correspond to the system ability to respond to a change according to an input signal and then return to its pre-stimulated state, even when the change in input signal persists. This is important in order to maintain sensibility of the system, once appropriate response has been provided to the stimulus (Ma et al., 2009). A single negative feedback loop might be sufficient to set oscillations in a system, but activation cascades are typically more complex and frequently integrate functional motifs relying on positive feedback loops, double-negative feedback loops, etc. A two-component, negative feedback loop can exhibit damped oscillations to a stable steady state but not sustained oscillations. These require a third component to introduce a time delay in the feedback loop, essential parameter for oscillations to be observe (Griffith, 1968; Tyson et al., 2003).

Positive feedback loops are known to amplify signals, being therefore responsible for sensitivity of the system. These loops can function as bistable, hysteretic or irreversible switches (Ferrell, 2013). Bistable systems are systems where two mutually exclusive steady-states exist, meaning that at equilibrium the system is in either one of the two stable states. The cell cycle is an example of a well-studied bistable system: during mitosis Cyclin-dependent kinase 1 (Cdk1) turns on its activator, a phosphatase called Cdc25 and turns off Wee1, when going back to interphase Cdc25 turns back off and Wee1 turns back on. Only one steady-state of Cdk1 activity is possible at a given time, these loops constitute a bistable trigger for the cell cycle oscillator. Cdk1/Cdc25/Wee1 is highly conserved in evolution. First theoretical and later experimental studies show that Cdk1/Cdc25/Wee1 bistable trigger functions as a hysteretic switch (Fig. 4, (Ferrell, 2013; Novak and Tyson, 1993a; 1993b; Pomerening et al., 2003; Sha et al., 2003)). Hysteresis means that the state of the system also depends on the state it is coming from, it works like a memory in which the system resists the change in steady-state. This characteristic allows the system to convert a continuous increase of an input signal

(concentration of a protein for example) into a discontinuous change in the output (the activity of an another protein for example) (Ferrell, 2013).

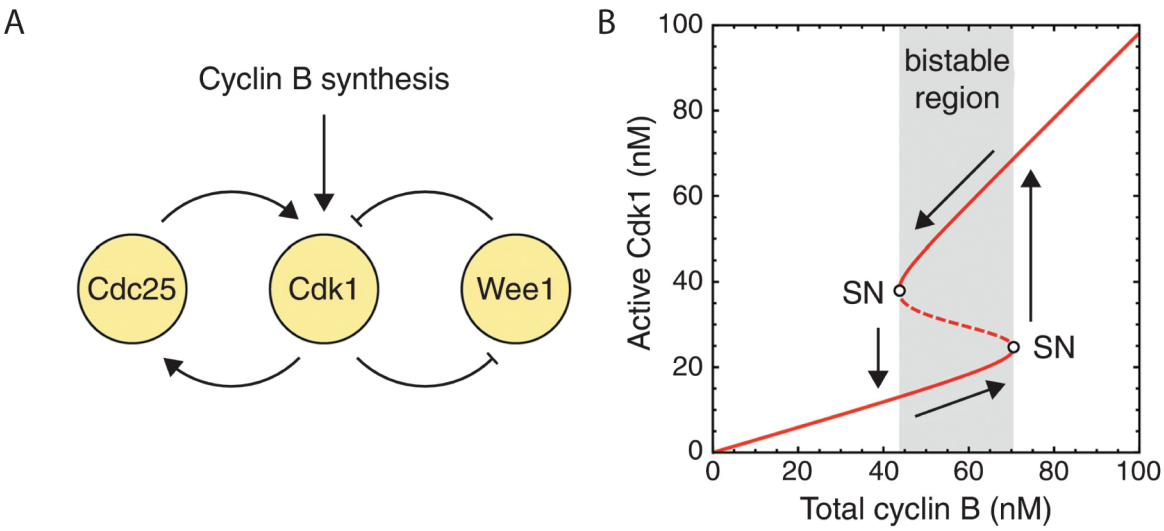

Figure 4. Positive feedback, hysteresis, and bistability. (A) The Cdk1/Cdc25/Wee1 mitotic trigger. **(B)** Input/output relationship for the mitotic trigger. The solid red curves represent stable steady states and the dashed curve represents an unstable steady state. The bistable region is shown in gray, and the positions for which the system switches to an equilibrium state to another (saddle-node bifurcations (SN)) are designated by open circles. From (Ferrell, 2013).

Observation of such behavior displayed by three-nodes systems and described above can already seem complex and yet biological system usually display a larger number of interconnected players. In biological context, activation cascades are intimately interconnected and regulate each other by a complex network of activations and inhibitions, therefore these models could seem doomed to fail to properly capture reality. Yet current models managed to describe a panel of experimentally observed behavior. This chapter aims to try and describe how these models have helped our understanding of biological processes.

During development, fated activation of specific cascades will regularly set up new steady-states, to which the cells of the embryo need to adapt, whereas keeping the ability to respond to potential perturbations (for example mechanical stress). In this section, we will expose the common ways of establishing new steady-states in this context. Adjusting to new steady-states, establishing patterns (transient or permanent), are a part of the repertoire of responses to signals, thereby shaping the cell's response to the information carried in the signal.

1.2.2 PATTERNING

Patterning is the establishment in a system of a chemically non-uniform steady-state. In his seminal 1952 paper entitled "the chemical basis of morphogenesis", Turing demonstrated that –under a very limited set of assumptions– the simple interplay between molecular diffusion and chemical interactions can give rise to spatial patterns temporally stable in time, also known as Turing patterns (Turing, 1952). Turing further showed that lateral diffusion can cause instability even if the system is in a stable chemical equilibrium. Turing found that the interaction between chemical reaction and molecular diffusion are sufficient to give rise to pattern formation, random perturbation being amplified just by lateral instability. Early on, this has been demonstrated for general reaction-diffusion system with two chemical components, the 'activator-inhibitor' mechanism by Gierer and Meinhardt (Gierer and Meinhardt, 1972). This mechanism relies on few principles: slow activator and fast inhibitor diffusion, autocatalytic production of the activator which stimulates the production of the inhibitor that in turn suppresses the production of the autocatalytic activator.

Another interpretation of Turing's mathematical analysis of two-component systems is the 'activator-depletion' model. Here, instead of an inhibitor, the system has a substrate, still diffusing rapidly, that is depleted by conversion into the activator (Gierer and Meinhardt, 1972; Meinhardt, 2008). The rate of conversion is limited by the available substrate.

While these mathematical models are extremely simple and generic, biological systems in contrast are typically much more complex and do not actually require an activator and an inhibitor to see pattern creation. Importantly, most intracellular patterns are membrane-bound patterns, meaning that part of the proteins implicated in the pattern formation are bound to the membrane: these intracellular patterns are inherently two-dimensional, and consequently highly constrained by the geometry of the membrane and the cell; and they display much lower diffusion coefficients than their cytosolic counterparts. *In vivo*, the 'activator-inhibitor mechanism' often takes the form of a switch in conformation or in activation state of the corresponding proteins, rather than changes in protein concentration driven by protein synthesis and degradation of proteins that drives the system and its pattern formation (Halatek et al., 2018). For example, in *C. elegans* zygote, pattern is established through active intracellular transport of PAR proteins, pattern forming from mutual exclusion of PAR proteins (details of mechanism will be discussed in III). In this type of reaction-diffusion

system, patterning reflects the redistribution of proteins across cells or tissues with underlying mass-conservation rules.

It can be tempting to think activation cascades as simple on/off switches. Overlooking the fact that the information of activation is highly dependent on the way the signal is coded would be a mistake, especially at the time of trying to analyze and control the activation cascades (in particular if searching of pharmacological targets). In response to a stimulus, biological signals can carry information using multiple coding features: timing of the signal peak, its rate of activation or inactivation (e.g. if it is a one-time signal or a periodic one), the phase, the amplitude (variation in maximum and minimum of the signal), the duration (e.g. transient or sustained activation) and the frequency of the signal (e.g. change in number of peaks of signal per time unit) (Fig. 5). Taken together they carry precisely the information for the cell to adapt to the stimulus. In biological system, a single activation cascade can lead to different response in identity (e.g proliferation vs differentiation in PC12 after ERK stimulation) or in intensity (with a linear response, like increase in protein expression level, or not, like response through a threshold). This variation in responses indicates that the system is equipped to decode the difference in the signal. We will see in the following sections, which are the possible decoding tools.

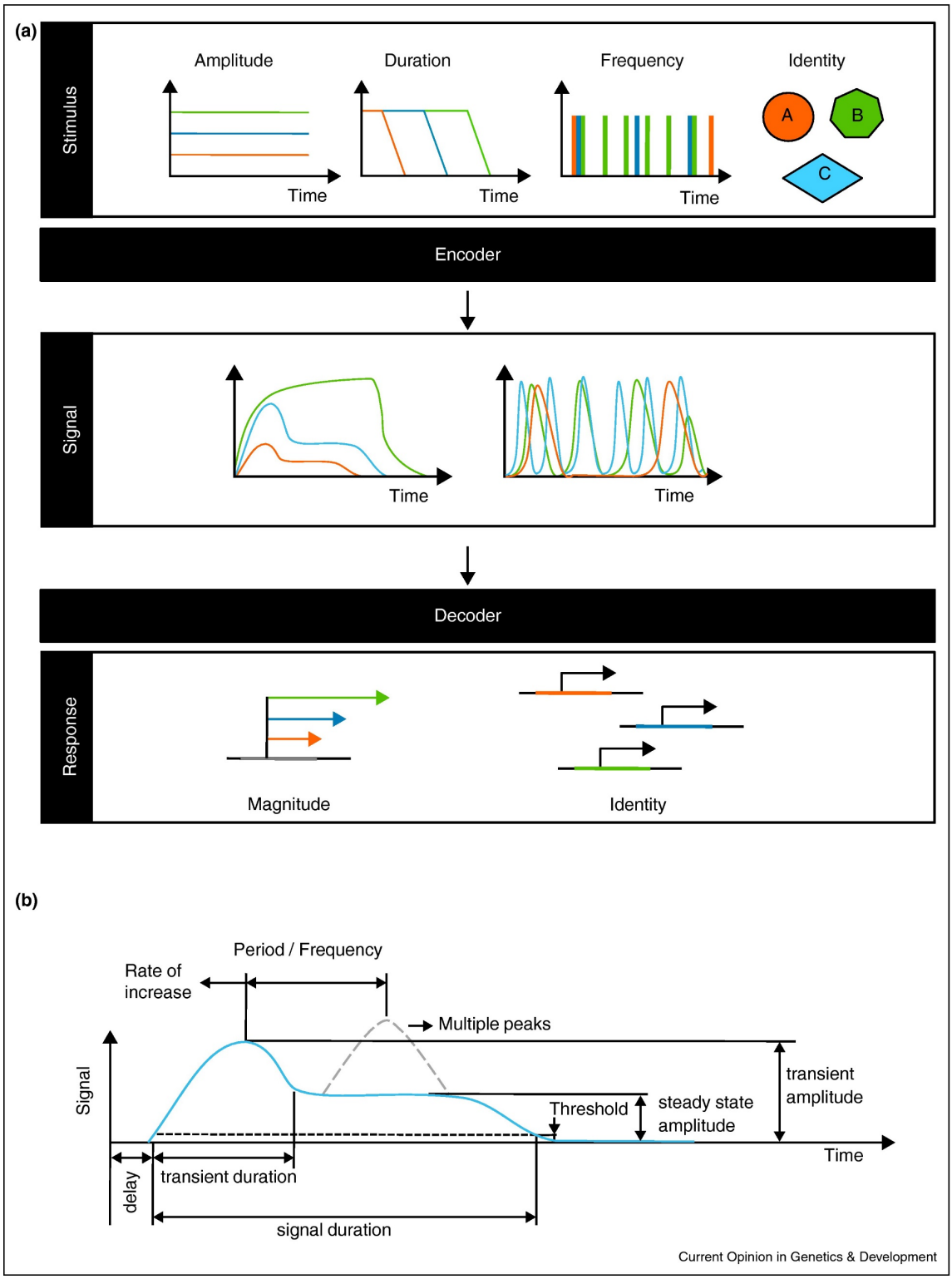

Figure 5. Features of the stimulus are encoded in features of the signal and determine the response. **(a)** features of the stimulus, such as its type (identity), amplitude, duration, or frequency, are encoded by signaling networks into different features. Information contained in the features is decoded and thus determines for example whether a specific gene is activated, by how much, if a specific behavior is triggered, for how long. **(b)** An example of a time course of an amplitude-modulated intra-cellular signal and potential coding features: transient and steady state amplitudes, transient duration, duration over a threshold, number and time between peaks, etc. Adapted from (Behar and Hoffmann, 2010).

1.2.3 DECODING THE SIGNAL

The integration of the signal by the downstream effectors –the decoder of the signal– plays a key role in the dynamics of the response to the signal (Behar and Hoffmann, 2010). Two obvious feature of signal decoders in the cell are identity and magnitude in the response (Fig. 5).

When MAPK/ERK stimulation in PC12 cells leads to proliferation or differentiation, it is a difference in identity of the response depending on the signal, the identity of the output is different depending on the integrated signal. The coding feature of duration of the signal leads two to distinct outcomes, two distinct responses. Importantly it is the stimulation from two different sources (NGF versus EGF), that stimulates the same pathway (MAPK/ERK) in two distinct manner (difference in signal duration) to trigger two different outputs.

In Saccharomyces cerevisiae, the concentration of mating pheromone determines whether cells undergo vegetative growth (low level), chemotropic growth (intermediate level) or mating (high level). The pheromone response pathway is coded as a dose-to-duration signal, meaning that concentration in pheromones is translated as duration of the signal at the MAP2K level but is decoded and converted into maximum amplitude by a MAPK with slow activation kinetics (Behar and Hoffmann, 2010; Behar et al., 2008). In this example, contrary to the previous one, the signal input is identical in identity but the duration of the stimulation of the cascade is different and lead to three different outcomes.

In these two examples, the identity, the type of the response is directly dependent on the identity of the signal, the input (here, the identity of the input itself is indifferent in determining the identity of the output) is different and leads to differential feature in the signal, thus the coding feature being different, the signal provided is different, the outcome is different.

Difference in magnitude can be observed in linear systems, where the intensity or quantity in the response correspond linearly to the transmitted signal. Nunns and Goentoro provided a mathematical model in which they show that canonical Wnt, ERK and Tgfβ pathways behave in some biological contexts as linear input-output systems and provided experimental evidence supporting this model for Wnt and ERK pathways (Nunns and Goentoro, 2018). For example, in RKO cells (human colon carcinoma cells), they show that for

Wnt pathway, β-catenin (output, protein which destruction is inhibited when Wnt pathway is activated) level increases linearly with the level of phosphorylated LRP (LDL-Related Protein, input, receptor which triggers Wnt pathway). The linearity persists until saturation of the input. For these three pathways, linear or non-linear increase in the input leads to a linear signal transmission through the core intracellular pathway.

Difference in magnitude of the response corresponds to an increase in the signal amplitude, duration or frequency for example leading to an increase in the response of the cell. This can be observed as an increase in gene expression, protein production or cell growth, depending linearly or not from the signal. Threshold effect can also be observed and response in the cell can be a stepwise increase or decrease of the corresponding effect.

1.2.4 KINETIC DELAYS IN SIGNALING CASCADES

Kinetic delay in the activation cascade has been observed and might also be accounted as part of the decoding cell toolbox. The work by Valon *et al*. on optogenetic, for example, illustrates nicely how several minutes might separate upstream CRY-2/CIBN recruitment upon laser illumination from Cdc42 GTPase activation and eventual formation of membrane protrusions (Fig. 6A-D, (Valon et al., 2015)). Work by Michaux, Robin *et al.*, in early *Caenorhabditis elegans* embryos, has shown delay in RhoA activation cascade (Fig. 6E-G, (Michaux et al., 2018)), this cascade being implicated in cytoskeleton remodeling during morphogenesis. This delay between RhoA activation and Myosin recruitment has also been further characterized during optogenetic induction of RhoA activation cascade in cultured cells (Kamps et al., 2020).

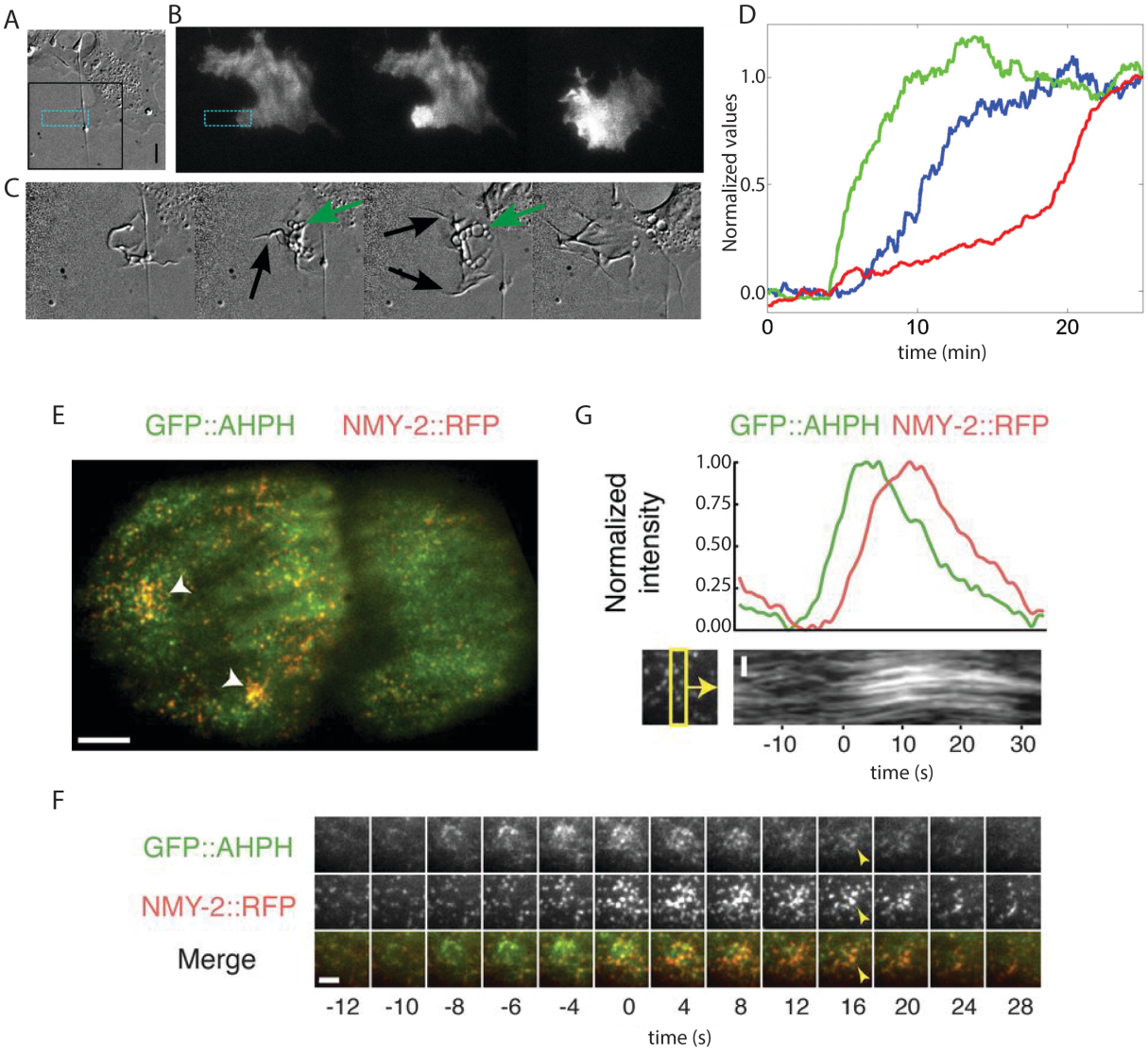

Figure 6. Kinetic delay can be observed in induced activation cascade and *in vivo*. (A-C) Local activation of Cdc42 in fibroblast cell generates membrane activity and cell barycenter displacement from ((Valon et al., 2015)). DIC images **(A and C)** and TIRF images **(B)** of a fibroblast illuminated locally by a rectangular ROI (1 pulse every 20 s, *blue region*). **(A)** The cell is represented before the activation routine. Scale bar = 10 μm**. (B)** TIRF images before, at 1 min, and 50 min after activation. **(C)** Zoom-in of the black area of (A) for 8, 17, 30, and 50 min after the beginning of the activation routine. (*Black arrows*) Presence of filopodia; (*green arrows*) localization of vesicles. **(D)** Quantification of pmCRY2 recruitment in the activation area (*green*), of membrane activity (*blue*) and of cell barycenter displacement (*red*) over time normalized between 0 and 1. **(E-G)** Local pulses of RhoA activation underlie pulsed accumulation and disappearance of F-actin and Myosin II from (Michaux et al., 2018). **(E)** Two-cell stage embryo expressing GFP::AHPH as a reporter for RhoA activity and NMY-2::RFP imaged by TIRF microscopy. **(F)** Temporal dynamics of GFP::AHPH and NMY-2::RFP accumulation during a single pulse. The time between frames is 2 s for the first five frames and 4 s thereafter. **(G)** Normalized fluorescence intensities of GFP::AHPH and NMY-2::RFP (*top*) and kymograph showing that local contraction (concerted movements of myosin puncta) begins after the accumulation of GFP::AHPH (*bottom*). The yellow box on the bottom left indicates the region used to generate the kymograph.

The functional relevance of this characteristic decoding modality, however, still remains unclear. So far it is not clear if the delays in activation cascade reflect imposed physical and/or chemical constrains or might have a physiological relevance. We do not know under

which selection these delays are, three hypotheses can be made: positive, negative or neutral selection. Delays could be negatively selected as they delay in response to a potential immediate stress and therefore delay adaptation or response to such stress could be considered as deleterious. They could alternatively be positively selected by giving time to the system to integrate the signal and time for temporal averaging, complete absence of delay in cascade might lead to no feedback nor oscillations in the system. Finally, selection toward delays in activation cascade might be neutral as they might not affect fitness of the organism.

The simple RhoA activation cascade can be used as a canonical example of activation cascade during development to try address the question of the regulation and importance of such kinetic delay. In this thesis, I will focus on this cascade and its effect on the cortical cytoskeleton of the early *C. elegans* embryo. The next chapter will give key information about the different components of the Actomyosin cytoskeleton as Actin and Myosin are the ultimate effectors of the RhoA activation cascade.

2 THE ACTOMYOSIN CYTOSKELETON COMPOSITION

During morphogenesis, the shapes of embryonic cells are dynamically controlled by the **cell cortex**, a thin layer of material that underlines the plasma membrane. This polymer meshwork (a structure where Actin bundles are absent or less present that in bundled networks like in cell protrusions) is composed by crosslinked Actin filaments and Myosin molecular motors.

In 1864, W. Kühne isolated a protein from muscle cells and named it Myosin. In 1939, Engelhardt and Liubimova reported its ATPase activity. Actin was discovered by Straub in 1942. Later studies by Szent-Gyorgyi in the early 1940s demonstrated the contractile property of the Actomyosin and its ATP-dependent activity (for review of history of Actomyosin, see (Szent-Györgyi, 2004)). Two decades later, new research have shown that Actin and Myosin are found in other cells and are a common mechanism for contractility.

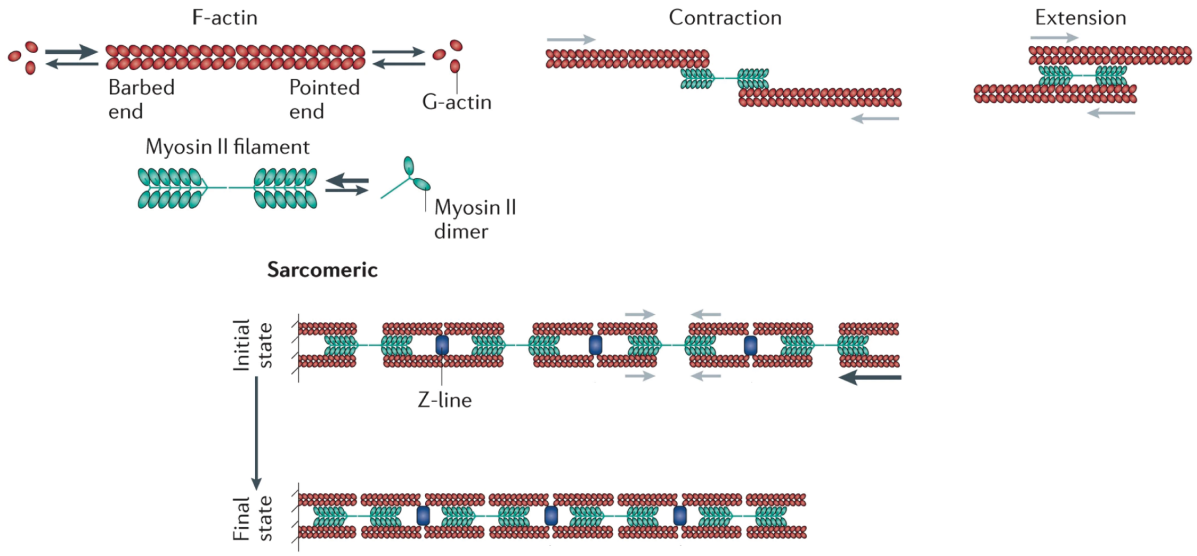

Figure 7. Myosin II contraction in muscle sarcomeres. Myosin II forms mini-filaments by binding through the tails and binds to Actin filaments through the globular heads. Myosin mini-filaments drive the translocation of Actin filaments towards their barbed-ends. This can result in the contraction or extension of two bound Actin filaments depending on the location of Myosin with respect to the middle of these filaments. Sarcomere: F-Actin barbed-end are localized at Z-bands, which contains numerous regulatory proteins, including α-actinin crosslinkers. Adapted from (Murrell et al., 2015).

The structure of Actin and Myosin was also described in muscle very early on (Szent-Györgyi, 2004). In muscle cells, Actin and Myosin have a nearly crystalline structure, that can be observed by electron microscopy, known as sarcomeres. The sarcomeric structure is composed of Actin and Myosin filaments. Actin filaments in the Z-line are crosslinked by α-

actinin and their barbed-ends are capped by Capping Protein (CapZ). Myosin thick filaments point towards the Actin filament pointed-end and Myosin pulls anti-parallel filaments, reducing the size of the sarcomere by contraction. These units, repeated throughout the length of the myofibrils, form the structural unit of striated muscle fibers (Fig. 7, (Huxley, 1957)).

Actin is a highly conserved protein in eukaryotes, human γ-Actin shares overall 91.2% identity with yeast Actin (identity being higher for residues from within the monomers than for the one exposed to the surface, the latter still being at 87% identical between the two species) (Gunning et al., 2015). In most eukaryotes, Myosin is also present (few taxonomic groups live without it: red algae and diplomonad protists (Foth et al., 2006; Vale, 2003)). Strikingly, all these organisms use the same combination of these two essential molecules to drive the mechanical forces underlying their essential processes: cell division, cell migration and cell shape changes. In metazoan, Actomyosin is involved in controlling and defining cell and tissue morphogenesis during early embryonic development. In non-muscle cells, contrary to muscle cells, cell contractility is controlled by distinct isoforms of Actin, Myosin and other Actin-binding protein (ABP), and Actomyosin displays a strikingly different organization, organized much more loosely, with no sarcomere-like structures. Actin and Myosin assemble in a thin, weakly organized, gel beneath the cell membrane, that often displays isotropic properties and structure (Charras et al., 2006; Morone et al., 2006; Salbreux et al., 2012).

The modification of these properties – regulated in part, in space and time, by signaling cascades – is the key for all cell behaviors in morphogenesis (cf. III) and is responsible for the shape of the cell and is involved in most of the morphogenetic events such as polarity establishment and gastrulation (Lecuit et al., 2011; Murrell et al., 2015; Pollard and Cooper, 2009).

This chapter will be articulated around Actin and Myosin, and will aim to described how the Actomyosin network is built, maintained and regulated. Additional information will be provided of what is currently known in model system *C. elegans* used in my thesis.

2.1 ACTIN

2.1.1 DYNAMICS

Actin is a globular protein of 42 kDa (Blanchoin et al., 2014). Actin is present in two states in the cell: G-Actin, monomeric and cytoplasmic, and F-Actin, polar filaments of Actin monomers. Actin filament are polarized: the fast-growing end is also called the barbed end or (+)-end, where the polymerization is more favorable, compared to the slow-growing end called the pointed end or (-)-end, where the depolymerization is dominant in physiological contexts. The first step of Actin filament assembly is nucleation: two to three monomers are associated to form a short filament. This step is rate-limiting as Actin dimers and trimers are highly unstable and sequestration of monomers due to sequestering factors suppress spontaneous nucleation in cell (Pollard and Borisy, 2003). Then, new monomers bound to ATP are added to the filament. ATP is hydrolyzed, inorganic Phosphate (Pi) is released and Actin subunit remains bound to ADP (Pollard et al., 2000). Terminology of barbed- and pointed-end refers to the observation that the (+)-end, the fast-growing end, when associated with Heavy-Mero-Myosin, displays an arrow-head shape when imaged using electron microscopy (Begg et al., 1978; MacLean-Fletcher and Pollard, 1980). Filaments have an average diameter size of 8 nm (Fig. 8, (Blanchoin et al., 2014)). *In vitro*, Actin can spontaneously polymerize into filament, nucleation occurs spontaneously above 0.1 µM of pure ATP-Actin at the barbed-end (above 0.6 µM at the pointed end) under physiological conditions (Pollard et al., 2000) and filaments then elongate into long unbranched filaments.

The *C. elegans* genome contains five Actin isoforms (*act-1* to *-5*), the sequence is highly conserved between isoforms (Files et al., 1983). ACT-4 is reported to be expressed in body-wall muscles (Stone and Shaw, 1993) and ACT-5 is required for intestinal microvilli formation (MacQueen et al., 2005). Willis *et al.* provided evidence with mutant and knock-down experiment that ACT-1, 2 and 3 are expressed in early embryo and play a redundant role (Willis et al., 2006). In particular, ACT-1 plays a crucial role in cytokinesis, cortical integrity and polarity establishment at 1-cell stage (Piano et al., 2000; Velarde et al., 2007).

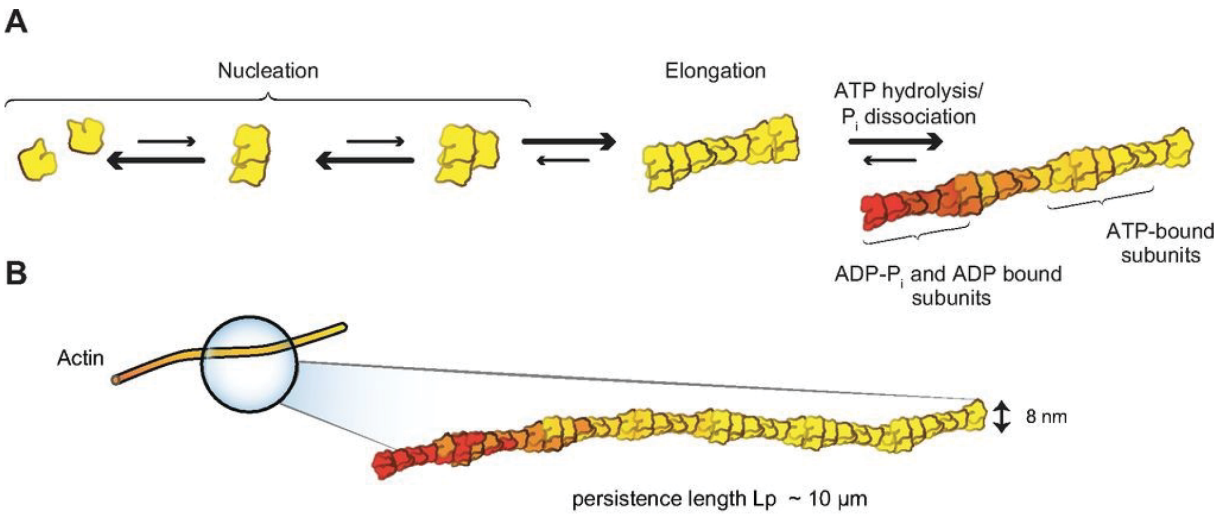

Figure 8. Single filament assembly. (A) Actin polymerization from the pool of actin monomers happens in two phases: nucleation and then elongation. The thermodynamically limiting step for actin assembly is nucleation and consist in the formation of dimers and trimers. This is followed by rapid elongation at the more dynamic end, the barbed end. Subunits added at the barbed-end are bound to ATP, ATP hydrolysis occurs next. (B) Actin filaments are semi-flexible polymers with a diameter of 8 nm and a persistence length of 10 µm. Adapted from (Blanchoin et al., 2014).

2.1.1.1 Sequestering factors

In cells most living cells, G-Actin concentration is ~100 µM and is relatively similar throughout the cell (Kiuchi et al., 2011; Koestler et al., 2009; Skruber et al., 2018), much above the critical concentration for Actin polymerization. Several classes of proteins, termed sequestering factors –and in particular Gelsolin, Thymosin b4 and Profilin– have been identified that sequester G-Actin monomers, effectively preventing polymerization in bulk of Actin monomers, and complete gelation of the cytoplasm (Kaiser et al., 1999; Pantaloni and Carlier, 1993). One of these factors, Profilin, plays a multifaceted role in Actin assembly.

Profilin is a small protein (14,2 kDa), it forms a multi-gene family highly conserved in evolution, members being found in animals, fungi, plants, bacteria and viruses (Pandey and Chaudhary, 2017; Schutt et al., 1993). Originally described as an Actin sequestering factor (Carlsson et al., 1977), it is reported to be in largely lower concentration than the Actin (Kaiser et al., 1999), which it binds to and forms with it a complex named Profilactin.

Then, Sagot *et al*. and Evangelista *et al*. showed that Profilin acts as co-factor of the F-actin elongation by Formin (Evangelista et al., 2002; Sagot et al., 2002). Profilin has been showed to increase velocity in Formin-mediated Actin filament elongation, but does not have an effect on Formin attachment to the filament barbed-end (Kovar et al., 2006). Additionally,

Profilin catalyzes the exchange of ADP for ATP on Actin, making Actin available to be integrated in a filament (Dominguez, 2009).

Profilin has been recently demonstrated to also be involved in regulation of the balance between Formin-mediated and Arp2/3-mediated Actin network as it favors Formin over Arp2/3 (Suarez et al., 2015). The competition for monomers will be discuss later in a further section. Profilin is also implicated in the regulation of filament growth speed by limiting polymerization by Formin at the barbed-end (Funk et al., 2019).

The *C. elegans* genome contains three Profilins genes (*pfn-1* to *-3*) though experimental studies show that only PFN-1 is expressed in early embryos and is required for cytokinesis (Polet et al., 2006; Severson et al., 2002).

As discussed before, complexation of G-Actin monomers by Profilin is partially responsible for rendering the spontaneous polymerization of F-Actin thermodynamically unfavorable in physiological context (Plastino and Blanchoin, 2018). In cells, assembly of Actin filaments therefore relies on assembly factors –nucleators and elongators– to drive cytoskeletal assembly. In the next sections, we will discuss what are Actin nucleators and elongators, and how their competition regulates the Actin network in biological context.

2.1.1.2 Nucleators and elongators

2.1.1.2.1 Formins

Formins are a family of multi-domain proteins, usually over 140 kDa, that is one of the Actin nucleators (Pring et al., 2003; Sagot et al., 2002). Formins can be found among metazoan (nine Formin subtypes) as well as non-metazoan (Pruyne, 2017), in particular Formin-homology domain 2 (FH2) is especially well conserved (Higgs and Peterson, 2005; Pruyne, 2016), and are responsible for Actin nucleation and filament elongation (Chesarone et al., 2010; Evangelista et al., 2002; Sagot et al., 2002). The Diaphanous-related Formins (DRFs) are required for cell division in early development (Castrillon and Wasserman, 1994). DRFs are frequently regulated by autoinhibition, in which an intramolecular interaction between the C-terminal autoregulatory domain, or DAD (Diaphanous autoregulatory domain), interacts with the N-terminal domain, or DID (Diaphanous inhibitory domain), causing a folding of the protein and autoinhibition (Fig. 9, (Alberts, 2001; Watanabe et al., 1999)). Binding of Rho GTPase to the GTPase binding site (GBD), competes with this autoinhibition and exposes FH1 and FH2 domains (Lammers et al., 2005; Watanabe et al., 1999) (Fig. 9). Upon this

conformational change, the Formin is in a *recruited* (activated) form, and is competent to bind to Actin filaments barbed-end and initiate processive filament elongation (Kühn and Geyer, 2014). Formins form dimers, prior to their association with an Actin filament (Xu et al., 2004). Recent *in vitro* study has shown that when put under tension, the presence of DRF Formin mDia (mouse) strengthen the bond of Actin dimers of Actin monomers within barbed-ends (Li et al., 2020).

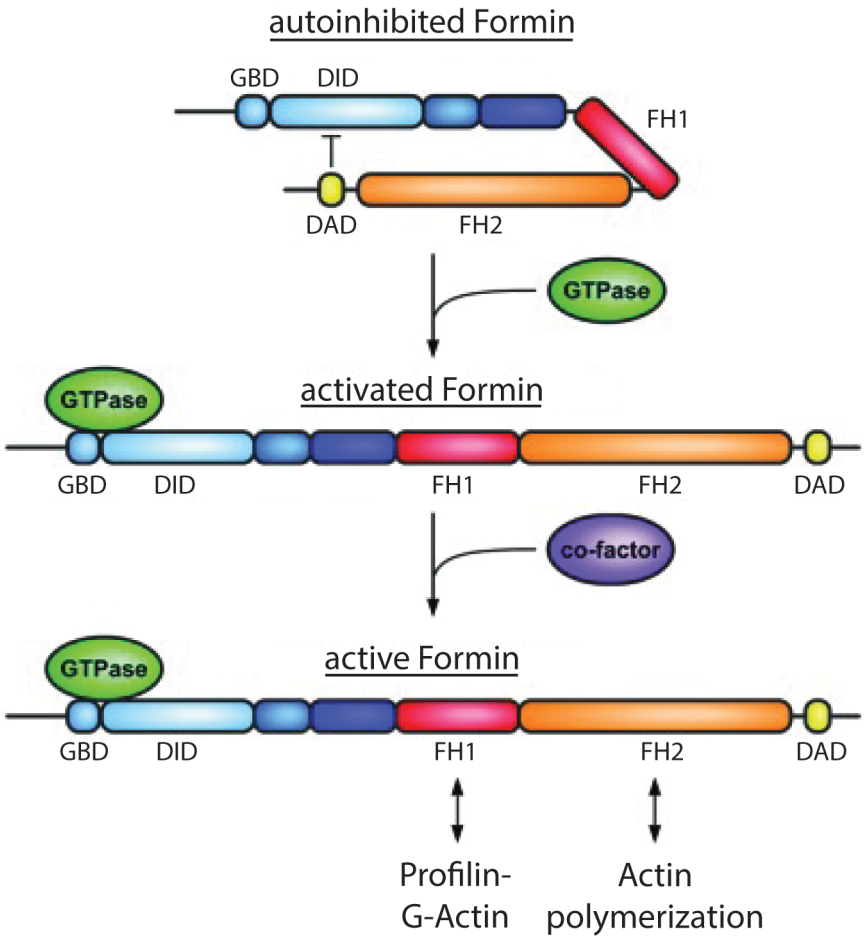

Figure 9. Typical regulation of a Diaphanous-related Formin. DID and DAD domains interacts in the auto-inhibited state. Binding to a GTP-bound Rho of a GTPase (RhoA for example) releases the auto-inhibited state to an activated form. Additional co-factors required to get an active (fully activated, elongating) Formin. GBD: GTPase-binding domain, DID: Diaphanous inhibitory domain, DAD: Diaphanous autoregulatory domain, FH1/2: Formin-homology domain 1/2. Adapted from (Kühn and Geyer, 2014).

FH1 and FH2 are crucial to polymerize filaments of Actin: FH2 is the domain binding to the barbed-end of the filament of Actin and stays bound as the filament elongates (Higashida, 2004; Pruyne et al., 2002), FH1 is the domain binding to a complex composed of Profilin and Actin, forming a Profilactin complex. *In vitro* studies suggest that the DAD domain at the C-

terminal of mDia1 is also crucial for G-Actin binding (Gould et al., 2011; Li et al., 2020; Vizcarra et al., 2014). FH2 domain encircles the barbed-end and competes with capping proteins, such that Formins actually behave as leaky capping-protein (Bombardier et al., 2015; Shekhar et al., 2015; Zigmond et al., 2003). FH1 is composed of Polyproline tracks (number of tracks correlates with the rate of barbed-end elongation) which associates to Profilactin and this step is rate-limiting (Fig. 10, (Paul et al., 2008)). Speed of F-Actin elongation is defined by Profilactin affinity for the FH1 domain (Zweifel and Courtemanche, 2020a) and the competition between Polyproline tracks to deliver the Profilactin to the barbed-end (Zweifel and Courtemanche, 2020b). In addition, *in vitro* studies show that force (e.g here the Actin filament being pulled) is also an important element for the stabilization of the interaction between Formin and Actin monomers (Li et al., 2020) and that Formin can put Actin filaments under tension (Jégou et al., 2013). Pulling forces (e.g extension force applied on the Formin) can increase the elongation rate in presence of Profilin for some Formins (mDia1 (Jégou et al., 2013) or Bni1p (Courtemanche et al., 2013)) or without Profilin (mDia1 (Kubota et al., 2017; Yu et al., 2017)); but is also responsible for slowing down elongation for other Formins (such as Cdc12p (Zimmermann et al., 2017) in presence of Profilin or Bni1p in absence of Profilin (Courtemanche et al., 2013)).

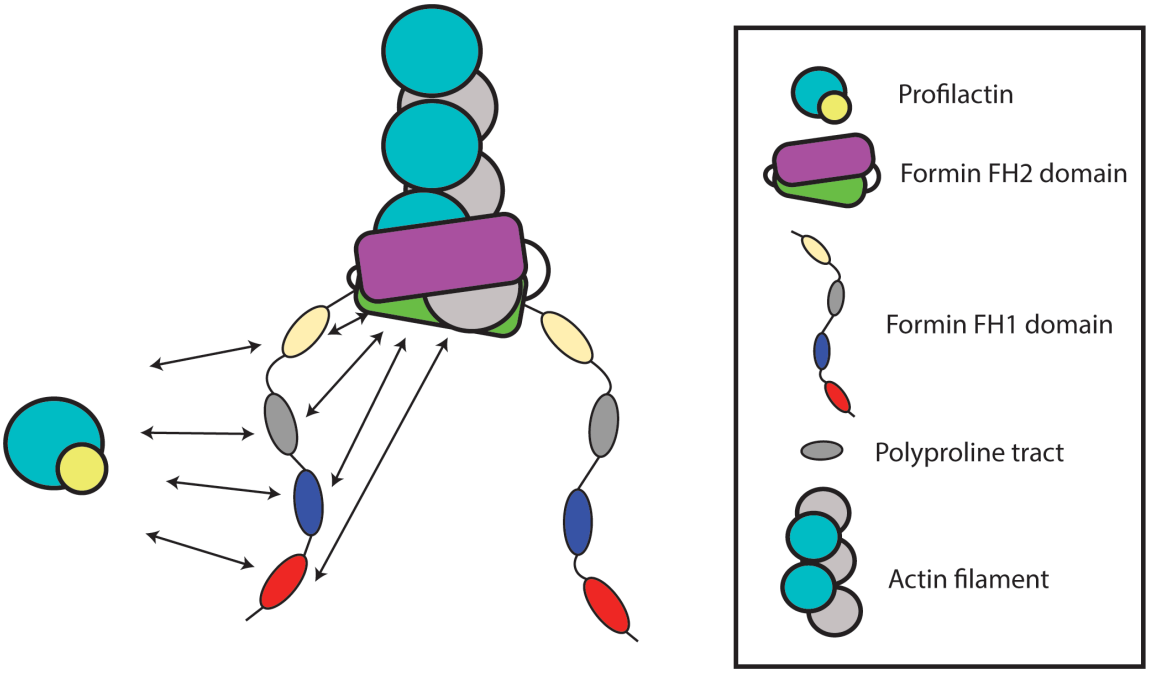

Figure 10. Addition of a new Actin subunit can be done via different routes. FH1 domain of the Formin is composed of different Polyproline tracts where Profilactin can bind before FH2 domain catalyzes the addition of the monomer to the filament barbed-end. Adapted from (Zweifel and Courtemanche, 2020b).

Moreover, the addition of new Actin subunits can only be made if the Actin filament is in the proper conformation: a switch in the angle of the last three subunits of the filament needs to occur between an angle of 180° (closed state) imposed by the FH2 domain but where elongation cannot occur (as the different elements of the binding sites are not aligned) to an 167° (open state) favorable to the elongation (Aydin et al., 2018; Otomo et al., 2005; Paul et al., 2008) (Fig. 11). Simulations points towards the 'stepping-second' model being valid, model in which the Actin monomer is added first and then the Formin translocates towards the (+)-end (Paul and Pollard, 2009), as the FH2 domain is not required to switch to the open state (Aydin et al., 2018). The addition of an Actin monomer to the elongating filament promotes the dissociation of the FH2 domain from the barbed-end, which means that for each new monomer addition the Formin goes through a phase, during translocation, where there is a chance that it detaches from the filament (Fig. 11, (Kovar et al., 2006; Paul et al., 2008)). A recent *in vitro* study showed that Formin dissociation is dependent on Actin concentration in absence of any force application on the system. They also showed that the moment of dissociation is dependent on the applied force on the Actin filament: when force is applied, the difference in dissociation rate associated with difference in Actin concentrations disappears. At low force the Formin is more likely to dissociate during the transition state after the addition of a new subunit to the filament, at high force however the dissociation does not depend on Actin concentration anymore and is more likely to occur during the open state during the rapid open-closed equilibrium (Cao et al., 2018).

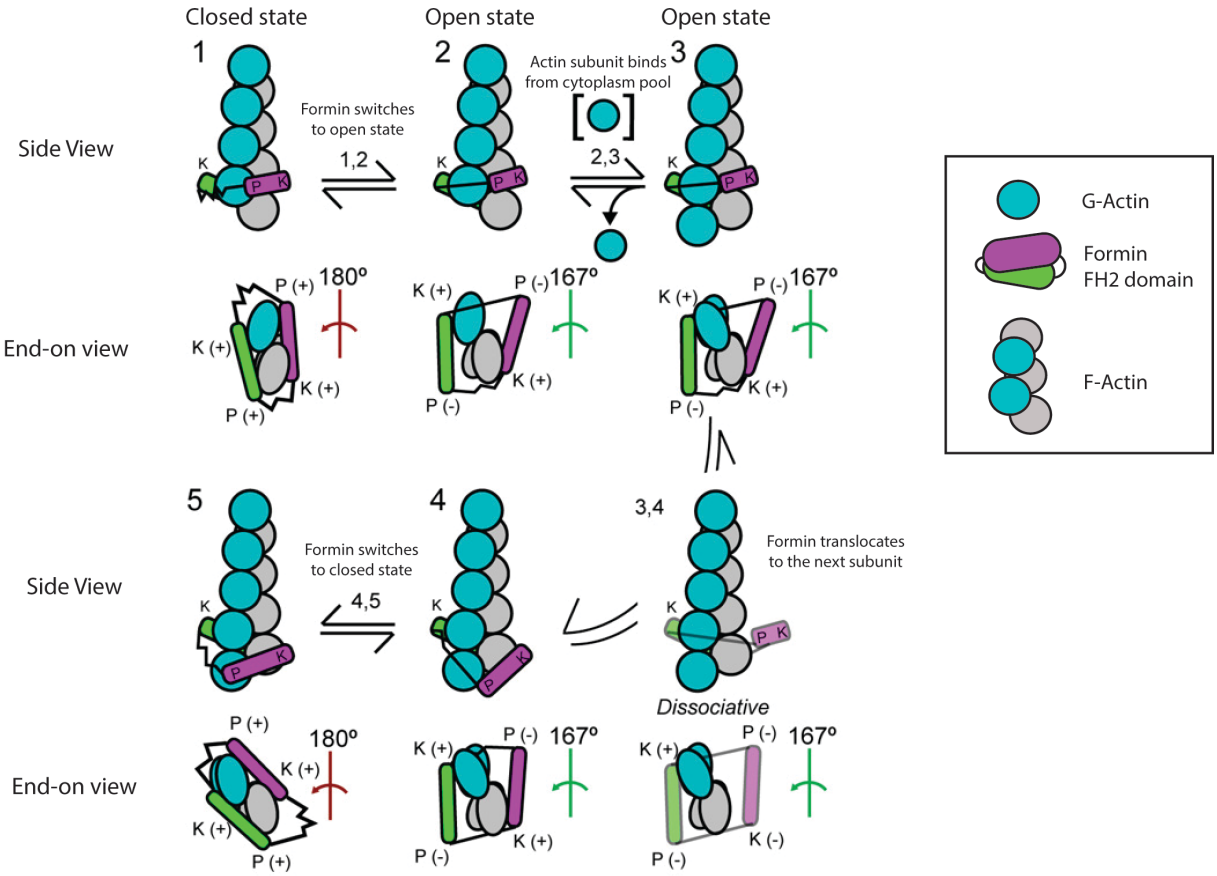

Figure 11. Actin subunit addition to a barbed-end associated with a Formin FH2 domain by the stepping-second mechanism. End-on and side views of Formin FH2 domain (green and magenta dimer) interacting with the barbed end of an Actin filament (gray and blue) in closed (180° angle) and open (167°) states. After addition of a new subunit (blue), Formin steps onto the new terminal subunit. Each FH2 subunit has two sites that can interact with Actin: the knob (K) and post (P). Sites engaged with the filament are labeled (+). Sites dissociated from the filament are labeled (−). States 1 and 2 (as 5 and 4, which are the same as 1 and 2 but the filament is one subunit longer) are rapid equilibria between the open and closed states. Adapted from (Aydin et al., 2018) and (Paul and Pollard, 2009).

The *C. elegans* genome contains six Formin genes (*fhod-1, cyk-1, daam-1, frl-1, exc-6* and *inft-2*), characterized by their conserved FH2 domain (Pruyne, 2016). CYK-1 is a Diaphanous-related Formin and is known to be essential for cytokinesis in the early embryo and throughout the development (Severson et al., 2002; Swan et al., 1998).

2.1.1.2.2 Arp2/3 complex

A second class of assembly factors is the Actin-related protein 2/3 (Arp2/3). Arp2/3 complex (~220 kDa) is composed of 7 subunits: Arp2, Arp3, ArpC1, ArpC2, ArpC3, ArpC4 and ArpC5 (Pollard, 2007), which, interestingly, are conserved in Metazoans, fungi and plants but not in algae and in Apicomplexa (Muller et al., 2005). Arp2 and Arp3 have the catalytic activity, the other five are supporting units (Pollard, 2007). To be able to polymerize Actin, Arp2/3

requires a primer and nucleation promoting factors (NPFs), most important ones being from the Wiskott-Aldrich syndrome protein (WASP)/WAVE family (Fig. 12, (Pollard, 2007)). The pre-existing filaments is bound by the Arp2/3 complex and nucleate a new filament (called daughter filament) to the side at a fixed angle of 70° forming a branched filament (Amann and Pollard, 2001; Mullins et al., 1998; Suarez and Kovar, 2016). Arp2 and Arp3 are close in their structure to the Actin monomers and are the first two subunits in the daughter filament, they serve as a template (Egile et al., 2005). Therefore, Arp2/3 gives a more dendritic structure to the Actin meshwork, which is key for motility through lamellipodia (Arp2/3 is excluded from filopodia (Svitkina and Borisy, 1999)).

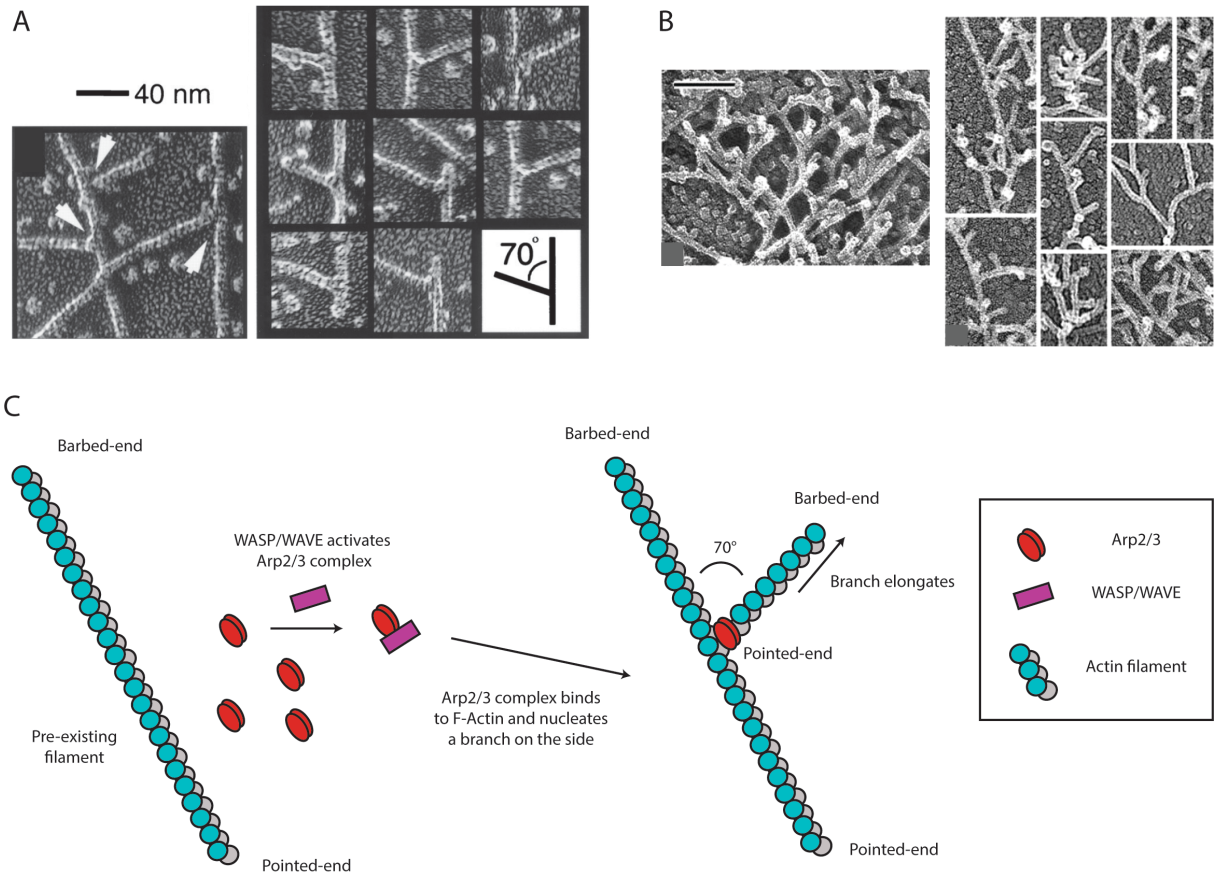

Figure 12. Arp2/3 complex nucleates a branch from a pre-existing filament. (A-B) Electron micrograph of Actin filament polymerized *in vitro* branched by Arp2/3 complex visible as a globular mass at the point of attachment, from (Mullins et al., 1998) (A) and mouse fibroblast lamellipodia after Latrunculin A treatment, from (Svitkina and Borisy, 1999) (B). Scale bar in (B): 0.1 µm. (C) WASP/WAVE/Scar activates Arp2/3 complex which binds to the side of a pre-existing filament and nucleates a daughter filament with an angle of 70°. Branches elongates from the barbed-end. Adapted from (Blanchoin et al., 2000; Machesky et al., 1999)

The requirement of a pre-existing filaments for Arp2/3 to nucleate Actin might be bound to the WASP-dependent path; indeed data suggests that other NPFs as Dip1 might work

differently and, therefore, Arp2/3 would be able in this condition to elongate short *de novo* filaments (Balzer et al., 2018; 2019; Wagner et al., 2013).

The seven subunits of the Arp-2/3 complex are present in *C. elegans*, a single gene for each subunit (Sawa et al., 2003). In the context of this thesis, I will exclusively refer to the Arp2 subunit, coded by the *arx-2* gene. Depletion of this subunit leads to defects in morphogenesis (including incomplete cell internalization during gastrulation and defects in ventral enclosure) (Roh-Johnson and Goldstein, 2009; Sawa et al., 2003).

2.1.1.2.3 Competition for monomers

Formin and Arp2/3 complex are present and active at the same time in the cell and therefore compete for Actin monomers (Burke et al., 2014). Arp2/3 is strongly implicated in cell motility, as it is present and essential in lamellipodia of migrating cells (Buracco et al., 2019). Formin are required in numerous species for cytokinesis in particular it elongates long Actin filaments that form the bundles which compose the contractile ring (Chan et al., 2019; Chang et al., 1997; Pelham and Chang, 2002; Severson et al., 2002; Watanabe et al., 2008), while Arp2/3 –despite its role regulating Formin activity (Chan et al., 2019)– does not seem an essential factor for this process, as the cytokinesis still occurs when Arp2/3 is depleted by RNAi (Severson et al., 2002).

In fission yeast, three Actin structures simultaneously exist in the cell: endocytic Actin patches composed of short-branched F-Actin assembled by Arp2/3 complex, contractile rings and polarizing Actin cables both composed of long-unbranched F-Actin assembled by Formins. In a recent study, Burke *et al.* showed that size of these Actin populations is controlled by the access to the Actin monomer pool, under the gating activity of Profilin. Burke *et al.* set up Actin under- and overexpression by replacing endogenous Actin promoter by a thiamine-sensitive promoter: in absence of thiamine this promoter express ~5-fold less than the endogenous Actin promoter, in presence of thiamine it express ~5-fold more. They observed that Actin overexpression (meaning a low Profilin/Actin ratio) favors Actin patches and therefore Arp2/3 mediated-Actin polymerization. Actin underexpression (meaning a high Profilin/Actin ratio) favors the contractile rings assembled by Formins (Burke et al., 2014). Therefore, in fission yeast, inhibition of Arp2/3 or Formin leads to excessive activity of its counterpart (Burke et al., 2014). This balance in Actin monomer distribution between Arp2/3 and Formin is mediated by Profilin, as Profilin favors Formin activity over Arp2/3 and even

antagonizes Arp2/3 complex activity in fission yeast and in animal fibroblasts (Fig. 13, (Rotty et al., 2015; Suarez et al., 2015)).

The simplest hypothesis is that Profilin and WASP/WAVE compete for Actin monomers in the cytoplasm, as both of them cannot bind G-Actin simultaneously (Suarez et al., 2015). Recent study in *C.* elegans embryo suggests that inhibition of Arp2/3 complex not only frees up G-Actin that can associate with Profilin to be polymerized by Formin, but that Formin recruitment at the cortex is increased, meaning Arp2/3 inhibition up-regulates the activity of Formin itself (Chan et al., 2019). However, it still remains unclear how Arp2/3 affects Formin activity, through a direct interaction with Formin or through an indirect effect on the RhoA activation cascade which activates Formin (see further details on this cascade in III). Recent research in mouse fibroblasts suggests that this might be the case: depletion of Arp2/3 leads to increase in RhoA abundance and reduction in RhoA activity specifically (neither Rac1 nor Cdc42, other GTPases, were affected). These results point towards an effect, directly or indirectly, of Arp2/3 over RhoA activation and recruitment (Huang et al., 2019).

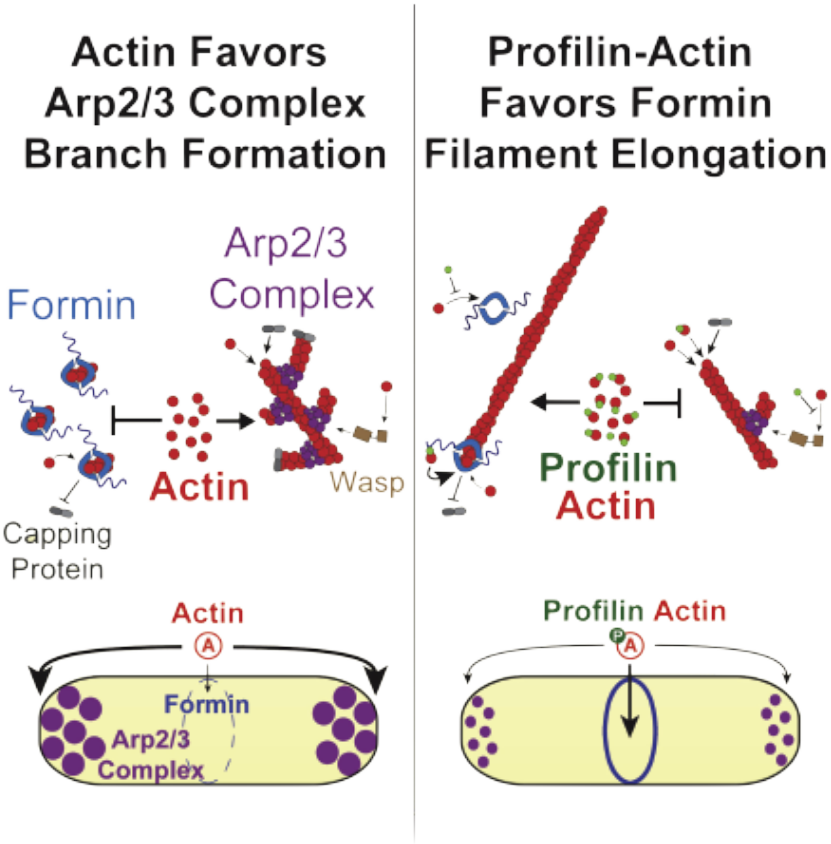

Figure 13. Competition for Actin monomers between Arp2/3 complex and Formin regulates Actin network organization. In fission yeast, free Actin monomers favor Actin patches formed by Arp2/3-mediated branched network at the cell poles. Profilactin complex favors Formin-mediated network, especially at the contractile ring. From (Suarez et al., 2015).

2.1.1.3 Capping

In vivo, in addition to Formins, the barbed-ends of the Actin filaments have a high affinity for another class of proteins: Capping Proteins. Capping Proteins (CP) are found in nearly all eukaryotic organisms (Wear and Cooper, 2004). Formins are in competition with CP for Actin filament barbed-end binding (Zigmond et al., 2003). This competition likely accelerates dissociation of Formins from barbed-ends, thereby potentially affecting/regulating of the length of Actin filaments *in vivo* (Bombardier et al., 2015). *In vitro* studies demonstrate that CP and Formin bind simultaneously to the barbed-end and form a "decision complex" intermediate (Bombardier et al., 2015; Shekhar et al., 2015). In this decision complex, CP could displace Formin from the barbed-end (Bombardier et al., 2015). Several Formins behaving in the same way points toward that this is a general characteristic of Formins (Shekhar et al., 2015). Importantly, the assembly of branched network requires CP, as it favors Arp2/3-mediated network by blocking the elongation of Actin filament from the barbed-ends. This is an important mechanism as the absence of branching leads to the creation of long Actin bundles growing away from the nucleation site. CP limits the growth of Actin filament used by Arp2/3 as primers (Achard et al., 2010).

2.1.1.4 Severing factors

In vivo, two main mechanisms drive Actin filament disassembly and Actin turnover: depolymerization from the filament end, and Actin filament severing, mediated by Actin severing proteins (Miyoshi and Watanabe, 2013). Here, I focus on one of these factors, ADF/Cofilin.

Actin depolymerizing factor (ADF)/Cofilin (17 kDa) is a widely conserved protein (found among others in yeast, *Drosophila, Dictyostelium* and plants (Moon and Drubin, 1995)) that binds the Actin filaments as it "ages" (Cofilin binds preferentially to ADP-F-Actin (Blanchoin and Pollard, 1999)) and accelerates the Pi release from filaments (Suarez et al., 2011). Cofilin binding promotes change in the twist of F-Actin, it binds cooperatively in domains without interaction between any neighboring Cofilin, severing occurring between Cofilin domains (Hayden et al., 1993; La Cruz, 2005; McGough et al., 1997; Suarez et al., 2011). Cofilin binds stoichiometrically to Actin: one Cofilin binds one F-Actin subunit (McGough et al., 1997). Decoration by Cofilin increases the probability of severing of the filament, hence depolymerization (Gressin et al., 2015; Lappalainen and Drubin, 1997). Genetic studies in a

number of model systems found that Cofilin is an essential gene (*unc-60* in *C. elegans* (McKim et al., 1994), *tsr* in *Drosophila* (Gunsalus et al., 1995), COF1 in yeast (Moon et al., 1993)), and Cofilin mutants display a homozygote lethal or sterile phenotype, underlying an important function for this protein.

Severing occurs between domains with Cofilin bound to the subunits and domains without (Suarez et al., 2011), and produces short Actin oligomers which depolymerize rapidly (Raz-Ben Aroush et al., 2017). Recent study by Raz Ben Aroush *et al.* in lamellipodial fragments shows that around a quarter of the diffusible Actin pool is in form of oligomers and therefore that the diffusible Actin concentration is ~1.6 mM (largely above the critical concentration for Actin polymerization of 0.1 µM (Pollard et al., 2000)). This work also proposes that the turnover of the Actin network is local, whereas the diffusible Actin transport is global (Raz-Ben Aroush et al., 2017). The liberated monomers and oligomers are free to go back to the pool of monomers in the cytoplasm to diffuse and later be reused in another filament (Pollard and Cooper, 2009) or diffuse and be reused locally, but might transiently be sequestrated in a "reserve" pool (Raz-Ben Aroush et al., 2017).

Cofilin is also known for accelerating depolymerization at the pointed-end (Moriyama and Yahara, 1999). Recent *in vitro* work from Wioland *et al.* also proposed that Cofilin promotes depolymerization from pointed-ends as well as barbed-ends. Actin filaments grow until they get capped, allowing saturation by Cofilin, this triggers the uncapping of the filament and its depolymerization from the barbed-end (Wioland et al., 2017). In addition, the ADF/Cofilin saturated Actin filaments are depolymerizing at the same rate from both ends (Wioland et al., 2017).

Data also shows that passing a certain threshold of decoration by Cofilin, the severing promotion is abolished and is replaced by a stabilization of the Actin filament as saturation in Cofilin increases flexibility of the filament (Fig. 14, (McCullough et al., 2008)).

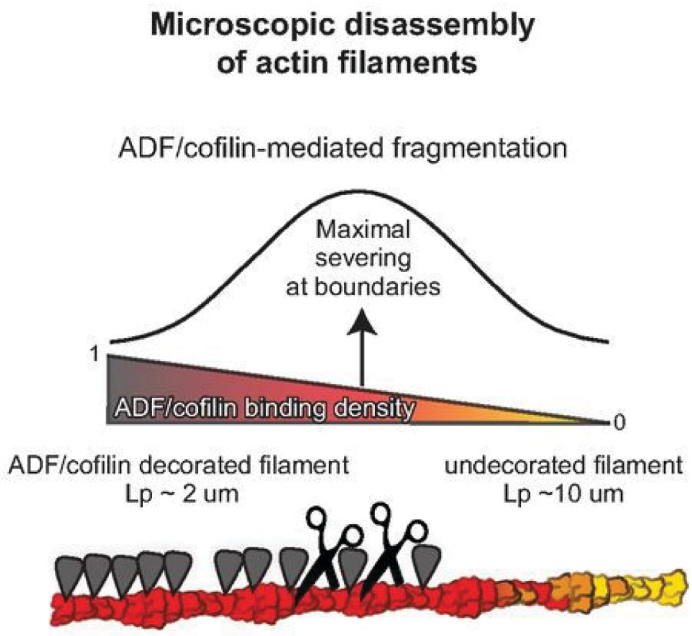

Figure 14. Cofilin decoration can promote severing or can stabilize Actin filaments. Cofilin decorates Actin filaments as it 'ages'. Severing occurs at intermediate density of Cofilin decoration. Cofilin can also stabilize Actin filament at high density by increasing filament flexibility. From (Blanchoin et al., 2014).

Work from Tinevez *et al.* in mouse fibroblasts shows that cortex tension depends on motor activity and on Actin turnover (Tinevez et al., 2009). Actin turnover ranges on the 10- to 100-s timescale (Fritzsche et al., 2013; Robin et al., 2014) and occurs through treadmilling. F-Actin turnover is considered an important mechanism to support the fluidization of the Actin cortex *in vivo*. The properties of the Actin network strongly depend on the turnover of the Actin filaments. At short time scales (less than a minute), Actin networks behave as elastic materials (going back to the original shape when the applied tension is removed). At long time scales (more than a minute) Actin filaments turnover drives rearrangements in the network, resulting in a dissipation of the applied stress and causing the network to behave as a viscous material (the network is not returning to the original shape when the tension is removed) (Pujol et al., 2012; Salbreux et al., 2012; Sato et al., 1985; Zaner and Stossel, 1983). Mechanically, Cofilin modulation of Actin turnover is responsible for the fluidity in F-actin networks *in vitro*, this through rapid disassembly of large filament portions (McCall et al., 2019).

The *C. elegans* genome contains one Cofilin gene, *unc-60*, which expresses two isoforms of the protein UNC-60A (non-muscle) and UNC-60B (muscle) (Anyanful et al., 2004). UNC-60A is known to be essential for early embryonic development: it is required for Actin

turnover during cytokinesis and also during polarity establishment (Ono, 2003). These two isoforms do not have the same properties: UNC-60A severs less but inhibits more the polymerization than UNC-60B; this apparently coming from differences in structure and dynamics (Shukla et al., 2015; Yamashiro et al., 2005). In this thesis when I will be referring to Actin I will be referring to globally all the Actins present at early stages, to CYK-1 when referring to Formin and UNC-60A when mentioned Cofilin or UNC-60 (except if specifically said otherwise).

A second pathway to promote Actin network disassembly is the action of Myosin motors on the filaments (in particular its implication on Actin treadmilling (Wilson et al., 2010)) and will be further discuss in II.B.

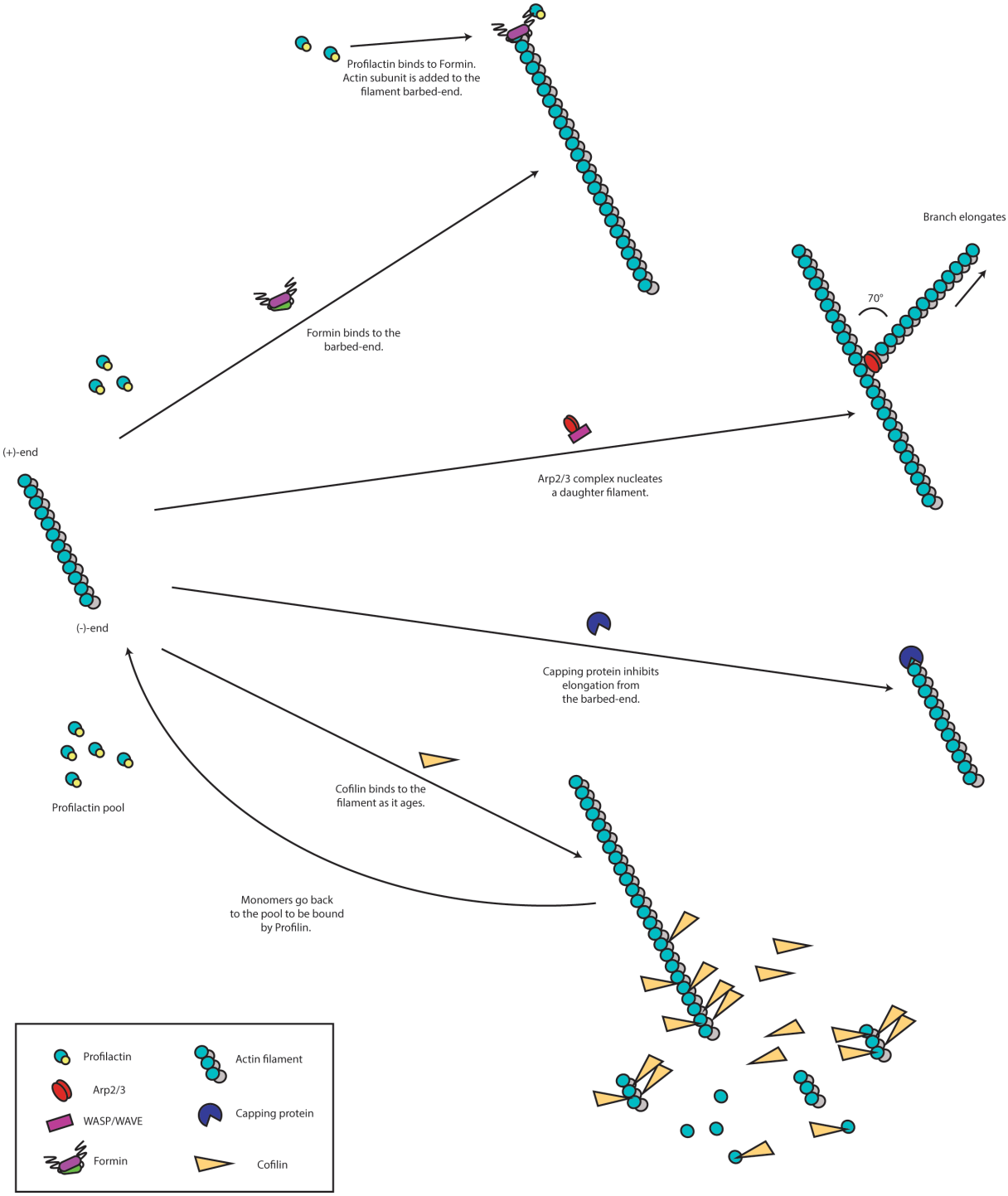

Figure 15. Multiple proteins bind F-Actin and regulates network architecture. Actin filaments are elongated from their barbed-ends by Formin. Formin binds Profilactin complex composed of Profilin and Actin monomer before adding a new Actin subunit to the elongating filament. Capping Protein binds the barbed-end of F-Actin and inhibits polymerization from this end. Arp2/3 complex is activated by NPFs such as WASP/WAVE and nucleates Actin filament branch on the side of a pre-existing filament with a stereotypical angle of 70°. Cofilin decorates F-Actin as it 'ages' and promotes severing between Cofilin clusters.

Actin turnover plays a central role in the dynamics of the Actin network, and tightly controls the temporal evolution of network architecture, and eventually Actomyosin

mechanics. Measuring Actin turnover is therefore central to understand both network assembly and mechanics. Two main tools are available to measure Actin turnover. The first one relies on Fluorescence Recovery After Photobleaching (FRAP). This method relies on the dynamic exchange of a fluorescent protein at a region of interest: intense laser illumination, all the fluorescent proteins are bleached. If there is diffusion then time of recovery of the fluorescence directly reflects the turnover of the photobleached protein. FRAP however can only be used in a system in steady state at the scale of the experiment. However, in the early *C. elegans* embryo, the cortex is highly dynamic, precluding this method.

For the purpose of this thesis, we thus turned to single-molecule (SiM) imaging using Total-Internal Reflection Fluorescence (TIRF) microscopy. Historically, SiM is based on Fluorescent Speckle Microscopy (FSM), technique based on the ability to image diffraction limited regions containing few fluorophores. Labeled molecules, in order to be properly imaged by FSM, need be microinjected in cells or alternatively expressed at low level, so that random distribution of such molecules in the imaged area result in a 'speckled' appearance, giving its name to the technique (Danuser and Waterman-Storer, 2006; Waterman-Storer et al., 1998; Waterman-Storer and Danuser, 2002). Studies such as Watanabe *et al.*, Ponti *et al.* and Burnette *et al.* have successfully used FSM to image Actin in migrating cells (Burnette et al., 2011; Ponti, 2004; Watanabe, 2002).

Single-molecule microscopy was implemented in the *C. elegans* early embryo to visualize, track and quantify proteins dynamics with high spatial and temporal resolution and, subsequently evaluate their kinetics (turnover) and kinematics (motion) (Robin et al., 2014). To be successful this technique depends on the fact that the labeled molecules reflect the behavior of the network in which they are incorporated (microtubules or Actin for example), low photobleaching and a good signal to ratio so that molecules can be visualized and faithfully tracked. In this paper, the authors measured the differential Actin turnover at the cleavage furrow and at the pole during cytokinesis, using an approximately steady-state context to establish the method. Michaux *et al*. subsequently applied this new method to study Actin dynamics during pulsed contractions at the 2-cell stage (Michaux et al., 2018). They could show that the change in Actin density during pulsed contractions resulted essentially from modulation of assembly and turnover (~ 95%), with only a minor contribution (~ 5%) from network contractility.

Now that we have a better overview on how Actin network is built and its turnover regulates, one must consider transformation endured by such network. A variety of proteins bind to F-Actin and gives specific mechanical properties to Actin networks. The following section will aim to describe the different networks encountered in a cell and give a few examples of crosslinking proteins, so to give a grasp of the complexity of Actin networks.

2.1.2 CROSSLINKING

Crosslinked networks include Actin filaments linked together through a protein that will bridge two filaments together. Crosslinkers bridge existing filaments that are already present, assembling the network in larger and more complex architectures. Crosslinkers of Actin filaments of small mass tend to tightly pack Actin filaments into parallel bundles. Large crosslinkers tend to have a larger crosslinking distance between two Actin filaments and organize Actin networks according to their concentration, high concentration of large crosslinkers tend to induce purely bundled networks, whereas at low concentration they crosslink Actin into networks or gels. The nature of network (with bundles or not) is of importance regarding the behavior of Actin filament when force is applied. Non-linear viscoelastic response of Actin networks to force application is dependent on crosslinker identity and concentration, temperature and type of crosslinked network (Lieleg et al., 2009a; 2009b; 2009c; Xu et al., 1998).

In this section, we will see a few examples of small and large crosslinkers and what are their impacts on the architecture of the Actin network, focusing on the ones present in our model organism, *C. elegans*.

2.1.2.1 Large crosslinkers

The class of large crosslinkers includes Rigor-Heavy meromyosin (HMM), Anilin, Filamin and α-actinin. Here, I will describe two well-characterized and archetypic members of this class, Filamin and α-actinin. These two proteins belonging to the same category of large crosslinkers but making fundamentally different Actin networks and are present during *C. elegans* embryogenesis.

Filamin is composed at its N-terminus region of an Actin Binding Domain (ABD) (composed of two Calponin homology domains) and a domain to bind as a dimer in C-terminus (Bresnick et al., 1990; Davies et al., 1980; Himmel et al., 2003; Stossel et al., 2001). Filamin

makes orthogonal crosslinks between Actin filaments, leading *in vitro* to the formation of gels that seemed to be more solid than equivalent concentrations of pure Actin (Brotschi et al., 1978; Stossel et al., 2001). Depending on the concentration, Filamin can form networks or gels at low concentration, bundles or even clusters of bundles at high concentration (Lieleg et al., 2009b). Two genes for Filamin can be found in *C.* elegans, *fln-1* and *fln*-2. Based on RNA-seq expression data only *fln-2* is expressed during embryogenesis (DeMaso et al., 2011).

A smaller crosslinker but still in the range of large crosslinkers is α-actinin, it is a member of the Spectrin superfamily and is found in almost all eukaryotes (Virel and Backman, 2004). α-actinin binding to F-Actin is mediated by its Calponin homology domain in the N-terminal region and dimerizes (as an anti-parallel homodimer) through a rode domain situated in the middle of the protein and composed of Spectrin repeats (Djinović-Carugo et al., 1999; Sjöblom et al., 2008; Virel and Backman, 2004). α-actinin is present in muscle (in the Z-disks) as well as non-muscle cells and interacts with cytoskeleton as well as adhesion proteins (Sjöblom et al., 2008). Different isoforms are found in filopodia, lamellipodia, in stress fibers, and in focal adhesions in non-muscle cells and in Z-disk sarcomeres muscle cells (Broderick and Winder, 2005). At high concentration, α-actinin will cause Actin filaments to bundle, however at low concentration it will form a looser meshwork, intermediate concentrations will lead to a mixture of both architecture (Lieleg et al., 2009b) (Fig. 17). Ability to form bundles might also be dependent on the rate of Actin assembly: increase in Actin dynamics prevents the formation of Actin bundles (Falzone et al., 2012). Electron microscopy has revealed that α-actinin is able to crosslink Actin in a large variety of orientations, in parallel and anti-parallel orientation and remains flexible even when engaged in active crosslink (Courson and Rock, 2010). In *C. elegans* genome, one gene has been reported for α-actinin, *atn-1*, depletion of ATN-1 by RNAi leads to early and late cytokinesis defects, mitotic defects and embryonic lethality (Skop et al., 2004; Sönnichsen et al., 2005).

2.1.2.2 Small crosslinkers

Small crosslinkers are almost exclusively found in tightly crosslink structures such as bundles. They include Scruin, Fascin, Espin and Fimbrin/Plastin. The *C. elegans* genome lacks some small crosslinkers such as Fascin that can be found in other organisms. However, it does possess one copy of Plastin, also known as Fimbrin, encoded by *plst-1*. Homologs can be found in yeast as well as humans (Delanote et al., 2005). It is monomeric and binds to Actin thanks

to two Actin Binding Domains (ABDs). In addition to its role in Actin bundling, it is also implicated in generating lose Actin networks (Zhang et al., 2016) (Fig. 16). Plastin is a versatile crosslinker that is implicated in cytokinesis, as it is implicated in cortical contractility (Ding et al., 2017), as well as other processes such as endocytosis and polarity (Skau et al., 2011). In *C. elegans*, Plastin is essential for polarity establishment and cytokinesis and its absence leads to increase in early embryonic lethality (Ding et al., 2017). Recent study suggests that during cytokinesis Plastin plays a key role in making an efficient contractile ring by being the main F-Actin bundler with the help of Myosin (Leite et al., 2020).

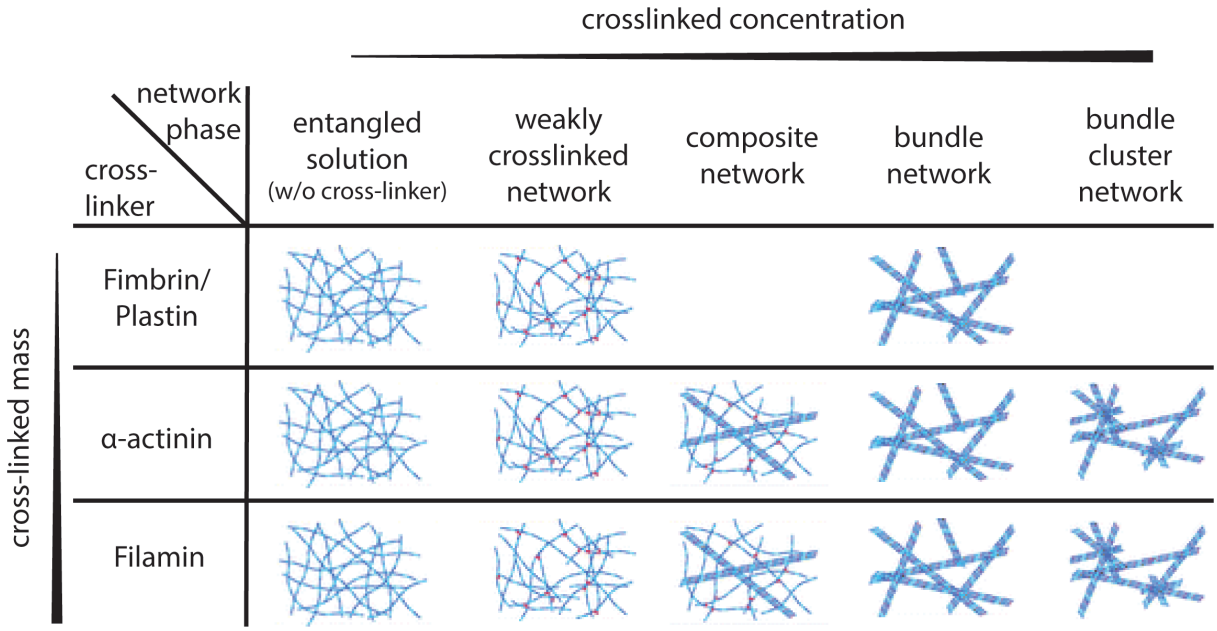

Figure 16. Type of Actin networks depending on crosslinker type and concentration. At low crosslinker concentrations, the network is always in a weakly linked phase while relatively high cross-linker concentrations are required to induce a structural transition to bundles of Actin filaments or a composite network formed by bundles and weakly linked filaments. At very high crosslinker concentrations clusters of Actin bundles are observed for long and flexible crosslinking molecules. In contrast, small crosslinkers tend to form homogeneous purely bundled phases. Adapted from (Lieleg et al., 2009b).

2.1.2.3 Network organization through crosslinking

Small and large crosslinkers build intrinsically different Actin networks. *In vitro* experiment by Winkelman *et al.* has provided evidence that crosslinkers facilitate their own binding, while inhibiting other crosslinkers, without any signaling mechanism, taking the example of α-actinin and Fascin (Winkelman et al., 2016). Furthermore, this promotes segregation of F-Actin networks, building networks of specific spacing according to the crosslinker type and concentration (tight bundles versus more widely space networks). Model by Freedman *et al.* show that this sorting can be controlled by non-equilibrium factors, such as Actin polymerization, and depends on the rates of binding and unbinding (Freedman et al.,

2019). They additionally predict that bundling proteins with larger length differences than α-actinin and Fascin, once sorted networks are formed, size difference in crosslinkers, kinetics and mechanics maintain the local concentration and molecular composition of a particular Actin network by excluding other crosslinkers.

Actin specific dynamic and architecture shape the cell ability to respond mechanically to a stimulus. Actin networks are diverse depending on the cell structure: stress fibers, lamellipodia, fillopodia, cortex, cytokinetic ring. Composition in crosslinkers and other ABPs define mechanical properties of the network. Local remodeling of such structure depends on nucleators, elongators and severing factors. Additionally, a key player of change in Actin mechanical properties is the molecular motors, Actomyosin networks having the ability to contract. The following section will focus on this protein and how its own structure and regulation has an impact on Actin networks.

2.2 MYOSIN, A HEXAMER COMPLEX

2.2.1 STRUCTURE AND REGULATION

Myosin is a superfamily of proteins that display an Actin-dependent motor activity. Very diverse –sorted in ~17–80 distinct classes depending on nomenclature (Hartman and Spudich, 2012; Sellers, 2000)– Myosins share a common domain which interacts with Actin, binds and hydrolyzes ATP, and produces movement (Sellers, 2000). Here, we will only focus on a class of conventional Myosins present during embryogenesis, the non-muscle Myosin II family.

Non-muscle Myosins II (which are also expressed in muscle cells) are a family of hexameric complexes that consists –similar to its counterparts skeletal muscle Myosin II– of a pair of Heavy-Chains (each Heavy-Chain is ~230 kDa), which contains the motor domains, a pair of Essential Light-Chains (17 kDa), and a pair of Regulatory Light-Chains (20 kDa) (Sellers, 2000; Warrick and Spudich, 1987). The C-terminal end of the two Heavy-Chains assemble in a coiled-coil tail, while the N-terminal ends folds into globular heads; the Light-Chains bind to the neck part, situated between head and tail (Heissler and Manstein, 2013). Each head has an Actin and an ATP binding sites (Sellers, 2000; Warrick and Spudich, 1987).

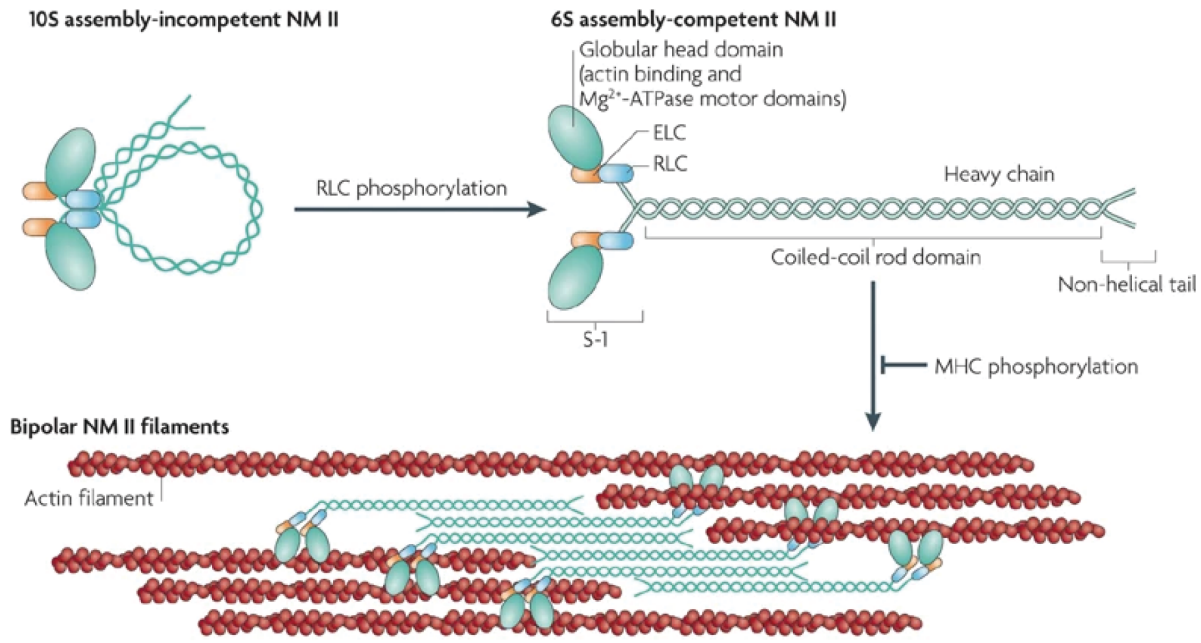

Figure 17. Myosin is a hexamer which inhibition is based on interaction between its domains. In the absence of RLC phosphorylation, Non-muscular Myosin II (NM II) forms a compact molecule through a head to tail interaction. This results in an assembly-incompetent form (10S; top left) that is unable to associate with other NM II dimers. On RLC phosphorylation, the 10S structure unfolds and becomes an assembly-competent form (6S; top right). Myosin is composed of three parts: a globular head domain which contains the Actin binding and the motor domain, a tail composed of a coiled-coil rod domain and a non-helical tail and a neck which the region between head and tail. RLC: Regulatory Light-Chain, ELC: Essential Light-Chain, MHC: Myosin Heavy-Chain. Once activated Myosin assemble into bipolar mini-filaments that bind to Actin filament. Adapted from (Vicente-Manzanares et al., 2009).

Myosin monomers are present in cells in two conformations: an extended conformation (6S) in absence of ATP and a compact conformation (10S) in presence of ATP. In its inhibited state, the two Myosin heads are interacting, thus blocking Actin binding and ATPase activity (Fig. 17) (Jung et al., 2008). Functionally, the inactive state represents a key element of energy balance, in muscle cells in particular, shifting Myosin from an inactive storage molecule to an active molecular motor. This inactive conformation is a shared feature of muscle and non-muscle Myosins across all animals (vertebrates and invertebrates) (Jung et al., 2008; Lee et al., 2018). Additional interactions between Myosin head and tail (S2 domain) also play a role in its inhibition (Jung et al., 2008; Miao and Blankenship, 2020).

Phosphorylation of two highly conserved residues (Thr18/Ser19 in mammals, Thr20/Ser21 in *Drosophila* (Karess et al., 1991)) of the Regulatory Light-Chain (RLC) represents one of the main modes of Myosin regulation. Historically, it is thought that it is the phosphorylation of RLC that promotes Myosin switch from inhibited to activated state by

disrupting intramolecular interactions (Craig et al., 1983; Kendrick-Jones et al., 1987; Trybus, 1991). This model is based on 10S conformation being incompetent for polymerization, however, recent *in* vitro studies on mammalian non-muscle Myosin 2 by Liu *et al.*, show evidence that RLC-unphosphorylated monomers are also capable of mini-filament assembly (Liu et al., 2017; 2018).

Two main enzymes support RLC phosphorylation *in vivo*: Rho-associated coiled-coil-containing kinase (ROCK) and Myosin Light-Chain Kinase (MLCK) (Amano et al., 1996; Totsukawa et al., 2000). ROCK activates Myosin through direct phosphorylation, but can also activate Myosin indirectly by inhibiting Myosin Phosphatase through phosphorylation of the Myosin Phosphatase target subunit (MYPT) (Hartshorne et al., 1998; Kimura et al., 1996; Matsumura and Hartshorne, 2008). Other kinases are known to play a role in Myosin activation, such as myotonic dystrophy related Cdc-42 binding kinase (MRCK) which is active during cell protrusion (Miao and Blankenship, 2020; Tan et al., 2008) and in *C. elegans* during polarization and gastrulation (Anderson et al., 2008; Kay and Hunter, 2001).

Myosin Phosphatase catalyzes the dephosphorylation of RLC (and therefore its switch back to an inhibited state). Myosin Phosphatase is an enzyme composed of a catalytic subunit (PP1c) and two non-catalytic subunits: a Myosin Phosphatase target (or targeting) subunit (MYPT, also referred as MYPT1 or Myosin Binding Subunit (MBS)) and a third small subunit (Hartshorne et al., 1998; Matsumura and Hartshorne, 2008). Less is known about the regulation of Myosin by its Phosphatase, but recent work in *Drosophila* shows that this mechanism is important for the oscillatory behavior of Actomyosin observed during morphogenesis (Qin et al., 2018; Valencia-Expósito et al., 2016).

Finally, work in *Dictyostelium* and *Acanthamoeba* has given evidence that phosphorylation of the Heavy-Chain tails plays an important role in Myosin mini-filament assembly regulation (Egelhoff et al., 1993; Kuczmarski and Spudich, 1980; Liang et al., 1999; Liu et al., 2013). In contrast, phosphorylation of the non-muscle Myosin Heavy-Chain by PKC is dispensable for viability in *Drosophila* (Su and Kiehart, 2001). *In vitro* studies by Dulyaninova *et al.* and Murakami *et al.* on human non-muscle Myosin-II show that Heavy-Chain phosphorylation is associated with disassembly of existing mini-filament (Dulyaninova et al., 2005; Murakami et al., 2000). Therefore, role of this Heavy-Chain phosphorylation in Myosin mini-filament assembly still needs to be further investigated (Dulyaninova and Bresnick, 2013; Heissler and Sellers, 2016).

2.2.2 Molecular interactions Myosin and Actin

Myosin is an Actin-dependent motor protein. All Myosins II assemble into mini-filaments of variable number of heads: from a dozen for non-muscle Myosin to hundreds of head for skeletal muscle Myosin (Niederman and Pollard, 1975; Pollard, 1982; Skubiszak and Kowalczyk, 2002; Sobieszek, 1972; Tonino et al., 2002). *In vitro*, Actin filaments promote Myosin assembly by significantly accelerating the rate-limiting nucleation phase of the reaction. Transient binding of Myosin along Actin filaments presumably concentrates and aligns dimers, accelerating initial tetramer formation (Mahajan and Pardee, 1996; Mahajan et al., 1989).

ATP hydrolysis induces a change in conformation that is transmitted from the head domain to the lever arm (the neck domain), which amplifies the rotation of the head (reviewed in (Vicente-Manzanares et al., 2009)). The Myosin translocation results in contraction or extension of the F-Actin filaments depending on the position of the Myosin mini-filament regarding the middle of the filaments (Murrell et al., 2015). Non-muscle Myosin family is inhomogeneous in term of processivity. In a Myosin mini-filament, not all the heads are likely to be in a geometrically favorable position and therefore among all the Myosin heads of the mini-filament only a few (number dependent on Myosin duty ratio) heads are effectively bound to Actin filaments (Melli et al., 2018).

Myosin motors plays an important role in Actin turnover but conflicting results have been exposed as to know the exact role of Myosin. Originally it has been demonstrated that, during cytokinesis, non-muscle Myosin II (hereafter referred as Myosin) does not only generates the forces required for cytokinesis but also disassemble Actin bundles for ingression which are the main components of the contractile ring (Burgess, 2005; Guha et al., 2005; Murthy and Wadsworth, 2005). In this hypothesis, it would be the motor activity of Myosin (not its F-Actin crosslinking activity) that is essential for the cytokinesis as it determines the pace of constriction (Osório et al., 2019). *In vitro* studies show that the regulation of Actin turnover by Myosin is occurring in two steps, first unbundling of Actin bundles into individual filaments then depolymerization of the filaments (Haviv et al., 2008). However recent research in lamellipodia and lamella suggests that the dynamics might be different as the one exposed above and that Myosin contributes to F-actin stabilization (Yamashiro et al., 2018).

In *C. elegans*, there are four genes for muscle Myosin II Heavy-Chains, two for non-muscle Myosin II Heavy-Chains (Sellers, 2000). At 1-cell stage non-muscle Myosin 2 (NMY-2, a

type II non-muscle Myosin) is expressed. NMY-2 plays a critical role in embryo polarization (Guo and Kemphues, 1996), cytokinesis (Davies et al., 2014; Osório et al., 2019), gastrulation (Lee and Goldstein, 2003), but also later in post-embryonic development (Ding and Woollard, 2017). Non-muscle Myosin 1 (NMY-1, also a type II non-muscle Myosin) is not expressed at early stages but plays an important role in later development (Gally et al., 2009; Piekny et al., 2003). The Myosin Regulatory Light-Chain MLC-4 is also known to be essential for cytokinesis, polarization and elongation (Shelton et al., 1999). It is therefore likely that NMY-2 and MLC-4 work together at early stages of embryogenesis in *C. elegans*. In the following results of my thesis, I will therefore focus on this two proteins and additionally on the MYPT as a reporter Myosin Phosphatase activity coded by *mel-11* in the nematode. I will also focus on ROCK LET-502. Both MEL-11 and LET-502 are reported to regulate cytokinesis in the early *C. elegans* embryo (Piekny and Mains, 2002).

Actomyosin plays a key role throughout cell physiology in most eukaryotes, and in particular cell and tissue morphogenesis during development in metazoan. This central role makes it fundamental to understand how cell shape changes are regulated during morphogenesis. Changes in Actomyosin meshwork composition and mechanical properties rely on the activation of the RhoA activation cascade. Stimulus is integrated through this cascade to trigger dynamic remodeling of the meshwork. Fine regulation of this cascade is, therefore, essential to a normal development. In the next chapter, we will go in further details of its roles during development in order to give an overview of what it is currently known about its regulation. We will give particular attention to what is known in our model organism, the *C. elegans* embryo.

3 ROLE OF THE CORTEX DURING EMBRYOGENESIS

During embryonic development, tissue morphogenesis is controlled by a limited repertoire of cell behaviors: cell division, cell death, cell migration and cell shape changes. In all these cases, cell behavior is controlled –at least in part– by modulations of cell mechanics, which is in turn governed by spatially and temporally localized remodeling the cell cytoskeleton. The Actomyosin network plays an important role in this process, and local modulation of Actomyosin dynamics in a cell can translate into shape changes at the scale of a tissue, through tension propagation through junctions with neighbor cells and the extracellular matrix (Martin, 2010). During apical constriction, for example, an increase in cortical Actomyosin contractility on the apical side of the cell drives apical constriction, leading to a 3D remodeling of the shape of the tissue, starting from a flat surface to form a tube. Similar mechanisms include *Drosophila* gastrulation (Sweeton et al., 1991), *Xenopus* neural tube formation (Inoue et al., 2016) and chicken otic placode vesicle closure (Alvarez and Navascués, 1990). However, the mechanisms by which the dynamic Actomyosin architectures drive cell shape changes, and how these macromolecular architectures are regulated, is not yet fully understood.

In this chapter, we will see what is known about the regulation and activation of RhoA activation cascade, when responsible for recruitment of Actomyosin. Then we will see specific examples where Actomyosin plays a key role in development, focusing specifically in our model, the *C. elegans* embryo. Finally, in order to have an overview of the nature of the signal transmitted through the activation cascade, we will see what is already known about kinetic delays in pulsed contractions during development.

3.1 ESTABLISHMENT OF THE ACTOMYOSIN NETWORK

Over the past 15 years, the role of the Rho family of GTPases has emerged as critical in the regulation of Actomyosin dynamics. Rho family belongs to the large superfamily of Ras proteins. Bound to GTP, these proteins are active and can drive the activation of downstream effectors and the assembly of specific cytoskeletal structures. The Rho family proteins is regulated by GEFs (Guanosine Exchanging Factors), GAPs (GTPases Activating Proteins) and GDIs (Guanine activating Dissociation Inhibitors). GEF molecules promote the switch between GDP and GTP groups, the GAP molecules promote the hydrolysis of GTP into GDP, and GDI

molecules stabilize the binding between Rho and the GDP group (Fig. 18A) (Bement et al., 2006). RhoA (Ras homology family member A), a small GTPase, activation can be delimited in space, leading to the creation of a region with local specific properties. Activated RhoA drives the activation of two downstream cascades, which ultimately recruit Actin and Myosin respectively, at the location of the activated RhoA. Transient accumulations of Actomyosin are known as pulsed contractions and have been identified originally in the *C. elegans* zygote (Munro et al., 2004). The activation and the recruitment at a cortical specific location of RhoA trigger the cascades as following: RhoA will recruit the Formin to promote the nucleation of the Actin, to form filaments and then promote its polymerization at the fast-growing ends. RhoA will also bind to and activate Rho-kinase (ROCK) and therefore activate the Myosin by phosphorylation (Kimura et al., 1996), eventually locally increasing local Actomyosin tension (also called contractility). In *C. elegans*, RhoA is coded by *rho-1* and controls Actomyosin contractility at early embryonic stages (Michaux et al., 2018; Motegi and Sugimoto, 2006; Nishikawa et al., 2017; Schonegg et al., 2007; Tse et al., 2012).

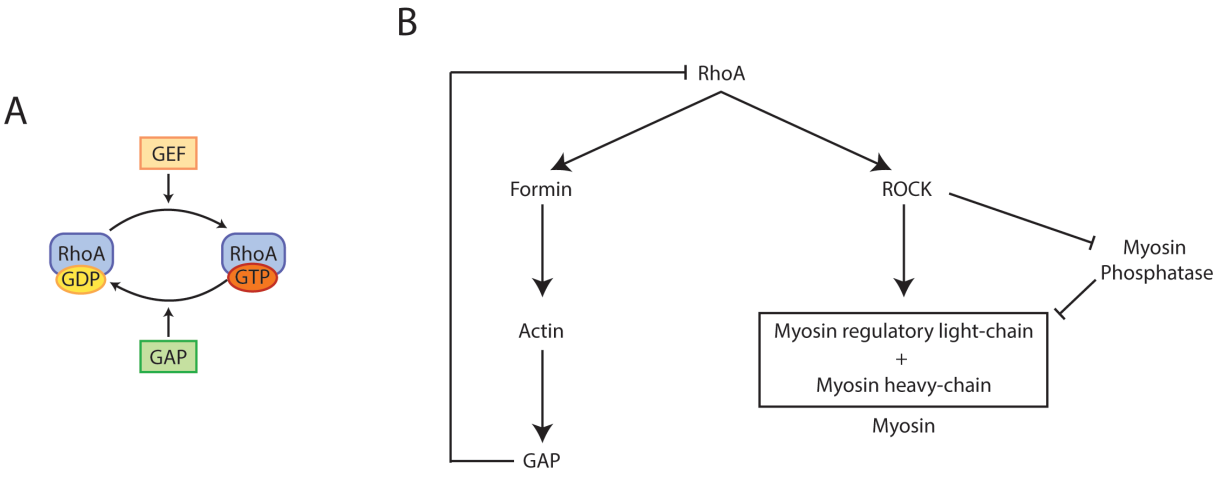

Figure 18. RhoA activation cascade. (A) Activation and deactivation of RhoA is made through GEFs and GAPs respectively. Adapted from (Kholodenko, 2006). (B) RhoA activation cascade in the early *C. elegans* embryo.

Pulsed Actomyosin contractility represents a widespread mode of Actomyosin contractility. Spatially and temporally regulated activation of Actin and Myosin drive contractions of the cortex, locally reducing its surface. One general mechanism has been proposed to explain how to generate oscillatory-pulsed behavior in a cascade is the use of delayed negative feedback. In *C. elegans*, one candidate to drive this negative feedback is the GAP proteins (RGA-3 and 4) activated by Actin, which will lead to the inhibition of active RhoA (Michaux et al., 2018). Hence in this system, excitable RhoA positively feeds the loop of the

Actomyosin activation cascade for its own activation and with a delay through RGA-3/4 feeds negatively to terminate the pulsed contraction (Michaux et al., 2018) (Fig. 18B). Study by Munjal *et al.* suggests that oscillatory behavior might alternatively also rely on contraction advection (Munjal et al., 2015).

3.2 Development is tightly linked to the Actomyosin cortex

3.2.1 1 and 2 cell stages and polarity establishment

Asymmetric cell division (ACD) is a fundamental process whereby the asymmetric inheritance of cellular components during mitosis defines distinct fates for each daughter cell. This process is observed broadly across evolution, frequently relying on conserved molecular toolkits. The difference in fate can be achieved by the unequal separation of components in the cytoplasm, RNAs (including mRNAs but also long non-coding RNAs and circular RNAs as demonstrated in human and *Drosophila* cells (Benoit Bouvrette et al., 2018; Lécuyer et al., 2007)) or proteins. The first description of a molecular system driving asymmetric cell division was performed by Kemphues *et al.* in *C. elegans* embryos (Kemphues et al., 1988). In *C. elegans*, the first division is asymmetric yielding a large anterior cell (AB cell) and a smaller posterior cell (P1 cell) (Fig. 19). This asymmetric cell division relies on the unequal segregation of PAR proteins in two mutually exclusive domains in the zygote.

This accumulation of PAR proteins is achieved by a mutual biochemical inhibition of anterior and posterior PAR proteins, leading to a mutual exclusion, combined with a contraction of the Actomyosin cortex (cortical flow of material can be observed) from the posterior end of the embryo, corresponding to the point of entry of the sperm (Goehring et al., 2011; Munro et al., 2004; Nance, 2005). Symmetry breaking in *C. elegans* zygote is mediated by the local recruitment of the mitotic kinase Aurora-A, which accumulates around centrosomes and locally disrupt the cortical Actomyosin contractile activity. Then Aurora-A mediates global disassembly of cortical Actomyosin networks, this leading to the disruption of the cortical flows (Klinkert et al., 2019; Zhao et al., 2019). This accumulation is actually sufficient by itself to induce symmetry breaking. Importantly, recent study has shown evidence that geometry plays also a key role in defining polarity in *C. elegans* zygote (Klinkert et al., 2019). Flows driven by Myosin contractions are critical as early as the 1-cell stage to initiate this first step in morphogenesis (but polarization can also be achieved even in absence

of contractility). While their function has not been clearly established, these contractions can be observed again during the interphase at later embryonic stages, in particular at the 2-cell stage and later in development as in gastrulation.

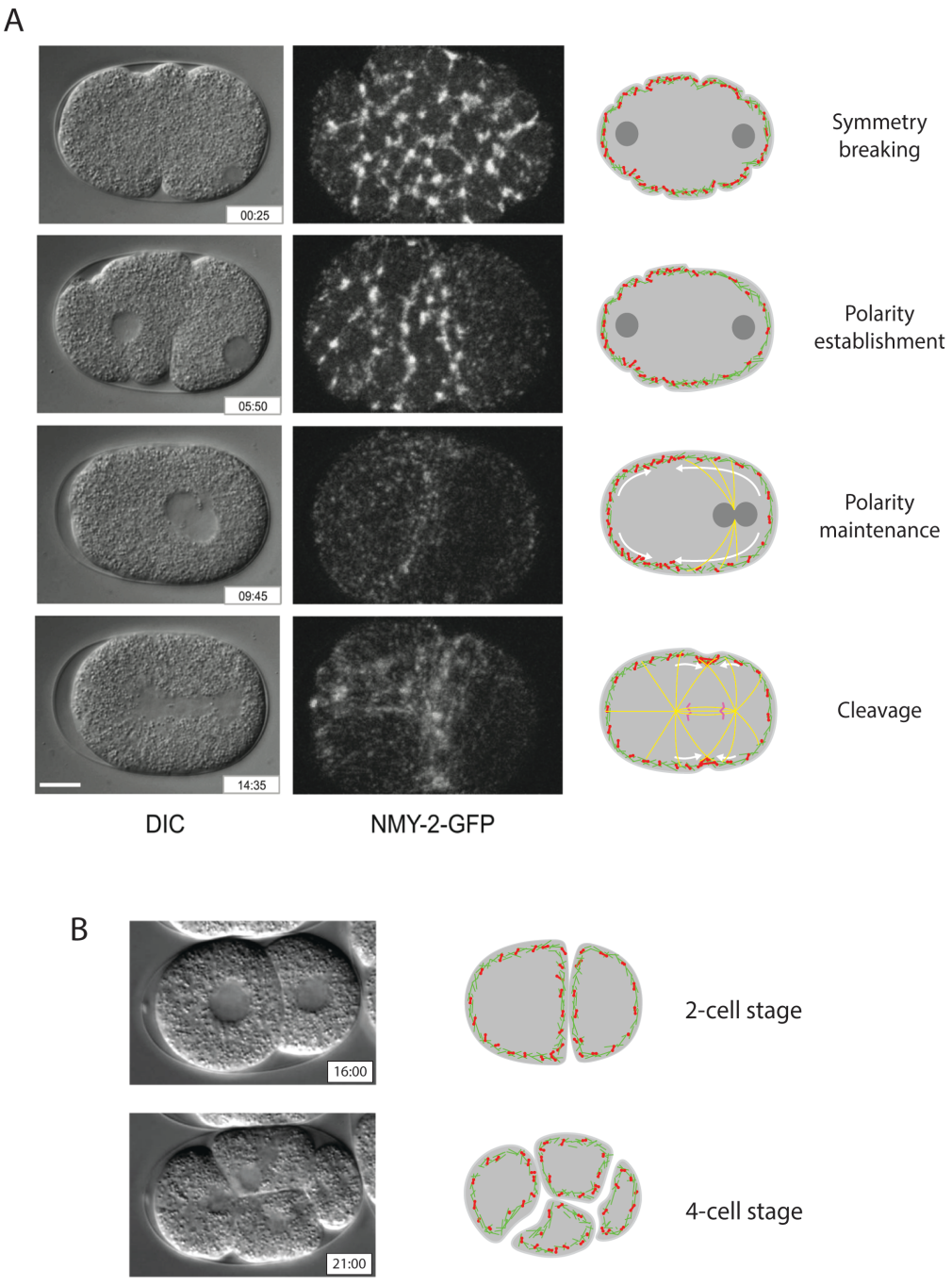

Figure 19. Polarity is established through Actomyosin cortical flow at one-cell stage in *C. elegans* embryo. (A) Left: images from time-lapse differential interference contrast (DIC) microscopy; time is displayed in min:sec from the beginning of the recording shortly after fertilization. Middle: images from time-lapse fluorescence confocal microscopy at approximately corresponding stages (from (Munro et al., 2004)). Right: corresponding schematics, illustrating the distribution of the Myosin (red) and Actin (green), nucleus (dark grey) and microtubules aster (yellow). Embryo is approximately 50 µm long. Adapted from (Rose and Gönczy, 2014). (B) Left: images from time-lapse DIC, right: corresponding schematics. Adapted from (Moser et al., 2009).

Interestingly, Roh-Johnson *et al.* has provided evidence that Actomyosin pulsed contractions can come in two flavors with difference in mechanical impact on cells during gastrulation. The following section will discuss gastrulation in *C. elegans*, in order to give an idea of difference in pulsed contractions mechanics.

3.2.2 GASTRULATION

Gastrulation is one of the first morphogenetic event occurring development, and a key step in embryonic development, as it defines the positions of tissue anlage in the organism. Specifically, gastrulation relies on the internalization of the prospective internal tissue, including the endodermal precursors (the prospective gut) and the mesoderm precursors cells (muscles). This internalization of the tissues can be synchronous (as in sea urchins or *Xenopus*), or separated in time. In *C. elegans*, for example, the two initial cells internalized are the endodermal precursors, (90' after fertilization), followed by the muscle precursors (150') after fertilization (Fig. 20, (Nance and Priess, 2002; Nance et al., 2005; Sulston et al., 1983)). Gastrulation may result from individual cell behaviors, as in *C. elegans* or from large scale tissue movements, as in *Drosophila melanogaster*, where the entire tissue is internalized (Leptin, 1999).

Lack of proper endoderm cell specification in *C. elegans* embryo will abolish the process of gastrulation (Maduro and Rothman, 2002). Endodermal cells, through a reorganization of their cytoskeleton undergo through an event of deformation prior to the invagination. This change in cell shape by remodeling of the Actomyosin network is dependent on Arp2/3 complex (Severson et al., 2002). Importantly, during gastrulation, the neighboring cells do not push (or with a relatively less important effect) the invaginating cells inside the embryo. These cells see their apical cortical Actomyosin increase in density and pulsed contractions can be observed, decreasing the apical surface of the cells, ultimately leading to their invagination. Intact Actomyosin cytoskeleton is key for this phenomenon to happen (Lee and Goldstein, 2003).

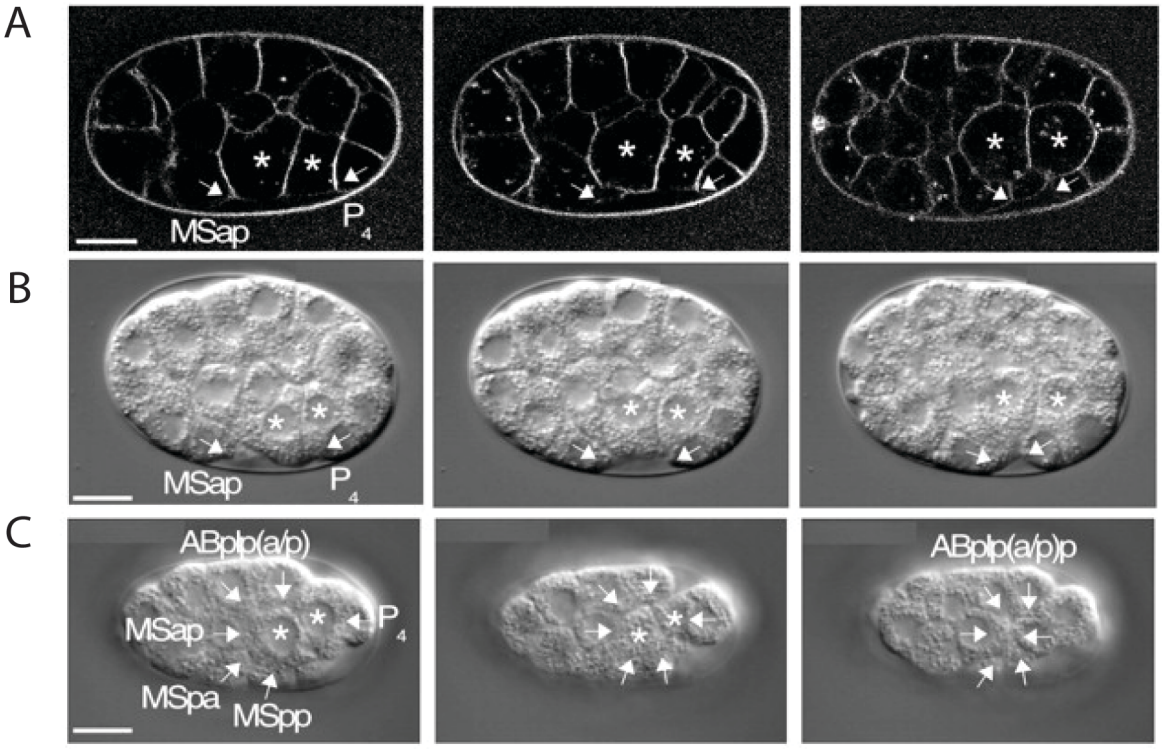

Figure 20. Gastrulation occurs between the 26- and 28-cell stage and consist in the invagination of the endodermal precursor cells. (A) Confocal images of lateral view of gastrulating embryos labeled with the membrane marker SynaptoRed to better visualize cell boundaries. Ea and Ep ingress towards the center of the embryo, and are eventually surrounded by MSap and P_4. Asterisks indicate Ea and Ep and neighboring cells are labeled with arrows in A-C. (B, C) Panels show DIC time-lapse views of gastrulation. (B) Lateral view of gastrulation, similar to A. Images are at 10 minutes intervals. (C) Ventral view of gastrulation. From left to right, time intervals are 0, 12 and 32 minutes. As Ea and Ep `sink' into the embryo, six cells close up the ventral cleft. Note that while ABplpa and ABplpp start moving toward the cleft, they divide and the posterior daughters of these cells finish the movement. Scale bars: 10 µm. Adapted from (Lee and Goldstein, 2003).

In *C. elegans* it has been suggested that the successive Actomyosin contractions during gastrulation can be separated in 2 phases: the first one where the pulsed contractions are not effectively reducing the cell surface, and a second one where the Myosin through MRCK-1 protein (Marston et al., 2016) provides the tension necessary to effectively invaginating the cells, altogether working as a molecular clutch during gastrulation (Roh-Johnson et al., 2012). Tension here is key for the effective reduction of the apical cell surface, Actin is hence polymerized as long cables to transmit this tension throughout the surface of the cell.

Work from Roh-Johnson *et al.* gives a hint as to potentially have difference in pulsed contractions mechanics; that at specific developmental stages, different phases of pulsed contractions can occur, even though biochemical input seems identical. To the best of our knowledge, such difference in pulsed contractions has not been reported at 1- and 2-cell stages, which are the one explored in my thesis. For sake of simplicity, I will consider all pulsed contractions being equals regarding this matter in further exposed experiments.

3.2.3 CYTOKINESIS

Cytokinesis is the ultimate process of cell division during which the two daughter cells are separated from one another. This process is crucial and requires the building of a transient structure composed of bundles of Actin filaments called the contractile ring. This ring is composed of two populations of opposite directionality of Actin filaments. During cytokinesis, Actin is organize in large bundles at the cytokinetic ring that can be seen by electron microscopy (Maupin and Pollard, 1986) and even the branching is depleted as Arp2/3 complex is rather excluded from the contractile ring (Chan et al., 2019). Through constriction by Myosin motors, which will slide the Actin filaments, this contractile ring reduces in size over time, forming a cleavage furrow that will ultimately separate the two cells (Pollard, 2010). Failure in producing an effective contractile ring will lead to lethality as early as one-cell stage (Guo and Kemphues, 1996). Formin, Profilin and Actin are essential in this process (Severson et al., 2002). Importantly physical disruption of the contractile ring, once it is in place, will not compromise the cytokinesis as the cell has the ability to recover, rebuild the contractile ring by repairing the gap(s) and speed up the closure of the cleavage furrow in order to make up for the time lost during reconstruction of the contractile ring (Silva et al., 2016). Even though active polymerization of Actin filaments is not require for constriction of the contractile ring (Mishra et al., 2013), proper Actomyosin contractility requires Actin turnover during cytokinesis in order to preserve Actin filaments homeostasis (Chew et al., 2017). In mouse, in addition to the activation of RhoA GTPase, the binding of Anillin is necessary for the proper localization and function of Formin mDia2 at the cleavage furrow location (Watanabe et al., 2008; 2010).

3.2.4 PULSED CONTRACTION AND KINETIC DELAY IN ACTIVATION CASCADE

A critical parameter to control the temporal dynamics of the pulses is the biochemical control of the time delay between different steps of the cascade which can create oscillations within the cortical Actomyosin network. This oscillating system explains the pulsatile state of the contractility in the cortex, as it is the case in gastrulating Drosophila embryos, where apical pulsed contractions of Actomyosin drive the internalization of the mesoderm (Martin and Goldstein, 2014). Activation cascades are a widespread mechanism to propagate biochemical input inside cells. Even though fine spatial and temporal tuning of signaling is often required, we lack an overview of the molecular mechanisms underlying signaling kinetics. We do not

know how to explain the signaling delays, their origin, robustness and variability. Several models have been reported to undergo pulsed contraction during their morphogenesis.

During *Drosophila* gastrulation, invaginating cells undergo an average of 3.2 +- 1.2 constriction pulses over 6 min, with an average interval of 82.8 +- 48 s between pulses. Constriction pulses are mostly asynchronous between adjacent cells. Discrete Myosin spots and fibers are present on the apical cortex and form a network that extended across the tissue. These Myosin structures are dynamic, with apical Myosin spots repeatedly increasing in intensity and moving together (at about 40 nm/s), which leads to coalescence of these. Apical Myosin spots are constrained by the cortical actin network (Martin and Goldstein, 2014).

In *Drosophila* germband extension (GBE), MyoII pulsed contractions have a duration of around 100s and most of the pulse amplitude (85%) is due to recruitment of new MyoII protein and not due to the densification of the network. Rho1 is essential, it activates MyoII and this is made through the dephosphorylation of the phosphatase. Inhibition of RLC-targeting subunit of MyoII leads to slower GBE and junction shrinkage (Munjal et al., 2015).

Average period of the basal contractions on follicle cells (all around in Drosophila egg chamber) is 6.3 min (most contraction-relaxation cycles being completed in 5-7 min). Basal membrane activity is fivefold higher in the dorso-ventral (D-V) than in the anterio-posterior (A-P) direction, Myosin local recruitment is responsible for this activity. Myosin density change is periodic at the basal side, contrary to the apical. 1 min delay can be observed between Myosin accumulation and basal cell area contraction. Myosin accumulation is not caused by changes in F-actin dynamics (only 20% change vs 70%, and this change coincide with change in Myosin intensity). At the apical surface Actin filaments change intensity with a similar amplitude to that of Myosin in apical constriction. Change in apical surface area is eventually stabilized whereas the change in basal follicle cell shape is temporary (He et al., 2010). In our model, the *C. elegans* embryo, pulsed contractions occur every 30 s (Michaux et al., 2018).

4 AIM OF THIS THESIS

In the past 20 years, with studies combining genetics, chemical perturbations, optogenetics, and physics, the scientific community has made significant headway to understand the regulation of the cell shape changes in early steps of the embryogenesis. Yet we still do not fully understand how the signals transduced by activation cascades regulate morphogenesis and shape cortical contractility, cell mechanics and behavior. In particular, the interplay between the mechanics of cell shape change and the finely tuned temporal regulation of Actomyosin activation still remains elusive. Even the simple molecular underpinnings of the *delay* in response to recruitment of a classical activator such as RhoA, which ultimately defines the temporal response of the cell, have remained elusive. Here, we decided to explore the molecular mechanisms and the impact of delays on the regulation of cortical contractility and cell behavior. To address this question, I focused on a canonical example of an activation cascade, the RhoA activation cascade, which recruits Actomyosin at the cell cortex, using the 2-cell stage *C. elegans* embryo as a model system. In the first chapter of the Results section, I will address the following questions:

1. What is the kinetic delay in this cascade?
2. How can we explain this delay?
3. What can we learn from a model explaining it?
4. Can we perturb this delay? What happens when we do?
5. Is the synchronous recruitment of Actin and Myosin important physiologically?

The RhoA cascade that we described previously drives, in early *C. elegans* embryos, local recruitment of Myosin and local actin assembly. In particular, cortical F-Actin is assembled by Formins. In a second study, we observed that Formins switch to an active mode once bound to a barbed-end leading to the creation of two distinct populations of recruited Formin: activated (not bound, *recruited*) and active (bound, *elongating*). In particular, following my work on the temporal dynamics of the RhoA cascade, I explored the kinetics of recruitment of these molecular species at the cell cortex. We further explored the architectures of the Actin network assembled by Active Formins during pulsed contractions. Specifically, this led me during the course of my graduate studies to explore the following questions, that I will present in the second chapter of the Results:

6. Can we visually separate the two populations of Formins?

7. Does the speed of the active Formin change during the first stages of embryonic development?
8. Can we determine the polarity of the pulsed contractions defined by the Formin?

Finally, I will present some work we performed to explore the hypothesis that Formins are in competition with Arp2/3 complex for the availability of G-Actin, as suggested by previous studies, in particular in *S. pombe*. In the third chapter of the Results, I will present some of my work to address the following question:

9. Does this competition affect and limit the Formin speed?

Results

Article 1:

Kinetic control of the temporal dynamics of a RhoA signaling cascade

Cascades of activation are defined by a succession of sequential activations of signaling proteins. This leads to the activation of a downstream effector, with a precise intensity and timing, to control a specific biological function. Failure in proper timing generally leads to failure in setting up the biological function. Even though we are aware of this crucial role in time regulation, we currently simply lack measurements and explanation for the kinetics delays happening in activation cascade.

Here, I proposed to analyze the unfolding of a simple cascade in the early embryonic development of a metazoan, using the example of RhoA activation cascade as a canonical example. The activation and the recruitment at a cortical specific location of RhoA trigger the cascades as following: RhoA will recruit the Formin to promote the nucleation of the Actin, to form filaments and then promote its polymerization at the fast-growing ends. RhoA will also bind to and activate Rho-kinase (ROCK) and therefore activate the Myosin by phosphorylation (Kimura et al., 1996), eventually locally increasing local Actomyosin tension (also called contractility). In this context, we can measure, at a specific location of the cell cortex, a stereotypical delay between the activation of the upstream regulator and the recruitment and activation of the downstream effector.

First, we proceeded to a careful characterization of the dynamics of two sequential steps of the cascade. Using TIRF microscopy, we focused on the different steps of the RhoA activation cascade, using the Myosin as a landmark to measure the delay within the cascade at the cortex of *C. elegans* early embryos. I observed that most of the delay found between RhoA and Myosin could be found again between ROCK and Myosin. Interestingly, my results also demonstrated that Actin is recruited briefly before Myosin at the pulsed contraction location.

Second, using single-molecule imaging, we focused on the last step of this cascade and measured the dynamic modulation of the binding (K_{on}) and the unbinding rate (k_{off}) of the Myosin. Hypothesizing that variation in number of molecules over time is only dependent on K_{on} and k_{off} we calculated a target density at equilibrium state. I observed that a delay could be measured between target density and actual number of molecules, this delay being equivalent to the one observed between ROCK and Myosin. Therefore, my results show that the kinetic delay between this two proteins could be almost completely explained by the dynamics of Myosin.

We then functionally challenged this simple numerical model that takes advantage of the dynamic measurements of K_{on} and k_{off} to predict the temporal evolution of this cascade. We decided to perturb the dynamic of Myosin by measuring the variation in number of molecule, K_{on}, k_{off} and target density in a context where the phosphatase responsible for the deactivation of Myosin is absent. We could observe that even though K_{on} and k_{off} can be affected by the perturbation, the delay is not changed in this context. This result underlines the robustness of the system against this type of change and suggest a biological relevance of this delay. Simulation and modelling of the effect of this delay on the contraction of the network show that this delay is important for efficient propagation of the tension induced by the pulsed contraction.

We propose that this simple and generic model – which can in essence fit any activation cascade – offers a simple mathematical framework to understand the temporal dynamics of signaling cascades, and the delay and change in the shape of the response which can be observed between the input and the output of a cascade.

Author contributions:

F.B. Robin conceived the project. S. Prigent Garcia performed experiments and data analysis described in Fig. 1–4 and S1-S4. L. Bourdon, C.N. Plancke and S.K. Suman generated strains and molecular reagents used in the study. TY. Kim and J. Li performed the numerical simulations shown in Fig. 5. S. Prigent Garcia, TY. Kim and F.B. Robin prepared figures and wrote the paper.

Additionally, acknowledgments to Simon Begnaud for developing an ImageJ macro used in this paper.

Kinetic control of the temporal dynamics of a RhoA signaling cascade

Serena Prigent Garcia[1], Camille N. Plancke[1], Jing Li[2], Shashi Kumar Suman[1], Loan Bourdon[1,3], Taeyoon Kim[2], François B. Robin[1,✉]

1 : CNRS UMR7622 and Inserm ERL 1156, Institut de Biologie Paris-Seine (IBPS), Sorbonne Université, Paris, France.

2: Weldon School of Biomedical Engineering, Purdue University, West Lafayette, Indiana.

3: Current address: Mechanisms of Epigenetic Inheritance, Department of Developmental and Stem Cell Biology, Institut Pasteur, UMR 3738, CNRS, Paris, France.

✉: Corresponding author. Email: francois.robin@sorbonne-universite.fr

Introduction

Signaling cascades are a widespread biological strategy to respond to, propagate and shape extracellular and intracellular inputs. The architecture and tuning of these cascades can lead to a variety of behaviors, ranging from hypersensitivity and bi-stability, to cyclic oscillations or chaotic dynamics, and even 3-components networks can drive a wide array of dynamics (Ma et al. 2009). During embryonic development, signaling cascades –proceeding from a variety of molecular reactions from GTP/GDP exchange, to second messenger production to regulation of transcription– carry information at multiple scales in space and time. While mathematical models provide a glimpse on how these signaling cascades are tuned, and even as optogenetic tools offer a handle to control cascade activation while monitoring its propagation, experimental measurements on dynamic systems still remain extremely limited. The experimental dissection of the molecular mechanisms underpinning the spatial and temporal dynamics of these activation cascades therefore represent a key objective to understand how signals propagate in the cell.

In order to study the dynamics of a simple, hierarchical cascade, we decided to focus on the RhoA RhoGTPase cascade driving actomyosin recruitment during pulsed contractions. Small RhoGTPases represent a key example of signaling cascades, and despite their central importance, the dynamics of activation of the downstream players of these cascades remain largely unexplored. Over the past 25 years, RhoA in particular has emerged as a central regulator of morphogenesis (Hariharan et al. 1995), from *Drosophila* germband extension (Munjal et al. 2015), salivary gland morphogenesis and amnioserosa contraction during dorsal closure (Solon et al. 2009), to cells convergent extension in *Xenopus* early embryo (Kim & Davidson 2011), to compaction in the early mouse embryo (Maître et al. 2015). In particular, in *C. elegans*, RhoA regulates contractility in the spermatheca (Tan & Zaidel-Bar 2015), contributes to epidermal cell migration (Wallace et al. 2018), and plays a critical role in embryo polarization (Motegi & Sugimoto 2006; Schonegg & Hyman 2006). At the molecular level, RhoA drives the dynamic remodeling of cortical actomyosin networks and actomyosin contractility through a dual effect on F-actin and Myosin II. RhoA activates and recruits the formin CYK-1 (*mDia*/*Dia* homolog), which processively elongates Actin filaments (Costache et al. 2021; Kohno et al. 1996; Kovar & Pollard 2004; Watanabe et al. 1997). RhoA also activates and recruits the Rho kinase/ROCK (LET-502), which phosphorylates Myosin Regulatory Light Chain and inhibits Myosin Phosphatase (MEL-11) (Diogon et al. 2007; Piekny & Mains 2002;

Wissmann et al. 1999; Wissmann et al. 1997) resulting ultimately in Myosin II activation and cortical recruitment (Fig. 1A).

Dynamically, RhoA local activation drives actomyosin activation leading to continuous contraction of actomyosin cables, but also frequently occurs in pulses (Miao & Blankenship 2020). Pulsed actomyosin contractility represents a widespread mode of actomyosin contractility, and drives a broad variety of morphogenetic processes, from cell and tissue invagination during gastrulation to cell behavior coordination. Depending on the biological context, the period of pulsed contractions varies widely, from 30 s in *C. elegans*, to 2 min in *Drosophila* gastrulation or germband extension (Martin et al. 2009; Munjal et al. 2015), to 6 min in *Drosophila* follicle cells (He et al. 2010). While recent work has started to explore how the duration and iteration of contractions is linked to deformation reversibility and effectiveness (Cavanaugh et al. 2020; Staddon et al. 2019), the molecular mechanisms underpinning signal transduction in this cascade still remain unclear, in particular regarding the delay between steps of the cascade (Michaux et al. 2018), the molecular origins of these delays, and their impact on cellular mechanics.

Here, we first describe the time delay between consecutive steps of this hierarchical cascade. Using single-molecule microscopy, we provide dynamic measurement in live embryos of the binding rate (number of molecules binding to the cortex per time unit, noted K_{on}) and the unbinding rate (fraction of molecules unbinding from the cortex per time unit, noted k_{off}), thereby exposing dynamic modulations of the signaling kinetics. Using Ordinary Differential Equations, we then explore numerically the impact of these modulations. Based on this simple model, we propose and execute experimental measurements to derive the systems dynamics by computing a target concentration, from the dynamic measurements of K_{on} and k_{off}. To modulate pulse period and challenge our model, we then used genetic perturbations to modulate F-actin assembly/disassembly and Myosin II binding/unbinding rates. Finally, we used computer simulations to explore the impact of the delay on F-actin contraction. Our results suggest that kinetic delay is an integral part of signaling cascades, but also that delay duration is critically important to drive efficient contraction. Equipped with these results, we propose a new, general working frame to explore and understand kinetic delays in membrane activation cascades.

Results

The RhoA cascade displayed four key features that were of interest to us. First, it is highly hierarchical, with two branches derived from the same upstream signal, a *F-actin* branch and a *Myosin II* branch. Second, these two branches of the cascade contribute to generate the output dynamics, raising the question of the importance and modalities of the synchronization between two outcomes in parallel transduction pathways from a single input. Third, the cascade displays a pulsatile activation, which we could use as triggers to study signal propagation in the cascade. Finally, the RhoA signaling cascade is interfaced with a mechanical output, raising generic questions regarding how mechanical and biochemical signaling can intertwine.

In the zygote, however, pulsed contractions are associated with deep invaginations of the cortex, potentially affecting measurements of pulse kinetics, hampering a detailed analysis of pulse kinetics, in particular for single-molecule microscopy analysis. We therefore decided to focus on the dynamics of the cascade at the 2-cell stage. We have previously shown that RhoA-driven pulsed activation causes local cortical actomyosin contractility (Michaux et al. 2018), potentially affecting the tension distributed in the actomyosin cortex and causing mechanosensitive recruitment of cascade components. The amount of contraction itself, however, remains reasonably small (~5%), arguably affecting only marginally the local concentration of the components of the cascade. Finally, the RhoA signaling cascade unfolds at the cell surface, simplifying greatly the observation.

Myosin II accumulation is delayed compared to RhoA activation

In order to explore the temporal dynamics of the RhoA signaling cascade, we first decided to proceed to an in-depth description of the temporal kinetics of the cascade. We thus set out to measure the dynamics of accumulation of the sequential players of the activation cascade, focusing initially on the Myosin II branch. To this end, we deployed a general strategy using strains co-expressing Myosin Heavy-Chain NMY-2 labelled with mKate2 (NMY-2::mKate2), and used near-total internal reflection microscopy to visualize the cell cortex and assess Myosin II accumulation and pulse initiation, along with GFP-tagged probes for each individual player of the cascade (Fig. 1A). We then identified pulses visually as local accumulations of Myosin II in the anterior (AB) cells during interphase at the 2-cell stage, and

quantified and compared the accumulation of Myosin II with the accumulation of the GFP-tagged probe (Fig. 1B,C).

To establish a baseline for our measurements, we used a strain co-expressing on the one hand NMY-2 fused with mKate2 (red fluorescent protein) at the genomic locus, and on the other hand an ectopic copy of NMY-2 fused with GFP inserted in the genome (Nance 2003). Simple observation revealed that both fusion proteins were expressed in overlapping patterns, with almost identical spatial distributions around the center of the pulse (Fig. S2E). We then measured the delay between the two channels. As expected, we observed on average no significant overall difference in accumulation kinetics of NMY-2::GFP and NMY-2::mKate2 (Fig. 1D, E).

Interestingly, however, we observed a small range of delays of ~1 s (Fig. 1D, Fig. S1E, E'). This suggests that the variability caused by the measurements is rather small compared to the real variability existing inside the data set for each observed delay. This also indicates that the system can operate with a range of delays and that the system is robust and can withstand a range of delay variability, without affecting embryonic development.

To compare the dynamics of accumulation of Myosin II with RhoA, we then used a RhoA biosensor derived from C-terminus of Anillin fused to GFP to monitor RhoA accumulation (hereon, GFP::AHPH, (Tse et al. 2012)). As previously described (Michaux et al. 2018), we observed a strong correlation between GFP::AHPH and NMY-2::mKate2, and NMY-2::mKate2 was delayed with respect to GFP::AHPH, with a median delay of ~4.5 s (Fig. 1D-E). These results however only reported on the dynamics of a RhoA biosensor, thus potentially inserting an additional intermediary step in the observed kinetics.

To observe directly a sequence of recruitment, we then decided to try and refine these measurements, and focused on the next step of the cascade. Myosin II activation depends on the phosphorylation level of the Regulatory Light-Chain. This phosphorylation balance is controlled by phosphorylation by ROCK and dephosphorylation by the Myosin Phosphatase (Karess et al. 1991).

We therefore compared the respective dynamics of ROCK and Myosin II. To this end, we used a strain coexpressing NMY-2::mKate2 with Rho Kinase fused with GFP at the endogenous genomic locus (GFP::LET-502, (Bell et al. 2020)). Interestingly, as for GFP::AHPH, we observed strongly coupled accumulation of GFP::LET-502 with NMY-2::mKate2.

Importantly, we measured a delay of ~4.5 s between ROCK and Myosin II, not significantly different from the delay between RhoA and Myosin II (Fig. 1D-E, Fig. S1A-D').

As the inhibition of the Myosin Phosphatase by ROCK has been proposed to contribute to the activation of Myosin II (Piekny & Mains 2002), we also decided to monitor the dynamics of the Myosin Phosphatase MEL-11. We therefore generated a transgenic strain expressing a fusion of the Myosin Phosphatase MEL-11 with GFP at the endogenous locus. In *C. elegans, mel-11* mutants display a range of phenotypes, demonstrating that *mel-11* plays multiple key roles at several stages during embryonic morphogenesis (Piekny & Mains 2002; Wissmann et al. 1999). As our transgenic strain displayed no functional phenotype, we concluded that the fusion protein was functional. In early embryos, MEL-11::GFP was cortically enriched, and displayed a dynamic, grainy distribution at the cell surface, accumulating in particular at the cleavage furrow during cell division, as previously proposed based on immunostaining (Piekny & Mains 2002). As previously, we then crossed this strain with NMY-2::mKate2, and compared the accumulation dynamics between MEL-11::GFP and NMY-2::mKate2. During pulsed contractions at the 2-cell stage, MEL-11 showed dynamic recruitment at the cortex which did not visually seem to match pulsed contractions. As expected from this observation, attempting to measure the delay between NMY-2::mKate2 and MEL-11::GFP resulted in very poorly synchronized curves (Fig. S1G) and broad dispersion of the delay measurements (Fig. S1G'), further supporting the absence of coordination between the dynamics of pulsed contractions and MEL-11::GFP cortical recruitment. Interestingly, this dispersion differed strongly from the dynamics we observed for all the other players of the activation cascade (Fig. 1D, Fig. S1A-F'), suggesting either that Myosin II is regulated by its activation, as is for example the case for RhoA, or that the regulation of Myosin II by its Phosphatase is not a local process, but instead takes place at the scale of the embryo.

In previous experiments, we used Myosin Heavy-Chain fusion NMY-2::mKate2 as a reporter of Myosin II dynamics. We however wondered if we could distinguish the accumulation dynamics of the Heavy-Chain and Myosin Regulatory Light-Chain, and identify a kinetic signature suggesting a dynamic exchange of the Myosin Regulatory Light-Chain from the Myosin Heavy-Chain. To address this question, we first generated a transgenic strain expressing a fusion of the Myosin Regulatory Light-Chain MLC-4 with GFP at the endogenous locus. Previous work showed that *mlc-4* is required for proper embryogenesis (Shelton et al. 1999). As the transgenic strain displayed no functional phenotype, we concluded that MLC-

4::GFP was functional. In early embryos, MLC-4::GFP displayed a distribution very similar to the distribution of NMY-2::GFP and NMY-2::mKate2. We then crossed MLC-4::GFP with NMY-2::mKate2 to compare their accumulation dynamics. Interestingly, MLC-4::GFP, and NMY-2::mKate2 were recruited with extremely similar spatial and temporal dynamics, actually reminiscent of our NMY-2::GFP/NMY-2::mKate2 control experiment (Fig. 1D, Fig. S1E-F', Fig. S2E-F), . As previously for NMY-2::GFP and NMY-2::mKate2, we could not measure a statistically significant delay between the recruitment of the two chains (Fig. 1D, Fig. S1F-F'). This observation supports the idea that Myosin II is recruited to the cortex as a hexamer, and that the Myosin Regulatory Light-Chain, once assembled, does not display an exchange dynamics on the Myosin Heavy-Chain, or that this exchange takes place at a timescale outside of our temporal resolution.

Myosin II-ROCK accumulation delay results from Myosin II binding/unbinding kinetics

Taken together, our results demonstrated that the accumulation of Myosin II at the cortex mirrored the accumulation of ROCK, with a time delay of 4.5 s. It remained unclear, however, whether the delay originated from the kinetics of the phosphorylation reaction or if it resulted from the recruitment dynamics of the Myosin II. In order to clarify the molecular mechanisms underlying the time delays that we observed in the cascade, we decided to focus on the kinetics of Myosin II accumulation.

We thus performed single-molecule microscopy with particle tracking. We previously established this method to explore kinetics and mobility of fusion proteins expressed at single-molecule levels in the early *C. elegans* embryo (Michaux et al. 2018; Robin et al. 2014). To visualize the dynamics of individual molecules during pulsed contractions, we used an overexpression strain carrying NMY-2 fused with GFP over an endogenous NMY-2 background, and used RNAi against the GFP to specifically decrease the expression of the NMY-2::GFP fusion protein, resulting in worms with wild-type phenotype expressing minute levels of NMY-2::GFP (Fig. 2A-C). Using automated particle tracking, we then tracked individual molecules, and measured the appearance, density and disappearance of molecules in pulsed contractions (Fig. 2F). As in previous studies (Michaux et al. 2018; Ponti 2004; Robin et al. 2014; Vallotton et al. 2004; Watanabe 2002), we assumed that appearance, fraction of disappearing molecules, and density, reported directly on the local cortical binding rate (hereon K_{on}) (Fig. 2D), unbinding rate (k_{off}) (Fig. 2E), and local density, respectively. Finally, we

previously showed that, provided that photobleaching rate is low compared to turnover, tracking indeed provides a reasonable estimate of the turnover rate, a condition which we verified for Myosin II (Michaux et al. 2018; Robin et al. 2014). We also accounted for the impact of local cortical shrinkage/expansion, using a routine to follow adaptive regions of interest (Fig. 2C). Briefly, we used the position of molecules to infer local strain and corrected the region of interest so as to proceed to our quantifications in an adaptive frame of reference, thereby removing confounding effects of advection of the cortex (for details, see Michaux *et al.*, 2018). These effects, however, only affect the measurements in a very limited manner (<5%).

To explore our data, we further hypothesized a very simple kinetic accumulation model, very similar to weakly activated cascades model ((Heinrich et al. 2002); see Supplementary Information):

$$\frac{d\left([Myo^*]\right)}{dt} = k_{on} \cdot [ROCK] \cdot [Myo_T] \cdot \left(1 - \frac{[Myo^*]}{[Myo_T]}\right) - k_{off} \cdot [Myo^*]$$

where [*Myo**] is the concentration of phosphorylated Myosin II, [Myo_T] is the total concentration of Myosin II. Under the assumption that the amount of activated Myosin II does not deplete the cytoplasmic stock ([*Myo**] $\ll$ [Myo_T]), and that ROCK recruitment is not affected by Myosin II, we can write:

$$\frac{d\left([Myo^*]\right)}{dt} \approx K_{on}^{eff} - k_{off} \cdot [Myo^*]$$

where the effective binding rate (K_{on}^{eff}, heron simply K_{on}) and the unbinding rate (k_{off}) determine the evolution of the cortical concentration of Myosin II (Fig. 3B).

Using this equation, and dynamic measurements of effective binding and unbinding rates, we can define a steady-state concentration [Myo^0] for each couple of {K_{on} , k_{off}}, such that [Myo^0] = K_{on}/k_{off}. Biologically, this concentration represents a cortical *target density* that the system would eventually reach if K_{on} and k_{off} were to remain constant over time. More specifically, the target density should reflect the local signaling intensity of the immediate upstream regulator in the signaling cascade, in this case active ROCK concentration. Interestingly, when compared to the current measurement of the cortical density, the **target density** actually provides a sense for the imbalance of the system, *i.e.* how far the system lies outside of steady state.

This experimental target density value therefore integrates modulations of binding and unbinding rate to reflect an activation intensity of the upstream signal in the system. Comparing *target density* with *effective density*, we could therefore measure a delay between the system and its target value, of ~4.25 s. We then compared the delay between ROCK and Myosin II, measured in the previous section, and the delay from the binding/unbinding kinetics, extracted from our single–molecule measurements. Strikingly, the two results were extremely close, showing that the core of the delay between the accumulation of ROCK and Myosin II essentially (4.25 s out of 4.5) results directly from Myosin II binding/unbinding kinetics (Fig. 2G).

As the target density should reflect the effect of local ROCK activity, we decided to compare target density with ROCK LET-502 local relative intensity. To this end, we aligned the average Myosin II effective density of our single-molecule Myosin II dataset with the average relative intensity of NMY-2::mKate2 of our 2-color GFP::LET-502/NMY-2::mKate2 dataset, thus synchronizing the two datasets (Fig. 2H). We then compared the dynamics of the Myosin II target density with ROCK accumulation. We observed that the two curves are highly overlapping, suggesting that our simple model captures fairly accurately the dynamics of the system.

In essence, our results thus showed that the cortical recruitment of ROCK virtually immediately modulates Myosin II kinetics. In contrast, the evolution of Myosin II concentration towards a dynamically modulated Myosin II target density, experimentally computed from K_{on} and k_{off}, takes place with a time constant of several seconds, in a manner resembling a capacitor's charge.

Exploring the effect of binding/unbinding kinetics using numerical simulations

To better understand how modulations of upstream RhoA/ROCK dynamics affected Myosin II cortical concentration, we turned to numerical simulations. In the cell, RhoA accumulation is sometimes pulsed and unsynchronized, but also sometimes resembles a pseudo-periodic sine wave (Fig. 3A). To get a sense of the effect of the modulation, by RhoA and ROCK, of the binding and unbinding rates, we decided to simulate K_{on} and k_{off} as sinusoid modulations. Setting binding and unbinding rates, we could then compute both effective and target concentrations, and numerically explore how these modulations affected the evolution of the system.

Upon sinusoidal modulations of the binding rate and constant unbinding rate, we observed the emergence of a delay between effective and target concentrations (Fig. 3C, blue and red curves, resp.). Unsurprisingly, this delay decreased with increasing k_{off} (Fig. S3A-C), the unbinding rate acting as a capacitor shifting the phase of the input signal, while the output concentration remained sinusoidal (which we also demonstrated analytically).

Conversely, upon constant binding rate and sinusoidal modulations of the unbinding rate, we observed that both effective and target concentration displayed a sharp periodic peak around the time k_{off} was minimal, and were essentially flat and overlapping as k_{off} was high (Fig. 3D). Interestingly the shape of the curve observed *in vivo* closely resembled this second situation, with K_{on} constant, varying k_{off} (Fig. 2G and 3D). Comparing the numerical simulations of the model to the single-molecule results thus suggested that unbinding rate modulation actually played a significant role in shaping Myosin II accumulation.

Perturbing Myosin II phosphorylation dynamics affects the dynamic range of the system

To test this model, we decided to perturb the unbinding dynamics of Myosin II by depleting the Myosin Phosphatase MEL-11. *mel-11(it26)* is a temperature-sensitive allele that behaves as a null allele at the restrictive temperature, and displays a hypercontractile phenotype during zygote polarization and early cell divisions (Piekny & Mains 2002). As expected from its biochemical activity, *mel-11(it26)* displays an increased accumulation of cortical Myosin II. We crossed *mel-11(it26)* with a strain expressing NMY-2::GFP, imaged 2-cell stage embryos at single-molecule levels as described in the previous section. We then measured the effective density, binding rate K_{on}, unbinding rate k_{off} (Fig. 2I–K) and computed the target density (Fig. 2L). Looking at the magnitude of our measurements, we first observed that the average K_{on} increased ~3-fold compared to control, while k_{off} strikingly remained in the same range. Focusing on the dynamics of K_{on} and k_{off}, we noted that relative amplitude of the variations in time of both variables, while still present, were much milder in *mel-11(it26)* compared to control (Fig. 2I–F, J–K). Strikingly, the maximum-to-minimum ratio of the target density was massively reduced in the mutant context. Indeed, in the control situation, the target density increased ~6- to 7-fold from minimum to maximum target density. In contrast, in the mutant, the minimum to maximum target density displayed only 2- to 3-fold variation (Fig. 2G, L, red curves, Fig. 2M). Similarly, the maximum-to-minimum ratio of the effective density was much lower in *mel-11(it26)* mutant background (~1.25-fold), compared to

control (~2-fold) (Fig. 2G, L, blue curves). Our results show that *mel-11(it26)*, while displaying a stronger cortical contractility (Piekny & Mains 2002) and higher cortical Myosin II density, also display weaker variations in cortical Myosin II density.

Taken together, these results show that Myosin II dephosphorylation by the Myosin Phosphatase MEL-11 promotes the emergence of strong, well defined pulses. The absence of Myosin Phosphatase thus shifts Myosin II activation out of the dynamic range of the cascade into a saturated regime where Myosin II remains constantly activated. Interestingly however, perturbing Myosin Phosphatase activity delay did not significantly affect the measured delay between target and effective density (Fig. 2L), suggesting a degree of a robustness of this delay to perturbations of the phosphatase activity.

Slowing down F-actin dynamics reduces Myosin II k_{off} but does not affect the delay

During pulsed contractions, in parallel with Myosin II, RhoA regulates F-actin dynamics by directly regulating the formin CYK-1/mDia, an efficient Actin filament elongation factor, locally increasing Actin assembly rates (Costache et al. 2021; Naganathan et al. 2018; Swan et al. 1998). In order to explore how the same activation input was transduced across two branches of a cascade, we thus decided to finely describe the temporal dynamics of the F-actin branch of the RhoA cascade.

We first focused on the formin CYK-1. We therefore generated a strain coexpressing CYK-1 fused with GFP at the endogenous genomic locus (CYK-1::GFP, (Costache et al. 2021)), with NMY-2::mKate2, using NMY-2::mKate2 to synchronize our pulses. Using our strategy to quantify cascade kinetics, we measured a delay of ~4.5 s (Fig. 4A-B). Interestingly, this delay was not significantly different from the RhoA/Myosin II and ROCK/Myosin II delays (Fig. 4A, Fig. S1A–B', D, D').

At this point, we suspected that F-actin and Myosin II were synchronously recruited at the cortex. To test this hypothesis, we used a strain coexpressing an Actin reporter –the F-actin-binding *Calponin Homology* domain of Utrophin, fused with GFP (hereon UTR::GFP)– and Myosin II. Surprisingly, we measured a statistically significant delay of ~0.5 s between F-actin and Myosin II, F-actin appearing briefly before Myosin II (Fig. 4A-B, Fig. S1C, C'). Additionally, as we were not directly observing F-actin, and instead using UTR::GFP to indirectly monitor F-actin accumulation, our results further pointed to the accumulation of F-actin predating the accumulation of Myosin II, with a delay strictly greater than 0.5 s.

To understand the kinetics underlying F-actin accumulation, we wanted to access Actin assembly and depolymerization rates. To this end, we used a strain expressing Actin fused with GFP at single-molecule levels (hereon Actin::GFP), and measured the density of F-actin during pulsed contractions, F-actin binding rate (assembly) and unbinding rate (depolymerization), and F-actin target density (Fig. 4G–J, (Costache et al. 2021; Michaux et al. 2018; Robin et al. 2014)). Interestingly, we observed that the ratio between the maximum and minimum binding rates during a pulse was much larger for F-actin (~5-fold increase, Fig. 4G) compared to Myosin II (~2-fold increase, Fig. 2D). In contrast, the comparative variations in k_{off} displayed the same order of magnitude (Fig. 4H, 2E). This observation suggested that F-actin and Myosin II cortical densities are modulated in very different ways, with a regulation relying largely on assembly for F-actin, while it relies largely on disassembly for Myosin II.

In previous work (Costache et al. 2021), we showed that during pulsed contractions, two populations of formins are recruited at the cortex: *recruited formins*, functionally inactive and immobile, and *elongating formins*, which actively elongate F-actin and move ballistically in the cortex. We then decided to compare single-molecule actin dynamics with the accumulation of the population of elongating formins. To synchronize these F-actin kinetics data with our data on pulse dynamics, we aligned Actin::GFP cortical density with the average curve of our UTR::GFP/NMY-2::mKate2 movies. Similarly, we generated single-molecule microscopy movies of formin fused with GFP (hereon CYK-1::GFP), and used our kinetics data from our CYK-1::GFP/NMY-2::mKate2 data to synchronize our single-molecule dataset with our 2-color dataset. Using these synchronized datasets, we then compared the dynamics of the F-actin target density with the dynamics of the population of elongating formin (Fig. 4K). As for Myosin II, we observed that the two curves readily overlapped, suggesting that we had captured the essential features of F-actin accumulation.

We finally wondered if F-actin dynamics could be affected by local capping dynamics mediated by the *C. elegans* capping protein CAP-1, which had previously been implicated in pulse dynamics (Naganathan et al. 2018). To this end, we generated a transgenic strain expressing a translational fusion between CAP-1 and GFP at the endogenous genomic locus (hereon CAP-1::GFP). The CAP-1::GFP strain displayed no specific phenotype, suggesting that the fusion was functional. Furthermore, we observed that CAP-1::GFP was cortically enriched and displayed among other features a pulsed dynamic. We subsequently crossed CAP-1::GFP with NMY-2::mKate2 to obtain a strain coexpressing both fusion proteins. We then proceeded

to measure the delay between our NMY-2::mKate2 and CAP-1::GFP. Interestingly, we observed a delay of ~0.5 s (Fig. 4A, Fig. S1H-H'), similar to the delay we had measured between Myosin II and F-actin. This observation suggests that F-actin is dynamically capped at the cortex after F-actin barbed-end are released by formins.

Perturbing F-actin severing affects the dynamic range of the system

To test the effect of actin turnover over pulse dynamics, we decided to perturb and try to predict the modification in kinetics in our activation cascade.

To do so, we decided to use RNAi against the actin severing protein gene, cofilin *unc-60.* In order to clarify the effects of Cofilin, we first performed *unc-60(RNAi)* in embryos expressing very low levels of a translational fusion of Actin with GFP, thus monitoring actin dynamics directly (Michaux et al. 2018; Robin et al. 2014) . Using single-molecule measurements of Actin::GFP, we first showed that Cofilin knock-down slowed F-actin turnover (Fig. S4E). We then measured the average pulse period, and observed a shift from a distribution of pulse periods tightly-centered around ~31 s in control embryos to a much broader distribution centered around 42 s in *unc-60* RNAi (Fig. S4F). Altogether, these results showed that *unc-60(RNAi)* embryos displayed a generally slower F-actin turnover and pulse dynamics.

We then combined *unc-60(RNAi)* with NMY-2::GFP single-molecule microscopy, as in our previous experiments, and measured Myosin II pulse density (Fig. 4E-F), binding rate (K_{on}, Fig. 4C), unbinding rate (k_{off}, Fig. 4D) and target density (K_{on}/k_{off}, Fig. 4F). As expected from the previous experiment (Fig. S4F), we observed broader pulses and an increased pulse period in *unc-60(RNAi)* compared to control (Fig. S4C-D). Interestingly, the unbinding rate only displayed very mild variations compared to the control. As for the Myosin Phosphatase mutant *mel-11(it26)*, we observed that the ratio between the maximum and minimum target density was reduced (Fig. 2G, 4F), demonstrating a decreased response to the upstream signal in *unc-60(RNAi)*. Strikingly, neither *unc-60(RNAi)* nor *mel-11(it26)* displayed strong changes in the delay we measured between the rises of target concentration and effective concentration.

Cascade activation delay is required for efficient contractility during pulsed contractions

Our results showed that the two pathways downstream of RhoA activation lead to a recruitment of the actin polymerizing enzyme, initiating an F-actin assembly ~4.5 s before

Myosin II accumulation, eventually resulting in F-Actin accumulation predating Myosin II accumulation by >0.5 s. We therefore wanted to know if this timing difference was functionally relevant for pulsed contractility. However, exploring this question experimentally was difficult, as perturbations would affect multiple aspects of pulsed contractions. In order to more clearly distinguish the effects of the dynamics of the cascade on contractility, we therefore turned to agent-based simulation, to separate the respective effects of timing, duration, and rate of filament elongation.

Using our established computational model of actomyosin networks (Fig. S4A, (Jung et al. 2015)), we probed the effect on cortical mechanics of the delay between the initiation of formin-induced F-actin elongation in cortex and the recruitment of Myosin II. Using a cortex-like F-actin meshwork (20 µm × 20 µm × 100 nm), we simulated RhoA-driven pulsed contraction by locally modulating the kinetics of Myosin II and F-actin elongation rates, based on previous experimental measurements (Costache et al. 2021). Specifically, to reproduce formin activity, we increased the elongation rate of a fraction of the barbed ends in the RhoA-activated region, resulting in rapid elongation of Actin filaments for ~10 s, or ~12 µm. We then locally turned on Myosin II activity in the RhoA-activated region for 15 s, setting the duration of the delay between formin activation and Myosin II activation as a variable to test the impact of delayed Myosin II recruitment on network architecture and the deployment of forces generated by Myosin II (Movie S8-10, (Michaux et al. 2018)).

We observed that simultaneous activation of formins and Myosin II lead to high contraction of both F-actin and Myosin II, and to the formation of long-lasting F-actin aggregates. In contrast, delay at 5 s and 10 s lead to less contraction of the network, avoiding network collapse. To better quantify the mechanical impact of the delay, we measured the network contraction for F-actin and Myosin II (Fig. 5B, C), as well as the sum of the forces and the average force generated locally on the network by the pulsed contraction (Fig. 5C, D). Using these metrics, we observed that Myosin II and F-actin contraction indeed decreased with increasing delay (Fig. 5B, C). Interestingly, we also observed that the force deployed by the contraction evolved non-monotonously and was maximal when the delay was set at 5 s (Fig. 5D, E).

The case without delay showed larger maximum F-actin contraction because there was shorter time for elongated filaments to form cross-linking points before Myosin II motors actively contract Actin filaments. Consistently, the sum of force acting on the network was

minimal in the case without the delay (Fig. 5D, E). From these observations, we concluded that the relative timing of Myosin II accumulation and F-actin assembly is actually linked to the contraction and force deployment in the network.

Discussion

The RhoA pathway driving actomyosin contractility is an evolutionary conserved signaling cascade that drives a broad range of morphogenetic processes, from cytokinesis to cell-cell rearrangements and apical cell constriction to smooth muscle contraction, in a number of physiological processes. Depending on the cellular context and RhoA activation specifics, how this signaling cascade is patterned and unfolds can be highly variable, from pulsed to steady-state dynamics, and from spatially localized to global activations. Here, we have identified the molecular bases underlying *in vivo* the temporal dynamics of the RhoA signaling cascade leading to actomyosin contraction.

We used the RhoA activation cascade in the early *C. elegans* embryo and followed the intensity variation of the different players of the cascade over time. Interestingly, in our measurements, formin, ROCK and RhoA essentially display identical dynamics and delays, suggesting all RhoA effectors/binding partners accumulate with similar kinetics. This suggests that our RhoA proxy –like Myosin II– is subject to a binding/unbinding delay, and that the RhoA dynamics we inferred from the proxy likely precedes the dynamics of the proxy. Further exploration of the kinetics of AHPH using single-molecule microscopy and particle tracking –as we did for Myosin II and F-actin– should actually resolve the accumulation kinetics of active RhoA.

Surprisingly, while these two RhoA targets, formin CYK-1 and the Rho Kinase ROCK/LET-502, accumulate with similar dynamics, F-actin and Myosin II did not appear synchronously at the location of pulsed contractions, F-actin preceding Myosin II by a small yet statistically significant ~0.5 s delay. Physiologically, this can result from the fact that Myosin II cortical recruitment is dependent on the presence of Actin filaments as binding substrate. In our quantitative analysis, this aspect of Myosin II dynamics was implicitly included in the measurement of K_{on}. While, on average, the delay is significant, at the scale of individual pulses, it is clear from the measured delay distribution (Fig. 4A) and accumulation curves (Fig. S1C, C') that a fraction of the pulses occurring *in vivo* displayed an inverted order

of recruitment. This suggests some degree of robustness of the contractility output to small variation in the timing of the recruitment sequence.

Using our single-molecule data analysis, we then established a simple model to extract from our dynamic measurements of K_{on} and k_{off} a dynamic *target density* value, in essence the instantaneous signaling activity of the system. Comparing this target density with effective density let us explore several interesting key properties of the system, and in particular delays, signaling intensity, and out-of-equilibrium dynamics. Importantly, this basic model approach that we used to study the kinetics of hierarchical activation in the context of the RhoA pathway is actually very generic, and could apply to any number of "weakly-activated" signaling cascades.

Specifically, the model provided a good framework to explore the molecular bases for the delays we observed along the steps of the cascade. In particular, we could show that Myosin II cortical dynamics relies essentially on the equilibration dynamics under constantly changing K_{on} and k_{off}. Numerical simulations of RhoA periodic variations and its impact on K_{on} and $k_{off,}$ independently, showed that k_{off} modulations under a constant K_{on} resulted in dynamics extremely closer to the one we observed (Fig. S3).

In order to challenge this model, we experimentally perturbed Actin turnover rate, by depleting the severing factor Cofilin with *unc-60(RNAi)*. While, as expected, this caused an increase in the pulsed contraction period, and abolished k_{off} variation, it did not affect the kinetic delay for Myosin II inferred from single-molecule measurements. This suggests that Myosin II unbinding is effectively unaffected by Actin turnover. In this context, it therefore seems that Myosin II unbinding operates independently from Actin filament severing.

To further challenge our model, we experimentally perturbed Myosin II dephosphorylation by depleting the Myosin Phosphatase with *mel-11(RNAi).* Surprisingly, this did not cause a decrease of the average Myosin II unbinding rate. We interpret this result by the fact that Myosin II actually is a low/intermediate duty ratio motor that works cooperatively as mini-filaments. Therefore, the Myosin II unbinding rate might simply represent the unbinding rate of fully phosphorylated Myosin II. Under this assumption, we would expect that an increased phosphatase activity translates superficially in an increased "available pool" of almost fully phosphorylated Myosin II that could be co-opted at the cortex by a weaker phosphorylation activity, thus exclusively affecting the magnitude of the binding rate.

Furthermore, this is consistent with a global, and slow, Myosin Phosphatase activity, which matches our experimental observations regarding MEL-11::GFP spatial localization.

Interestingly, the model also gave indications regarding the molecular bases underlying the magnitude of the response in this dynamic system. In particular, we observed that the control dynamics relied strongly on out-of-equilibrium modulation of Myosin II dynamics, with a target density tuned very far from the effective density. In contrast, in Myosin Phosphatase *mel-11(RNAi)* knockdown conditions, the dynamics of the system was much more stable biochemically, suggesting that the signaling cascade likely operated outside of its dynamic range.

Finally, our agent-based simulations shed some light on how the synchronization of F-actin and Myosin II could actually interplay and subsequently affect Myosin II contractility. We could show that the delay between F-actin and Myosin II may play a physiologically relevant role by promoting long range actomyosin contractility. In this specific context, agent-based simulations of cortical mechanics thus offer an attractive alternative to active gel hydrodynamic models, as they are well suited to capture this type of specifics of emergent properties relying on the detailed architecture of the network. Interestingly, this work underlines a new and striking type of interaction in signaling cascades at the crossroads of signaling dynamics, the cytoskeletal architecture they assemble, and the resulting mechanical properties of these contractile assemblies, and the complexities of analyzing chemo-mechanical machines, as predicted by Turing over half-a-century ago.

Materials and methods

Strains

List of strains used in this study can be found in Supplementary Table 4. Some strains were provided by the CGC, which is funded by NIH Office of Research Infrastructure Programs (P40 OD010440).

C. elegans culture

We cultured *C. elegans* at 20°C under standard conditions (Brenner 1974).

RNA interference

Worms mutant *mel-11(it26)/+* and carrying a Myosin II overexpression *zuIs45[nmy-2::gfp]* were grown at permissive temperature (15°C). L3-L4 homozygous for *it26* worms (selected on phenotype, therefore *mel-11(it26); zuIs45[nmy-2::gfp])* were fed bacteria expressing GFP RNAi for 40 h at 15°C, then 1 h prior to the imaging were placed at restrictive temperature (25°C).

Bacteria targeting *unc-60* (C38C3.5) were obtained from the Kamath feeding library (Kamath & Ahringer 2003) L4 larval stage worms carrying a Myosin II overexpression *zuIs45[nmy-2::gfp]* were placed on Nematode Growth Media (NGM) plates (Brenner 1974) containing 2 mM IPTG for 24 h at 20°C with HT115 *E. coli* strain expressing GFP RNAi (L4440 GFP RNAi construct) 40 h prior imaging the embryos. After 24 h on the GFP RNAi the worms are moved to a plate with HT115 *E. coli* strain expressing GFP RNAi mixed with HT115 *E. coli* strain expressing *unc-60* RNAi. The worms were imaged after 20 h on this plate.

Microscopy

We mounted the embryos between glass slides with squares wells of 20 µm thick Epoxy and #1.5 coverslips (170 µm thick) in 2.5 µL of filtered water with 15.4 µm polystyrene beads in order to have a uniform compression of the embryos and reach a flat surface to perform an optimal TIRF microscopy approach. We used the HILO microscopy (Tokunaga et al. 2008). We used a Nikon Eclipse Ti microscope, 488 nm and 561 nm 90 mW laser excitation, 100x objective NA 1.4, cameras: Andor iXon 897 EMCCD and Photometrics Prime 95B, Optovar 1.5x, Nikon

Perfect focus©. Data acquisition was performed with NIS software version 4.50. The laser diodes of 300 mW are both set up at 30% for 488 nm and 561 nm, which means a laser power of 90 mW maximum.

Pulsed contractions imaging and image analysis procedures

For the 2-cell stage, we used: two-color imaging with alternatively 488 nm and 561 nm, 50 ms exposure, 100 ms between two consecutive frames of the same color, laser power at 30% of 90 mW. Laser angle was set at 65°. Room temperature is set up between 19 and 20,5°C. We grouped five consecutive frames in time by averaging the intensity for each channel.

We used ImageJ software (NIH Image, Bethesda, MD) for extraction of subregions containing a single pulsed contraction. After isolating the pulses in separate files (one for the red channel, one for the green), the images were loaded and analyzed in Matlab software (R2018a version). The average image intensity was measured for each time frame for each pulse; the intensity was then normalized, according to this equation:

$$I_{normalized} = \frac{I - I_{min}}{I_{max} - I_{min}}$$

where: I = mean (Image intensity)

I_{max} = maximal intensity

I_{min} = minimal intensity

Maximum intensity of the red channel is considered as 1 and the immediate precedent minimum is as 0, minimum taken in the 50 preceding frames. Data for the Myosin II intensity were aligned at 0.45, where the slope is maximal and provides the most accurate measure of pulse alignment to fix the time at 0 s for all the red curves. This information is propagated to data from the other channel (green) (which is also normalized to get an intensity between 0 and 1) (Fig. 0). The average for each distribution (red and green) is plotted with its confidence interval (95%).

For measuring pulse size, 5 pulses per embryo were selected manually and a line is drawn across the pulse to collect the intensity through the line with ImageJ for both green and red channels. To compare pulse sizes, full width at half maximum (fwhm) function was performed and difference between fwhm in green and red was measured.

Statistical analysis

One-sample Student tests (t-tests) were performed to measure the significance of each delay between the red and green curves. Paired-sample Student tests were performed between the delays of two molecules to measure the significance of the difference between the two delays. *** means p<0.001, **: p<0.01, *: p<0.05, ns: non-significant.

Single-molecule imaging and Myosin II turnover analysis

We performed single-molecule imaging as described previously (Robin et al. 2014). We used RNAi against GFP to reduce the number of imaged fluorescent molecules. We imaged single molecules using 5% of 90 mW of 488 nm laser, 500 ms of exposure, no delay between frames. Laser angle was set to 65°. Room temperature is set up between 19 and 20,5°C.

We used Matlab implementation of the Crocker-Grier algorithm (Crocker & Grier 1996) by the Kilfoil lab for single-particle tracking. The following parameters were used for both experiments at single-molecule level: particle size, 3 pixels, maximal displacement of the particle between two consecutive frames, 4 pixels and the memory to link trajectories in non-consecutive frames, 3 frames. This last parameter allowed the tracking software to look for the particle until three frames later than the immediately following one, this avoided artifactual loss of the particle track due to fluctuations of GFP fluorescence.

Subsequent image analysis was performed in Matlab. Location and time frame of each pulse was loaded in Matlab. At the “seed time”, we defined a Region Of Interest (ROI) corresponding to a polygon defined by molecules in the ellipse previously defined in ImageJ (convex envelope of all the particles present in the ROI at the seed time frame). We then displaced this ROI according to the motions of the molecules of the edges –if present– or by extracting a local velocity field from the motion of the surrounding molecules in a radius of 30 px if the “edge molecule” had disappeared. The ROI thus faithfully described dynamics of the cortex during a pulsed contraction excluding effects from advection caused by the local contraction/expansion of the cortex. We then counted the number of molecules in each frame, the number of molecules appearances (binding rate, K_{on}) and the fraction of molecules disappearing between two consecutive frames (unbinding rate, k_{off}).

Data was normalized to the minimum/maximum number of detected NMY-2 particles, then aligned to 0.45, where the slope is maximal and provides the most accurate measure for pulse

alignment. The time of alignment is defined as time = 0 s and is set from the curve of number of molecules and propagated to the curves of binding and unbinding rate. To avoid effects of the beginning and the end of the movie on the binding and unbinding rate, data of number of molecules, K_{on} and k_{off} for each pulse has been truncated of its first and final three values (replaced by NaN in Matlab). Average for each measurement was plotted with its confidence interval (95%). Equilibrium state value is obtained by division of measured binding and unbinding rates.

We performed the turnover analysis as previously described (Robin et al. 2014). Under the assumption of a single population, homogeneously distributed in the cytoplasm the number of molecules *N(t)* within a defined region over time is governed by:

$$\frac{dN}{dt} = k_{app} - k_{off}N$$

$$\Leftrightarrow N_{t+1} - N_t = k_{app} - k_{off}N$$

2 different states of equilibrium, state 1 and state 2, will be defined by their k_{app} and k_{off} as following: state 1 having a $k_{app} = K_1$ and $k_{off} = k_1$, where the equilibrium is $\frac{K_1}{k_1}$, and state 2 having a $k_{app} = K_2$ and $k_{off} = k_2$, where the equilibrium is $\frac{K_2}{k_2}$. Then the equation governing the change in molecule density following a step-change from (k_1, K_1) to (k_2, K_2) is governed by:

$$N(t) = \frac{K_2}{k_2} + \left(\frac{K_1}{k_1} - \frac{K_2}{k_2}\right) e^{-k_2 t}$$

To evaluate difference between target density and measured number of molecules we measured a difference in fold as following:

$$\Delta = \frac{Max_{target} - Min_{target}}{Max_{measured} - Min_{measured}}$$

Comparison between total intensity and dynamic variation at single-molecule level

Normalized average value for ROCK and Myosin II variation in total intensity were extracted from the two-color imaging experiment (GFP::LET-502 and NMY-2::mKate2). Average for Myosin II total intensity was aligned at 0.45 of the maximum with the normalized value of the measured number of molecules in Myosin II single-molecule experiment.

Alignment was propagated to the K_{on}, k_{off} and target intensity of the same experiment. Were displayed on Fig. 2H only Myosin II K_{on}, k_{off} and target density, and ROCK and Myosin II normalized average total intensity.

Normalized average value for formin and Myosin II variation in total intensity were extracted from the two-color imaging experiment (CYK-1::GFP and NMY-2::mKate2). Normalized average value for Myosin II total intensity in this experiment was aligned at 0.45 of the maximum with normalized average value for Myosin II total intensity of the two-color imaging experiment for F-actin and Myosin II (UTR::GFP and NMY-2::mKate2). Normalized average value for F-actin total intensity was aligned at 0.45 of the maximum with the normalized value of measured number of molecules in F-actin single-molecule experiment. Alignment was propagated to the K_{on}, k_{off} and target intensity of the same experiment. Normalized average value for formin total intensity in the two-color imaging experiment was aligned at 0.45 of the maximum with the normalized number of superdiffusive formin in formin single-molecule experiment (data published in Fig. 2A-B (Costache et al. 2021). Were displayed on Fig. 4K only F-actin K_{on}, k_{off}, target density, formin superdiffusive population normalized variation and normalized average Actin total intensity.

References

Bell, K.R. et al., 2020. Novel cytokinetic ring components drive negative feedback in cortical contractility. *Molecular Biology of the Cell*, 31(15), pp.1623–1636.

Brenner, S., 1974. The genetics of Caenorhabditis elegans. *Genetics*, 77(1), pp.71–94.

Cavanaugh, K.E. et al., 2020. RhoA Mediates Epithelial Cell Shape Changes via Mechanosensitive Endocytosis. *Developmental Cell*, 52(2), pp.152–166.e5.

Costache, V. et al., 2021. Rapid assembly of a polar network architecture drives efficient actomyosin contractility. *bioRxiv*, pp.1–38.

Crocker, J.C. & Grier, D.G., 1996. Methods of digital video microscopy for colloidal studies. *Journal of Colloid and Interface Science*, 179(1), pp.298–310.

Diogon, M. et al., 2007. The RhoGAP RGA-2 and LET-502/ROCK achieve a balance of actomyosin-dependent forces in C. elegans epidermis to control morphogenesis. *Development*, 134(13), pp.2469–2479.

Hariharan, I.K. et al., 1995. Characterization of rho GTPase family homologues in Drosophila melanogaster: overexpressing Rho1 in retinal cells causes a late developmental defect. *The EMBO Journal*, 14(2), pp.292–302.

He, L. et al., 2010. Tissue elongation requires oscillating contractions of a basal actomyosin network. *Nature Cell Biology*, 12(12), pp.1133–1142.

Heinrich, R., Neel, B.G. & Rapoport, T.A., 2002. Mathematical models of protein kinase signal transduction. *Molecular cell*, 9(5), pp.957–970.

Jung, W., Murrell, M.P. & Kim, T., 2015. F-actin cross-linking enhances the stability of force generation in disordered actomyosin networks. *Computational Particle Mechanics*, 2(4), pp.317–327.

Kamath, R.S. & Ahringer, J., 2003. Genome-wide RNAi screening in Caenorhabditis elegans. *METHODS*, 30(4), pp.313–321.

Karess, R.E. et al., 1991. The regulatory light chain of nonmuscle myosin is encoded by spaghetti-squash, a gene required for cytokinesis in Drosophila. *CELL*, 65(7), pp.1177–1189.

Kim, H.Y. & Davidson, L.A., 2011. Punctuated actin contractions during convergent extension and their permissive regulation by the non-canonical Wnt-signaling pathway. *Journal of Cell Science*, 124(4), pp.635–646.

Kohno, H. et al., 1996. Bni1p implicated in cytoskeletal control is a putative target of Rho1p small GTP binding protein in Saccharomyces cerevisiae. *The EMBO Journal*, 15(22), pp.6060–6068.

Kovar, D.R. & Pollard, T.D., 2004. Insertional assembly of actin filament barbed ends in association with formins produces piconewton forces. *Proceedings of the National*

Academy of Sciences of the United States of America, 101(41), pp.14725–14730.

Ma, W. et al., 2009. Defining network topologies that can achieve biochemical adaptation. *CELL*, 138(4), pp.760–773.

Maître, J.-L. et al., 2015. Pulsatile cell-autonomous contractility drives compaction in the mouse embryo. *Nature Cell Biology*, 17(7), pp.849–855.

Martin, A.C., Kaschube, M. & Wieschaus, E.F., 2009. Pulsed contractions of an actin-myosin network drive apical constriction. *Nature*, 457(7228), pp.495–499. Available at: http://www.nature.com/doifinder/10.1038/nature07522.

Miao, H. & Blankenship, J.T., 2020. The pulse of morphogenesis: actomyosin dynamics and regulation in epithelia. *Development*, 147(17).

Michaux, J.B. et al., 2018. Excitable RhoA dynamics drive pulsed contractions in the early C. elegans embryo. *J Cell Biol*, 217(12), pp.4230–4252.

Motegi, F. & Sugimoto, A., 2006. Sequential functioning of the ECT-2 RhoGEF, RHO-1 and CDC-42 establishes cell polarity in Caenorhabditis elegans embryos. *Nature Cell Biology*, 8(9), pp.978–985.

Munjal, A. et al., 2015. A self-organized biomechanical network drives shape changes during tissue morphogenesis. *Nature*, 524(7565), pp.351–355.

Naganathan, S.R. et al., 2018. Morphogenetic degeneracies in the actomyosin cortex. *eLife*, 7, p.354.

Nance, J., 2003. C. elegans PAR-3 and PAR-6 are required for apicobasal asymmetries associated with cell adhesion and gastrulation. *Development*, 130(22), pp.5339–5350.

Piekny, A.J. & Mains, P.E., 2002. Rho-binding kinase (LET-502) and myosin phosphatase (MEL-11) regulate cytokinesis in the early Caenorhabditis elegans embryo. *Journal of Cell Science*, 115(Pt 11), pp.2271–2282.

Ponti, A., 2004. Two Distinct Actin Networks Drive the Protrusion of Migrating Cells. *Science*, 305(5691), pp.1782–1786.

Robin, F.B. et al., 2014. Single-molecule analysis of cell surface dynamics in Caenorhabditis elegans embryos. *Nature Methods*, 11(6), pp.677–682.

Schonegg, S. & Hyman, A.A., 2006. CDC-42 and RHO-1 coordinate acto-myosin contractility and PAR protein localization during polarity establishment in C. elegans embryos. *Development*, 133(18), pp.3507–3516.

Shelton, C.A. et al., 1999. The nonmuscle myosin regulatory light chain gene mlc-4 is required for cytokinesis, anterior-posterior polarity, and body morphology during Caenorhabditis elegans embryogenesis. *J Cell Biol*, 146(2), pp.439–451.

Solon, J. et al., 2009. Pulsed Forces Timed by a Ratchet-like Mechanism Drive Directed Tissue

Movement during Dorsal Closure. *CELL*, 137(7), pp.1331–1342.

Staddon, M.F. et al., 2019. Mechanosensitive Junction Remodeling Promotes Robust Epithelial Morphogenesis. *Biophysical Journal*, 117(9), pp.1739–1750.

Swan, K.A. et al., 1998. cyk-1: a C. elegans FH gene required for a late step in embryonic cytokinesis. *Journal of Cell Science*, 111 (Pt 14), pp.2017–2027.

Tan, P.Y. & Zaidel-Bar, R., 2015. Transient membrane localization of SPV-1 drives cyclical actomyosin contractions in the C. elegans spermatheca. *Current biology : CB*, 25(2), pp.141–151.

Tokunaga, M., Imamoto, N. & Sakata-Sogawa, K., 2008. Highly inclined thin illumination enables clear single-molecule imaging in cells. *Nature Methods*, 5(2), pp.159–161.

Tse, Y.C. et al., 2012. RhoA activation during polarization and cytokinesis of the early Caenorhabditis elegans embryo is differentially dependent on NOP-1 and CYK-4. *Molecular Biology of the Cell*, 23(20), pp.4020–4031.

Vallotton, P. et al., 2004. Simultaneous mapping of filamentous actin flow and turnover in migrating cells by quantitative fluorescent speckle microscopy. *Proceedings of the National Academy of Sciences*, 101(26), pp.9660–9665.

Wallace, A.G. et al., 2018. The RhoGAP HUM-7/Myo9 integrates signals to modulate RHO-1/RhoA during embryonic morphogenesis in Caenorhabditiselegans. *Development*, 145(23).

Watanabe, N., 2002. Single-Molecule Speckle Analysis of Actin Filament Turnover in Lamellipodia. *Science*, 295(5557), pp.1083–1086.

Watanabe, N. et al., 1997. p140mDia, a mammalian homolog of Drosophila diaphanous, is a target protein for Rho small GTPase and is a ligand for profilin. *The EMBO Journal*, 16(11), pp.3044–3056.

Wissmann, A. et al., 1997. Caenorhabditis elegans LET-502 is related to Rho-binding kinases and human myotonic dystrophy kinase and interacts genetically with a homolog of the regulatory subunit of smooth muscle myosin phosphatase to affect cell shape. *Genes & development*, 11(4), pp.409–422.

Wissmann, A., Ingles, J. & Mains, P.E., 1999. The Caenorhabditis elegans mel-11 myosin phosphatase regulatory subunit affects tissue contraction in the somatic gonad and the embryonic epidermis and genetically interacts with the Rac signaling pathway. *Developmental Biology*, 209(1), pp.111–127.

Figure 1

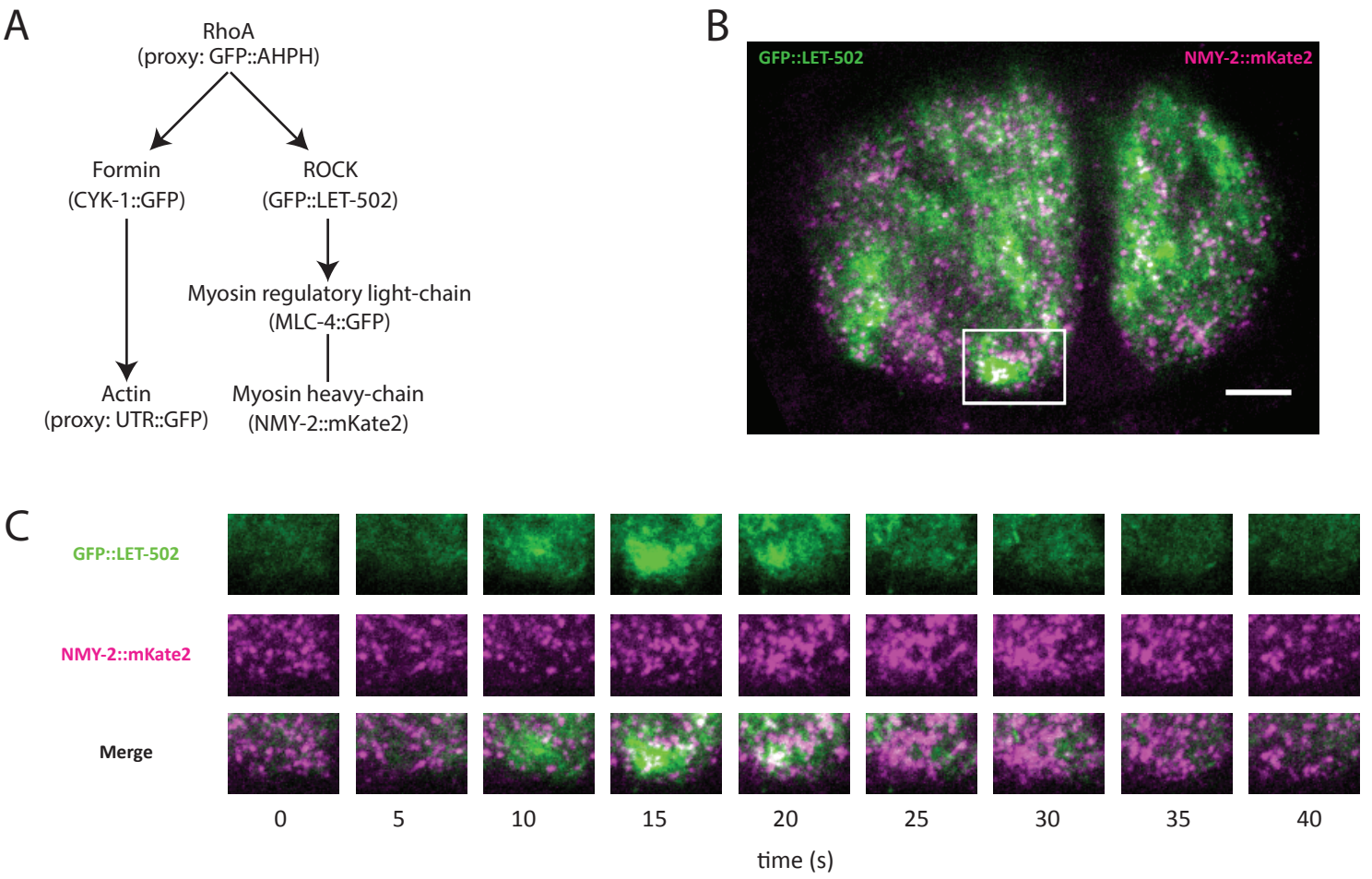
A
RhoA
(proxy: GFP::AHPH)
Formin
(CYK-1::GFP)
ROCK
(GFP::LET-502)
Myosin regulatory light-chain
(MLC-4::GFP)
Actin
(proxy: UTR::GFP)
Myosin heavy-chain
(NMY-2::mKate2)
B
GFP::LET-502
NMY-2::mKate2
C
GFP::LET-502
NMY-2::mKate2
Merge
0
5
10
15
20
25
30
35
40
time (s)
D
ns
ns
***
***
time (s)
20
15
10
5
0
-5
-10
AHPH/NMY-2
LET-502/NMY-2
MLC-4/NMY-2
NMY-2/NMY-2
E
RhoA
ns
Formin
ROCK
>4.5s
~4.5s
Actin
Myosin

Figure 1. RhoA hierarchical signaling cascade reveals a delay between RhoA, ROCK and Myosin. (A) RhoA activation cascade of Actomyosin pulsed contractions with the different strains and proxys used in (D). **(B)** Near-TIRF microscopy image of a 2-cell stage *C. elegans* embryo showing ROCK in green (GFP::LET-502) and Myosin in magenta (NMY-2::mKate2), scale bar: 5 µm. **(C)** Timelapse of the pulsed contraction in white box in (A). **(D)** Quantifications of time delay. Blue dots: time delay distribution red over green channel, red dotted line: time delay of 0 s, blue shade: histogram of distribution. N(embryos) ≥ 10, N(pulses) ≥ 165 (See Supplementary Table S1 and S2 for statistical details), ns: not significant, ***: p-value ≤ 0.001. **(E)** Summary of the observed time delay within the RhoA activation cascade.

Figure 2

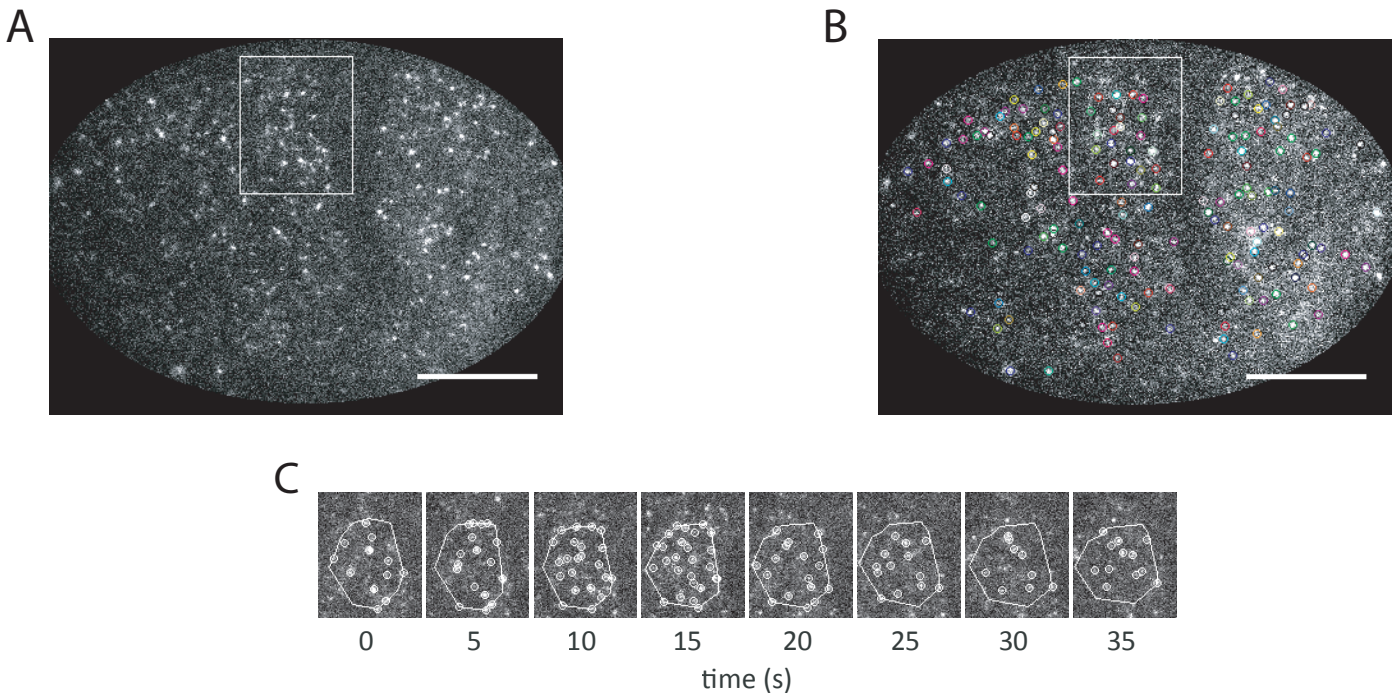
A
B
C
0
5
10
15
20
25
30
35
time (s)
single-molecule Myosin
D
average
median
binding rate (molecule.s-1)
time (s)
E
unbinding rate (s-1)
F
normalized pulse density
G
Target density
Effective density
pulse density
H
normalized values
ROCK Intensity
Kon Myosin
koff Myosin
Target Density Myosin
Effective Density Myosin
M
***
Ratio of amplitudes (target over effective)
control
mel-11(it26)
single-molecule Myosin mel-11(it26)
I
J
K
L

Figure 2. Single-molecule dynamics resolve Myosin binding/unbinding kinetics, revealing the origins of the ROCK/Myosin delay. (A-B) Near-TIRF microscopy image of single-molecule of Myosin, scale bar: 10 µm. **(B)** Colored circles: particles detected in image (A) by tracking, each molecule with a circle of a different color. **(C)** Time-lapse of the pulsed contraction in white box in (A). **(D-G)** Measurements from single-molecule microscopy data analysis of Myosin (NMY-2::GFP overexpression). N(embryos) = 5, N(pulses) = 38, thin line: median, thick line: average, shade: (D-F): std, (G): sem **(D)** Binding rate (K_{on}) of Myosin as function of time, **(E)** unbinding rate (k_{off}), **(F)** normalized effective density, **(G)** target density (K_{on}/k_{off}, red) and effective density (blue). **(H)** Variation of normalized values over time of ROCK intensity average (Fig. S1B), Myosin intensity average from Supp Fig. 1B, aligned and hence standing for average of Myosin intensity in Fig. 2F (red straight line), Myosin K_{on} average from Fig. 2D (cyan straight line), Myosin k_{off} average from Fig. 2E (black straight line), and Myosin target density (K_{on}/k_{off}) (magenta dashed line). **(I-L)** Single-molecule tracking of Myosin (NMY-2::GFP overexpression) in Myosin Phosphatase mutant context *mel-11(it26)*. N(embryos) = 9, N(pulses) = 54, thin line: median, thick line: average, (I-K): std, (L): sem **(I)** Binding rate (K_{on}), **(J)** Unbinding rate (K_{off}), **(K)** Normalized effective density, **(L)** effective density (blue) and target density (K_{on}/K_{off}, red). **(M)** Descriptor to quantify the out-of-equilibrium dynamics of the Myosin, based on the ratio of target density amplitude over effective density amplitude for Myosin: (maximum of target density – min of target density)/(max of effective density – min of effective density) from (G) for the control and (L) for *mel-11(it26)*, *** : p-value ≤ 0.001.

Figure 3

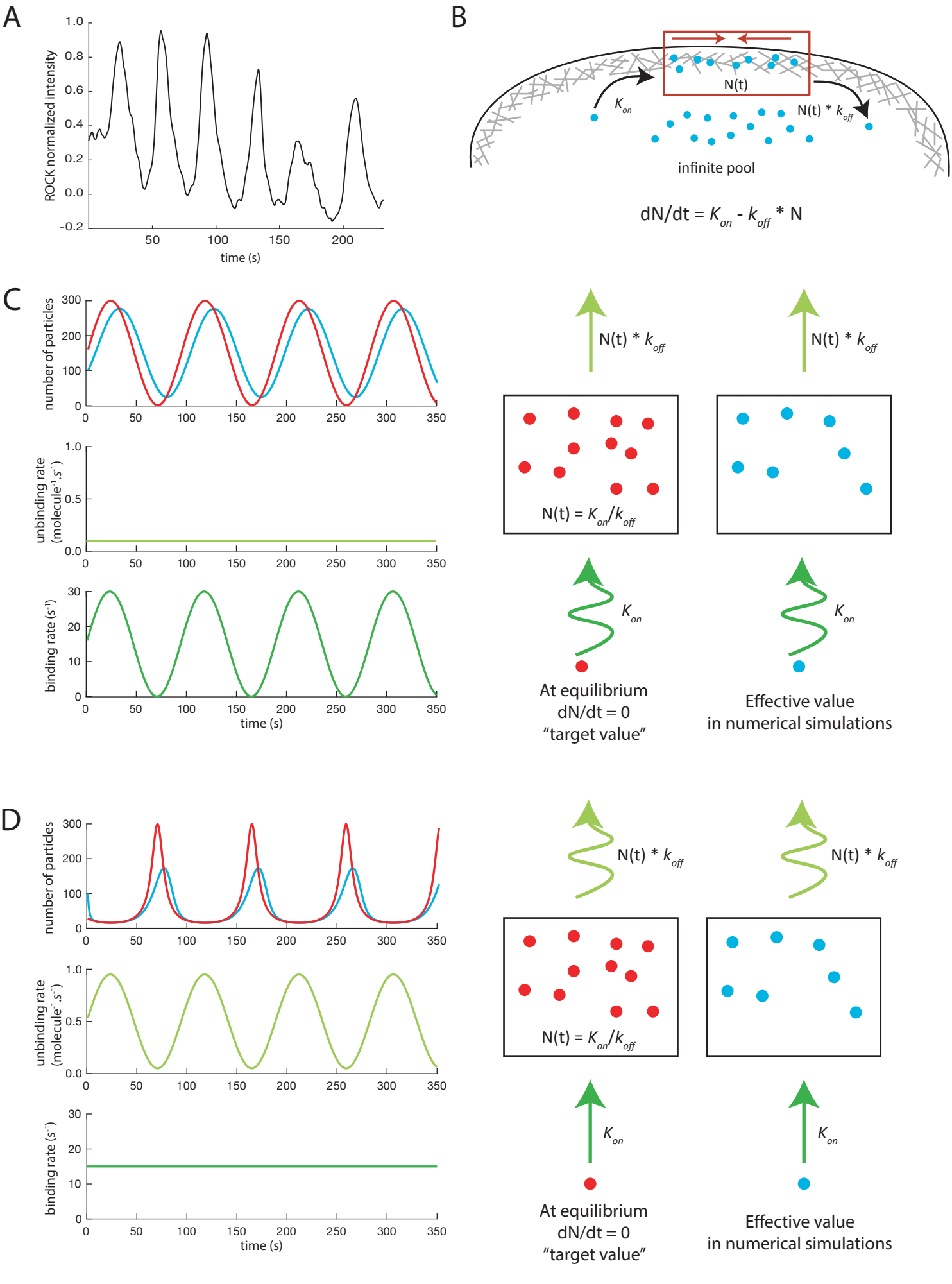
A
ROCK normalized intensity
time (s)
B
N(t)
K_{on}
N(t) * k_{off}
infinite pool
dN/dt = K_{on} - k_{off} * N
C
number of particles
unbinding rate (molecule^{-1}.s^{-1})
binding rate (s^{-1})
time (s)
N(t) * k_{off}
N(t) = K_{on}/k_{off}
K_{on}
At equilibrium
dN/dt = 0
"target value"
Effective value
in numerical simulations
D
number of particles
unbinding rate (molecule^{-1}.s^{-1})
binding rate (s^{-1})
time (s)
N(t) * k_{off}
N(t) = K_{on}/k_{off}
K_{on}
At equilibrium
dN/dt = 0
"target value"
Effective value
in numerical simulations

Figure 3. Simple kinetic model supports kinetic control of the delay and highlights the role of unbinding kinetics in shaping Myosin accumulation. (A) Normalized intensity variation of ROCK as a function of time, over 6 successive pulsed contractions. **(B)** Schematic of the proposed model for the RhoA activation cascade. **(C)** Blue line: simulation of the effect RhoA periodic variation on the K_{on} (dark green line), with a constant k_{off} (light green line), red line: K_{on}/k_{off}. **(D)** Blue line: simulation of the effect RhoA periodic variation on the k_{off} (light green line), with a constant K_{on} (dark green line), red line: K_{on}/k_{off}.

Figure 4

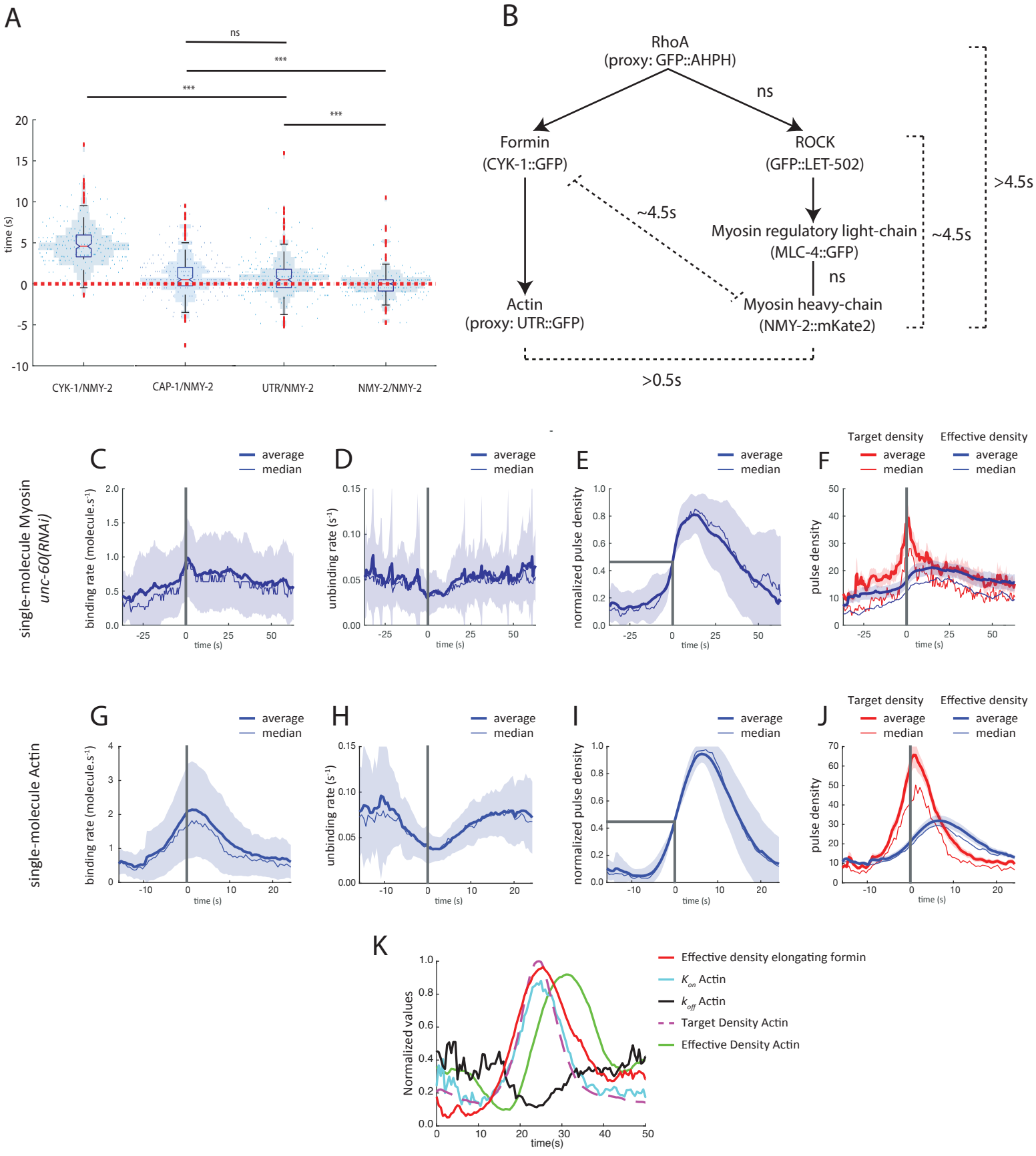
A
ns
***
***
***
time (s)
CYK-1/NMY-2
CAP-1/NMY-2
UTR/NMY-2
NMY-2/NMY-2
B
RhoA
(proxy: GFP::AHPH)
ns
Formin
(CYK-1::GFP)
ROCK
(GFP::LET-502)
~4.5s
Myosin regulatory light-chain
(MLC-4::GFP)
~4.5s
>4.5s
ns
Actin
(proxy: UTR::GFP)
Myosin heavy-chain
(NMY-2::mKate2)
>0.5s
single-molecule Myosin
unc-60(RNAi)
C
D
E
F
average
median
binding rate (molecule.s-1)
unbinding rate (s-1)
normalized pulse density
pulse density
time (s)
Target density
Effective density
single-molecule Actin
G
H
I
J
K
Normalized values
time(s)
Effective density elongating formin
Kon Actin
koff Actin
Target Density Actin
Effective Density Actin

Figure 4. Perturbation in the Actin dynamics does not alter Myosin *unbinding kinetics*. (A) Quantifications of time delay. Blue dots: time delay distribution red over green channel, red dotted line: time delay of 0 s, blue shade: histogram of distribution. N(embryos) = 10, N(pulses) ≥ 200 (See Supplementary Table S1 and S2 for statistical details), ns: not significant, ***: p-value ≤ 0.001. **(B)** Summary of the observed times delay within the RhoA activation cascade. **(C-F)** Single-molecule tracking of Myosin::GFP in cofilin knockdown *unc-60(RNAi).* N(embryos) = 8, N(pulses) = 39. **(C)** Binding rate (K_{on}) of Myosin over time, **(D)** unbinding rate (k_{off}), **(E)** normalized density, **(F)** effective density (blue) and target density (K_{on}/k_{off}, red). **(G-J)** Single-molecule tracking of Actin::GFP. N(embryos) = 6, N(pulses) = 55. (C-J) thin line: median, thick line: mean. (C-E, J-K) shade: std, (F,J) shade: sem. **(G)** Polymerization rate (K_{on}) of Actin over time, **(H)** unbinding rate (k_{off}), **(I)** normalized density, **(J)** effective density (blue) and target density (K_{on}/k_{off}, red). **(K)** Variation of normalized intensities over time of Actin average from Supp Fig. 1C (green straight line), Formin super-diffusive population, aligned (red straight line), Actin K_{on} average from Fig. 4G (cyan straight line), Actin k_{off} average from Fig. 4H (black straight line), calculated target intensity value (K_{on}/k_{off}) (magenta dashed line).

Figure 5

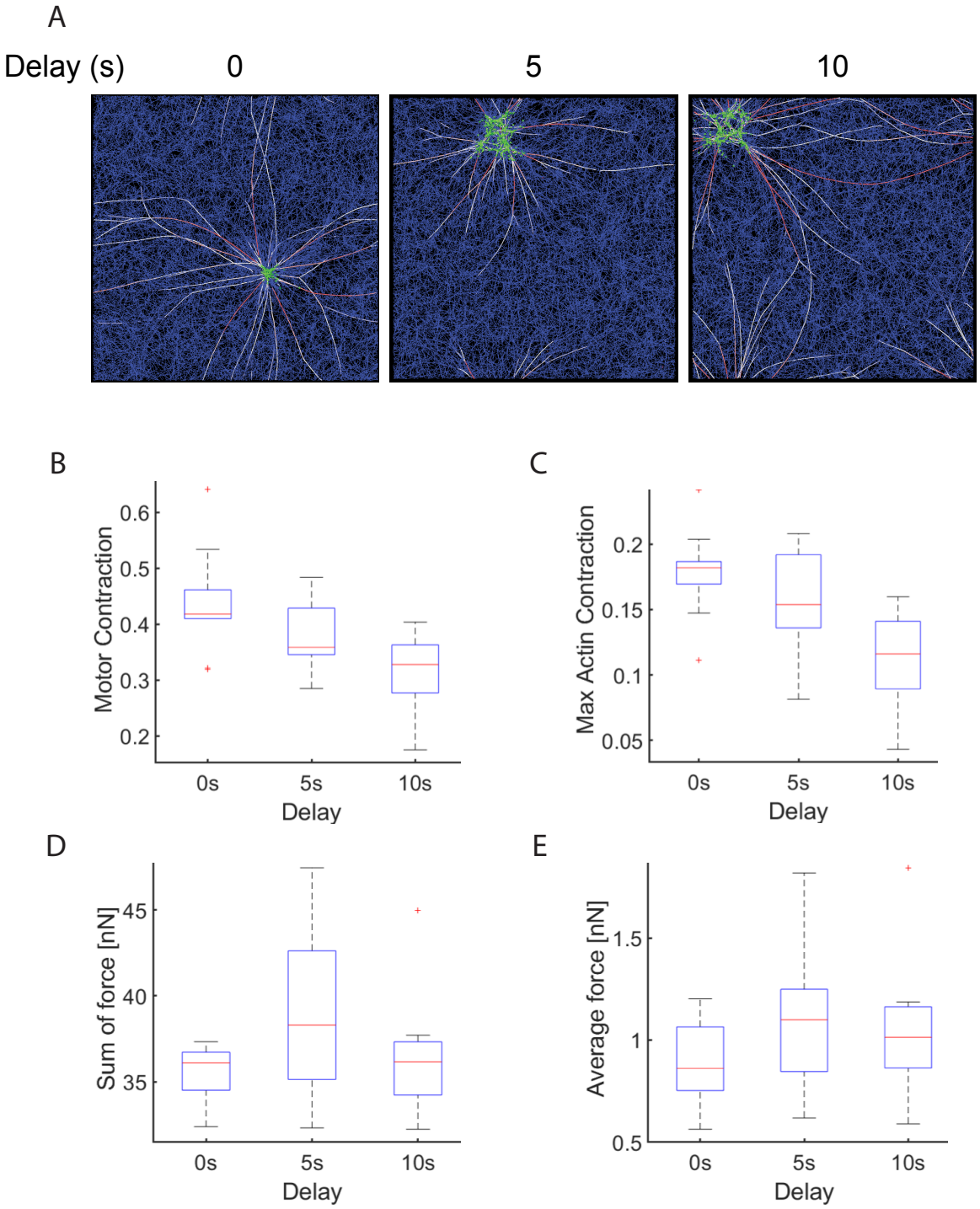
A
Delay (s)
0
5
10
B
Motor Contraction
0.6
0.5
0.4
0.3
0.2
0s
5s
10s
Delay
C
Max Actin Contraction
0.2
0.15
0.1
0.05
0s
5s
10s
Delay
D
Sum of force [nN]
45
40
35
0s
5s
10s
Delay
E
Average force [nN]
1.5
1
0.5
0s
5s
10s
Delay

Figure 5. Numerical simulations of actomyosin mechanics reveal that delay between Actin assembly and Myosin accumulation affects force deployment during pulsed contractions.(A) Snapshots taken at the end of first myosin activation cycle with an increasing delay between formin-mediated Actin filament elongation and Myosin accumulation. **(B)** Quantification of the extent of motor contraction during pulsed contraction. **(C)** Quantification of actin contraction during pulsed contraction. **(D)** Sum of tensile forces acting and on formin-elongated filaments. **(E)** Average force generated locally and acting on the overall network.

Figure S1

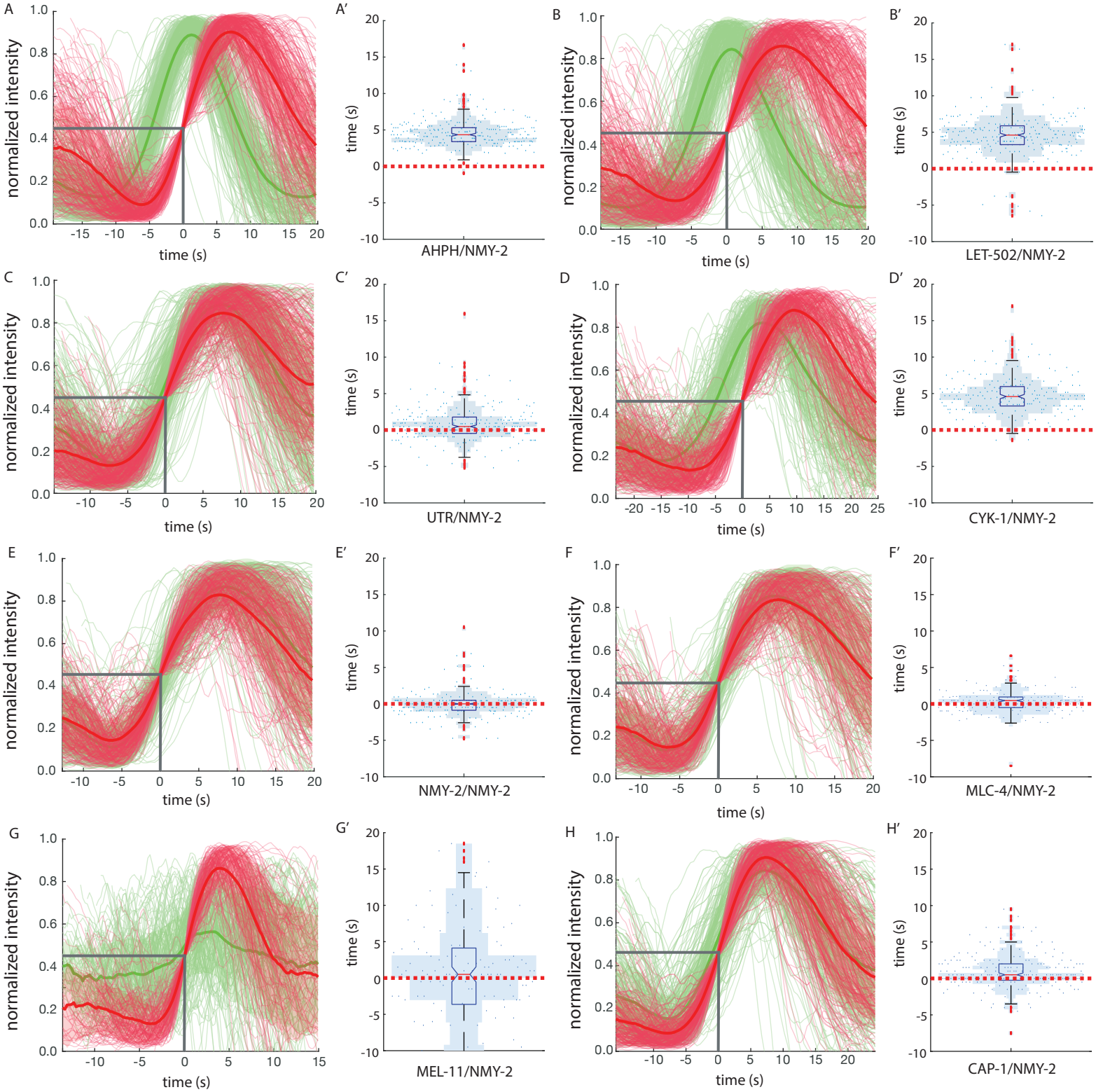
A
A′
B
B′
C
C′
D
D′
E
E′
F
F′
G
G′
H
H′
normalized intensity
time (s)
AHPH/NMY-2
LET-502/NMY-2
UTR/NMY-2
CYK-1/NMY-2
NMY-2/NMY-2
MLC-4/NMY-2
MEL-11/NMY-2
CAP-1/NMY-2

Supplemental figure 1. Most of the time delay observed between RhoA and Myosin can be explained by the delay between ROCK and Myosin. (A-G') Time delay between in red Myosin heavy-chain NMY-2 and in green RhoA's proxy AHPH (A-A'), the ROCK LET-502 (B-B'), Actin's proxy UTR (C-C'), the Formin CYK-1 (D-D'), the control with the Myosin overexpression (E-E'), the Myosin regulatory light-chain MLC-4 (F-F'), the Myosin Phosphatase MEL-11 (G-G'), Actin capping-protein CAP-1 (H-H'). **(A-H)** Fainted lines: distribution of normalized intensity through time, solid line: mean, shade: std. **(A'-H')** Blue dots: time delay distribution red over green channel, red dotted line: time delay of 0 s, blue shade: histogram of distribution.

Figure S2

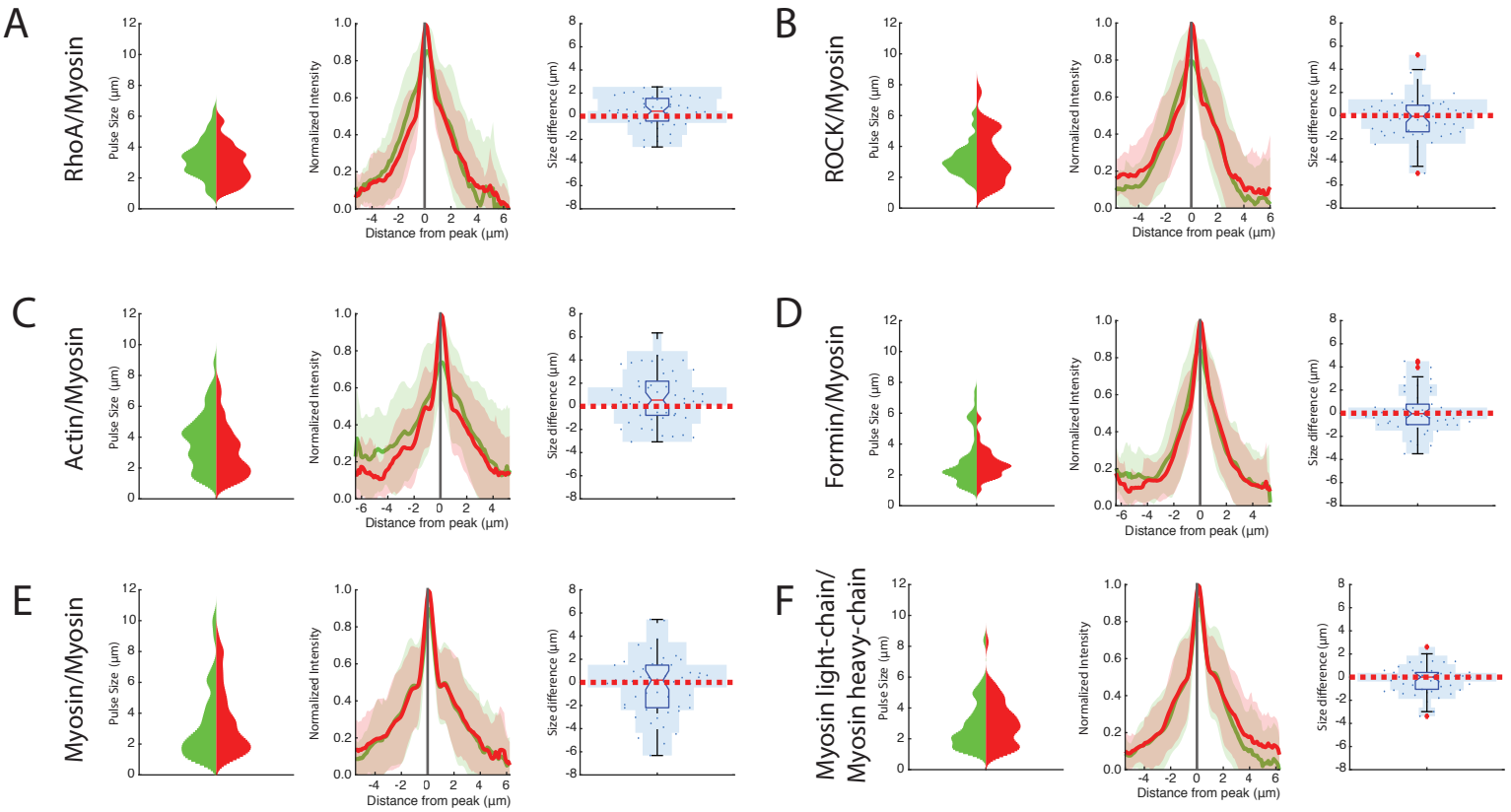
A
RhoA/Myosin
B
ROCK/Myosin
C
Actin/Myosin
D
Formin/Myosin
E
Myosin/Myosin
F
Myosin light-chain/
Myosin heavy-chain
Pulse Size (μm)
Normalized Intensity
Distance from peak (μm)
Size difference (μm)

Supplemental figure 2. The size of Myosin pulse is smaller compared to the one of RhoA and Actin. Left: distribution of pulse sizes, center: mean of the pulse size (solid line) with the std (shade), right: quantification of the difference in size (green – red). N(embryos) = 10, N(pulses) = 50. See statistical details in Supplementary Table S3. **(A-F)** Comparison in pulse sizes between in red Myosin (NMY-2) and in green RhoA (AHPH) (A), ROCK (LET-502) (B), Actin (UTR) (C), Formin (CYK-1) (D), the control Myosin (E) and Myosin Light-Chain (MLC-4) (F).

Figure S3

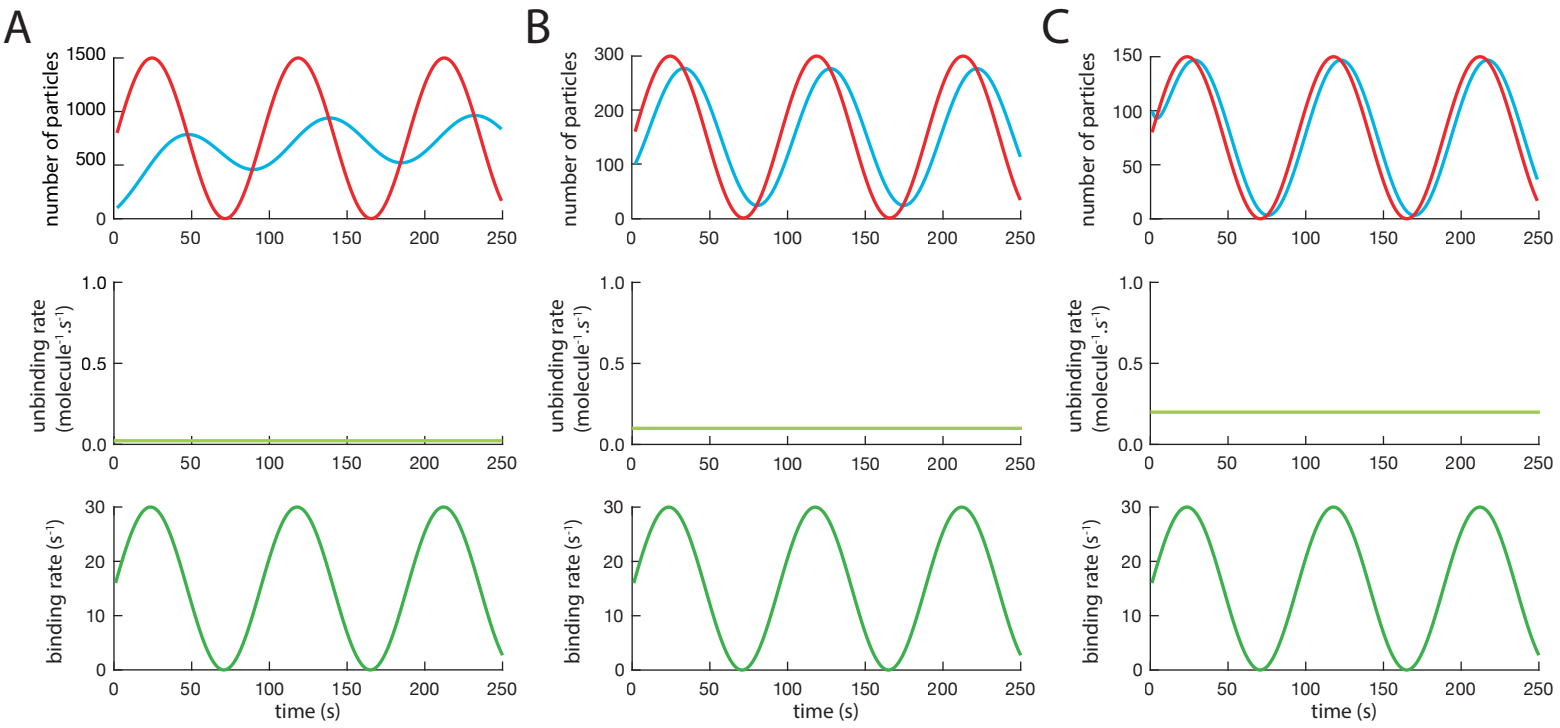
A
B
C
number of particles
unbinding rate (molecule^{-1}.s^{-1})
binding rate (s^{-1})
time (s)

Supplemental figure 3. The arbitrary constant number used for the K_{off} influences the delay between the simulated and the calculated number of particles. (A-C) The simulations (blue line) shows that the system is more delayed and is further apart from the equilibrium state (red line: K_{on}/k_{off}) when the constant is lower like in (A) k_{off} = 0.01 molecules^{-1}.s^{-1}, than it is when the k_{off} is higher like in (B) k_{off} = 0.1 molecules^{-1}.s^{-1}. When the k_{off} is high like (C) k_{off} = 0.2 molecules^{-1}.s^{-1} then the simulation almost matches the equilibrium state and time delay is minimal.

Figure S4

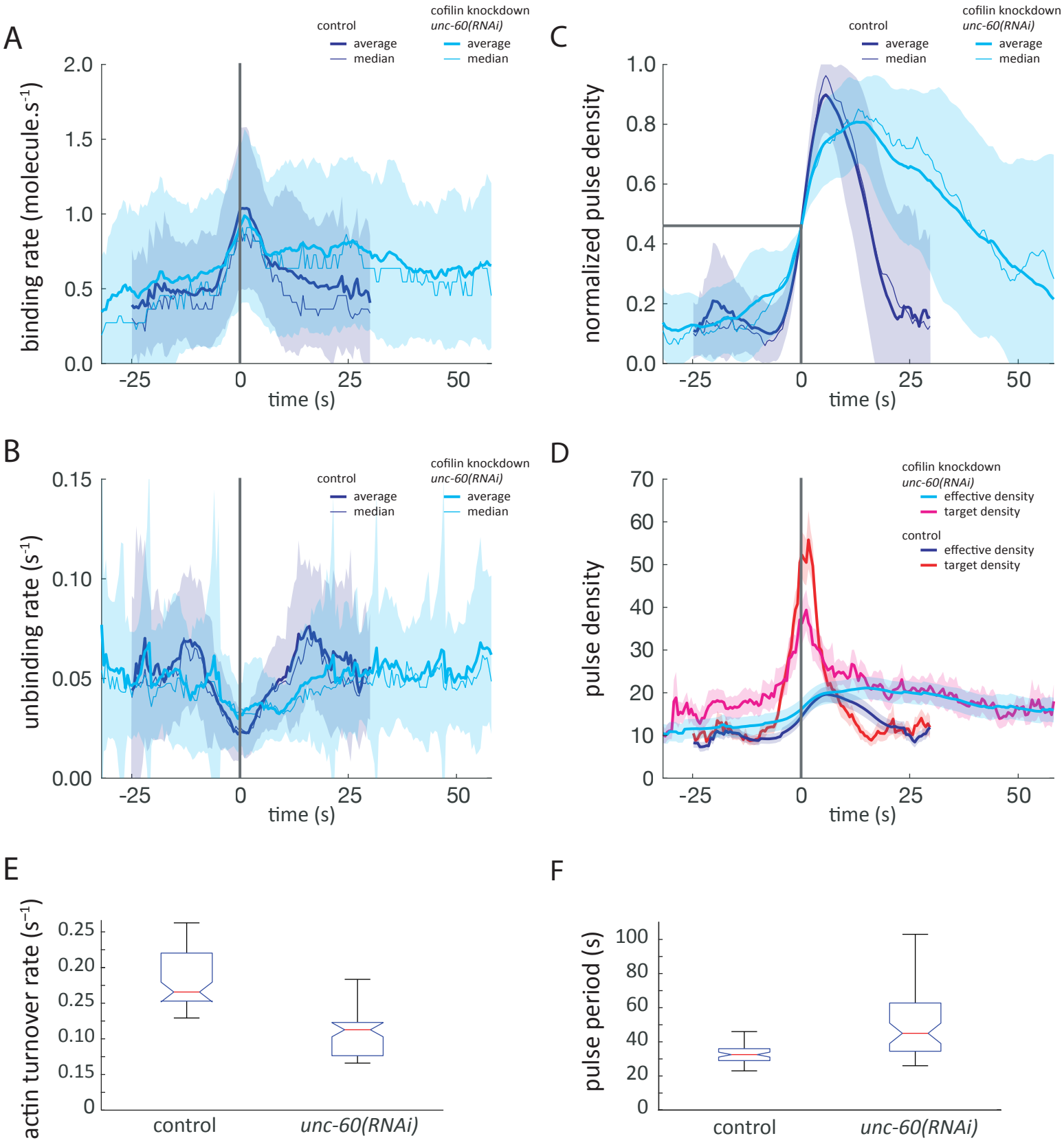
A
control
average
median
cofilin knockdown
unc-60(RNAi)
average
median
binding rate (molecule.s-1)
time (s)
B
unbinding rate (s-1)
time (s)
C
normalized pulse density
time (s)
D
cofilin knockdown
unc-60(RNAi)
effective density
target density
control
effective density
target density
pulse density
time (s)
E
actin turnover rate (s-1)
control
unc-60(RNAi)
F
pulse period (s)
control
unc-60(RNAi)

Supplemental figure 4. Cofilin depletion results in increased pulse period. (A-D) Comparison between wild-type (dark blue) and Cofilin knockdown *unc-60(RNAi)* (light blue). Thin line: median, thick line: average. (A-C) Shade: std. **(A)** Binding rate (K_{on}) of Myosin over time, **(B)** unbinding rate (k_{off}), **(C)** Normalized pulse density. **(D)** Effective density, with control (dark blue) and *unc-60(RNAi)* (light blue) and target density (K_{on}/k_{off}), with control (red), *unc-60(RNAi)* (pink). Shade: sem. **(E)** Actin turnover rates from Actin::GFP single-molecule microscopy measurements in control and Cofilin (RNAi). (F) Pulse period measured from Actin::GFP TIRF microscopy movies in control and Cofilin (RNAi).

Table S1. Statistics from two-color and single-molecule imaging experiments

	number of embryos	number of pulses	one-sample t-test	delay median (s)	delay mean (s)	delay std
GFP::AHPH;NMY-2::mKate2	10	247	1,61E-102	4,34	4,6168	1,9608
GFP::LET-502;NMY-2::mKate2	10	249	4,49E-73	4,605	4,5991	2,7811
UTR::GFP;NMY-2::mKate2	10	249	1,52E-08	0,4835	0,8653	2,3328
CYK-1::GFP;NMY-2::mKate2	10	200	1,06E-66	4,5825	4,761	2,5593
NMY-2::GFP;NMY-2::mKate2	10	200	8,67E-01	0	0,021	1,7657
MLC-4::GFP;NMY-2::mKate2	11	165	2,22E-02	0,4555	0,2825	1,5685
CAP-1::GFP;NMY-2::mKate2	10	200	2,51E-08	0,5	1,3775	3,356
MEL-11::GFP;NMY-2::mKate2	10	148	1,88E-04	1,5	2,1934	6,6863
NMY-2::GFP SiMI (GFP RNAi)	5	38				
NMY-2::GFP SiMI (unc-60 + GFP RNAi)	8	39				
CYK-1::GFP SiMI	8	56				
ACTIN::GFP SiMI	6	55				
NMY-2::GFP SiMI (mel-11(it26) + GFP RNAi)	9	54				

Table S2. Statistics from the two-sample t-test in two-color imaging experiment

	two-sample t-test
AHPH::GFP;NMY-2::mKate2 vs GFP::LET-502;NMY-2::mKate2	0,9346
AHPH::GFP;NMY-2::mKate2 vs UTR::GFP;NMY-2::mKate2	1,19E-62
GFP::LET-502;NMY-2::mKate2 vs UTR::GFP;NMY-2::mKate2	7,90E-48
GFP::LET-502;NMY-2::mKate2 vs CYK-1::GFP;NMY-2::mKate2	0,5257
UTR::GFP;NMY-2::mKate2 vs CYK-1::GFP;NMY-2::mKate2	1,24E-49
UTR::GFP;NMY-2::mKate2 vs NMY-2::GFP;NMY-2::mKate2	2,77E-05
MLC-4::GFP;NMY-2::mKate2 vs NMY-2::GFP;NMY-2::mKate2	1,40E-01
CAP-1::GFP;NMY-2::mKate2 vs NMY-2::GFP;NMY-2::mKate2	6,45E-07
UTR::GFP;NMY-2::mKate2 vs CAP-1::GFP;NMY-2::mKate2	5,77E-02

Table S3. Statistics for Pulse Size difference in two-color imaging experiment

pulse size difference	one-sample t-test	median size Myosin (μm)	mean size Myosin (μm)	std size Myosin	median size GFP tagged (μm)	mean size GFP tagged (μm)	std size GFP tagged protein
RhoA vs Myosin Heavy-Chain	0,041	2,6966	2,8899	1,2308	3,2693	3,2786	1,257
ROCK vs Myosin Heavy-Chain	0,5441	2,9282	3,3485	1,6764	3,038	3,1872	1,0657
Formin vs Myosin Heavy-Chain	0,4596	2,6051	2,7484	0,9695	2,2733	2,9391	1,6572
Actin vs Myosin Heavy-Chain	0,0187	2,7216	3,0774	1,679	3,8541	3,8322	1,8207
Light Chain vs Myosin Heavy-Chain	0,2273	2,8104	3,0503	1,5231	2,3001	2,8495	1,5473
Control: Myosin Heavy-Chain	0,4627	2,7617	3,5149	2,181	2,4139	3,2478	2,3388

pulse size difference	median size difference (μm)	mean size difference (μm)	std size difference
RhoA vs Myosin Heavy-Chain	0,4342	0,3887	1,3093
ROCK vs Myosin Heavy-Chain	-0,0636	-0,1613	1,8666
Formin vs Myosin Heavy-Chain	-0,0371	0,1908	1,8099
Actin vs Myosin Heavy-Chain	0,5377	0,7547	2,1937
Light Chain vs Myosin Heavy-Chain	0,004	-0,2007	1,1609
Control : Myosin Heavy-Chain	0,1952	-0,2671	2,5511

Table S4. List of strains used in Prigent Garcia e*t al.*

Robin lab strain name	genotype	source
EM264	*nmy-2(cp52[nmy-2::mKate2 + LoxP unc-119(+) LoxP]) I; xsSi5[cb-unc-119 (+) GFP::ANI-1(AH+PH)] II; unc-119(ed3) III*	Michaux et al., 2018
JH1541	*unc-119(ed4) III; pJH7.03[pie-1p::GFP::actin::pie-1 3' UTR + unc-119(+)]*	Courtesy of G. Seydoux
LP229	*nmy-2(cp52[nmy-2::mKate2 + LoxP unc-119(+) LoxP]) I; unc-119 (ed3) III*	Dickinson et al, 2017
SWG282	*gesIs008[cyk-1p::cyk-1::GFP::cyk-1UTR, unc-119+]*	Costache, Prigent Garcia
FBR175	*nmy-2(cp52[nmy-2::mKate2 + unc-119(+)]) I; cyk-1(jme14[cyk-1::eGFP]) unc-119(ed3) III*	Costache, Prigent Garcia
FBR10	*nmy-2(cp52[nmy-2::mKate2 + unc-119(+)]) I; xsSi3[cb-unc-119(+) pie-1::GFP::utrophin::pie-1 3' UTR] II; unc-119(ed3) III*	Tse et al., 2012
ML2508	*let-502(mc74[GFP::let-502]) I*	Bell et al., 2020
FBR28	*let-502(mc74[GFP::let-502]) nmy-2(cp52[nmy-2::mKate2 + LoxP unc-119(+) LoxP]) I; unc-119 (ed3) III*	this study
JJ1473	*unc-119(ed3) III; zuIs45[nmy-2p::nmy-2::GFP + unc-119(+)] V*	Nance et al., 2003
FBR189	*nmy-2(cp52[nmy-2::mKate2 + LoxP unc-119(+) LoxP]) I; unc-119 (ed3) III; zuIs45 [nmy-2p::nmy-2::GFP + unc-119(+)] V*	this study
FBR96	*mlc-4(jme4[mlc-4::eGFP + LoxP]) III*	this study
FBR119	*nmy-2(cp52[nmy-2::mKate2 + LoxP unc-119(+) LoxP]) I; mlc-4(jme4[mlc-4::eGFP+loxP]) unc-119 (ed3) III*	this study
FBR157	*mel-11(syb753[mel-11::GFP]) II*	this study
FBR227	*nmy-2(cp52[nmy-2::mKate2 + LoxP unc-119(+) LoxP]) I; mel-11 (syb753[mel-11::GFP]) II; unc-119 (ed3) III*	this study
ML2519	*cap-1(mc76[cap-1::GFP + unc-119(+)]) IV*	Courtesy of M. Labouesse
FBR212	*nmy-2(cp52[nmy-2::mKate2 + LoxP unc-119(+) LoxP]) I; unc-119 (ed3) III; cap-1(mc76[cap-1::GFP + unc-119(+)]) IV*	this study
SWG282	*gesIs008[Pcyk-1::CYK-1::GFP::cyk-1UTR, unc-119+]*	Costache, Prigent Garcia
KK332	*mel-11(it26) unc-4(e120) sqt-1(sc13)/mnC1 [dpy-10(e128) unc-52(e444)] II*	CGC
FBR236	*mel-11(it26) unc-4(e120) sqt-1(sc13)/mnC1 [dpy-10(e128) unc-52(e444)] II; unc-119(ed3) III; zuIs45[nmy-2p::nmy-2::GFP + unc-119(+)] V*	this study

Article 2:

Rapid assembly of a polar network architecture drives efficient actomyosin contractility

Actin network architecture and dynamics play a central role in cell contractility and tissue morphogenesis. Cortical Actomyosin contractions play a key role in several important morphogenetic events including polarity establishment and gastrulation. Local densification of Actin network depends on the local activation of RhoA which will in turn recruit and activate Formin at the pulse location. Formin binds to the Actin filament barbed-end and starts polymerizing, adding new subunits to the filament. Pulsed contractions driven by RhoA represent a generic mode of Actomyosin contractility but the mechanisms underlying (1) how their specific architecture emerges, and (2) how this architecture supports the contractile function of the network, remain unclear.

In this work, we combined quantitative microscopy using TIRFM, single-molecule imaging, numerical simulations and simple mathematical modelling, to explore the dynamic network architecture underlying pulsed contraction. First, we showed that during pulsed contractions, two subpopulations of Formins are recruited by RhoA from the cytoplasm and bind to the cell surface in the early *C. elegans* embryo: *recruited* Formins, a functionally inactive population that is in an activated state but does not assemble new Actin subunits at the filament barbed-end, and *elongating* Formins, which actively participate in Actin filaments elongation.

Second, we observed that the speed of the elongating Formin is function of the state of the cell cycle. We measured that the speed is reduced during cytokinesis and stable during interphase and mitosis. First division is asymmetric in *C. elegans* and give rise to two daughter cells with two distinct fate. The observations we made regarding speed is equivalent in both daughter cells, Formin speed being, therefore, independent from the cell fate.

Focusing on Formin dynamics during pulses, we showed that minority elongating Formins precede recruited Formins. These kinetic dynamics is compatible with Formins capturing and rapidly saturating barbed ends available for filament elongation. Once all barbed ends are saturated, newly recruited Formins do not switch to an active mode as they do not bind to any barbed end. We then showed that these elongating Formins assemble a polar network of Actin, with barbed ends pointing out of the pulse, suggesting a kinetic rather than mechanical control of network architecture.

Finally, our numerical simulations demonstrate that this geometry favors rapid network contraction. Our results thus show that Formins saturate available Actin filaments

barbed ends and convert a local, biochemical gradient of RhoA activity into a polar network architecture, thereby driving rapid and efficient network contractility, an important evolutionary feature in a metazoan with rapid embryonic cell cycles.

Author contributions:

F.B. Robin conceived the project. V. Costache and S. Prigent Garcia shared equally in its intellectual development. V. Costache performed single-molecule experiments and tracking analysis described in Fig. 1, 3 and 5. S. S. Prigent Garcia performed single-molecule experiments and tracking analysis described in Fig. 2 and pulse spatial dynamics in Fig. 3. S. Begnaud developed supporting code for pulse analysis in Fig. 4 and Fig. S3. C. Plancke, S.K. Suman and A-C. Reymann generated strains and molecular reagents used in the study. F.B. Robin performed the modeling shown in Fig. 4. TY. Kim and J. Li performed the numerical simulations shown in Fig. 6. V. Costache, S. Prigent Garcia, TY. Kim and F.B. Robin prepared figures and wrote the paper.

Rapid assembly of a polar network architecture drives efficient actomyosin contractility

Vlad Costache[1,*], Serena Prigent Garcia[1,*], Camille N. Plancke[1], Jing Li[2], Simon Begnaud[1], Shashi Kumar Suman[1], Anne-Cécile Reymann[3], Taeyoon Kim[2], François B. Robin[1,✉]

1: CNRS UMR7622 and Inserm ERL 1156, Institute for Biology Paris-Seine (IBPS), Sorbonne University, Paris, France.
2: Weldon School of Biomedical Engineering, Purdue University, West Lafayette, Indiana.
3: IGBMC, CNRS UMR7104, Inserm U1258, and Université de Strasbourg, Illkirch, France.

*: Contributed equally
✉: Corresponding author. Email: francois.robin@sorbonne-universite.fr

SUMMARY

Actin network architecture and dynamics play a central role in cell contractility and tissue morphogenesis. Pulsed contractions driven by RhoA represent a generic mode of actomyosin contractility, but the mechanisms underlying (1) how their specific architecture emerges, and (2) how this architecture supports the contractile function of the network, remain unclear. Here, we combine quantitative microscopy, single-molecule imaging, numerical simulations and simple mathematical modelling, to explore the dynamic network architecture underlying pulsed contraction. We show that during pulsed contractions, two subpopulations of formins are recruited by RhoA from the cytoplasm and bind to the cell surface in the early *C. elegans* embryo: *recruited* formins, a functionally inactive population, and *elongating* formins, which actively participate in actin filaments elongation. Focusing on formin dynamics during pulses, we show that minority elongating formins precede recruited formins, a kinetic dynamics compatible with formins capturing and rapidly saturating barbed ends available for filament elongation. We then show that these elongating formins assemble a polar network of actin, with barbed ends pointing out of the pulse, pointing to a kinetic rather than mechanical control of network architecture. Finally, our numerical simulations demonstrate that this geometry favors rapid network contraction. Our results thus show that formins saturate available actin filaments barbed ends and convert a local, biochemical gradient of RhoA activity into a polar network architecture, thereby driving rapid and efficient network contractility, an important evolutionary feature in a metazoan with a rapid embryonic cell cycles.

HIGHLIGHTS

1. The formin CYK-1 drives actin network assembly during RhoA-driven pulses
2. The process is extremely rapid, with a formin-based actin elongation rate higher than 1.3 $\mu m \cdot s^{-1}$
3. A barbed-end saturation mechanism allows for responsive F-actin assembly
4. Rapid and responsive F-actin elongation results in the assembly of aster-like polar actin networks
5. Numerical simulations show network polarity drives very efficient network contractility

INTRODUCTION

Vastly conserved in eukaryotes, the actomyosin cytoskeleton is a major determinant of the mechanical properties of embryonic cells and tissues (Munjal & Lecuit 2014). Modulation of actomyosin networks activity plays a critical role in cell shape changes, cell division, cell migration and polarization. The integration of these behaviors, at the tissue scale, drive tissue deformation and morphogenesis (Lecuit & Lenne 2007). At the molecular scale however, the role of the architecture of actomyosin networks has been a research focus and subject to some debate (Blanchoin et al. 2014; Koenderink & Paluch 2018; Agarwal & Zaidel-Bar 2019). In muscle, the mechanisms for actomyosin contractility has been historically well-characterized, showing that in this quasi-crystalline organization, the sliding of bipolar Myosin II mini-filaments along actin filaments drives network contractility. In other cell types however, and in particular in the cell cortex of developing embryos, the seemingly disordered actin network remains poorly understood in terms of network polarity, length distribution, mesh size, turnover rates or crosslinking levels, and we still do not fully understand how F-actin architecture is linked to network contractility. Theoretical studies (Galkin et al. 2010; Galkin et al. 2011; Lenz, Gardel, et al. 2012) and computational models (T. Kim 2015) have shown that asymmetry between compressive and extensive modulus—the ability to withstand tension but buckle under compressive forces—can drive contraction of disordered bundles. Similarly, numerical simulations and *in vitro* experiments have clearly demonstrated that non-polar actin networks can contract (Yu et al. 2018). Cellular networks however often display characteristic organizations, suggesting that specific network dynamics and geometries may play a critical role in network contractility (Koenderink & Paluch 2018).

RhoGTPase zones have recently emerged as essential regulators to template the architecture of the actomyosin meshwork by defining active, task-tuned zones of cytoskeletal assembly (Benink 2005; Miller & Bement 2009; Burkel et al. 2012; Bement et al. 2005). Examples of such zones include the leading edge of migrating cells, the cleavage furrow during cell division, or the apical cortex during apical constriction. During embryonic morphogenesis in particular, a wide class of morphogenetic processes are driven by brief iterative contractions of the cortical actomyosin network termed pulsed contractions (He et al. 2010; H. Y. Kim & Davidson 2011; Martin et al. 2009; Rauzi et al. 2010; Munro et al. 2004; Roh-Johnson et al. 2012). Previous work showed that pulsed contractions are driven by excitable dynamics of the Rho GTPase RhoA, leading to the formation of activation zones that drive the recruitment of downstream effectors formin, Anillin, F-actin and Myosin II (Maddox et al. 2005; Munro et al. 2004; Michaux et al. 2018; Naganathan et al. 2018; Reymann et al. 2016). Excitable dynamics, with a feedforward activation and delayed negative feedback, seem to play an important role to establish Rho activation (Bement et al. 2015; Maître et al. 2015; Nishikawa et al. 2017; Michaux et al. 2018).

RhoGTPases thus spatially and temporally pattern the recruitment, turnover and activity of downstream effectors. It remains unclear, however, how these orchestrated modulations of actomyosin dynamics support the specific cellular function of Rho zones. Here, we show that the dynamics and topology of RhoA

activation, converting a RhoA chemical gradient into the assembly of a polar actin network, drives the formation of a network structure tuned to its contractile function.

In the nematode *C. elegans*, pulsed contractions occur from the 1-cell stage onwards during interphase (Munro et al. 2004; Mayer et al. 2010) and support cell polarization and apical constriction (Nance & Priess 2002; Nance 2003; Roh-Johnson et al. 2012). Here, we show that RhoA pulses control the accumulation of the formin CYK-1 (diaphanous/mDia homolog), driving F-actin accumulation during pulsed contractions. We further show that actin network assembly is kinetically controlled by the saturation of actin filaments barbed ends, resulting in a time-optimal response to RhoA activation. Using single-molecule microscopy to infer local actin filament orientation during pulse assembly, we show that formin-assembled actin networks are polar, generating networks with barbed ends pointing outside of the pulse. Finally, our computational exploration shows that this polar network architecture is favorable to the generation of efficient actomyosin contractility. Taken together, these results underline a kinetic rather than mechanical control for actomyosin network orientation during pulsed contractions. They also underline the tinkering evolution of billion-years old machinery, reusing the molecular machines—formin, F-actin and Myosin II—to drive a fundamentally conserved phenomenon, precisely-tuned force generation, with opposite geometries reflecting organism-specific construction rules and constraints.

RESULTS

Cortical dynamics of formins in a developing embryo

Formins are actin nucleators and processive actin elongators, catalyzing the addition of actin monomers to the barbed end of actin filaments while protecting the filament against capping (Pruyne et al. 2002). In *C. elegans*, 7 formin genes have been identified (Mi-Mi et al. 2012). Among these, *cyk-1* (cytokinetic defective-1), the only ortholog of the Diaphanous family of formins, is required for cell division (Swan et al. 1998).

To study CYK-1 in the early *C. elegans* embryos, we first used CRISPR-Cas9 homologous recombination to insert a GFP in the genomic *cyk-1* locus. We then used live single-molecule fluorescence microscopy to visualize the dynamics of individual formin molecules fused with GFP (Robin et al. 2014). We first observed that formins apparently classified in at least two populations (Movie S1), a population of ballistic molecules and a static population. To better visualize these two populations, we used maximum intensity projection to overlay the position of molecules over 100 consecutive time-points (Movie S2). Using this visualization tool, static formins appeared as dots, while moving formins appeared as a trail on the cell surface.

To quantitatively characterize these two populations, we performed single-particle tracking and analyzed the trajectories of 19137 individual formin molecules from 5 embryos. Based on the logarithmic regression of the mean-squared displacement to an anomalous diffusion model $MSD = 2*D.t^{\alpha}$ (Robin et al. 2014), we

characterized all particle trajectories longer than 15 frames (Fig. 1A,B) by their anomalous diffusion coefficient D and scaling exponent α. Strikingly, we observed the emergence of two clear populations, corresponding to the static and ballistic populations, with apparent distributions of scaling exponent peaking at $\alpha = 0.3$ (subdiffusive) and $\alpha = 1.6$ (superdiffusive), respectively (Fig. 1C,D, Movie S3).

Previous work suggested that these super-diffusive particles represented formins actively elongating actin filaments (Higashida 2004; Funk et al. 2019). To confirm this, we used RNAi against *perm-1*, a known component eggshell protein (Carvalho et al. 2011; Olson et al. 2012), to permeabilize the eggshell, and subsequently treated the embryos with the microtubule depolymerizing drug Nocodazole and the actin depolymerizing drug Latrunculin A (Movie S4). Performing the same analysis as previously, we observed that the superdiffusive population essentially disappeared after Latrunculin A treatment, while it was unaffected by Nocodazole treatment (Fig. 1E, Movie S4). These results strongly supported the idea that superdiffusive cortical CYK-1::GFP speckles corresponded to formin dimers actively and processively elongating actin filaments at the barbed-end of the filament at the cell cortex.

To measure the speed of formins, we selected a collection of trajectories projected formin motion on a smoothed version of their trajectory, and quantified the traveled distance along this trajectory, or using MSD measurements presented before. Both metrics, quite conservative, yielded very similar result of $1.1 \pm 0.2\ \mu m \cdot s^{-1}$ and $1.3 \pm 0.2\ \mu m \cdot s^{-1}$ (standard deviation)—in line with previously reported speeds (Higashida 2004), but slower than recent *in vivo* reports (Funk et al. 2019). Interestingly, single-molecule microscopy of actin::GFP speckles, serving as fiducial markers on the network of actin filaments, remained largely immobile (Fig. 1F, Movie S5, (Robin et al. 2014)), supporting the idea that actin filaments are not extruded by immobile formins, and that filament elongation instead fully translates in formin directional motion. These data show that CYK-1 velocity is a reliable *in vivo* proxy for formins elongation rate, demonstrating an average elongation rate of ~400–468 monomers$\cdot s^{-1}$. Incidentally, our results also suggest that CYK-1 could be used as a biosensor to measure cellular modulations of the concentrations of profilin-ATP-G-Actin, calibrated on elongation rates previously reported *in vitro* in the presence of profilin (Neidt, Scott, et al. 2008; Neidt, Skau, et al. 2008). Provided that in our system formin-mediated actin filament elongation rates are not buffered by slow dissociation of profilin from the barbed end (Funk et al. 2019), or modulated by mechanical forces (Jégou et al. 2013; Courtemanche et al. 2013; Kubota et al. 2017), our results would point to a local G-actin concentration in the early embryo in the ~10-12 μM range.

Formin-mediated actin filament elongation rates during the cell cycle

To explore if actin elongation was dynamically modulated during embryonic development, we then measured formin velocity at the 1-, 2- and 4-cell stages during distinct phases of the cell cycle (Fig. 2A, see Material and Methods). To avoid confounding effects of overcrowding on tracking at high particle density, we decided to use a strain over-expressing GFP fused with CYK-1, which displays essentially identical

dynamics as GFP fusion at the endogenous site, but allowed us to visualize formins at much lower densities, improving particle tracking. At the 1-cell stage, elongation rate remained unchanged from polarization to maintenance phase (1.25 ± 0.18 μm·s^{-1} and 1.27 ± 0.16 μm·s^{-1}, resp.), but decreased significantly over the entire cortex during cytokinesis, to 1.05 ± 0.22 μm·s^{-1}.

The velocity increased again after cytokinesis, going back to its level at corresponding 1-cell stage polarization establishment (1.24 ± 0.19 μm·s^{-1}), stable or slightly decreasing during mitosis (1.18 ± 0.18 μm·s^{-1}) in the AB cell, to drop down again during AB cytokinesis (1.04 ± 0.18 μm·s^{-1}). Again, during interphase at the 4-cell stage in ABp, formin velocity increased again though notably lower in interphase compared to mitosis (1.15 ± 0.17 μm·s^{-1} at interphase and 1.24 ± 0.18 μm·s^{-1} during mitosis). Taken together, these results show that formin speed drops significantly during cytokinesis but increases when interphase resumes.

To compare actin elongation rates across lineages, we also measured formin speed in AB and P1 at the 2-cell stage during interphase (1.24 ± 0.19 μm·s^{-1} and 1.18 ± 0.18 μm·s^{-1}, respectively), and during mitosis (1.18 ± 0.18 μm·s^{-1} and 1.22 ± 0.19 μm·s^{-1}, resp.) (Fig. 2B). Our results suggest that formin speed does not vary between the two cell types.

In summary, actin elongation dynamics is distinctly modulated during phases of the cell cycle, decreasing significantly by >10% during cytokinesis, to increase again after cytokinesis completion. Strikingly, measured elongation rates seemed relatively robust and only changed marginally from the 1-cell to 4-cell stage. These results suggest that F-actin dynamics might be differentially regulated by G-actin concentration, but remains largely robust across cell lineages during early embryonic development.

Formin kinetics and implications on actin filament length *in vivo*

The length of formin-elongated actin filaments is controlled by a combination of the formin elongation rate, formin global off-rate (combining unbinding and competition), and the turnover rate of F-actin monomers in the cortex. Specifically, we assumed that F-actin turnover and elongation dynamics are independent processes and follow exponential laws with characteristic rate $1/\tau_{actin}$ and $1/\tau_{formin}$. For an F-actin monomer at the time of its disassembly, the length of filament from monomer the to the barbed-end of the filament follows an exponential law with characteristic length $L_{filament} = V_{formin} \times \tau_{filament}$, where $1/\tau_{filament} = 1/\tau_{actin} + 1/\tau_{formin}$ is a characteristic "off" rate of formins and V_{formin} their speed (see Suppl. Material for detailed derivation). To estimate filament length, we thus needed to access actin and formin off-rates, and use our measured actin filament elongation rates.

We expected a significant fraction of trajectory to be interrupted, either by tracking failure or photobleaching, barring us from using single-molecule tracking as a proxy (Fig. 2C). We therefore turned

to a previously established strategy, smPReSS (Robin et al. 2014) to estimate a bulk turnover rate for formins. Briefly, by measuring the depletion of cortical formins caused by laser illumination of the cortex in a CYK-1 overexpression strain, we can estimate a *bulk* formin turnover rate, over all formin populations. We could thus establish that the bulk cortical turnover rate of the formin CYK-1 is ~0.11 s^{-1} (Fig. 2D).

Combining our results with previous measurements of Actin::GFP turnover rates (0.05–0.15 s^{-1}, (Robin et al. 2014; Michaux et al. 2018)), we estimate that formin-elongated actin filaments scale to ~6 μm on average in the 2-cell stage *C. elegans* embryo.

Dynamics of formin at the cortex during pulsed contractions

We then decided to focus on the dynamics of formins during pulsed contractions. During polarity establishment in the 1-cell embryo, and during interphase at the 2-cell stage, formins accumulate in well-identifiable pulses corresponding to RhoA-driven actomyosin pulsed contractions (Fig. 3A-E, Movie S2, Fig. S1A, (Munro et al. 2004; Piekny et al. 2005; Naganathan et al. 2014; Reymann et al. 2016; Michaux et al. 2018)). To infer the biochemical sequence of formin activation during pulsed contractions, we thus decided to measure the timing of arrival of the various formin populations over the course of a pulsed contraction.

As described previously, in order to categorize into subdiffusive or superdiffusive, a minimal track length was required. We thus divided the population into 3 tiers: short tracks (<15 consecutive time frames), which could not be categorized into a specific population, long subdiffusive and long superdiffusive. Using this technique, we were able to demonstrate that the ratio between the different populations was finely modulated during pulses (Fig. 3F-K). To characterize the dynamics of arrival of these populations at the cell cortex, we first focused on the kinetics of these populations on a sequence of successive pulses (Fig. 3F). Strikingly, we observed an iterated sequence of accumulation (Fig. 3G,H). Using cross-correlation, we measured a delay between the arrival of the superdiffusive and subdiffusive populations of ~3 s (Fig. 3L). This suggested that the distinct populations accumulated at the cortex in a sequence, superdiffusive formins (hereon, *elongating* formins) accumulating first, followed by subdiffusive formins (hereon *recruited* formins).

To confirm this result, we collected a series of 115 pulses from 10 embryos, and quantified the dynamics of the different formin subpopulations. Based on these results, we observed that formins indeed accumulated at the cortex in a well-defined sequence, starting with superdiffusive followed by subdiffusive formins (Fig. 3I-K, Movie S6). We further confirmed this observation using a different metrics (based directly on particle displacements instead of trajectory classification) to measure this delay (Fig. S1B-E), and yielding very similar delays (Fig. S1F-I).

This result was somewhat surprising, as based on previous work on formin structure and domain activity, we expected an activation sequence whereby formins would be first recruited to the cortex by RhoA, then

transferred to barbed-ends of actin filaments to promote elongation (F. Li & Higgs 2005; Higgs 2005; F. Li & Higgs 2003). Numerically however, the number of recruited formins out-weighted the elongating population (see Fig. S1F, Class 1 vs. Class 2) , suggesting that the system might be running in a regime in which formins are in excess, and elongate a limiting pool of barbed ends available for elongation.

A barbed end saturation mechanism allows for responsive actin assembly

To test this hypothesis, we designed a simple kinetic model for CYK-1 recruitment, and used this model to explore the temporal dynamics of formin accumulation (Fig. S2A,B). We postulated that:

(1) active RhoA concentration pulses periodically, with period 30 s (Michaux et al. 2018),

(2) cytoplasmic formins are activated by active RhoA and *recruited* to the cortex, shifting in the "**recruited"** population (F. Li & Higgs 2005),

(3) CYK-1 formins are poor nucleators but good elongators—we considered that formins do not efficiently nucleate new filaments under physiological conditions (*in vitro* actin assembly yields ~1 new nucleated filament per 550 CYK-1 formin molecule at 2.5 μM actin and 2.5 μM profilin PFN-1 (Neidt, Skau, et al. 2008)),

(4) once recruited at the cortex, formins bind to barbed ends through a bimolecular reaction to drive actin assembly, becoming **"elongating"** formins,

(5,6) recruited and elongating formins unbind from the cortex, returning back to the cytoplasmic pool with characteristic rates $1/\tau_{recruited}$ and $1/\tau_{elongating}$.

To seed our model, we used measured parameter values for RhoA activity, formin unbinding rates and relative ratios between the different formin populations. Using these parameters, and provided that in our parameters (1) the binding reaction of recruited formins to barbed ends is very fast, and (2) barbed ends are scarce and are depleted when formin density increases, our model indeed captured the key observation that elongating formins accumulated before recruited formins (Fig. 4A-C). Indeed, under these conditions, during an early phase elongating formins accumulate rapidly following the RhoA pulse, followed by a late phase during which recruited formins accumulate (Fig. 4B,F, Fig. S2C-H).

We favored a model for activation in which RhoA binding preceded dimerization (Fig. S2A), though other models—e.g. dimer exists before the formin binds to RhoA and unfolds—are also plausible. The simulation however proved robust to these modifications of the biochemical scheme (Fig. 4D,E).

Another class of model could invoke the delayed activation by RhoA of a formin competitor for barbed-end binding. Recently, the capping protein CapZ/CAP-1 was described as forming a *ménage-à-trois* with formins at the barbed, weakening formin-barbed ends binding affinity and eventually leading to formin displacement (Shekhar et al. 2015). While, in this scenario, the shift from elongating to recruited/inactive formins would result from a mechanism relying on competition for barbed ends rather than saturation of barbed ends,

such a model would essentially present the same kinetic signature, with a "pulse" of barbed-ends available for polymerization.

These results show that given a small set of assumptions, we could explain the emergence of a significant delay between recruited and elongating formins. This model suggests that the saturation by CYK-1 of the barbed-ends of actin filament allows for a rapid response to pulsed RhoA activation (Fig. S2C-H). This suggests that the kinetics of the actin cytoskeleton in the early *C. elegans* embryo is wired to drive fast response to an upstream activation of actin dynamics.

Relative rates of actin assembly and contractility support polar network assembly

During pulsed contractions, cortical contractile dynamics results in peak cortical flow rates of ~0.3 $\mu m \cdot s^{-1}$ (Michaux et al. 2018; Munro et al. 2004; Nishikawa et al. 2017). In comparison, elongating formins move relatively rapidly, with a measured speed of 1.1–1.3 $\mu m \cdot s^{-1}$. As a consequence, even at the peak of contraction, elongating formins can "exit" the contraction zone easily and assemble an actin network of filaments up to several microns around the pulse region. To describe the architecture of this network, we measured the orientation of formin-based actin elongation during pulse assembly. To this end, we focused on elongating formins, and measured the orientation of elongation radially away from the zone of formin accumulation (Fig. 5A-D), which essentially corresponds to the RhoA recruitment zone (Fig. S1A). Displaying only orientations where we could collect >200 individual elongation measurements, we observed that while formins are not heavily oriented outside of the pulse time-window (Fig. 5E,F). In contrast, during the peak of assembly (approx. corresponding to the period where elongating formins >50% max.), formins displayed a strong polarization (Fig. 5E).

These results show that formins elongate the actin network with a polar dynamics, elongation during the pulse occurring from the center of the pulse to the outside. As formin-based elongation increases local actin concentration ~2-fold (Michaux et al. 2018), we propose that pulses assemble a polar actin network with barbed-ends pointing outwards of the pulse akin to an "actin aster" (see discussion).

To test if this orientation resulted purely from the transient local gradient of elongating formins between the pulsing region and its surroundings, or if additional mechanisms should be invoked, we designed a simple spatial model of formin orientation. To seed our model, we exclusively used measured parameters of formin recruitment and elongation dynamics (formin-mediated actin filament elongation rate, density, activation/elongation duration, and off-rate, and pulsed contractions localizations), and generated synthetic formin pulsed accumulations with random orientations. Modelled formin dynamics displayed similar orientations, with filaments pointing outwards, and closely mirroring the dynamics observed *in vivo* (Fig. S3, Movie S7). Altogether, these results demonstrate that local formin accumulation drives the assembly of a polar actin network architecture with a majority of barbed ends pointing out.

Actomyosin network polarity supports efficient contractility

While previous work, both theoretical (Lenz, Thoresen, et al. 2012; Lenz, Gardel, et al. 2012) and *in vitro* (Linsmeier et al. 2016), showed that actin contraction does not require a specific network orientation, *in vivo* observations suggested that pulsed contractions form a polar actin network (Coravos & Martin 2016). Strikingly, recent *in vitro* and computational work show that Myosin II contractility can drive polar network reorganization by barbed end filament sorting, with an opposite polarity (Kreten et al. 2018; Wollrab et al. 2018). We thus wondered if the polar network architecture we observed, barbed end pointing out—combined with Myosin II intrinsic polarity as a plus-end directed motor (Howard 2001)—would not support either stronger contractions or contraction over larger distances. Controlling independently network orientation and density, while faithfully constraining other parameters, however, was not experimentally manageable *in vivo* or *in vitro*. We decided to turn to agent-based models of cortical mechanics to decipher the impact of network architecture on contractility.

Using our established computational model of the actomyosin networks (Fig. S4A, (Jung et al. 2015; Bidone et al. 2017; T. Kim 2015)), we probed the roles of formin-induced F-actin elongation in cortex mechanics and architecture. Using a cortex-like actin meshwork (20 μm × 20 μm × 100 nm), we simulated RhoA-driven pulsed contraction by locally modulating the kinetics of Myosin II and F-actin elongation rates, based on experimental measurements (Fig. S4B). Specifically, to reproduce formin activity, we increased the elongation rate of a fraction of the barbed ends in the RhoA-activated region, resulting in rapid elongation of actin filaments for ~10 s, or ~12 μm (Fig. 6A, top row). We then locally turned on Myosin II activity in the RhoA-activated region for 15 s, and with a delay of ~5s to reproduce delayed Myosin II activation by RhoA (Movie S8-10, (Michaux et al. 2018)).

Using this tailored model of pulsed contraction, we then evaluated the impact of formin activation levels on network architecture and the deployment of forces generated by Myosin II. We observed that actin and myosin tended to contract toward the center of the activated region upon motor activation, peak, then relax towards a plateau upon Myosin II inactivation (Fig. 6B inset, Fig. S4C). Interestingly, the maximum levels of actomyosin contraction decreased with formin activation level (Fig. 6B, Fig. S4D). Meanwhile the sum of forces experienced by formin-elongated actin filaments increased with formin activation level (Fig. 6A(second row),C): long, formin-elongated actin filaments are cross-linked with many other short actin filaments, propagating the force generated by Myosin II farther in the network (Fig. S4E). We also observed that weaker local contraction and long-ranged force transmission in the network prevented the formation of contraction-induced actin aggregates separated from the rest of the network (Fig. 6A-B). At high formin activation levels, myosin and actin contraction were both inhibited, preventing the appearance of aggregates (Fig. 6B, Movie S10). In summary, as more actin filaments are elongated by formin, resistance to contraction increased, preventing local network collapse, while enabling force transmission farther in the cortex.

Finally, in order to explore the specific impact on contractility of network polarity (Fig. 5), we decided to probe the mechanics of network displaying inverted architectures. We therefore set out the numerical simulations to assemble actin networks with pointed ends emerging from the aster (by inverting formin polymerization dynamics, enhancing formin-mediated actin filament elongation at the pointed ends instead of the barbed end). Strikingly, we observed that myosin concentration was enhanced, but the overall actin network contraction was significantly reduced compared to the architecture previously simulated and observed *in vivo* (Fig. 6D-F). Importantly, the forces acting on formin-elongated actin filaments were severely reduced (Fig. 6G). Indeed, with this network architecture, myosin motors merely moved toward the pulse center, in a polarity sorting mechanism (Fig. 6D, (Wollrab et al. 2018)), rather than pulling actin filaments to generate forces. These simulations therefore showed that the rapid assembly—by RhoA-driven pulses of formins—of a polar network architecture drives efficient actomyosin network contractility, supporting the remodeling of cell shape during pulsed contractions.

Altogether, these simulations results show that actomyosin network architecture —largely governed by the kinetics of formin-mediated actin filament assembly— controls the mechanics of pulsed contraction, thereby playing a key role to support the cellular function of pulsed contractions.

DISCUSSION

Precise architectural organization of the actomyosin network is crucial for force generation at the cell cortex. How such architectures are assembled in a dynamic network with fast turnover stands as a multiple answer question during development where force deployment is critical for embryo morphogenesis. Here, we show that formins organize a polar actin network during cortical pulsed contraction, in a biochemical system primed for rapid assembly.

Our results are based on a detailed description of the kinetics of actin assembly by formins. We show that formins elongate actin filaments at 1.2 $\mu m \cdot s^{-1}$, or ~450 $monomers \cdot s^{-1}$. Formin-mediated actin filament elongation *in vitro* has been proposed to overcome diffusion limiting rates (Drenckhahn & Pollard 1986), likely by allowing formins to "explore" a larger volume to "find" monomers (Courtemanche 2018). Assuming that elongation rates scale with the concentration of actin (in our experimental configuration formins are not anchored and unlikely to be directly subject to mechanical forces), in a solvent-independent manner (i.e. independently of viscosity—affecting the diffusion rate, or crowding effects, where solutes in the cell do not affect elongation rates of CYK-1), then formin velocity may provide a good indicator of the modulations of free G-actin concentration in the cell. Recent work however has shown that under saturating conditions, at concentrations of actin > 200 μM formins velocity could actually prove robust to variations in G-Actin and profilin concentration (Funk et al. 2019)).

Our analyses further revealed that two distinct populations with specific mobilities are recruited at the cell surface: superdiffusive and subdiffusive formins. We attributed these populations to elongating and recruited formins populations, respectively. Upon binding with RhoA, cytoplasmic formins would bind to the cortex, diffuse locally, bind an available filament barbed-end and start elongation. Kinetically, therefore, we expected the observe the sequential recruitment of recruited **then** elongating formins, but instead observe the opposite sequence. To explore how this dynamics could emerge, we developed a biochemical model to see if we could reconcile our biochemical scheme with our observations. Our model showed that the two models come together under a specific set of assumptions, where barbed ends available for elongation are limiting, formins are recruited in large numbers and the conversion reaction is fast compared to other reactions in the system. And while our approach does not exclude other possible models—for example that formins are initially elongating, then somehow stall after some time— the set of assumptions we designed seems robust to variations in the biochemical activation scheme used. While this analysis of CYK-1 dynamics provides a new and interesting perspective on the dynamics of barbed ends at the cortex during activation by RhoA, we still lack tools to conclusively explore a collection of issues: when are barbed ends generated and by which mechanisms, what is the dynamics of capping during pulses, how many barbed ends are generated? We also do not have yet the resolution to explore the specific nature of the observed barbed ends: are formins capable of hetero-dimerizing or co-assembling with other factors (e.g. CapZ), and could this lead to the formation of inactive barbed ends, these other formins acting as competitive inhibitors for CYK-1 formin at the filament barbed end? Our results however clearly show that the actin in *C. elegans* is biochemically primed for rapid response. When the RhoA signaling cascade is activated, actin assembly is saturated by formins to drive an efficient and optimally rapid response to signaling cues.

Strikingly, the geometry of the assembled network is controlled by the geometry of the upstream signaling factors: local RhoA activation drives the assembly of a polar actin network. This suggests that, at this scale, actin architecture seems to be fundamentally driven by the spatial patterning of assembly kinetics, rather than by a reorganization of the actin cytoskeleton by the mechanical motor activity of Myosin II (Reymann et al. 2016).

The architecture of the assembled structure is well tuned for actomyosin contractility, with Myosin II recruited at the center of the prospective pulsed contraction (Fig. S2), while actin is assembled in a polar aster network, with barbed ends pointing outwards of the assembled architecture. Our numerical simulations show that, while actomyosin networks can generate tension in the absence of a specific network architecture, actomyosin networks perform differently depending on their organization and the contractile efficiency of actomyosin network remains functionally linked to their geometry. Therefore, the actin assembly transduction machinery downstream of RhoA converts a chemical RhoA gradient into a polar actin network architecture, with a structure well adapted to the contractile function of actomyosin pulses in morphogenesis.

With precisely timed cell cycles, similar in duration to the ones in Drosophila syncytial embryo, lasting ~10', *C. elegans* embryonic early development cell cycles unfold very fast (Brauchle et al. 2003)—compared to other early embryos, for instance in mouse embryos early cell cycles last about 20 h (Yamagata & FitzHarris 2013), sea urchin 150 min (Chassé et al. 2016) or even ascidians (~30 min) (Dumollard et al. 2013). In *C. elegans*, the 10 min cycles are divide roughly equally, into ~5 min for mitosis and 5 min interphase with cortical pulses. As a consequence, cell polarity, compartmentalization, and cell shape changes are heavily constrained in time. An actin network primed for fast assembly, together with the polar architecture of actomyosin pulsed contractions, may set the stage for rapid and efficient contractions and cell shape changes. During gastrulation, this very same organization may thus drive a fast apical constriction, and a subsequent timely internalization of endodermal cells.

Actomyosin network contractility is a key conserved feature of eukaryotic cells. Biochemically, the contractile structure assembled in *C. elegans* is very similar to the nodes assembled in fission yeast during contractile ring assembly: formin actin-filament elongators, Myosin II motors and actin cables (Vavylonis et al. 2008; Munro et al. 2004). However, several key differences separate the two contractile modules. Structurally, the size of the biological systems diverge strongly. At the level of the cell, a fission yeast cell spans ~14 µm long and 3 µm wide during cell division, against 50 µm in length and 30 µm in width for the *C. elegans* embryo (Fig 7A,B). The two contractile macromolecular assemblies are also very different: fission yeast nodes are <600nm wide and initially distant by <1 µm on average, while *C. elegans* actomyosin pulses are 3-5 µm wide and separated by 5-10µm (Fig. S2, (Michaux et al. 2018; Naganathan et al. 2014)). The two systems are also biochemically distinct. The fission yeast formin Cdc12p elongates actin filaments with high processivity (k_{off} ~7.10^{-5} s^{-1}) but slow speed (10.6 monomers·s^{-1} at 1.5 µM [Actin], 4 µM [SpPRF], fission yeast profilin), while the *C. elegans* formin CYK-1 elongates actin filaments with a lower processivity (k_{off} ~4.10^{-3} s^{-1}) but much higher speed (63.2 monomers·s^{-1} at 1.5 µM [Actin] and 4 µM [PFN-1], the *C. elegans* profilin). In the *Search-Pull-Capture-Release* model, actin filament elongation takes place from a static barbed end (Pollard & Wu 2010; Vavylonis et al. 2008). However, in *C. elegans*, a similar mechanism would result in filament buckling or stalling in actin filament elongation. To drive the same functional output—contraction—the molecular homologs assemble a structurally distinct, geometrically opposite, architecture which is tuned to the scale of the biological system, revealing here an interesting instance of the tinkering of evolution.

ACKNOWLEDGEMENTS

We thank Anne-Cecile Reymann, Stephan Grill, Ronen Zaidel-Bar and Geraldine Seydoux for worm strains. We thank Marie Breau and Michel Labouesse for critical reading of the manuscript, Michel Labouesse, Marie Breau and members of the Labouesse laboratory for valuable discussions, as well as members of the

Robin laboratory for discussions and technical assistance. We thank the IBPS imaging facility, and in particular Susanne Bolte, and France Lam, for excellent technical support.
This work used the Extreme Science and Engineering Discovery Environment (XSEDE, (Towns et al. 2014)), which is supported by National Science Foundation grant number ACI-1548562. The computations were conducted on the Comet supercomputer, which is supported by NSF award number ACI-1341698, at the San Diego Supercomputing Center (SDSC).
This work was supported by the ATIP/Avenir, ERC-Tremplin programs (to F.B. Robin) and Marie Curie Program MSCA-IF (661451).
The authors declare no competing financial interests.

MATERIAL AND METHODS

C. elegans culture and strains

See attached Supplementary Table 3.

RNA interference

We performed RNAi using the feeding method as previously described (Timmons & Fire 1998). Bacteria targeting *perm-1* and *gfp* were obtained from the Kamath feeding library (Kamath et al. 2003).

The L4417 plasmid targeting *perm-1* and the entire GFP sequence (generated by the Fire lab and available at http://www.addgene.org/1649/) were transformed into HT115(DE3) bacteria. Bacterial cultures for feeding were grown for 10–12 h and then induced on standard nematode nutritional growth media plates containing 50 µg/ml ampicillin and 1 mM IPTG for 16–24 h at 20–25 °C, then stored at 4 °C. For *perm-1* RNAi, L4 stage larvae were placed on feeding plates for 16–24 h before imaging.

Imaging conditions

We dissected gravid hermaphrodites and mounted one-cell embryos under #1.5 22-mm square coverslips in 2.5 µl of water or standard Egg Salts buffer (118 mM NaCl, 40 mM KCl, 3.4 mM CaCl2, 3.4 mM MgCl2, 5 mM HEPES, pH 7.4) containing ~500 uniformly sized polystyrene beads (15.6 ± 0.03 µm diameter, Bangs labs, #NT29N) to achieve uniform compression of the embryo surface across experiments (Robin et al. 2014).

We performed near-TIRF imaging at 19–21°C on an inverted Nikon Ti-E N-Storm microscope, equipped with motorized TIRF illuminator, Apo TIRF 100x Oil-immersion DIC N2 objective (Nikon) with 1.49– numerical aperture (NA), and PFS-S Perfect Focus unit (Nikon). Laser illumination at 488 nm and 561 nm from 300 mW solid-state sapphire laser (Coherent) was set at 30 % of maximal power and delivered by fiber

optics to the TIRF illuminator. Images were magnified by a 1.5× lens and collected on an Andor iXon Ultra DU-897 EMCCD camera, yielding a pixel size of 107 nm.

We controlled laser illumination angle and intensity and image acquisition using NIS Elements software (Nikon). For all experiments, we set the laser illumination angle to a standard value that was chosen empirically to approximately maximize signal intensity while maintaining even illumination across the field of view. For all SPT experiments, we collected images in streaming mode with continuous illumination at 15–60% laser intensity (100% ≈ 1.6 $\mu W \cdot \mu m^{-2}$) with 50 ms exposures to achieve frame rates of 20 frames/s.

Tuning GFP levels to achieve single-molecule densities

The quasi-steady-state densities observed during imaging depend on the initial (unobserved) densities, photobleaching rates and the intrinsic exchange kinetics of the target molecule (see main text and below). We thus determined the appropriate initial densities empirically for a given strain and experiment. We achieved these initial densities by using two methods as previously described (Robin et al. 2014). For SWG282 (CYK-1::GFP over-expression), we used RNAi directed against the GFP sequence to deplete the pool of GFP-tagged proteins. RNAi against maternal proteins typically yields an exponential decrease in the maternal protein with time of exposure (Oegema & Hyman 2006). We controlled the degree of depletion by synchronizing larvae and sampling embryos at different times after the initiation of feeding to identify times at which discrete diffraction-limited speckles were observed at the cell surface. The optimal time was relatively consistent across experiments for a given strain and varied from 12–36 h depending on transgene expression levels and relative abundance at the cell surface vs. cytoplasm. To fine-tune density levels, we used brief (<10 s) pulses in epi-illumination mode at high laser power until adequate density was reached (Robin et al. 2014).

Drug perfusion experiments

For exposing embryos to 10 μM of Latrunculin A (Sigma L5163) or to 10 μg/mL of Nocodazole (Sigma M1404) in Egg Salts buffer during image acquisition, we used wider coverslips (22 mm x 30 mm) so that a perfusion chamber is formed between coverslip and slide, and the coverslip passes about 3 mm from the side of the slide. On the inverted microscope, this outer side of coverslip helps as support to able to deposit the perfusion volume as a drop (4 μL) while imaging. The drug solution likewise perfused by capillarity between slide and coverslip exposes the embryos to the drug instantly. The perfusion timepoint is visible in the corresponding movies as a brief brightfield illumination and used as a reference during analysis.

Assessing potential adversary effects of compression, laser exposure and GFP fusion

We followed experimental procedures as previously tested (Robin et al. 2014). Using photobleaching to reduce GFP-tagged protein levels from full to single-molecule levels in one step resulted in arrested development. However, the laser exposure required to fine-tune densities by photobleaching, or that occurring during single-molecule imaging, did not cause embryos to arrest. In all of our single-molecule

imaging experiments, we verified that embryos initiated and completed cytokinesis with normal timing or, in the case of nocodazole treated embryos multiple nuclei were present in the cell. To confirm that no adverse effects on population dynamics were associated with GFP fusion in the CYK-1::GFP CRISPR strain, we also used a CYK-1::mNeon CRISPR fusion to confirm our results (data not shown, strain available upon request).

Single-molecule detection and tracking

We used a publicly available Matlab implementation of the Crocker-Grier algorithm for single-particle detection and tracking (Pelletier et al. 2009; Crocker & Grier 1996). In brief, the Crocker-Grier method localizes particles to subpixel resolution in individual frames by fitting local intensity peaks to a Gaussian point spread function. The two key detection parameters—peak and mean intensity of the candidate particles—are adjusted empirically for given imaging conditions using a graphical user interface. The particles are then linked frame to frame by minimizing the global displacement across all particles, given a user-chosen cutoff value for maximum particle displacement. A second parameter, the gap size, allows the possibility of ignoring 'gaps' in a trajectory due to transient failures to detect particles. These transient failures occur mainly because motion blur causes the particle intensity to fall transiently below the detection threshold.

To estimate actin concentration, we assumed that elongation rates scale linearly with actin concentration, and used previously measured elongation rates of 60 monomers·s^{-1}, at 1.5 μM ATP-Actin (Neidt, Scott, et al. 2008; Neidt, Skau, et al. 2008).

To infer filament length, we made the following assumptions:

1. actin monomers display simple mono-exponential half-life at the cortex,
2. actin monomers display a half-life measured by tracking and smPReSS of 0.08-0.15 s (Robin et al. 2014; Michaux et al. 2018),
3. elongating formins display simple mono-exponential half-life at the filament barbed end,
4. elongating formins display a half-life measured by smPReSS of ~0.11 s (Fig. 2D).

Under these assumptions, we consider solely actin filaments assembled by formins. From the perspective of an actin monomer at the time of disassembly, two options are possible:

(1) the monomer disassembles while the formin is still elongating,

(2) the formin unbinds and elongation stops before the monomer disassembles.

The "effective" elongation time of the formin on the filament is then the minimum value between (1) and (2). If actin lifetime and formin mediated actin-filament elongation time have independent exponential distributions of parameters $1/\tau_{actin}$ and $1/\tau_{formin}$, then the minimum between the two values also has exponential distribution of parameter $1/\tau_{filament} = 1/\tau_{actin} + 1/\tau_{formin}$. Under these conditions, the length of the elongated filament is:

$$L_{filament} = V_{elongation} \times \tau_{filament} = \frac{V_{elongation}}{\frac{1}{\tau_{actin}} + \frac{1}{\tau_{formin}}}$$

Formin Speed measurement analysis

We performed single-molecule imaging as described previously. We mounted the embryos between glass slides with squares wells of 20 µm thick Epoxy and #1.5 coverslips (170 µm thick) in 2.5 µL of 0.22 µm filtered water with 15.4 µm polystyrene beads. We imaged single molecules using 50% of 90mW of 488 nm laser, 50 ms of exposure, no delay between frames, using Photometrics 95B prime 22 mm sCMOS camera. Laser angle was set to 65°. Room temperature maintained between 19 and 20.5 °C. After acquisition, we averaged two consecutive frames, in order to achieve 10 frames per second using ImageJ software (NIH Image, Bethesda, MD). We used Matlab implementation of the Crocker-Grier algorithm (Crocker & Grier 1996) by the Kilfoil lab for single-particle tracking. We selected manually a ROI to exclude tracks from residual particles outside the cell for each stage: whole embryo for one-cell stage, anterior (AB) cell for two-cell stage, posterior AB daughter cell (ABp) for four-cell stage. Each stage was separated into three phases based on observed cortical dynamics: interphase (pulsed contractions at the cortex); mitosis (cortex "stable" with no identifiable pulsed contractions) ; and cytokinesis (visualized by cleavage furrow assembly).
Subsequent image analysis was performed in Matlab. We selected the trajectories based on their anomalous diffusion coefficient *D* and scaling exponents α. Tracks were classified as subdiffusive and superdiffusive, and selected specifically superdiffusive trajectories. In order to calculate the velocity only during elongation of actin filaments, we performed a second selection to exclude tracks displaying multiple behaviors during their lifetime (due to switches between subdiffusive and superdiffusive) and retained tracks displaying exclusively superdiffusive behavior. Finally, we screened individual trajectories manually to retain tracks that were closer to a line to avoid skewing our estimates of particle speed.

Statistical analysis

23 to 40 tracks per embryo were selected. Normal distributions were verified. Two-sample Student tests (t-tests) were performed to measure the significance of the difference in speed between each stage and phase. *** means $p<0.001$, ** means $p<0.01$, ns: non-significant.

Two-color imaging microscopy

We performed single-molecule imaging as described previously. Acquisitions were performed with the Andor iXon 897 EMCCD camera. We imaged at 30% of 90 mW for 488 nm and 561 nm, with 50 ms exposure and no delay between frames (100 ms between two successive frames of the same channel). After acquisition, we averaged five consecutive frames, in order to achieve 2 frames per second using ImageJ. Pulsed contractions were selected manually and data from the intensity profile of a line drawn through the pulse is collected in a single frame. 3 pulses per embryo in 6 embryos (total of 18) were analyzed in Matlab (R2018a version). Intensities are smoothened and normalized with maximum being 1 and immediately preceding minimum being 0. Data for myosin (NMY-2::mKate2, in red channel) is aligned at 0,98% of the maximum and this alignment is propagated to the corresponding data in the green channel.

Tracking of individual pulses of CYK-1::GFP

We used a semi-automatic approach to identify and follow CYK-1 pulses during the two-cell stage interphase, in the anterior blastomere. We manually identified isolated pulses and drew a ROI over the surface of each pulse (about 6 μm in diameter), at about 5 frames before maximum contraction of the area can be detected. The ROI was then automatically propagated in time before and after t0, and also we designed a Matlab script (A-STAR Methods PipelineSimPulse) allowing to adapt automatically the surface of the ROI in order to include the full trajectory of particles appearing within the ROI. To eliminate drift of the ROI associated with cortical flows, independently of CYK-1 mobility within the pulse area, we used a dedrifting routine on each particle based on the displacement of its neighbors. This was important for mobility analysis as particles registered with a global drift—and therefore displaying a persistent directional motion—would otherwise register as superdiffusive.

Single particles tracking and pulse analysis pipeline in Matlab

We designed an analysis pipeline based on Matlab scripts (A-STAR Methods PipelineSimPulse, code available upon request) that includes CYK-1::GFP particles detection and tracking, reduction to the surface of the embryo and the AB cell, de-drifting of the trajectories and MSD analysis for segregation in different mobility populations (mainly superdiffusive CYK-1 vs. subdiffusive CYK-1). The further step is to intersect the matrix of all these trajectories with the specific ROI of each pulse. The final step is to normalize and align all the pulses (number of particles in time) with respect to their maximum and the minimum number of particles before, then to measure the angle orientation of every vector formed by the trajectories with respect to the center of the ROI.

Numerical simulation of formin local recruitment

We used MATLAB to compute a 2D simulation of local formin activation and actin filament elongation. Pulses were spatially and temporally distributed in an embryo's shaped mask in a random manner. Pulse were defined by a fixed 5x5 μm window (100x100 pixels) and a 20 seconds time window (400 frames). Pulses could not overlap in time and space. Using experimental data, density of formin recruitment, position around the pulse center and kinetics of recruitment could be computed in each pulse. We added 0.01 formins recruitment /μm^2/frame all over the embryo mask (independent of pulses generation) corresponding to the formin recruitment rate observed in areas away from a pulse. According to experimental data, 80% of the formin recruited were assigned to be subdiffusive while 20% of them were assigned superdiffusive. Since we aimed to study superdiffusive particles, we approximate sub-diffusive and diffusive particles as a unique population of immobile particles. Each position of superdiffusive tracks were computed using the following sequence. The length of the step R_n was picked in a normal distribution whose mean is 1.23 μm/s and standard deviation is 0.30 μm/s (values extracted from experimental data).

The orientation θ_n of the step was calculated assuming a persistent length P_L of 15μm (close to the actin persistence length, (Howard 2001)).

$$\theta_{n+1} = \theta_n + X \times \arccos\left(e^{-\frac{R}{2 \cdot P_L}}\right),\ with\ X \sim \mathcal{N}(0,1)$$

Length of track were assigned using the distribution of track length for sub-diffusive and super-diffusive particles, respectively. Simulated data were analyzed using the same methods as experimental data.

Overview of the computational model of actomyosin mechanics

For simulations in this study, we used a well-established agent-based model of actomyosin networks based on the Langevin equation (J. Li et al. 2017; Jung et al. 2015; T. Kim et al. 2009; Mak et al. 2016). The detailed descriptions about the model and all parameters used in the model are explained in Supplementary Text and Table S1. In the model, actin filament (F-actin), motor, and ACP are coarse-grained using cylindrical segments (Fig. S4A). The motions of all the cylindrical segments are governed by the Langevin equation for Brownian dynamics. Deterministic forces in the Langevin equation include bending and extensional forces that maintain equilibrium angles formed by segments and the equilibrium lengths of segments, respectively, as well as a repulsive force acting between neighboring pairs of segments for considering volume-exclusion effects.

The formation of F-actin is initiated by a nucleation event, followed by polymerization at the barbed end and depolymerization at the pointed end. ACPs bind to F-actin without preference for cross-linking angles at a constant rate and also unbind from F-actin at a force-dependent rate determined by Bell's law (Bell 1978). Each arm of motors binds to F-actin at a constant rate, and it then walks toward the barbed end of F-actin or unbinds from F-actin at force-dependent rates determined by the parallel cluster model (Erdmann et al. 2013; Erdmann & Schwarz 2012). For all simulations in this study, we used a thin computational domain (20×20×0.1 μm) with periodic boundary conditions only in x and y directions (Fig. S4B). In z direction, the boundaries of the domain exert repulsive forces on elements that moved beyond the boundaries. At the beginning of each simulation, a thin actin network is formed via self-assembly of F-actin and ACP.

For implementing RhoA activation, the domain is divided into 16 subdomains (4×4 in x and y directions). Every 30 s, one of the subdomains is randomly selected and then activated. In the activated subdomain, a fraction of the barbed ends of F-actins are randomly chosen and then undergo faster polymerization by a factor, ϱ_f, for the duration of τ_f. With the reference values of ϱ_f = 10 and τ_f = 10 s, F-actins are elongated by ~10 μm on average. After the time delay of d_M, motors in the activated subdomain are allowed to self-assemble into thick filament structures for the duration of τ_M. The reference values of d_M and τ_M are 5 s and 15 s, respectively. These active motors in the form of thick filaments can contract the part of the network in the activated subdomain. Once they become inactive after τ_M, the motors are disassembled into monomers that cannot bind to F-actin.

BIBLIOGRAPHY

Agarwal, P. & Zaidel-Bar, R., 2019. Principles of Actomyosin Regulation In Vivo. *Trends in Cell Biology*, 29(2), pp.150–163.

Bell, G.I., 1978. Models for the specific adhesion of cells to cells. *Science*, 200(4342), pp.618–627.

Bement, W.M. et al., 2015. Activator-inhibitor coupling between Rho signalling and actin assembly makes the cell cortex an excitable medium. *Nature Cell Biology*, 17(11), pp.1471–1483.

Bement, W.M., Benink, H.A. & Dassow, von, G., 2005. A microtubule-dependent zone of active RhoA during cleavage plane specification. *The Journal of Cell Biology*, 170(1), pp.91–101.

Benink, H.A., 2005. Concentric zones of active RhoA and Cdc42 around single cell wounds. *The Journal of Cell Biology*, 168(3), pp.429–439.

Bidone, T.C. et al., 2017. Morphological Transformation and Force Generation of Active Cytoskeletal Networks. A. R. Asthagiri, ed. *PLoS computational biology*, 13(1), p.e1005277.

Blanchoin, L. et al., 2014. Actin dynamics, architecture, and mechanics in cell motility. *Physiological Reviews*, 94(1), pp.235–263.

Brauchle, M., Baumer, K. & Gönczy, P., 2003. Differential activation of the DNA replication checkpoint contributes to asynchrony of cell division in C. elegans embryos. *Current Biology*, 13(10), pp.819–827.

Burkel, B.M. et al., 2012. A Rho GTPase signal treadmill backs a contractile array. *Developmental Cell*, 23(2), pp.384–396.

Carvalho, A. et al., 2011. Acute drug treatment in the early C. elegans embryo. B. Lehner, ed. *PLoS ONE*, 6(9), p.e24656.

Chassé, H. et al., 2016. Cyclin B Translation Depends on mTOR Activity after Fertilization in Sea Urchin Embryos. *PLoS ONE*, 11(3), p.e0150318.

Coravos, J.S. & Martin, A.C., 2016. Apical Sarcomere-like Actomyosin Contracts Nonmuscle Drosophila Epithelial Cells. *Developmental Cell*, 39(3), pp.346–358.

Courtemanche, N., 2018. Mechanisms of formin-mediated actin assembly and dynamics. *Biophysical reviews*, 10(6), pp.1553–1569.

Courtemanche, N. et al., 2013. Tension modulates actin filament polymerization mediated by formin and profilin. *Proceedings of the National Academy of Sciences of the United States of America*, 110(24), pp.9752–9757.

Crocker, J.C. & Grier, D.G., 1996. Methods of digital video microscopy for colloidal studies. *Journal of Colloid and Interface Science*, 179(1), pp.298–310.

Drenckhahn, D. & Pollard, T.D., 1986. Elongation of actin filaments is a diffusion-limited reaction at the barbed end and is accelerated by inert macromolecules. *The Journal of biological chemistry*, 261(27), pp.12754–12758.

Dumollard, R. et al., 2013. Beta-catenin patterns the cell cycle during maternal-to-zygotic transition in urochordate embryos. *Developmental Biology*, 384(2), pp.331–342.

Erdmann, T. & Schwarz, U.S., 2012. Stochastic force generation by small ensembles of myosin II motors. *Physical Review Letters*, 108(18), p.188101.

Erdmann, T., Albert, P.J. & Schwarz, U.S., 2013. Stochastic dynamics of small ensembles of non-processive molecular motors: the parallel cluster model. *The Journal of Chemical Physics*, 139(17), p.175104.

Funk, J. et al., 2019. Profilin and formin constitute a pacemaker system for robust actin filament growth. *eLife*, 8, p.1826.

Galkin, V.E. et al., 2011. Remodeling of actin filaments by ADF/cofilin proteins. *Proceedings of the National Academy of Sciences of the United States of America*, 108(51), pp.20568–20572.

Galkin, V.E. et al., 2010. Structural polymorphism in Factin. *Nature Structural & Molecular Biology*, 17(11), pp.1318–1323.

He, L. et al., 2010. Tissue elongation requires oscillating contractions of a basal actomyosin network. *Nature Cell Biology*, 12(12), pp.1133–1142.

Higashida, C., 2004. Actin Polymerization-Driven Molecular Movement of mDia1 in Living Cells. *Science*, 303(5666), pp.2007–2010.

Higgs, H.N., 2005. Formin proteins: a domain-based approach. *Trends in biochemical sciences*, 30(6), pp.342–353.

Howard, J., 2001. *Mechanics of motor proteins and the cytoskeleton,* Sinauer Ed, pp. 110–111.

Jégou, A., Carlier, M.-F. & Romet-Lemonne, G., 2013. Formin mDia1 senses and generates mechanical forces on actin filaments. *Nature Communications*, 4, p.1883.

Jung, W. et al., 2015. F-actin cross-linking enhances the stability of force generation in disordered actomyosin networks. *Comp. Part. Mech.*, 2, pp.317-327.

Kamath, R.S. et al., 2003. Systematic functional analysis of the Caenorhabditis elegans genome using RNAi. *Nature*, 421(6920), pp.231–237.

Kim, H.Y. & Davidson, L.A., 2011. Punctuated actin contractions during convergent extension and their permissive regulation by the non-canonical Wnt-signaling pathway. *Journal of Cell Science*, 124(4), pp.635–646.

Kim, T., 2015. Determinants of contractile forces generated in disorganized actomyosin bundles. *Biomechanics and Modeling in Mechanobiology*, 14(2), pp.345–355.

Kim, T. et al., 2009. Computational analysis of viscoelastic properties of crosslinked actin networks. D. A. Fletcher, ed. *PLoS computational biology*, 5(7), p.e1000439.

Koenderink, G.H. & Paluch, E.K., 2018. Architecture shapes contractility in actomyosin networks. *Current Opinion in Cell Biology*, 50, pp.79–85.

Kreten, F.H. et al., 2018. Active bundles of polar and bipolar filaments. *Physical Review E*, 98(1-1), p.012413.

Kubota, H. et al., 2017. Biphasic Effect of Profilin Impacts the Formin mDia1 Force-Sensing Mechanism in Actin Polymerization. *Biophysj*, 113(2), pp.461–471.

Lecuit, T. & Lenne, P.-F., 2007. Cell surface mechanics and the control of cell shape, tissue patterns and morphogenesis. *Nature Reviews Molecular Cell Biology*, 8(8), pp.633–644.

Lenz, M., Gardel, M.L. & Dinner, A.R., 2012. Requirements for contractility in disordered cytoskeletal bundles. *New Journal of Physics*, 14(3), p.033037.

Lenz, M., Thoresen, T., et al., 2012. Contractile Units in Disordered Actomyosin Bundles Arise from F-Actin Buckling. *Physical Review Letters*, 108(23), p.238107.

Li, F. & Higgs, H.N., 2005. Dissecting requirements for auto-inhibition of actin nucleation by the formin, mDia1. *The Journal of biological chemistry*, 280(8), pp.6986–6992.

Li, F. & Higgs, H.N., 2003. The mouse Formin mDia1 is a potent actin nucleation factor regulated by autoinhibition. *Current Biology*, 13(15), pp.1335–1340.

Li, J. et al., 2017. Buckling-induced F-actin fragmentation modulates the contraction of active cytoskeletal networks. *Soft Matter*, 13(17), pp.3213–3220.

Linsmeier, I. et al., 2016. Disordered actomyosin networks are sufficient to produce cooperative and telescopic contractility. *Nature Communications*, 7, p.12615.

Maddox, A.S. et al., 2005. Distinct roles for two C. elegans anillins in the gonad and early embryo. *Development*, 132(12), pp.2837–2848.

Maître, J.-L. et al., 2015. Pulsatile cell-autonomous contractility drives compaction in the mouse embryo. *Nature Cell Biology*, 17(7), pp.849–855.

Mak, M. et al., 2016. Interplay of active processes modulates tension and drives phase transition in self-renewing, motor-driven cytoskeletal networks. *Nature Communications*, 7, p.10323.

Martin, A.C., Kaschube, M. & Wieschaus, E.F., 2009. Pulsed contractions of an actin-myosin network drive apical constriction. *Nature*, 457(7228), pp.495–499.

Mayer, M. et al., 2010. Anisotropies in cortical tension reveal the physical basis of polarizing cortical flows. *Nature*, 467(7315), pp.1–7.

Mi-Mi, L. et al., 2012. Z-line formins promote contractile lattice growth and maintenance in striated muscles of C. elegans. *The Journal of Cell Biology*, 198(1), pp.87–102.

Michaux, J.B. et al., 2018. Excitable RhoA dynamics drive pulsed contractions in the early C. elegansembryo. *The Journal of Cell Biology*, 217(12), pp.4230–4252.

Miller, A.L. & Bement, W.M., 2009. Regulation of cytokinesis by Rho GTPase flux. *Nature Cell Biology*, 11(1), pp.71–77.

Munjal, A. & Lecuit, T., 2014. Actomyosin networks and tissue morphogenesis. *Development*, 141(9), pp.1789–1793.

Munro, E., Nance, J. & Priess, J.R., 2004. Cortical flows powered by asymmetrical contraction transport PAR proteins to establish and maintain anterior-posterior polarity in the early C. elegans embryo. *Developmental Cell*, 7(3), pp.413–424.

Naganathan, S.R. et al., 2014. Active torque generation by the actomyosin cell cortex drives left-right symmetry breaking. J. Ferrell, ed. *eLife*, 3, p.e04165.

Naganathan, S.R. et al., 2018. Morphogenetic degeneracies in the actomyosin cortex. *eLife*, 7, p.354.

Nance, J., 2003. C. elegans PAR-3 and PAR-6 are required for apicobasal asymmetries associated with cell adhesion and gastrulation. *Development*, 130(22), pp.5339–5350.

Nance, J. & Priess, J.R., 2002. Cell polarity and gastrulation in C. elegans. *Development*, 129(2), pp.387–397.

Neidt, E.M., Scott, B.J. & Kovar, D.R., 2008. Formin Differentially Utilizes Profilin Isoforms to Rapidly Assemble Actin Filaments. *The Journal of biological chemistry*, 284(1), pp.673–684.

Neidt, E.M., Skau, C.T. & Kovar, D.R., 2008. The cytokinesis formins from the nematode worm and fission yeast differentially mediate actin filament assembly. *The Journal of biological chemistry*, 283(35), pp.23872–23883.

Nishikawa, M. et al., 2017. Controlling contractile instabilities in the actomyosin cortex. *eLife*, 6, p.058101.

Oegema, K. & Hyman, A.A., 2006. Cell division. *WormBook*, pp.1–40.

Olson, S.K. et al., 2012. Hierarchical assembly of the eggshell and permeability barrier in C. elegans. *The Journal of Cell Biology*, 198(4), pp.731–748.

Pelletier, V. et al., 2009. Microrheology of Microtubule Solutions and Actin-Microtubule Composite Networks. *Physical Review Letters*, 102(18), p.188303.

Piekny, A., Werner, M. & Glotzer, M., 2005. Cytokinesis: welcome to the Rho zone. *Trends in Cell Biology*, 15(12), pp.651–658.

Pollard, T.D. & Wu, J.-Q., 2010. Understanding cytokinesis: lessons from fission yeast. *Nature Reviews Molecular Cell Biology*, 11(2), pp.149–155.

Pruyne, D. et al., 2002. Role of Formins in Actin Assembly: Nucleation and Barbed-End Association. *Science*, 297(5581), pp.612–615.

Rauzi, M., Lenne, P.-F. & Lecuit, T., 2010. Planar polarized actomyosin contractile flows control epithelial junction remodelling. *Nature*, 468(7327), pp.1110–1114.

Reymann, A.-C. et al., 2016. Cortical flow aligns actin filaments to form a furrow. *eLife*, 5, p.e17807.

Robin, F.B. et al., 2014. Single-molecule analysis of cell surface dynamics in Caenorhabditis elegans embryos. *Nature Methods*, 11(6), pp.677–682.

Roh-Johnson, M. et al., 2012. Triggering a cell shape change by exploiting preexisting actomyosin contractions. *Science*, 335(6073), pp.1232–1235.

Shekhar, S. et al., 2015. Formin and capping protein together embrace the actin filament in a ménage à trois. *Nature Communications*, 6(1), pp.1–12.

Swan, K.A. et al., 1998. cyk-1: a C. elegans FH gene required for a late step in embryonic cytokinesis. *Journal of Cell Science*, 111 (Pt 14), pp.2017–2027.

Timmons, L. & Fire, A., 1998. Specific interference by ingested dsRNA. *Nature*, 395(6705), pp.854–854.

Towns, J. et al., 2014. XSEDE: Accelerating Scientific Discovery, Computing in Science & Engineering, vol.16, no. 5, pp. 62-74.

Vavylonis, D. et al., 2008. Assembly Mechanism of the Contractile Ring for Cytokinesis by Fission Yeast. *Science*, 319(5859), pp.97–100.

Wollrab, V. et al., 2018. Polarity sorting drives remodeling of actin-myosin networks. *Journal of Cell Science*, 132(4), p.jcs219717.

Yamagata, K. & FitzHarris, G., 2013. 4D imaging reveals a shift in chromosome segregation dynamics during mouse pre-implantation development. *Cell cycle*, 12(1), pp.157–165.

Yu, Q. et al., 2018. Balance between Force Generation and Relaxation Leads to Pulsed Contraction of Actomyosin Networks. *Biophysical Journal*, 115(10), pp.2003–2013.

Figure 1

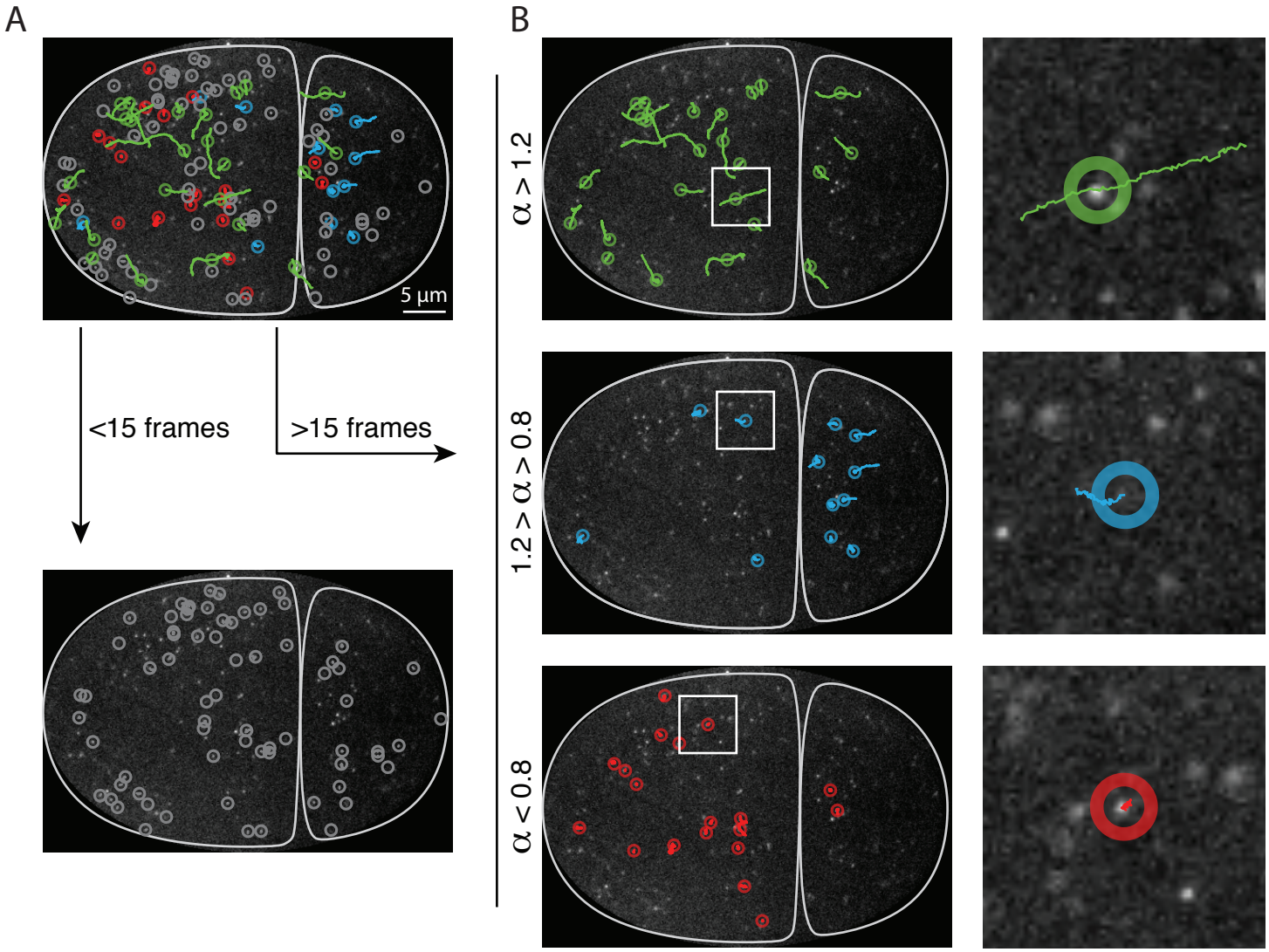
A
B
5 µm
<15 frames
>15 frames
α > 1.2
1.2 > α > 0.8
α < 0.8

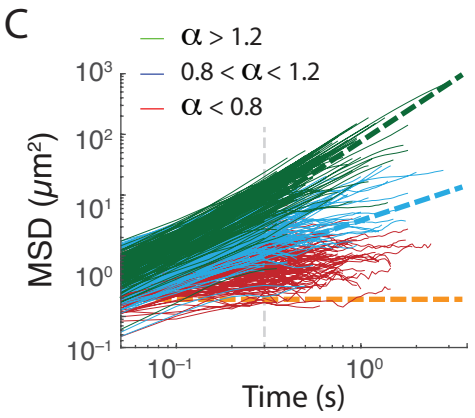
C
α > 1.2
0.8 < α < 1.2
α < 0.8
MSD (µm²)
Time (s)

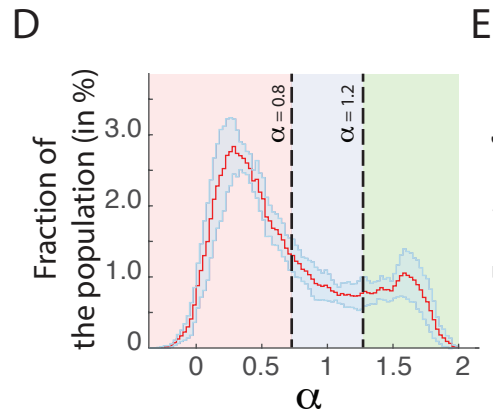
D
Fraction of the population (in %)
α = 0.8
α = 1.2
α

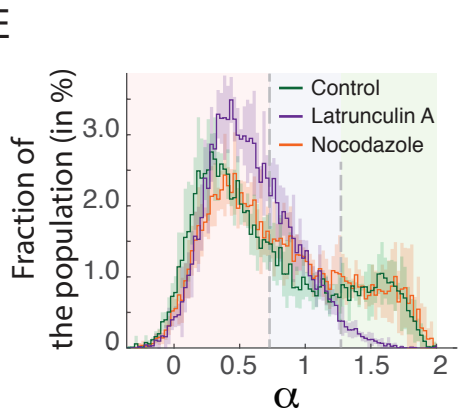
E
Fraction of the population (in %)
Control
Latrunculin A
Nocodazole
α

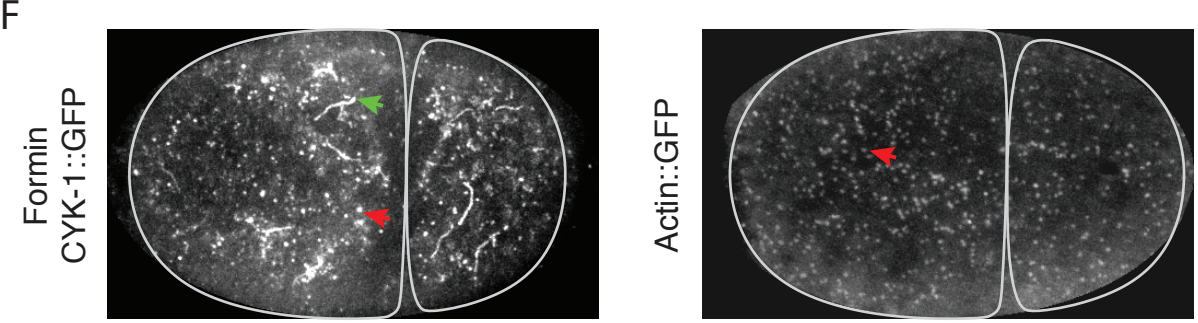
F
Formin CYK-1::GFP
Actin::GFP

Figure 1. Anomalous diffusion of individual formin molecules identifies a subpopulation of actin-elongating formins. (A) Single-molecule imaging and tracking of formins fused with GFP (CYK-1::GFP) shows individual behaviors ranging from superdiffusive (green) to diffusive (blue) to subdiffusive (red). **(B)** Mean-square displacement against lag time. Slope curve reports on the anomalous diffusion exponent. Particles with anomalous diffusion exponent larger than 1.2 in green, between 0.8 and 1.2 in blue, and smaller than 0.8 in red. Pure superdiffusive corresponds to $\alpha = 2$ (green dashed), pure diffusive $\alpha = 1$ (blue dashed), and immobile (orange dashed). **(C)** Distribution of the fraction of particles displaying a given anomalous diffusion exponent in 5 movies (average +/- SD). Background shows the domains corresponding to the classification used here. Two peaks seem to emerge, centered at $\alpha = 0.3$ and $\alpha = 1.6$. **(D)** Detected mobilities correspond to different classes of behaviors. Superdiffusive display a characteristic ballistic motion (green, top panel), while subdiffusive particles appear immobile in the cortex (red, bottom). **(E)** Compared to control (green curve), the superdiffusive population is absent in embryos treated with Latrunculin A (purple), but not Nocodazole (orange). More than 2000 tracks analyzed per embryo for, with >5 embryos per condition presented. **(F)** Projection over 5s (100 consecutive frames) of formin CYK-1::GFP (left) and Actin::GFP (right) speckles, showing subdiffusive speckles (red arrow) and superdiffusive trails (green arrow). Actin::GFP does not display superdiffusive trails.

Figure 2

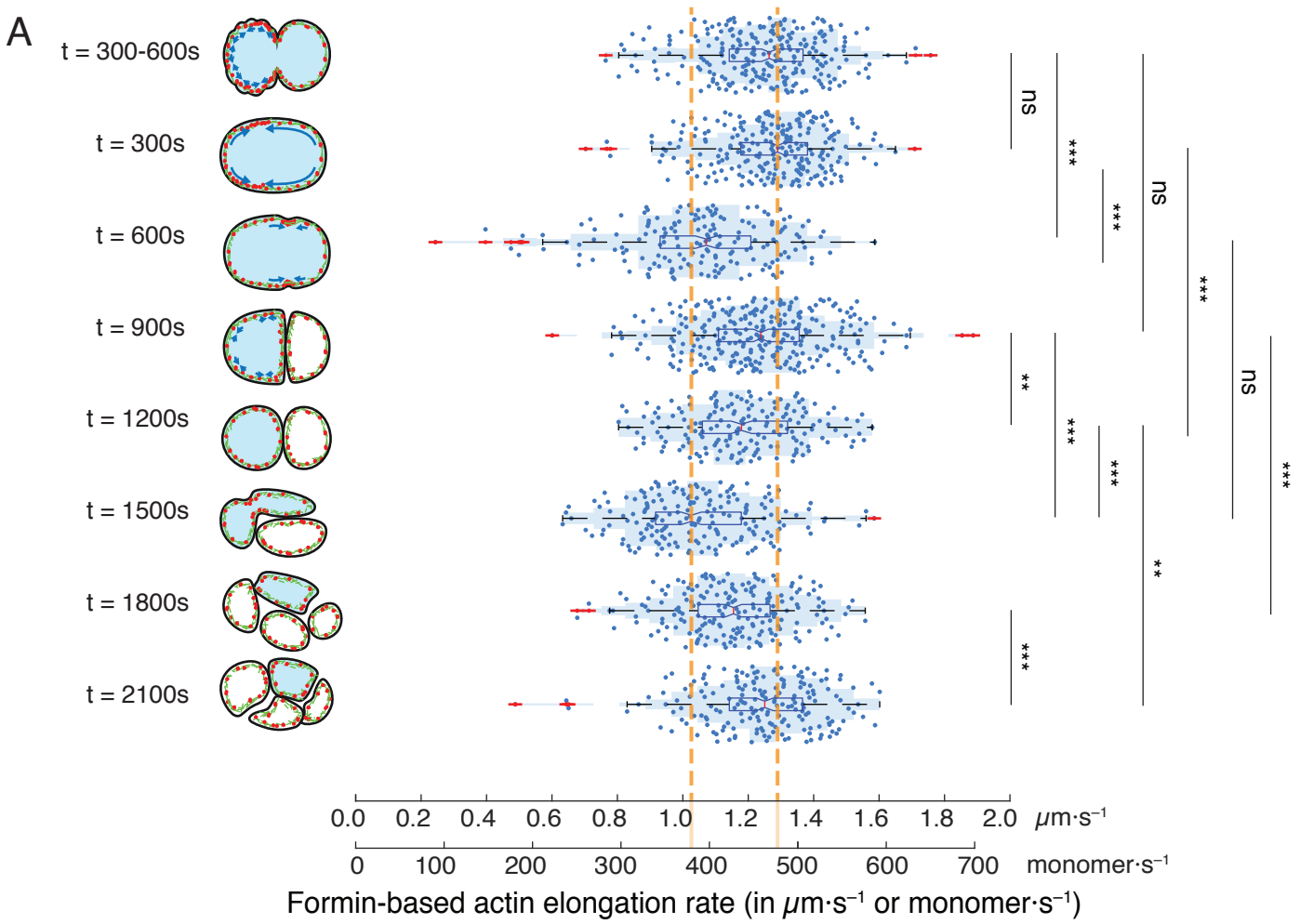
A
t = 300-600s
t = 300s
t = 600s
t = 900s
t = 1200s
t = 1500s
t = 1800s
t = 2100s
ns
***
***
ns
***
ns
***
**
***
***
**
***
0.0 0.2 0.4 0.6 0.8 1.0 1.2 1.4 1.6 1.8 2.0 μm·s⁻¹
0 100 200 300 400 500 600 700 monomer·s⁻¹
Formin-based actin elongation rate (in μm·s⁻¹ or monomer·s⁻¹)

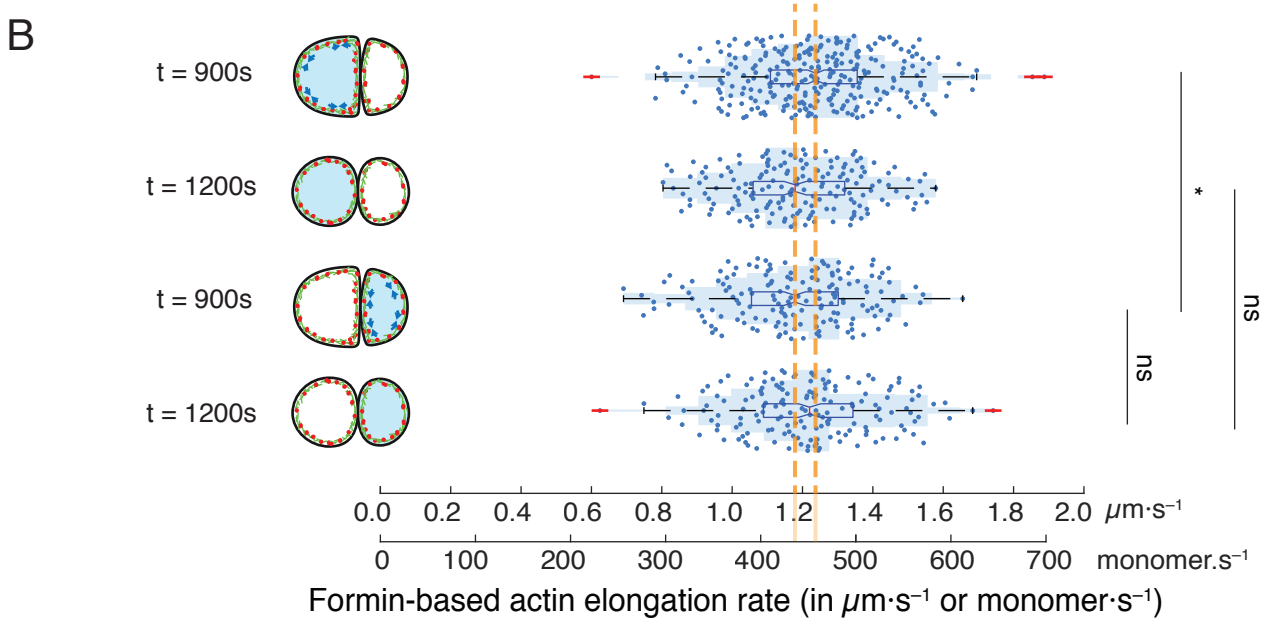
B
t = 900s
t = 1200s
t = 900s
t = 1200s
*
ns
ns
0.0 0.2 0.4 0.6 0.8 1.0 1.2 1.4 1.6 1.8 2.0 μm·s⁻¹
0 100 200 300 400 500 600 700 monomer.s⁻¹
Formin-based actin elongation rate (in μm·s⁻¹ or monomer·s⁻¹)

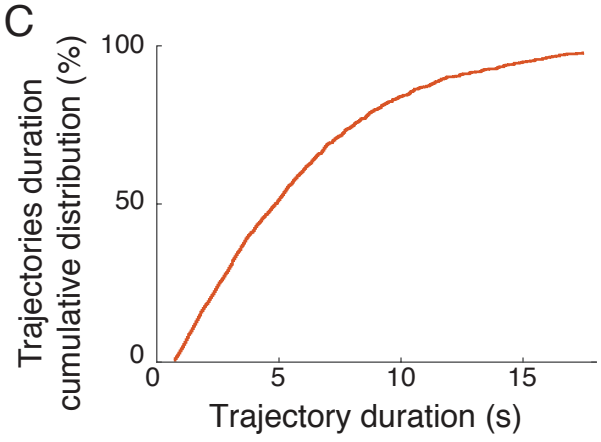
C
Trajectories duration cumulative distribution (%)
100
50
0
0
5
10
15
Trajectory duration (s)

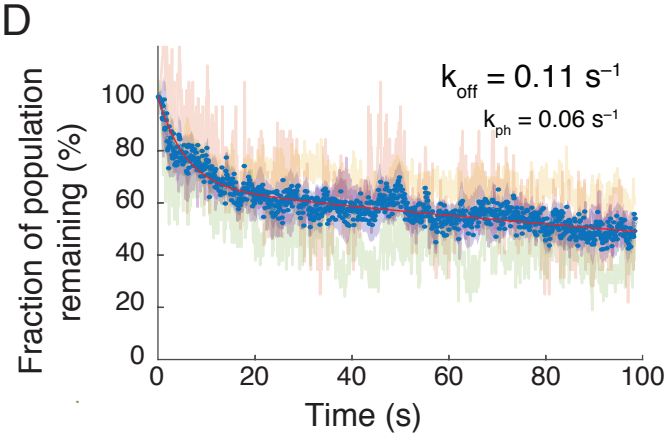
D
Fraction of population remaining (%)
100
80
60
40
20
0
koff = 0.11 s⁻¹
kph = 0.06 s⁻¹
0
20
40
60
80
100
Time (s)

Figure 2. Formin speed is changed by the cell cycle but is conserved through cell lineage. **(A-B)** Formin speed in AB (A) and P1 (B) cell. Right: Distribution of elongating Formins speed. Left: Schematic of the stage and location of the cell from which the tracks are extracted, with measured cell in light blue. Myosin in red, Actin in green. * ≥ 0.05, ** ≥ 0.01, *** ≥ 0.001, ns: not significant. Dashed orange line marks upper and lower averages. Outliers in red. (See Table S1,2 for detailed statistical information). **(C)** Cumulative distribution of CYK-1::GFP trajectory duration, as a fraction of detection events, showing a half-life of ~5 s. **(D)** The surviving fraction of cortical CYK-1::GFP as a function of photobleaching time reports both on the turnover rate k_{off} and the photobleaching rate k_{ph}. Bi-exponential fit in solid red. Experiments performed on strain over-expressing CYK-1 fused with GFP.

Figure 3

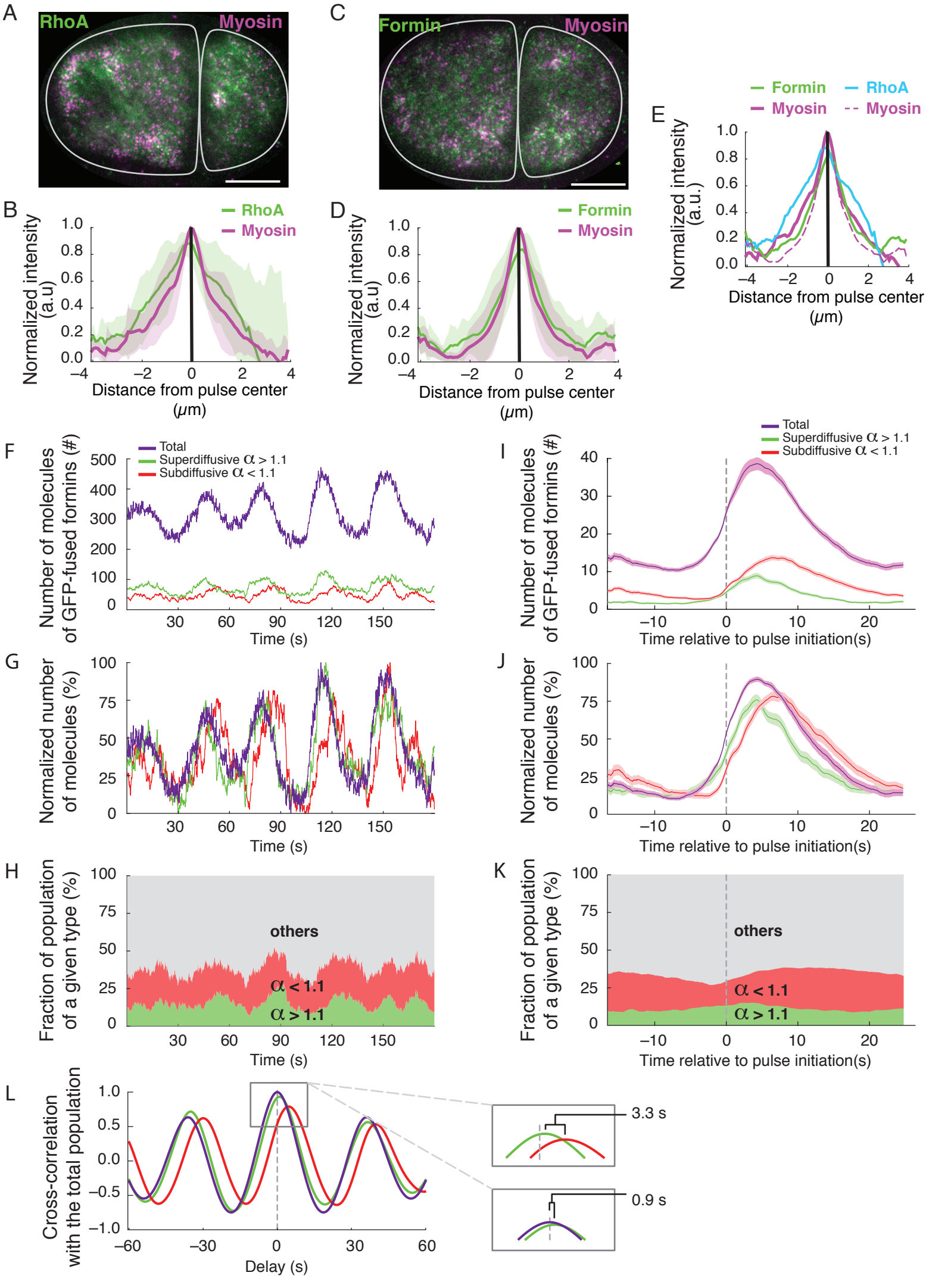
A
RhoA
Myosin
C
Formin
Myosin
B
RhoA
Myosin
Normalized intensity (a.u)
Distance from pulse center (μm)
D
Formin
Myosin
Normalized intensity (a.u)
Distance from pulse center (μm)
E
Formin
RhoA
Myosin
Myosin
Normalized intensity (a.u.)
Distance from pulse center (μm)
F
Total
Superdiffusive α > 1.1
Subdiffusive α < 1.1
Number of molecules of GFP-fused formins (#)
Time (s)
I
Total
Superdiffusive α > 1.1
Subdiffusive α < 1.1
Number of molecules of GFP-fused formins (#)
Time relative to pulse initiation(s)
G
Normalized number of molecules (%)
Time (s)
J
Normalized number of molecules (%)
Time relative to pulse initiation(s)
H
Fraction of population of a given type (%)
others
α < 1.1
α > 1.1
Time (s)
K
Fraction of population of a given type (%)
others
α < 1.1
α > 1.1
Time relative to pulse initiation(s)
L
Cross-correlation with the total population
Delay (s)
3.3 s
0.9 s

Figure 3. Recruited and actin-filament elongating formins display distinct dynamics during pulsed contractions. (A) Two-cell stage embryo showing RhoA biosensor (green, AHPH::GFP) and Myosin II (magenta, NMY-2::mKate2 at endogenous locus). **(B)** Mean normalized intensity of RhoA and myosin density profile across pulses. **(C)** Two-cell stage *C. elegans* embryo expressing fluorescent protein fusions of formin fused with GFP in green (CYK-1::GFP) and myosin in magenta (NMY-2::mKate2), at the endogenous loci. **(D)** Formin normalized mean intensity (solid green) and myosin (solid magenta) density profile along an axis drawn through pulses. **(E)** Compiled results from (B,D). (A,C) scale bar: 10 μm. (B,D,E) shaded curves represent standard deviations from 18 pulses from 6 embryos. **(F-H,L)** Population dynamics of formin CYK-1 fused with GFP, in a single embryo during 5 consecutive pulsed contractions. **(F)** Number of total (purple), super-diffusive (green) and subdiffusive (red) GFP-fused formins molecules during pulsed contractions varies in a periodic manner. **(G)** Normalized number of molecules during pulsed contractions. The populations display distinct accumulation dynamics. **(H)** Temporal evolution of the relative fraction of superdiffusive (green) and subdiffusive (red) subpopulations within the total population during pulsed contractions. **(I-K)** Dynamics of formin populations during pulsed contractions averaged over 115 pulses from 10 embryos. Individual pulses are synchronized to pulse initiation (t=0, see also Fig. 5F). **(I)** Number of total (purple), superdiffusive (green) and subdiffusive (red) GFP-fused formins molecules during pulsed contractions. **(J,K)** Absolute (J) and normalized (K) number of molecules during pulsed contractions shows that superdiffusive (green), subdiffusive (red) and total formin (purple) populations accumulate with distinct dynamics. **(L)** Cross-correlation with total population of superdiffusive (green), subdiffusive (red), and total (purple) formin populations. Offset show that subdiffusive formins accumulate 3.3 s after superdiffusive. (F-L) Strain over-expressing CYK-1 fused with GFP.

Figure 4

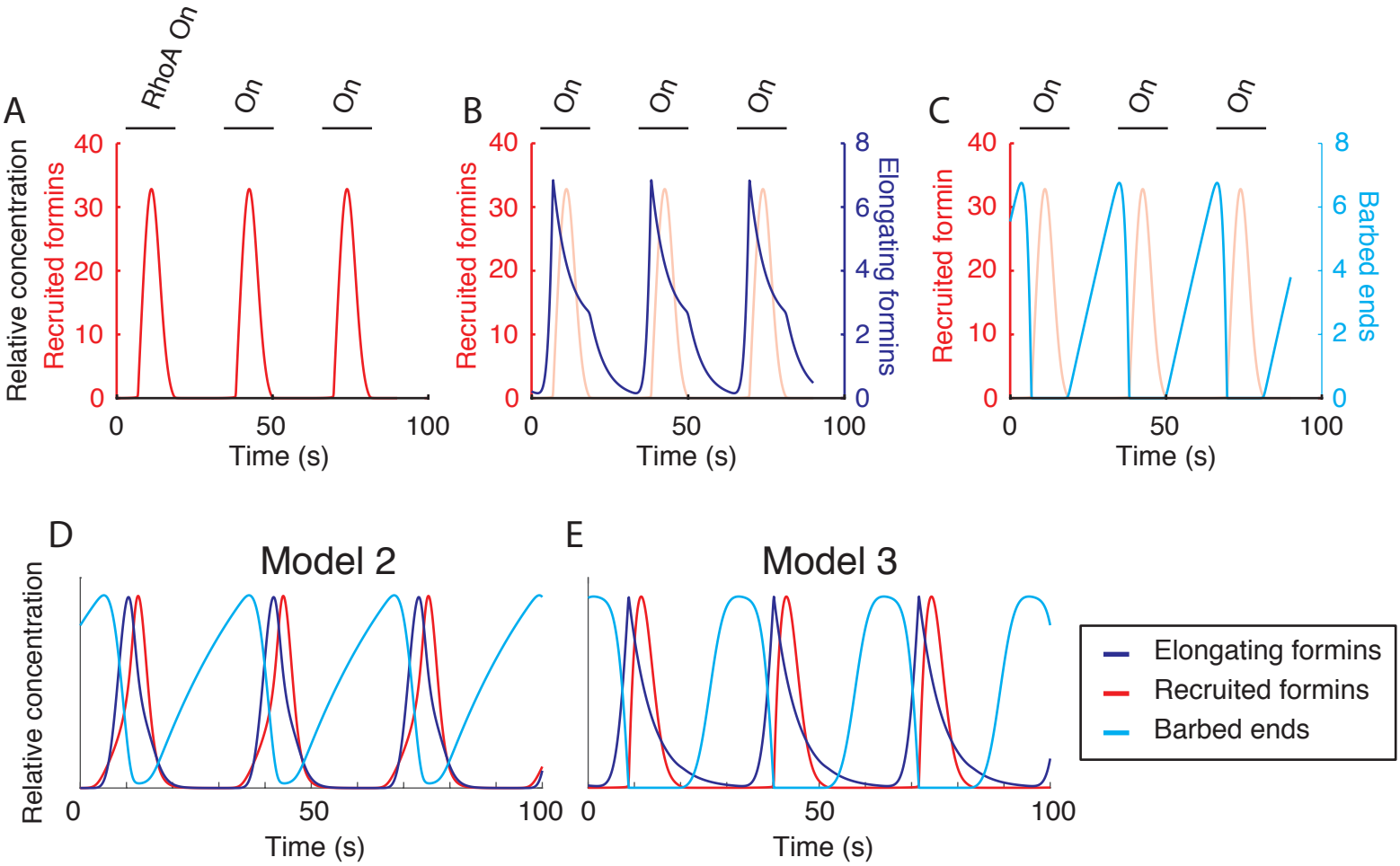
A
B
C
RhoA On
On
On
Relative concentration
Recruited formins
Elongating formins
Recruited formin
Barbed ends
Time (s)
0
50
100
0
10
20
30
40
2
4
6
8

D
Model 2
E
Model 3
Relative concentration
Time (s)
Elongating formins
Recruited formins
Barbed ends

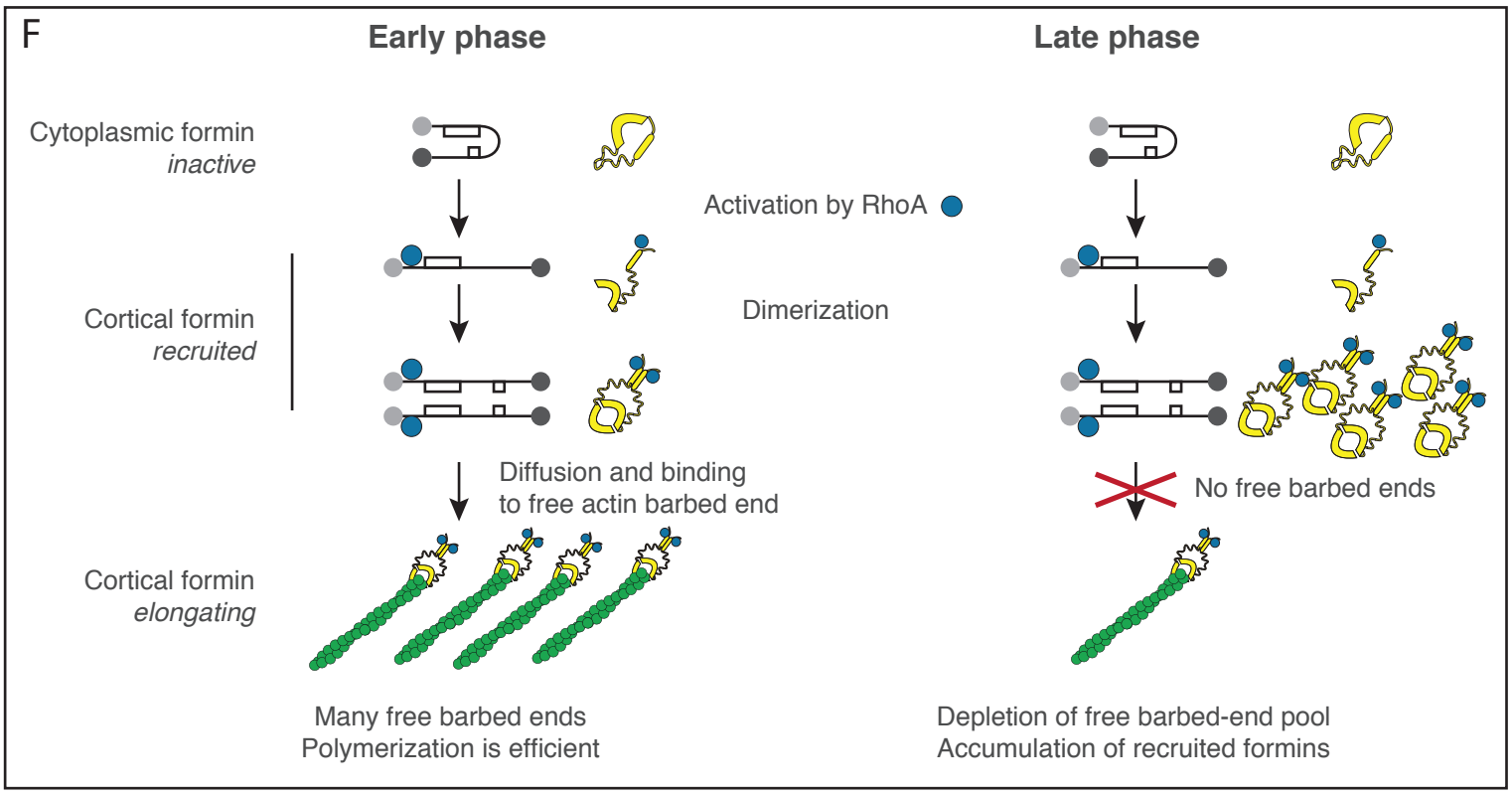
F
Early phase
Late phase
Cytoplasmic formin
inactive
Activation by RhoA
Cortical formin
recruited
Dimerization
Diffusion and binding
to free actin barbed end
No free barbed ends
Cortical formin
elongating
Many free barbed ends
Polymerization is efficient
Depletion of free barbed-end pool
Accumulation of recruited formins

Figure 4. Modeling formin recruitment dynamics with an excess of formins over barbed ends reproduces *in vivo* recruitment sequence. (A) Temporal dynamics of recruited formins during a sequence of 3 pulses. Red: Recruited formins. **(B)** Same, with elongating formins (purple: elongating formins, light red: recruited formins). Recruited formins accumulate after elongating formins. **(C)** Temporal dynamics of barbed ends (Cyan: barbed ends, light red: recruited formins). The model uses two free parameters and 4 parameters set based on experimental measurements. Barbed ends accumulated progressively in the absence of formins (between pulses), but are rapidly used upon formins recruitment. Recruited formins are immediately converted in elongating formins, such that elongating formins accumulate until depletion of the built-up barbed ends (C, purple). RhoA activation period is denoted by a black line and denoted by "Rho On", or "On". **(D)** Same model with a different choice of parameter values for the free parameters of the model. Outcome is similar. **(E)** Distinct model, where barbed ends are generated periodically during the end of the pulsed contractions, mimicking a myosin-driven actin buckling/severing activity. This model also readily reproduced the expected outcome without additional refinement. **(F)** Schematic representation of the two phases of the pulse, representing a first-come first served scenario. **Early phase:** formins arrive at the cell surface, barbed ends are available, and recruited formins are immediately converted into elongating formins. **Late phase:** Upon depletion of the barbed end pool, formins are trapped in the recruited state.

Figure 5

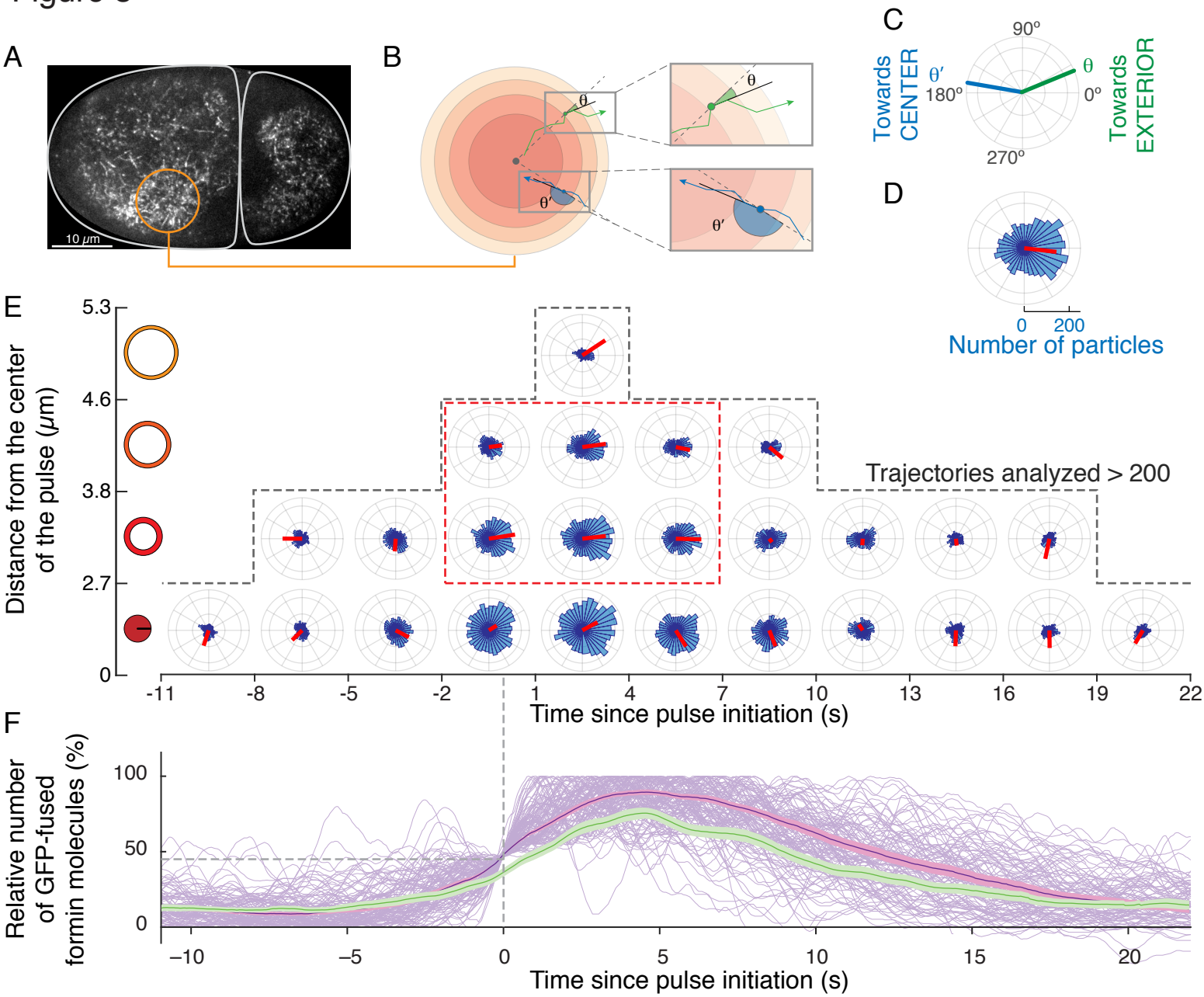
A
10 μm
B
θ
θ′
C
90°
180°
0°
270°
θ′
θ
Towards CENTER
Towards EXTERIOR
D
0
200
Number of particles
E
Distance from the center of the pulse (μm)
5.3
4.6
3.8
2.7
0
Trajectories analyzed > 200
-11
-8
-5
-2
1
4
7
10
13
16
19
22
Time since pulse initiation (s)
F
Relative number of GFP-fused formin molecules (%)
100
50
0
–10
–5
0
5
10
15
20
Time since pulse initiation (s)

Figure 5. CYK-1 formin-driven actin filament elongation during pulsed contractions drives the formation of a transient polar actin network, barbed ends pointing out. (A) Image of a 2-cell stage embryo labelled with CYK-1::GFP and displaying the area corresponding to a pulsed contraction (white dashed line). **(B)** Measure of the angle is performed with respect to the center of the pulse and the local orientation of the formin trajectory. **(C)** Green (resp. blue) track oriented with filament barbed-end pointing away (resp. towards) from the center of the pulse. **(D)** Angle distribution for steps of elongating formins. Average elongation orientation as a red segment. **(E)** Angle distribution of superdiffusive formin trajectory steps during pulsed contractions. **During the peak of the pulse, around pulse center, superdiffusive formins display on average an outwards orientation (dashed orange box).** 115 pulses derived from 10 distinct embryos were used to collect >50 000 trajectories. Steps are binned according to the distance from the center of the pulse (vertical) and time from t=0 (horizontal, 3s intervals) to produce each rose plot. Steps are then mapped in the polar histogram as in (C). Individual pulses are synchronized to pulse initiation (t=0, first pass at 45% of the normalized number of particles in the considered pulse), as shown in (F). Average step orientation displayed as a red segment, length reflecting statistical significance. Rose plots with less than 200 steps not represented (dash line outlines plots with >200 steps). **(F)** Evolution of the number of particles in a pulse. Same axis as (E). In light purple, total number of formin particles in individual pulses. In dark purple (resp.), the corresponding average and SEM. In green, average and SEM for the super-diffusive population. Same dataset as Fig. 3I-K.

Figure 6

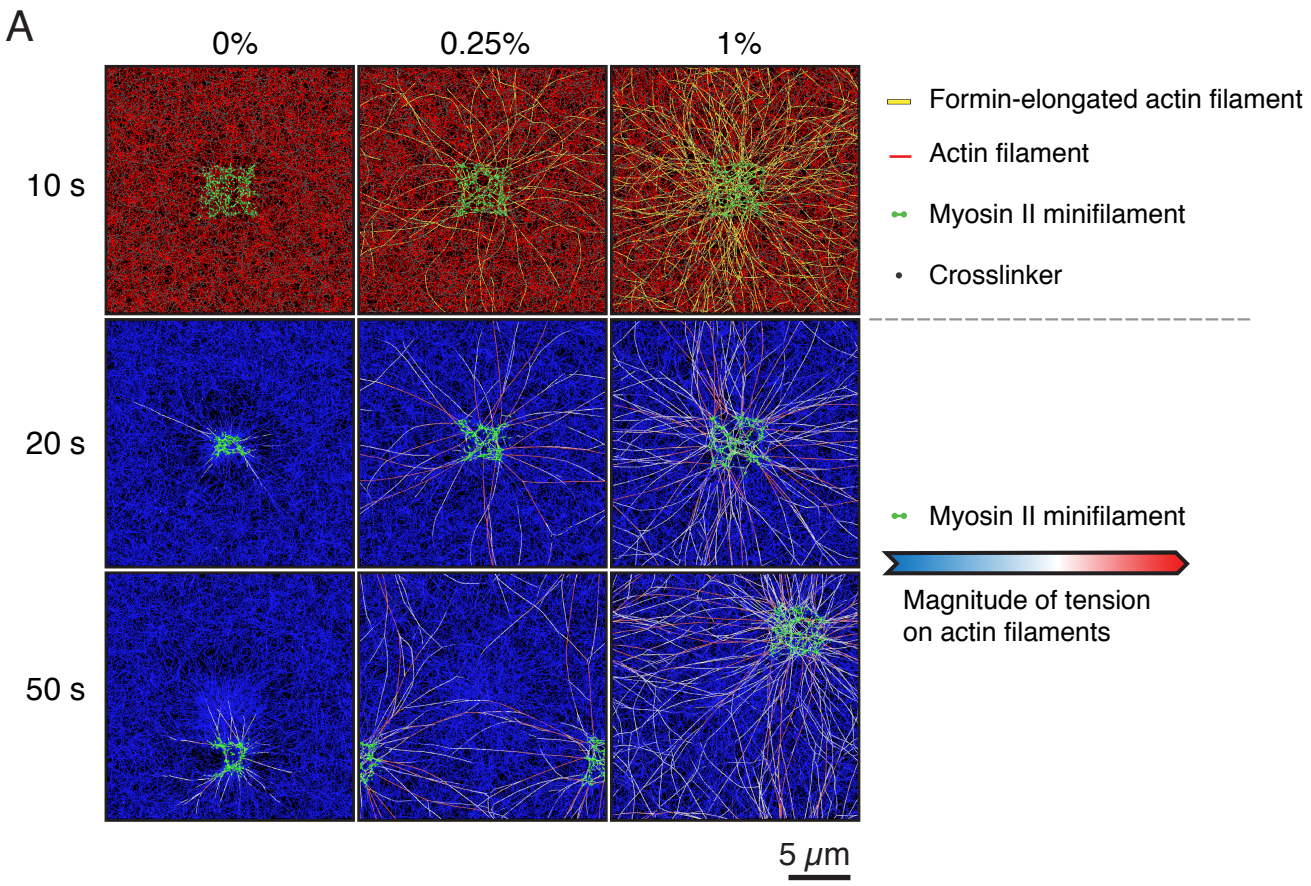
A
0%
0.25%
1%
10 s
20 s
50 s
Formin-elongated actin filament
Actin filament
Myosin II minifilament
Crosslinker
Myosin II minifilament
Magnitude of tension
on actin filaments
5 μm

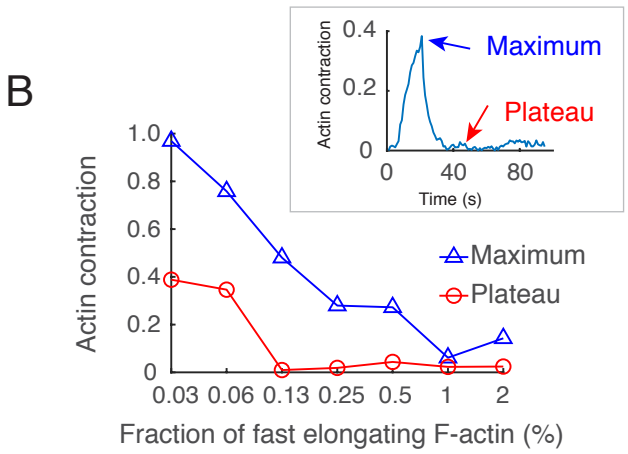
B
Actin contraction
Fraction of fast elongating F-actin (%)
Maximum
Plateau
Time (s)

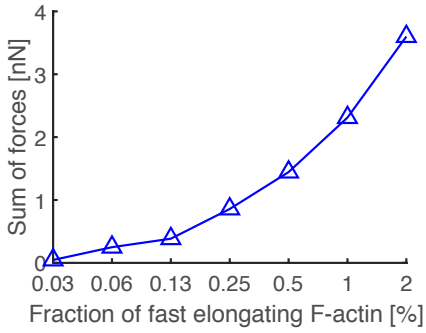
C
Sum of forces [nN]
Fraction of fast elongating F-actin [%]

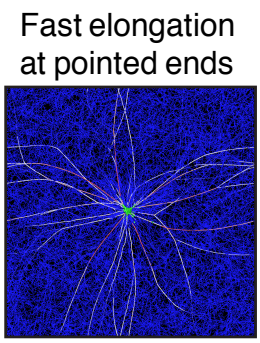
D
Fast elongation
at pointed ends

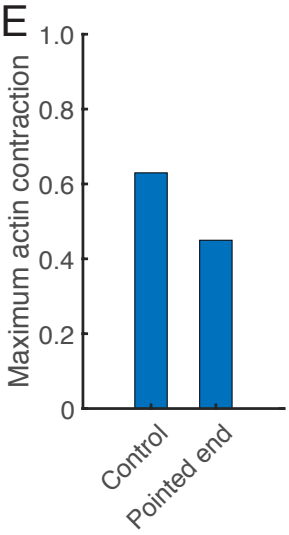
E
Maximum actin contraction
Control
Pointed end

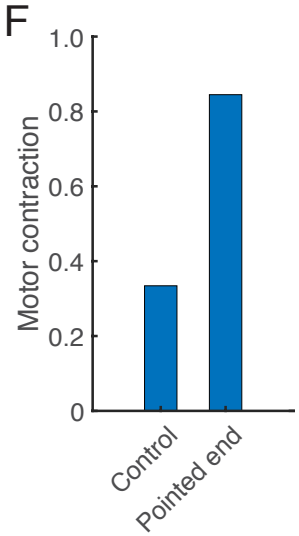
F
Motor contraction
Control
Pointed end

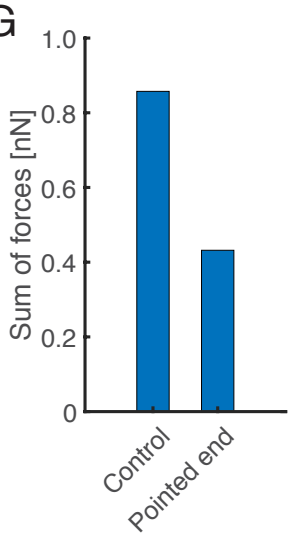
G
Sum of forces [nN]
Control
Pointed end

Figure 6. Agent-based numerical simulations of the mechanics of pulsed contractions demonstrate that polar network architecture supports efficient actomyosin contractility. **(A)** Simulating a sequence of two successive pulsed contractions. First pulse occurs in the center, while second pulse location is stochastic. Snapshots taken at $t = 10$, 20, and 50 s (resp. during pulse initiation, first pulse, and second pulse, see Fig. S4B) with three different fractions of barbed ends undergoing quick elongation: 0%, 0.25%, and 1%. Top row: Actin, myosin, and actin cross-linking protein resp. in red, green, and gray. Formin-elongated actin filaments assembled in yellow. Bottom rows: Magnitude of tensile forces on filaments. Green overlay represents active myosin motors. Simulations have periodic boundaries conditions. **(B)** Maximum and plateau values (blue triangles, red circles, resp. ; see inset for definition) of the actin contraction as a function of the fraction of fast elongating actin filaments. Contraction is computed in the pulsing region (see Methods for details). Inset shows time evolution of actin contraction (fast elongation at 0.25%), maximum and plateau. **(C)** Sum of tensile forces acting on quickly elongated filaments depending on the fraction of long filaments. **(D)** Snapshot at $t = 20$ s of a network with actin filaments elongated from pointed ends. Color schemes identical to second and third rows of (A). **(E, F, G)** Maximum actin contraction (E), motor contraction (F) and sum of tensile forces on elongated filaments (G) quantified at $t = 20$ s. In the control case, filaments are elongated from barbed ends, whereas in the other case, filaments are elongated from pointed ends.

Figure 7

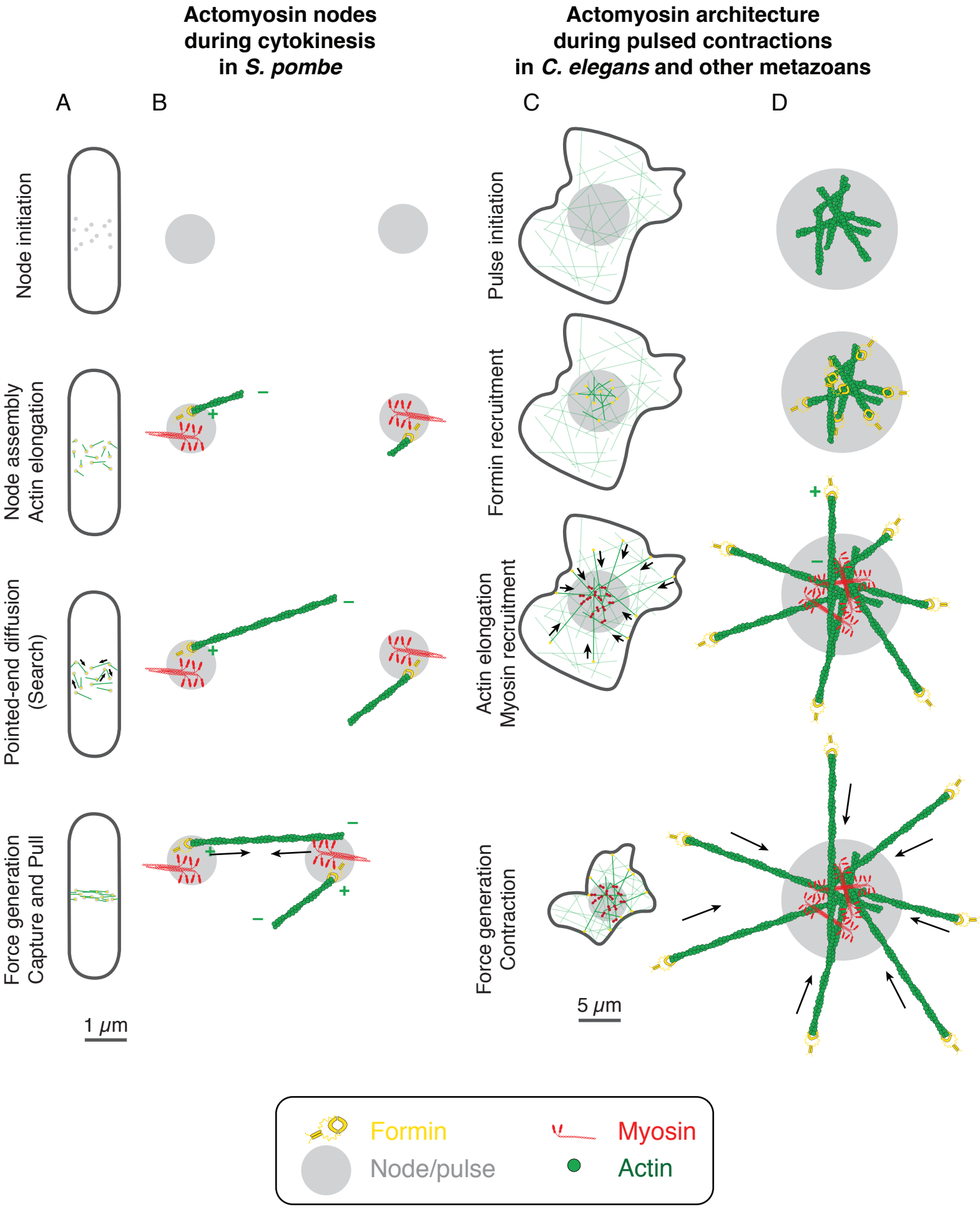
Actomyosin nodes during cytokinesis in S. pombe
Actomyosin architecture during pulsed contractions in C. elegans and other metazoans
A
B
C
D
Node initiation
Node assembly Actin elongation
Pointed-end diffusion (Search)
Force generation Capture and Pull
Pulse initiation
Formin recruitment
Actin elongation Myosin recruitment
Force generation Contraction
1 μm
5 μm
Formin
Myosin
Node/pulse
Actin

Figure 7. Compared analysis of contractility between pulsed contractility in metazoans (*Drosophila*, *C. elegans*) and yeast. (A) During cytokinesis in *S. pombe*, nodes form, cluster and align, forming the contractile to drive cell division, with a process scale size of 1-2 μm. Comparatively, in metazoan, pulsed contractions drive apical constriction over 10 to 50 μm micrometers. **(B)** In *S. pombe*, the formin Cdc12p is recruited in the nodes and drives filament elongation. Pointed-ends of filaments are proposed to explore until they are captured and pulled by Myo2p myosin filaments of another node. **(C)** During pulsed contractions in *C. elegans,* Rho recruits formins, which elongate actin filaments, followed by Myosin recruitment in the pulse center. Processive actin elongation by formins recruited at the pulse by Rho drives the formation of a polar actin network initiated at the pulse and extending over >10 μm from the pulse, with actin barbed-end pointing outwards. Myosin recruited by Rho in the center of the pulse then efficiently drives actin network contraction, pulling on actin cables assembled during the pulse to "reel in" the network towards the center of the pulse.

Inventory of supplementary information

Costache, Prigent Garcia, et al.

The following elements are provided as supporting information:

1. Figures S1–4, with legends,
2. Movies S1–10, with movie legend file,
3. Tables S1–3:
    a. Tables S1–2, statistical information pertaining to Figure 2,
    b. Table S3 summarizes all strains used in this study,
4. Method: Description of mathematical model of formin recruitment kinetics,
5. Method: Detailed description of the computational model of actomyosin mechanics,
6. Protocol: Flowchart of the image analysis procedure to study formin pulse dynamics.

Supplemental Figures S1–S4

Costache, Prigent Garcia et al.

Figure S1

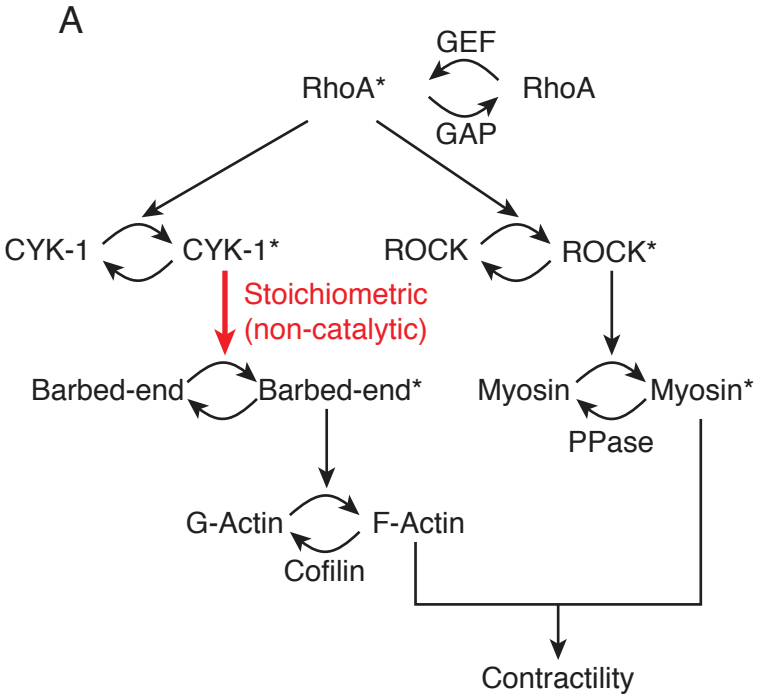
A
GEF
RhoA*
RhoA
GAP
CYK-1
CYK-1*
ROCK
ROCK*
Stoichiometric
(non-catalytic)
Barbed-end
Barbed-end*
Myosin
Myosin*
PPase
G-Actin
F-Actin
Cofilin
Contractility

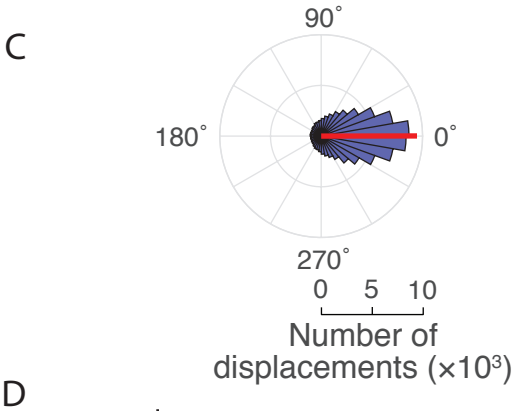
C
90˚
180˚
0˚
270˚
0 5 10
Number of
displacements (×10³)

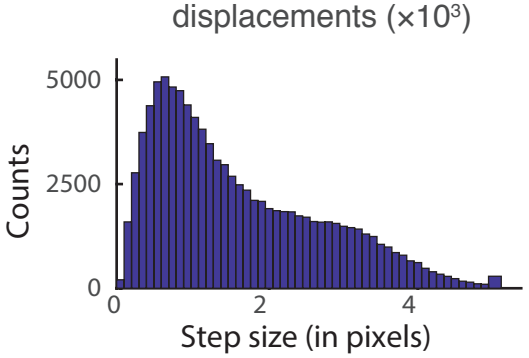
D
5000
2500
0
Counts
0 2 4
Step size (in pixels)

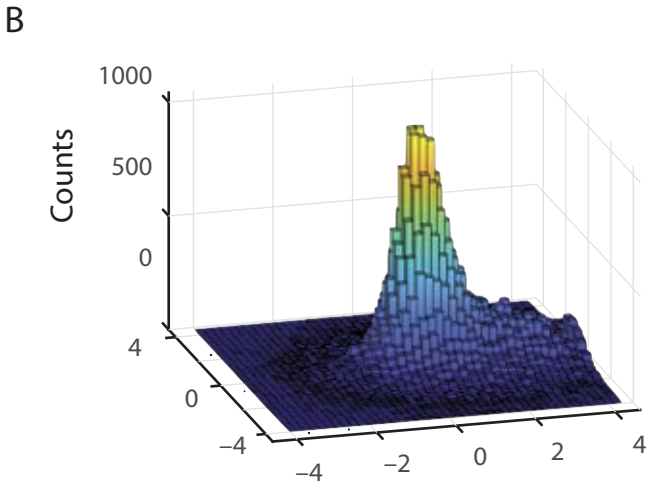
B
1000
500
0
Counts
4
0
−4
−4 −2 0 2 4

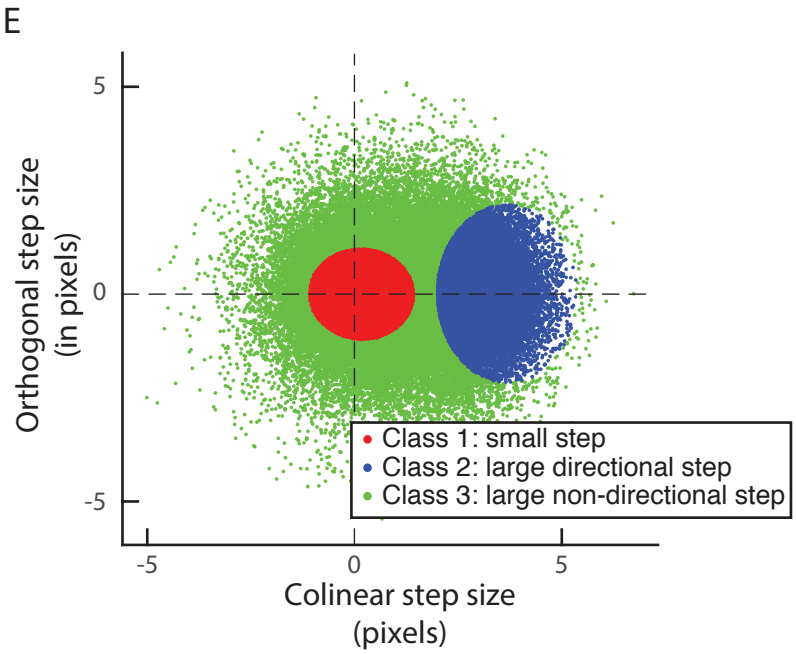
E
5
0
-5
Orthogonal step size
(in pixels)
-5 0 5
Colinear step size
(pixels)
Class 1: small step
Class 2: large directional step
Class 3: large non-directional step

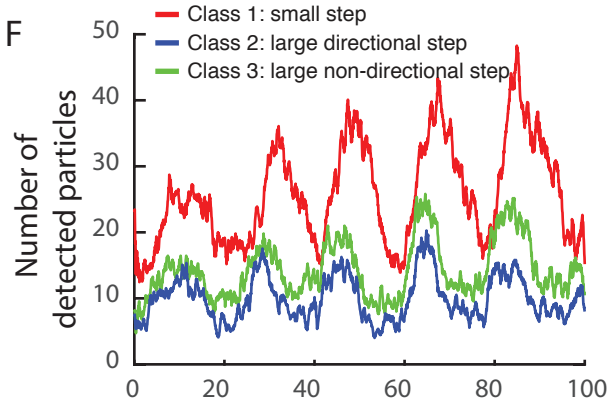
F
Class 1: small step
Class 2: large directional step
Class 3: large non-directional step
Number of
detected particles
0 10 20 30 40 50
0 20 40 60 80 100

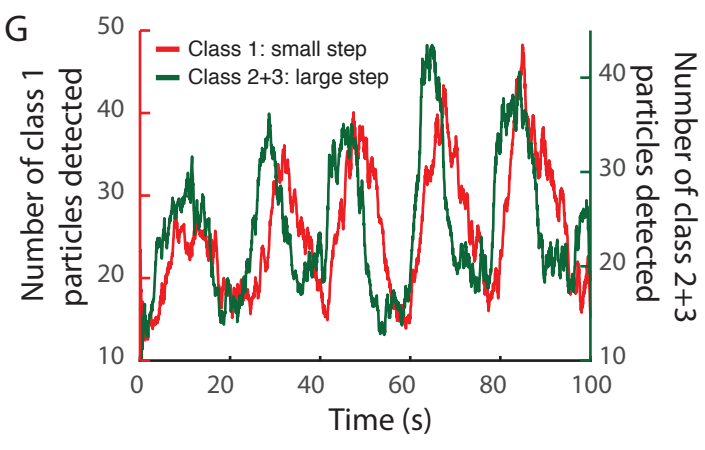
G
Class 1: small step
Class 2+3: large step
Number of class 1
particles detected
Number of class 2+3
particles detected
10 20 30 40 50
10 20 30 40
0 20 40 60 80 100
Time (s)

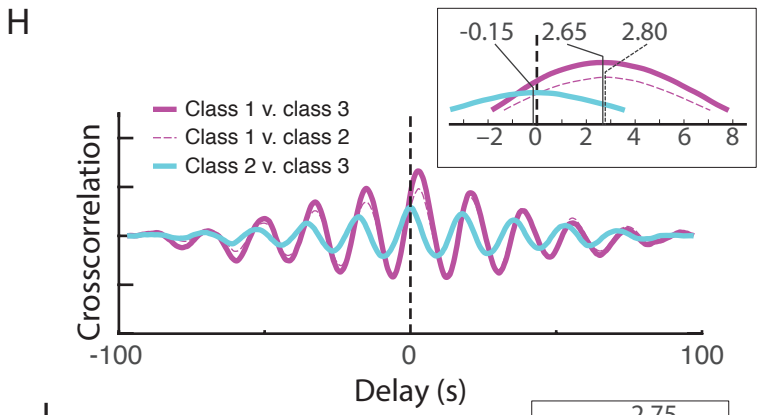
H
-0.15
2.65
2.80
−2 0 2 4 6 8
Class 1 v. class 3
Class 1 v. class 2
Class 2 v. class 3
Crosscorrelation
-100 0 100
Delay (s)

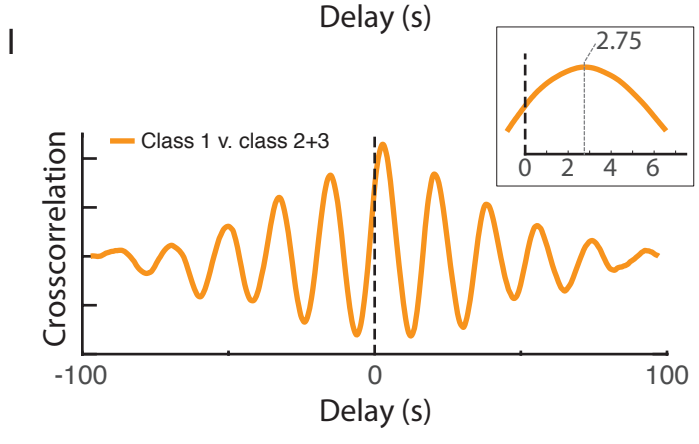
I
2.75
0 2 4 6
Class 1 v. class 2+3
Crosscorrelation
-100 0 100
Delay (s)

Figure S1. Sorting and timing distinct populations of the formin CYK-1 reveals the kinetic signature of formin accumulation during pulsed contractions. (A) Activation cascade of the formin CYK-1 by RhoA. **(B)** 3D histogram of step displacement with respect to the orientation of the previous step of the particle trajectory. Steps are taken of over 7 frames (350 ms). The histogram shows a large peak in zero, and a second additional peak around 3.5 pixels forward. **(C)** Distribution of angles of the steps in (B). **(D)** Distribution of step size, showing a merged but discernibly bimodal distribution of step sizes. **(E)** Automated classification of steps in (B) in 3 classes by 2-d gaussian fitting. Red: small/subdiffusive steps. Blue: large steps in the same direction as the previous step, corresponding to the second peak discussed in (B). Green: non-directional step, corresponding to formins changing course, or initiating elongation. **(F)** Temporal dynamics of the various step classes during a pulse, akin to Fig. 3A-C, but based on individual steps instead of whole trajectories. Green, red and blue as in (E). Note that Green and Blue curves, representing two classes of large steps (directional and non-directional) present similar temporal dynamics. **(G)** Temporal dynamics of subdiffusive steps vs "large steps"/superdiffusive steps. Dark green: merger of both classes of large steps (green and blue above). Red: small/subdiffusive steps. **(H, I)** Cross-correlation between the different populations of steps, and measured lags between these populations. Subdiffusive formins arrive ~2.7 s after superdiffusive (large steps) formins. Insets show an enlarged view of the peak region.

Figure S2

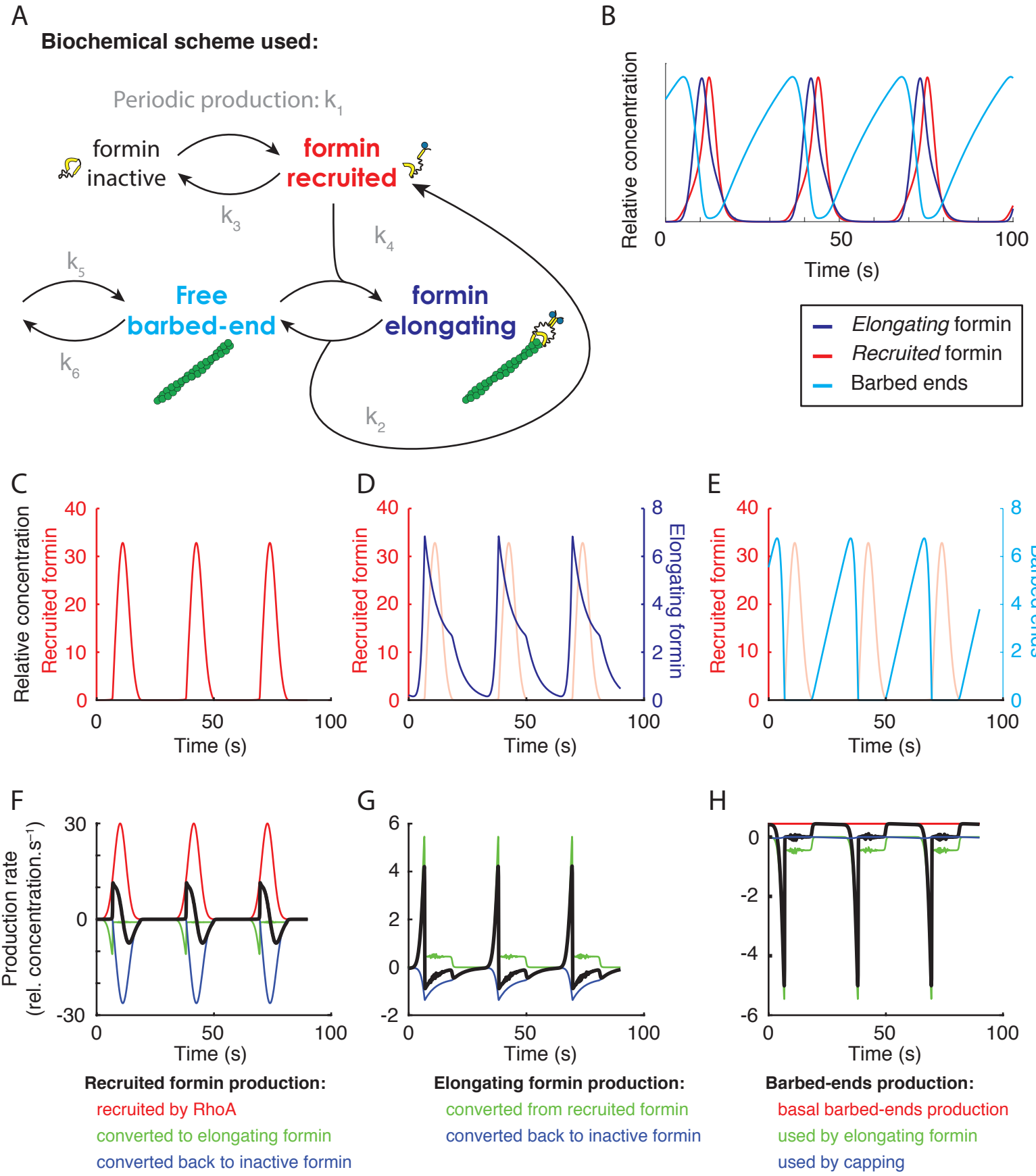
A
Biochemical scheme used:
Periodic production: k1
formin inactive
formin recruited
k3
k4
k5
k6
k2
Free barbed-end
formin elongating
B
Relative concentration
0
50
100
Time (s)
Elongating formin
Recruited formin
Barbed ends
C
Relative concentration
Recruited formin
Time (s)
D
Recruited formin
Elongating formin
Time (s)
E
Recruited formin
Barbed ends
Time (s)
F
Production rate (rel. concentration.s⁻¹)
Time (s)
G
Time (s)
H
Time (s)
Recruited formin production:
recruited by RhoA
converted to elongating formin
converted back to inactive formin
Elongating formin production:
converted from recruited formin
converted back to inactive formin
Barbed-ends production:
basal barbed-ends production
used by elongating formin
used by capping

Figure S2. Mathematical simulation of a barbed end depletion model – a detailed view. **(A)** Biochemical scheme for formin recruitment, activation and formation of a complex with barbed ends. **(B)** An example of the evolution formin populations during a series of 3 pulses on the same graph. Cyan: Barbed ends, red: Recruited formins, purple: elongating formins. **(C-E)** Same as Fig. 4A-C, provided for reference for (F-H). **(C)** Temporal dynamics of recruited formins during a sequence of 3 pulses. Red: Recruited formins. **(D)** Same, with elongating formins (purple: elongating formins, light red: recruited formins). Recruited formins accumulate after elongating formins. **(E)** Temporal dynamics of barbed ends (Cyan: barbed ends, light red: recruited formins). **(F)** Sources and sinks affecting formin concentration are represented with a color code. Total derivative is presented in black, the positive contribution (production) and negative contribution (conversion) as described in the figure. **(G,H)** Same as (F) for the concentration of elongating formins (G) and barbed ends (H).

Figure S3

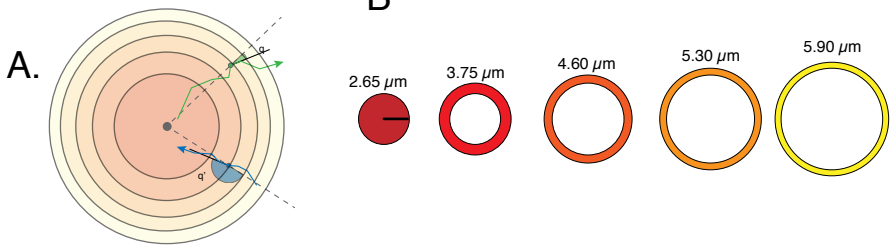
A.
B
2.65 μm
3.75 μm
4.60 μm
5.30 μm
5.90 μm
C
90°
120°
60°
150°
30°
180°
0°
q'
q
Towards CENTER
Towards EXTERIOR
D
Distribution
Number of particles
0
80
G
Formin
Myosin
Actin
E
F
10 μm
Relative number of particles
Time (s)
Real formin trajectories
n = 10 embryos, 115 pulses
Simulated formin trajectories
n = 105 pulses

Figure S3. **Simulated CYK-1 formin trajectories display similar polar orientation (barbed ends pointing out) during pulsed contractions, as measured in real embryos. (A)** Cartoon of a considered region of pulsed accumulation of formins, two examples of trajectories are drawn with the measured angle of the tangent from the center of the region to the vector of each particle in every position: green formin is directed outwards meanwhile blue formin is directed towards the center of the pulsed contraction region. **(B)** The pulsed contraction region is separated in concentric circular regions that have the same surface. The radius of each circular region is indicated. **(C)** Measure of the angle for two formin trajectories is performed with respect to the center of the pulse and the local orientation of the formin trajectory. The green track ($\theta \sim 25°$) is oriented with the barbed end of the filament pointing away from the center of the pulse, while the blue track ($\theta \sim 170°$) is oriented towards the center of the pulse. **(D)** All the measured angles of trajectories within a circular region from the pulsed contraction are displayed as distributions on 180° polar plots. **(E)** Measured angles of formins trajectories in pulsed contractions from real embryos, with respect to a spatial coordinate (horizontal) and a time coordinate (vertical) of the pulsed accumulation. The vertical red curves display the accumulation of formin particles for each pulse. All pulses are aligned at 45% ratio between minimum and maximum, at time 0, and we signal this time with a horizontal dashed line. Dataset is the same as Fig. 5. The regions around the pulse, and when pulse intensity is high (dashed black box), display a distribution skewed towards 0, showing that the orientation of the formins point outwards of the pulse region. **(F)** Similar analysis as in (E), with simulated formin tracks based on formin kinetics extracted from measurements in real embryos (see Methods section for details). **(G)** Mechanistic model of actin filament orientation during pulsed contractions.

Figure S4

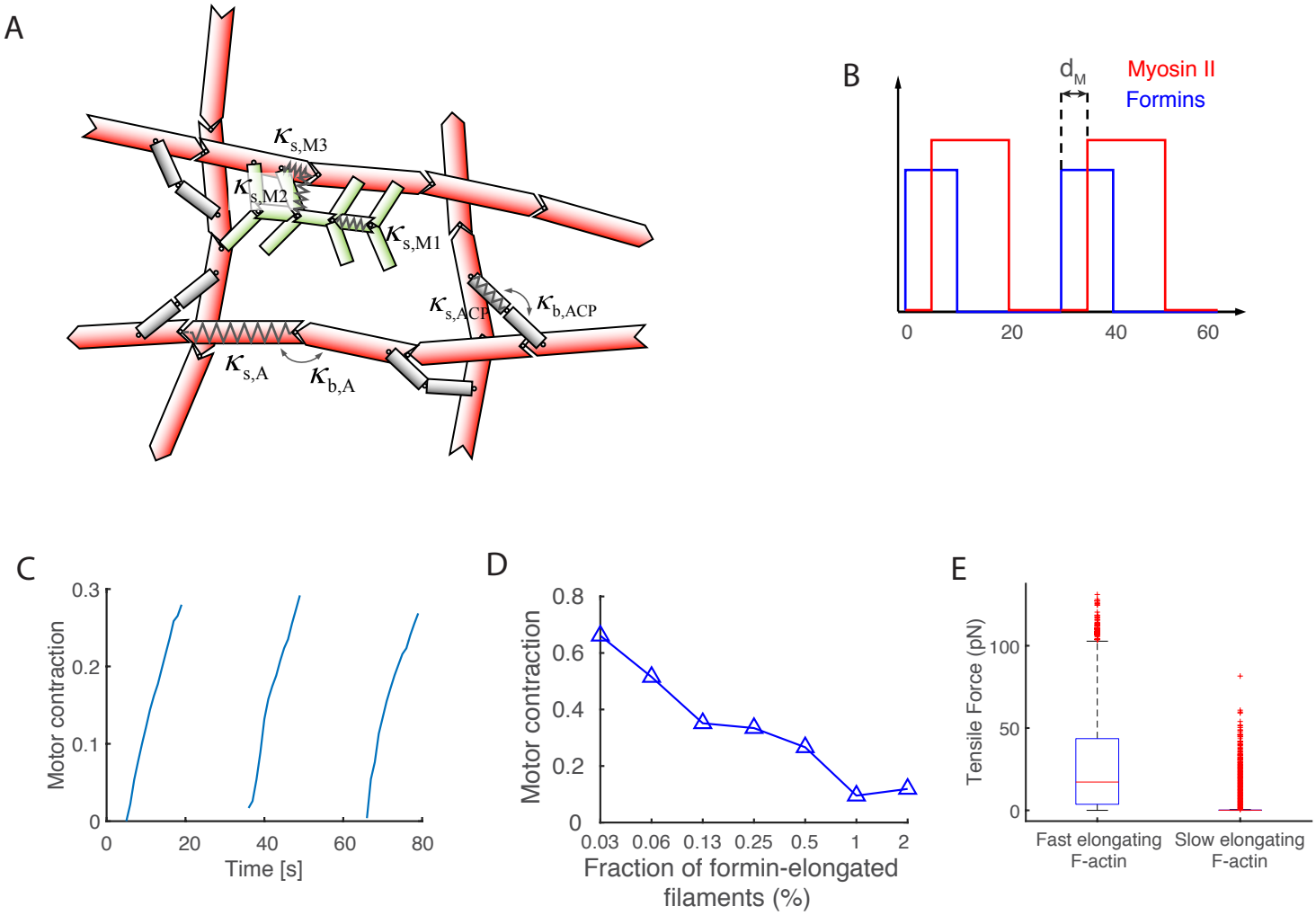
A
$\kappa_{s,M3}$
$\kappa_{s,M2}$
$\kappa_{s,M1}$
$\kappa_{s,ACP}$
$\kappa_{b,ACP}$
$\kappa_{s,A}$
$\kappa_{b,A}$
B
d_M
Myosin II
Formins
0
20
40
60
C
Motor contraction
0.3
0.2
0.1
0
0
20
40
60
80
Time [s]
D
Motor contraction
0.8
0.6
0.4
0.2
0
0.03
0.06
0.13
0.25
0.5
1
2
Fraction of formin-elongated filaments (%)
E
Tensile Force (pN)
100
50
0
Fast elongating F-actin
Slow elongating F-actin

Figure S4. Numerical simulation of the mechanics of actomyosin networks during pulsed contractions. (A) Agent-based model for simulating actomyosin networks. Actin (red), actin cross-linking protein (ACP), and motor (green) are simplified by cylindrical segments. Spring and bending forces with stiffness ($\varkappa$'s) maintain equilibrium lengths and angles, respectively. **(B)** Activation scheme of myosin and formins during pulsed contractions. **(C)** An example showing the extent of myosin contraction measured in three different activated regions. **(D)** Boxplot showing the distribution of tensile forces acting on fast elongating actin filaments (left) and slow elongating filaments (right) in the control condition. **(E)** The average of the maximum values of the motor contraction shown in (C) as a function of the fraction of quickly elongating filaments.

Movies Legends

Costache, Prigent Garcia et al.

Movies S1. TIRF Single-molecule imaging of CYK-1::GFP formins localized at the cell cortex in the 2-cell stage *C. elegans* embryo. Different mobility behavior of the formins can be observed, some of them travel long distances in the cortex (white arrow), whereas some of them have a more confined mobility behavior (yellow arrow). Strain over-expresses CYK-1 fused with GFP. Scale bar is 5μm.

Movie S2. CYK-1::GFP formin trajectories can be easily observed by using a running time projection (bottom) of 100 time points (average of 4 frames, then running projection of 25 frames). Here is shown a 2-cell stage *C. elegans* embryo (TIRF imaging) during the pulsed contractions phase and the cortical stationary phase that follows. Strain over-expresses CYK-1 fused with GFP. Scale bar is 5μm.

Movie S3. Tracking of different mobility populations. Red circles indicate subdiffusive (confined) formins, green circles show the superdiffusive (active) formines and black circles indicate the formins that are present at the cortex for less than 15 frames in time and not categorized with a mobility profile. Strain over-expresses CYK-1 fused with GFP. Scale bar is 5μm.

Movie S4. Effect of drug treatment on formin mobility dynamics. TIRF microscopy of 2-cell stage *C. elegans* embryos expressing formin CYK-1::GFP (CRISPR) and permeabilized by *perm-1* RNAi. **(Left)** Embryo perfused with actin destabilizing drug Latrunculin A (10 μM) at indicated time (0min:45sec) on the movie. Following actin network destabilization, formins formed stable aggregates at the cell cortex, probably pulled by microtubules towards the cell center. **(Right)** Embryo perfused with microtubules destabilizing drug Nocodazole (10 $\mu g.ml^{-1}$) at indicated time (0min:45sec) on the movie. Formins still display normal mobility, after Nocodazole perfusion. In the projection of the same embryo (bottom), long formin trajectories are readily observed. Scale bar is 5μm.

Movie S5. Near-TIRF imaging of a 2-cell stage embryo during cortical stationary phase (mitosis) overexpressing actin fused with GFP. Acceleration x6. Scale bar: 10 μm. Actin molecules are rather immobile once recruited at the cortex.

Movie S6. Tracking of CYK-1 formins within a pulsed accumulation of formins in a 2-cell stage embryo using an adaptable region of interest. Green circles indicate subdiffusive, confined formins, whereas magenta circles show the superdiffusive, ballistic formins. Strain over-expresses CYK-1 fused with GFP.

Movie S7. Simulated 2-cell stage C. elegans embryo displaying CYK-1 formin trajectories as running projections. The tracks respect the spatial distribution (density, length, pulsed accumulations) as native formin trajectories, but the track orientation has been completely randomized. Yellow dots indicate formin pulsed accumulations.

Movie S8. A network without accelerated actin polymerization. In this movie, the magnitude of tensile forces acting on the network is visualized by color scaling; blue, white, and red represent low, intermediate, and high forces, respectively. Green represents active myosin motors. The duration of this movie is 80 s in the simulation.

Movie S9. A network with a moderate number of actin filaments undergoing fast polymerization. In this movie, the magnitude of tensile forces acting on the network is visualized by color scaling; blue, white, and red represent low, intermediate, and high forces, respectively. Active myosin motors are represented by green. The duration of this movie is 96 s in the simulation.

Movie S10. A network with a large number of actin filaments experiencing accelerated polymerization. In this movie, the magnitude of tensile forces acting on the network is visualized by color scaling; blue, white, and red represent low, intermediate, and high forces, respectively. Green indicates active myosin motors. The duration of this movie is 96 s in the simulation.

Table S1: Statistical information supporting Fig. 2A,B, *Costache, Prigent-Garcia, et al.*

	number of embryos	number of tracks	mean	median	high notch	low notch	std
1c interphase	6	240	1.2497	1.2641	1.2869	1.2412	0.1764
1c mitosis	6	240	1.272	1.2896	1.3102	1.2689	0.1626
1c cytokinesis	5	170	1.0496	1.0716	1.105	1.0382	0.2222
2c AB interphase	7	280	1.2413	1.2385	1.2617	1.2153	0.1933
2c AB mitosis	7	168	1.1848	1.1794	1.211	1.1479	0.1756
2c AB cytokinesis	5	180	1.0442	1.026	1.0567	0.99534	0.1838
4c ABx interphase	5	190	1.1546	1.155	1.1801	1.13	0.1675
4c ABx mitosis	5	185	1.2407	1.2506	1.2764	1.2248	0.1768
2c P1 interphase	7	161	1.1795	1.178	1.2086	1.1475	0.1849
2c P1 mitosis	7	161	1.2176	1.2204	1.2519	1.1889	0.1929

Table S2: Statistical information supporting Fig. 2A,B, *Costache, Prigent-Garcia, et al.*

	paired	Two-sample ttest speed on tracks	Paired-sample ttest speed on mean	Two-sample ttest speed on mean
1-cell interphase/ 1-cell mitosis	y	0.1503	0.3676	0.5396
1c interphase/ 1c cytokinesis		9.92E-22		0.0016
1c mitosis/ 1c cytokinesis		1.78E-27		0.0013
2c AB interphase/ 2c AB mitosis	y	0.0021	0.0082	0.3185
2c AB interphase/ 2c AB cytokinesis		1.12E-24		0.0091
2c AB nitosis/ 2c AB cytokinesis		2.19E-12		0.0429
4c ABp interphase/ 4c ABp mitosis	y	1.91E-06	0.0328	0.0321
1c interphase/ 2c AB interphase		0.609		0.8609
2c AB interphase/ 4c ABp interphase		6.99E-07		0.0962
1c mitosis/ 2c AB mitosis		3.88E-07		0.1
2c AB mitosis/ 4c ABp mitosis		0.0031		0.3138
1c cytokinesis/ 2c AB cytokinesis		0.8027		0.9341
2c P1 interphase/ 2c P1 mitosis	y	0.071	0.4844	0.5465
2c AB interphase/ 2c P1 interphase	y	0.0011	0.1845	0.2725
2c AB mitosis/ 2c P1 mitosis	y	0.1066	0.1871	0.6054

Table S3: List of strains used in *Costache, Pirgent-Garcia, et al.*

Strain name	Genotype	Source
N2	Wild-type Bristol strain	CGC
EM302	*mgSi5[cb-UNC-119 (+) GFP::ANI-1(AH+PH)]II; nmy-2(cp52[nmy-2::mKate2 + unc-119(+)]) I; unc-119(ed3) III*	Michaux et al, 2018
FBR104	*cyk-1(jme06[cyk-1::mNeon])III*	This study
FBR106	*cyk-1(jme06[cyk-1::mNeon])III; gesIs001[Pmex-5::Lifeact::mKate::nmy-2UTR, unc-119+]*	This study
FBR160	*cyk-1(jme14[cyk-1::eGFP])III*	This study
FBR175	*cyk-1(jme14[cyk-1::eGFP])III; nmy-2(cp52[nmy-2::mKate2 + unc-119(+)]) I; unc-119(ed3) III*	This study
JH1541	*unc-119(ed4); pJH7.03 [unc-119; pie-1:GFP:actin::pie-1 3′ UTR]*	Courtesy of G. Seydoux
LP229	*nmy-2(cp52[nmy-2::mKate2 + LoxP unc-119(+) LoxP]) I; unc-119 (ed3) III*	Dickinson et al, 2017
SWG001	*gesIs001[Pmex-5::Lifeact::mKate::nmy-2UTR, unc-119+]*	Reyman et al, 2016
SWG282	*gesIs008[Pcyk-1::CYK-1::GFP::cyk-1UTR, unc-119+]*	This study

Methods
Description of mathematical model of formin recruitment kinetics
Costache, Prigent Garcia et al.

Assembly of a polar network architecture downstream of a signaling cascade

Vlad Costache[1], Séréna Prigent-Garcia[1], Camille Plancke[1], Jing Li[2], Simon Bégnaud[1], Shashi Kumar Suman[1], Taeyoon Kim[2], and François B. ROBIN[1]

[1]CNRS UMR7622 and Inserm ERL 1156, Institut de Biologie Paris Seine (IBPS), Sorbonne Université, Paris, France.
[2]Weldon School of Biomedical Engineering, Purdue University, West Lafayette, Indiana.

January 1, 2021

1 Assumptions

The proposed model is based on the following set of assumptions:

1. RhoA activation activity is represented as a smooth periodic function ($sin^6(\omega t)$,
2. inactive formins are activated by RhoA and recruited to the cortex, becoming "recruited",
3. CYK-1 formins are poor nucleators but good elongators – we considered formins do not efficiently nucleate new filaments under physiological conditions (in vitro actin assembly yields ∼1 new nucleated filament per 550 CYK-1 formin molecule at 2.5 μM actin and 2.5 μM profilin PFN-1, Neidt:2008df)
4. once recruited at the cortex, formins bind to barbed ends through a trimolecular reaction to drive actin assembly, becoming "elongating",
5. recruited formins unbind from the cortex to the cytoplasmic pool, (6) elongating formins unbind from the cortex to the cytoplasmic pool.

2 Definitions

$[CYK-1_{recruited}] : [CYK1^{*}]$
$[CYK-1_{elongating}] : [CYK1^{**}]$
$[Barbedends] : [BE]$
$Period : T$

3 Equations

$$\frac{d\left([CYK1^*]\right)}{dt} = k_1 \cdot \sin^6\left(\frac{\pi t}{T}\right) - k_3 \cdot [CYK1^*] - 2 \times k_4 \cdot [CYK1^*]^2 \cdot [BE] \quad (1)$$

$$\frac{d\left([CYK1^{**}]\right)}{dt} = k_4 \cdot [CYK1^*]^2 \cdot [BE] - k_2 \cdot [CYK1^{**}] \quad (2)$$

$$\frac{d\left([BE]\right)}{dt} = -k_4 \cdot [CYK1^*]^2 \cdot [BE] + k_5 - k_6 \cdot [BE] \quad (3)$$

4 Origin of the terms

$$\frac{d\left([CYK1^*]\right)}{dt} = k_1 \cdot \sin^6\left(\frac{\pi t}{T}\right) - k_3 \cdot [CYK1^*] - 2 \times k_4 \cdot [CYK1^*]^2 \cdot [BE] \quad (4)$$

The **first term** describes the pulse activation by Rho, which is transient and has a period of ∼30s. The **second term** describes inactivation of the recruited species. The **third term** describes the conversion from recruited to elongating species, as a trimolecular reaction, corresponding to the assumption that cytoplasmic, inactive formins are monomeric and assemble as dimers upon binding with barbed-ends.

$$\frac{d\left([CYK1^{**}]\right)}{dt} = k_4 \cdot [CYK1^*]^2 \cdot [BE] - k_2 \cdot [CYK1^{**}] \quad (5)$$

The **first term** equates the conversion from inactive to active species (third term above), while the **second term** describes inactivation of the active species which is not converted back to recruited but is instead inactivated in the cytoplasmic species.

$$\frac{d\left([BE]\right)}{dt} = -k_4 \cdot [CYK1^*]^2 \cdot [BE] + k_5 - k_6 \cdot [BE] \quad (6)$$

The **first term** corresponds to the conversion of *free* barbed ends. These *free* barbed ends are likely to correspond to capped barbed ends: formins will displace the equilibrium and replace capping proteins, due to their higher affinity for barbed ends compared to capping proteins (*Neidt et al, 2008*). The **second term** corresponds to a low, continuous source/production of barbed ends. The **third term** corresponds to an inactivation of free barbed ends, representing the disappearance of barbed ends after some time. A typical value for that term will be on the order of magnitude of actin turnover rate ($\sim 0.1 - 1\ s^{-1}$)

Methods
Description of the computational model of actomyosin mechanics
Costache, Prigent Garcia et al.

SUPPLEMENTAL INFORMATION

Brownian dynamics via the Langevin equation

In our agent-based model, F-actin is simplified into serially connected cylindrical segments with barbed and pointed ends. Motors have a backbone structure with eight arms ($N_a = 8$) attached, and each of the motor arm represents four myosin heads. Therefore, the total number of myosin heads represented by one motor is 32, which is not quite different from 56 myosin heads in one non-muscle myosin thick filament [8]. The backbone and arms of the motors are also described by cylindrical segments. ACPs are comprised of two cylindrical arm segments.

The displacements of all the cylindrical segments are determined by the Langevin equation with the negligence of inertia:

$$\mathbf{F}_i - \zeta_i \frac{\mathrm{d}\mathbf{r}_i}{\mathrm{d}t} + \mathbf{F}_i^{\mathrm{T}} = 0 \tag{S1}$$

where $\mathbf{r}_i$ is a position vector of the ith element, ζ_i is a drag coefficient, t is time, $\mathbf{F}_i$ is a deterministic force, and $\mathbf{F}_i^{\mathrm{T}}$ is a stochastic force satisfying the fluctuation-dissipation theorem [9]:

$$\left\langle \mathbf{F}_i^{\mathrm{T}}(t)\mathbf{F}_j^{\mathrm{T}}(t) \right\rangle = \frac{2k_{\mathrm{B}}T\zeta_i\delta_{ij}}{\Delta t}\boldsymbol{\delta} \tag{S2}$$

where $\boldsymbol{\delta}$ is a second-order tensor, δ_{ij} is the Kronecker delta, and $\Delta t = 1.15\text{x}10^{-5}$ s is a time step. The drag coefficients are calculated via an approximated form for cylindrical objects [10]:

$$\zeta_i = 3\pi\mu r_{\mathrm{c},i}\frac{3 + 2r_{0,i}/r_{\mathrm{c},i}}{5} \tag{S3}$$

where μ is the viscosity of surrounding medium, and $r_{0,i}$ and $r_{c,i}$ are the length and diameter of segments, respectively. The positions of all the cylindrical segments are updated at each time step via the Euler integration scheme:

$$\mathbf{r}_i(t+\Delta t) = \mathbf{r}_i(t) + \frac{\mathrm{d}\mathbf{r}_i}{\mathrm{d}t}\Delta t = \mathbf{r}_i(t) + \frac{1}{\zeta_i}\left(\mathbf{F}_i + \mathbf{F}_i^{\mathrm{T}}\right)\Delta t \tag{S4}$$

Deterministic forces

Deterministic forces include extensional forces maintaining equilibrium lengths, bending forces maintaining equilibrium angles, and repulsive forces accounting for volume-exclusion effects between actin segments. The extensional and bending forces originate from the following potentials:

$$U_{\mathrm{s}} = \frac{1}{2}\kappa_{\mathrm{s}}(r - r_0)^2 \tag{S5}$$

$$U_{\mathrm{b}} = \frac{1}{2}\kappa_{\mathrm{b}}\left(\theta - \theta_0\right)^2 \tag{S6}$$

where κ_{s} and κ_{b} are extensional and bending stiffnesses, r and r_0 is the instantaneous and equilibrium lengths of cylindrical segments, and θ and θ_0 are instantaneous and equilibrium angles formed by segments. The equilibrium length of actin segments ($r_{0,\mathrm{A}}$ = 140 nm) and an equilibrium angle formed by two adjacent actin segments ($\theta_{0,\mathrm{A}}$ = 0 rad) are maintained by extensional ($\kappa_{\mathrm{s,A}}$) and bending ($\kappa_{\mathrm{b,A}}$) stiffnesses of actins, respectively. The reference value of $\kappa_{\mathrm{b,A}}$ corresponds to the persistence length of ~9 μm [11]. The equilibrium length of ACP arms ($r_{0,\mathrm{ACP}}$ = 23.5 nm) and an equilibrium angle formed by the two arm segments of each ACP ($\theta_{0,\mathrm{ACP}}$ = 0 rad) are regulated by extensional ($\kappa_{\mathrm{s,ACP}}$) and bending ($\kappa_{\mathrm{b,ACP}}$) stiffnesses of ACPs, respectively. The equilibrium

length of motor backbone segments ($r_{s,M1}$= 42 nm) and an equilibrium angle formed by adjacent backbone segments ($\theta_{0,M}$ = 0 rad) are maintained by extensional ($\kappa_{s,M1}$) and bending ($\kappa_{b,M}$) stiffnesses, respectively. The value of $\kappa_{s,M1}$ is equal to that of $\kappa_{s,A}$, whereas the value of $\kappa_{b,M}$ is larger than that of $\kappa_{b,A}$. The extension of each motor arm is regulated by the two-spring model with stiffnesses of transverse ($\kappa_{s,M2}$) and longitudinal ($\kappa_{s,M3}$) springs. The transverse spring maintains an equilibrium distance ($r_{0,M2}$ = 13.5 nm) between the endpoint of a motor backbone and an actin segment where the arm of the motor binds, whereas the longitudinal spring maintains a right angle between the motor arm and the actin segment ($r_{0,M3}$ = 0 nm).

The repulsive force is represented by a harmonic potential [3]:

$$U_{\mathrm{r}} = \begin{cases} \dfrac{1}{2}\kappa_{\mathrm{r}}\left(r_{12} - r_{\mathrm{c,A}}\right)^2 & \text{if} \quad r_{12} < r_{\mathrm{c,A}} \\ 0 & \text{if} \quad r_{12} \geq r_{\mathrm{c,A}} \end{cases} \tag{S7}$$

where κ_{r} is the strength of repulsive force, and r_{12} is a minimum distance between two actin segments. Forces exerted on actin segments by bound motors and ACPs or by the repulsive force are distributed onto the barbed and pointed ends of the actin segments as described in our previous work [2].

Dynamics of ACPs

ACPs bind to binding sites located on actin segments every 7 nm without preference for cross-linking angles at a constant rate and also unbind from F-actin at a force-dependent rate determined by Bell's law [5]:

$$k_{\mathrm{u,ACP}} = \begin{cases} k^0_{\mathrm{u,ACP}} \exp\left(\dfrac{x_{\mathrm{u,ACP}} \left| \vec{F}_{\mathrm{s,ACP}} \right|}{k_{\mathrm{B}}T} \right) & \text{if } r \geq r_{0,\mathrm{ACP}} \\ k^0_{\mathrm{u,ACP}} & \text{if } r < r_{0,\mathrm{ACP}} \end{cases} \quad \text{(S8)}$$

where $\left|\vec{F}_{\mathrm{s,ACP}}\right|$ is a spring force acting on an ACP arm, $k^0_{\mathrm{u,ACP}}$ is the zero-force unbinding rate constant, $x_{\mathrm{u,ACP}}$ is sensitivity to an applied force, and $k_{\mathrm{B}}T$ is thermal energy. The values of $k^0_{\mathrm{u,ACP}}$ (= 0.115 s^{-1}) and $x_{\mathrm{u,ACP}}$ (= 1.04×10^{-10} m) are determined based on filamin A [12].

Dynamics of motors

Motor arms bind to binding sites on actin segments at the rate of $40N_{\mathrm{h}}$ s^{-1}, where $N_{\mathrm{h}} = 8$ is the number of myosin heads represented by each motor arm. The walking ($k_{\mathrm{w,M}}$) and unbinding ($k_{\mathrm{u,M}}$) rates of the motor arms are determined by the parallel cluster model to mimic the mechanochemical cycle of non-muscle myosin II [6, 7]. The details of implementation and benchmarking of the parallel cluster model in our models are described in detail in our previous study [13]. Note that $k_{\mathrm{w,M}}$ and $k_{\mathrm{u,M}}$ are smaller with larger applied loads because motors exhibit a catch-bond behavior. The unloaded walking velocity and stall force of motors are ~140 nm/s and ~5.7 pN, respectively.

Actin dynamics

The formation of F-actin is initiated from a nucleation event with the appearance of one cylindrical segment with polarity (i.e., with barbed and pointed ends) in a random orientation

perpendicular to the z direction. The polymerization and depolymerization of actins are simulated by the addition and removal of cylindrical segments, respectively, as in our previous studies [4]. The average length of F-actin ($<L_f>$) used in simulations is ~1 μm. This value is comparable to that estimated in our in vivo experiments. In addition, with the reference values of the rate constants for actin dynamics, each F-actin turns over every ~10 s.

Contraction of actin

In order to quantitatively analyze the network morphology, we evaluate the contraction of actin, using the spatial distribution of F-actins in activated regions whose dimension is 5×5 μm in x and y directions. First, the activated region is divided into $N_G \times N_G$ grids. We found that the optimal level of N_G is 20. All grids are indicated by their own coordinate, (*i, j*). In each grid, we measure the intensity of actin segments, $\rho_A^{i,j}$. Then, the standard deviation of $\rho_A^{i,j}$ in all 400 grids is calculated and divided by the mean value of actin density, $\overline{\rho_A}$. The normalized value represents the extent of actin contraction:

$$\text{Actin contraction} = \frac{1}{\overline{\rho_A}} \sqrt{\frac{\sum_{i=1}^{N_G} (\rho_A^{i,j}\big|_{i,j=1\ldots N_G} - \overline{\rho_A})^2}{N_G - 1}} \qquad \text{(Eq. S9)}$$

We calculate the time evolution of actin contraction by subtracting the initial value of actin contraction from the instantaneous value at each time step. From the time evolution curve, we obtain the maximal contraction and contraction at a plateau phase.

Contraction of myosin motors

We calculate the extent of motor contraction using the coordinates of the centers of motor thick filaments, $(\overline{x_{m,i}}, \overline{y_{m,i}})$. We calculate a distance between each thick filament and the center position of a currently activated region at each time step. We assume that the average of all the distances represents the rough size of motor clusters. The average is further divided by an initial value:

$$\text{Motor contraction} = \frac{r_i}{r_0} = \frac{\sum_{j=1}^{N_{m,j}} \sqrt{(x_{m,j} - \overline{x_{m,i}})^2 + (y_{m,j} - \overline{y_{m,i}})^2} \,/\, N_{m,j}}{\sum_{j=1}^{N_{m,0}} \sqrt{(x_{m,j} - \overline{x_{m,0}})^2 + (y_{m,j} - \overline{y_{m,0}})^2} \,/\, N_{m,0}} \qquad \text{(Eq. S10)}$$

In the time evolution of motor contraction, we average the maximum values of the motor contraction in all pulse periods to use it as an indicator for the extent of motor contraction.

Table S1. List of parameters employed in the model. For some of the parameters, references are provided if the parameters were determined based on specific previous studies.

Symbol	Definition	Value
$r_{0,A}$	Length of an actin segment	1.4×10^{-7} [m]
$r_{c,A}$	Diameter of an actin segment	7.0×10^{-9} [m] [14]
$\theta_{0,A}$	Bending angle formed by adjacent actin segments	0 [rad]
$\kappa_{s,A}$	Extensional stiffness of F-actin	1.69×10^{-2} [N/m]
$\kappa_{b,A}$	Bending stiffness of F-actin	2.64×10^{-19} [N·m] [11]
$r_{0,ACP}$	Length of an ACP arm	2.35×10^{-8} [m] [15]
$r_{c,ACP}$	Diameter of an ACP arm	1.0×10^{-8} [m]
$\theta_{0,ACP}$	Bending angle formed by two ACP arms	0 [rad]
$\kappa_{s,ACP}$	Extensional stiffness of ACP	2.0×10^{-3} [N/m]
$\kappa_{b,ACP}$	Bending stiffness of ACP	1.04×10^{-19} [N·m]
$r_{0,M1}$	Length of a motor backbone segment	4.2×10^{-8} [m]
$r_{0,M2}$	Length of a motor arm	1.35×10^{-8} [m]
$r_{c,M}$	Diameter of a motor arm	1.0×10^{-8} [m]
$\theta_{0,M}$	Bending angle formed by motor backbone segments	0 [rad]
$\kappa_{s,M1}$	Extensional stiffness of a motor backbone	1.69×10^{-2} [N/m]
$\kappa_{s,M2}$	Extensional stiffness 1 of a motor arm	1.0×10^{-3} [N/m]
$\kappa_{s,M3}$	Extensional stiffness 2 of a motor arm	1.0×10^{-3} [N/m]
$\kappa_{b,M}$	Bending stiffness of a motor backbone	5.07×10^{-18} [N·m]
N_h	Number of heads represented by a motor arm	4
N_a	Number of arms per motor	4
$k_{n,A}$	Nucleation rate of actin	0.001 [$\mu M^{-1}s^{-1}$]
$k_{p,A}$	Polymerization rate of actin at the barbed end	5 [$\mu M^{-1}s^{-1}$]
$k_{d,A}$	Depolymerization rate of actin at the pointed end	50 [s^{-1}]
$k_{u,ACP}^{0}$	Zero-force unbinding rate constant of ACP	0.115 [s^{-1}] [12]
$x_{u,ACP}$	Sensitivity of ACP unbinding to applied force	1.04×10^{-10} [m] [12]
κ_r	Strength of repulsive force	1.69×10^{-3} [N/m]
Δt	Time step	1.15×10^{-5} [s]
μ	Viscosity of surrounding medium	8.6×10^{-1} [kg/m·s]
k_BT	Thermal energy	4.142×10^{-21} [J]
C_A	Actin concentration	200 [μM]
R_M	Ratio of motor concentration to C_A	0.01
R_{ACP}	Ratio of ACP concentration to C_A	0.04
$<L_f>$	Average length of F-actins	~1 [μm]
ρ_f	Enhancement factor for faster actin polymerization	10 (5 in one simulation)
τ_f	Duration of faster actin polymerization	10 s (5 s in one simulation)
d_M	Time delay of myosin activation	5 s (0 s in one simulation)
τ_M	Duration of myosin activation	15 s

1. Li, J., et al., *Buckling-induced F-actin fragmentation modulates the contraction of active cytoskeletal networks.* Soft Matter, 2017. **13**(17): p. 3213-20.
2. Jung, W., M. P Murrell, and T. Kim, *F-actin cross-linking enhances the stability of force generation in disordered actomyosin networks.* Comput Part Mech, 2015. **2**(4): p. 317-27.
3. Kim, T., et al., *Computational analysis of viscoelastic properties of crosslinked actin networks.* PLOS Comput Biol, 2009. **5**(7): p. e1000439.
4. Mak, M., et al., *Interplay of active processes modulates tension and drives phase transition in self-renewing, motor-driven cytoskeletal networks.* Nat Commun, 2016. **7**: p. 10323.
5. Bell, G.I., *Models for the specific adhesion of cells to cells.* Science, 1978. **200**(4342): p. 618-27.
6. Erdmann, T., P.J. Albert, and U.S. Schwarz, *Stochastic dynamics of small ensembles of non-processive molecular motors: the parallel cluster model.* J Chem Phys, 2013. **139**(17): p. 175104.
7. Erdmann, T. and U.S. Schwarz, *Stochastic force generation by small ensembles of myosin II motors.* Phys Rev Lett, 2012. **108**(18): p. 188101.
8. Tyska, M.J., et al., *Two heads of myosin are better than one for generating force and motion.* Proc Natl Acad Sci U S A, 1999. **96**(8): p. 4402-7.
9. Underhill, P.T. and P.S. Doyle, *On the coarse-graining of polymers into bead-spring chains.* J Non-Newtonian Fluid Mech, 2004. **122**(1): p. 3-31.
10. Clift, R., J.R. Grace, and M.E. Weber, *Bubbles, drops, and particles*. 2005: Courier Corporation.
11. Isambert, H., et al., *Flexibility of actin filaments derived from thermal fluctuations. Effect of bound nucleotide, phalloidin, and muscle regulatory proteins.* J Biol Chem, 1995. **270**(19): p. 11437-44.
12. Ferrer, J.M., et al., *Measuring molecular rupture forces between single actin filaments and actin-binding proteins.* Proc Natl Acad Sci U S A, 2008. **105**(27): p. 9221-6.
13. Kim, T., *Determinants of contractile forces generated in disorganized actomyosin bundles.* Biomech Model Mechanobiol, 2015. **14**(2): p. 345-55.
14. Kishino, A. and T. Yanagida, *Force measurements by micromanipulation of a single actin filament by glass needles.* Nature, 1988. **334**(6177): p. 74-6.
15. Meyer, R.K. and U. Aebi, *Bundling of actin filaments by alpha-actinin depends on its molecular length.* J Cell Biol, 1990. **110**(6): p. 2013-24.

Protocol

Flowchart of image analysis procedure to study formin pulse dynamics

Costache, Prigent Garcia et al.

Flowchart of the image analysis procedure

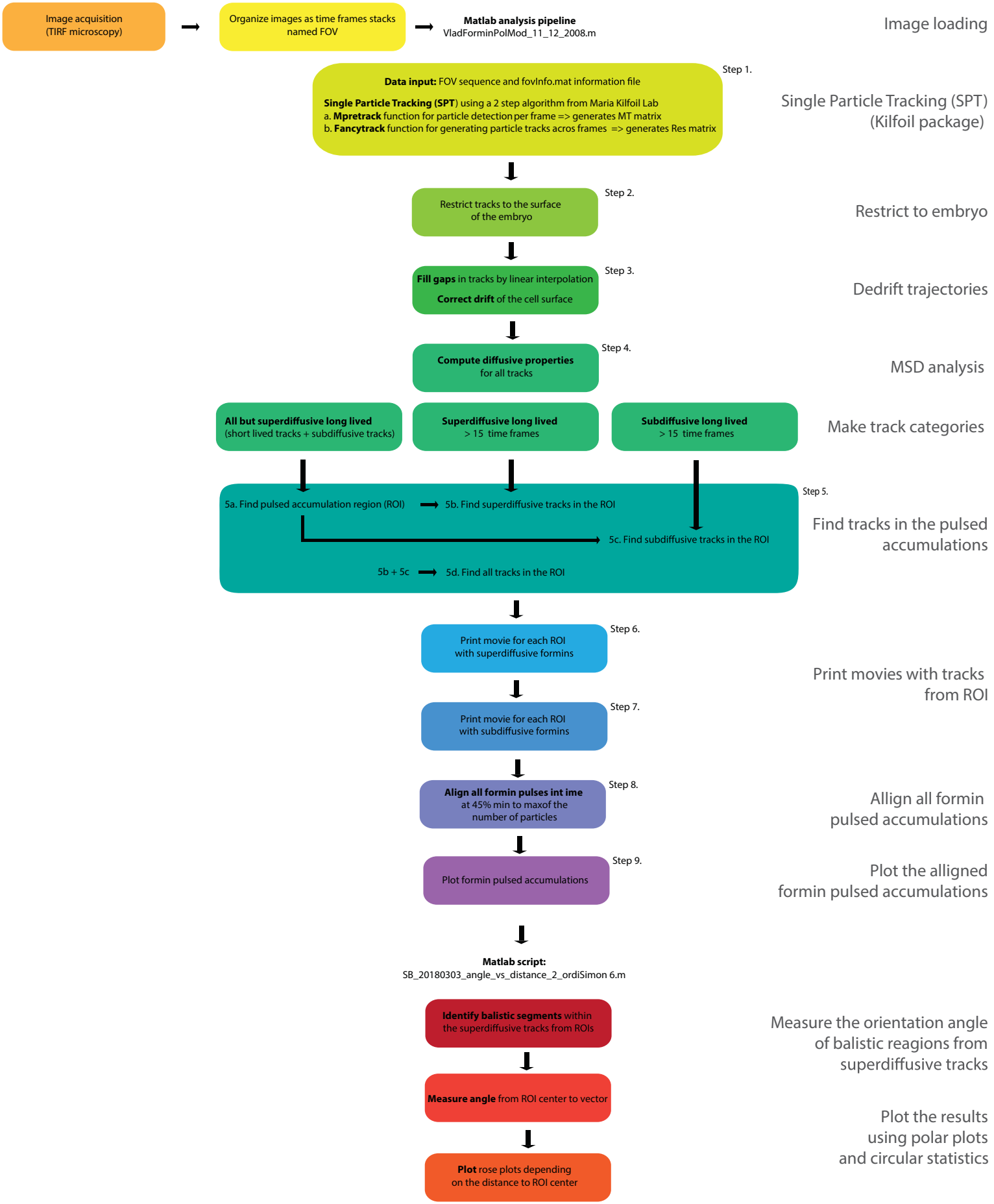

Flowchart of the image analysis pipeline for measuring formin trajectories mobility and their orientation during pulsed accumulations at the cortex.

All 9 steps are organized as code sections that include single particle tracking (SPT) using a previously published algorithm [1]. Data is further on managed as a matrix, throughout further processing steps: (1) elimination of particles outside the cell cortex, (2) correction of the drift and the MSD analysis (3) separation of the different mobility classes of formins : superdiffusive/ballistic (active formins), subdiffusive/confined (activated formins). Short-lived and subdiffusive particles serve as support to define the adaptive region of interest (ROI) corresponding to each pulsed accumulation region of formins. Pulses are then aligned in time with respect to the threshold ratio between minimum (before) and the maximum number of particles during the pulse, set at 45%. This analysis sets the stage for synchronizing across pulses the time sequences of arrival of the different formin populations at the cell cortex. A second script is used to measure the orientation angle between (1) the displacement vector of the active formins and (2) a vector starting at the center of the ROI/pulse and ending on the starting point of displacement. Results are printed as rose plot with circular statistics included. Circular statistics are performed using a matlab toolbox developed by Philipp Berens[2]. Images used in this analysis pipeline were obtained by near-TIRF microscopy at continuous 20 fps stream, mostly 16 bit, 6000 time frames stacks, 512x512 pixels, saved as single image sequences, named FOV that were directly recognized by Matlab during the first step of the pipeline.

1. V. Pelletier, N. Gal, P. Fournier, M. Kilfoil, *Phys. Rev. Lett.* **102**, 188303 (2009).

2. P. Berens, *Journal of Statistical Software*. **31**, 1–21 (2009).

Supplemental Movie 1

Click here to access/download

Supplemental Videos and Spreadsheets

Movie_S1.mov

Supplemental Movie 2

Click here to access/download

Supplemental Videos and Spreadsheets

Movie_S2.mov

Supplemental Movie 3

Click here to access/download

Supplemental Videos and Spreadsheets

Movie_S3.mov

Supplemental Movie 4

Click here to access/download

Supplemental Videos and Spreadsheets

Movie_S4.mov

Supplemental Movie 5

Click here to access/download

Supplemental Videos and Spreadsheets

Movie_S5.mov

Supplemental Movie 6

Click here to access/download

Supplemental Videos and Spreadsheets

Movie_S6.mov

Supplemental Movie 7

Click here to access/download

Supplemental Videos and Spreadsheets

Movie_S7.mov

Supplemental Movie 8

Click here to access/download

Supplemental Videos and Spreadsheets

Movie_S8.mov

Supplemental Movie 9

Click here to access/download

Supplemental Videos and Spreadsheets

Movie_S9.mov

Supplemental Movie 10

Click here to access/download

Supplemental Videos and Spreadsheets

Movie_S10.mov

Complementary results:

I. Formin activity is not significantly influenced by the presence of Arp2/3 in our model

G-Actin is the common substrate of two enzymes: Formin and the Arp2/3 complex. In yeast and in mammal cells, both proteins have been shown to be in a competition for G-Actin and this competition has an impact on the activity of both proteins (Burke et al., 2014; Rotty et al., 2015; Suarez et al., 2015). In order to test this hypothesis during development, we decided to measure the variation in Formin activity when its competitor, Arp2/3, is depleted in the early *C. elegans* embryo. We hypothesized that if Formin does not have to compete with Arp2/3 for Actin monomers to elongate F-Actin, it will polymerize faster and/or for a longer time. Using single molecule imaging, we followed the variation in Formin speed and time of elongation. During the embryonic cell cycle of *C. elegans*, two phases prior to the cytokinesis can be observed: a phase when the cortex is highly dynamic and pulsed contractions, in which Formin CYK-1 are locally transiently more recruited, can be observed (the interphase) and a second phase where the cell is more round and pulsed contractions have stopped (the mitosis). We decided to measure the speed of the Formin and the length of the tracks separately for these two phases in the anterior cell (AB) of the 2-cell stage embryos.

We imaged 2-cell stage *C. elegans* embryo carrying an overexpression of the *cyk-1* gene fused with a GFP (*cyk-1::gfp*) depleted by RNAi of the Arp2 subunit (ARX-2), disrupting the function of the Arp2/3 complex. We tracked the molecules and selected the superdiffusive Formins as they are the ones actively polymerizing the Actin filaments (active, elongating Formins). We observed a significant difference of speed in the control experiment between interphase and mitosis (1.15 $\mu m.s^{-1}$ and 1.12 $\mu m.s^{-1}$ respectively (Fig. 21A), consistent with what was observed in the Article 2 of this manuscript (Costache, Prigent Garcia *et al.*), but surprisingly with lower values). This significant decrease in speed is maintained when ARX-2 is depleted (1.16 $\mu m.s^{-1}$ in interphase and 1.09 $\mu m.s^{-1}$ during mitosis (Fig. 21A)). No significant difference could be observed when the same phase is compared with or without depletion of the Arp2/3 complex. This result suggests that the competition between Arp2/3 and Formin does not affect Formin's speed at these stages. We measured the length of the tracks for the control and no significant difference could be observed between the two phases (2.75 s for interphase and 2.61 s for mitosis) (Fig. 21B). Interestingly we observed a difference between

the two phases when ARX-2 is depleted: the length of the tracks is shorter at interphase (2.46 s) than during the mitosis (2.78 s), this is supported by the observation of a significant difference at the interphase with or without ARX-2, tracks being shorter when ARX-2 is depleted (Fig. 21B). This observation points surprisingly towards an Arp2/3 dependent effect on the length of Formin tracks depending on the cell cycle phase.

Together these results suggest that Formin speed is not regulated by the availability in Actin monomers but that the time of elongation and/or the length of Actin filament polymerized can be dependent on this availability during interphase, whereas during mitosis track length is more robust or more tightly regulated. It is important to note that considering how the data for the track length was collected (see Methods for details), all the short tracks (too short to classify the Formin behavior between sub- and superdiffusive and give a satisfying measurements of the speed) were excluded from the selection, this inducing a bias towards longer tracks. This is particularly important as we do not measure the speed and track length of all the active Formins present in the AB cell but only a sample. This method of selection can mask a potential decrease in the statistical mode of the track length.

Formin activity is regulated by Arp2/3 during cytokinesis, as shown in *C.* elegans embryo, by preventing excessive activity (Chan et al., 2019). As the Formin speed is shown to decrease during cytokinesis in Costache, Prigent Garcia *et al.*, we could hypothesize that this is controlled, at least partly, by the Arp2/3 complex. It would be interesting in one hand to measure if the track length is also modified during this phase and on the other hand if the decrease in speed (and perhaps in track length) is maintained in absence of the Arp2/3 complex.

Taking back the data used for calculating the speed in Costache, Prigent Garcia *et al.*, I measured the track length for this set of data from 1-cell stage interphase to 4-cell stage mitosis (Fig. 21C). Surprisingly, in this experiment, we can observe a significant decrease in track length at 2-cell stage between interphase and mitosis, underlying the lack of reproducibility in the measurements of the track length. This observation proves the limit of the methods in measuring the track length. The same cannot be said for the measurements of the speed, as even if the absolute value might vary from an experiment to another, the interpretation still stands.

In conclusion, these results show that Formin speed is not dependent on the sequestration of the monomers by the Arp2/3 complex by itself.

II. The Actin filament length does not drastically vary between interphase and mitosis

Early steps of development rely on cell division of the embryo without significant increase in amount of available Actin monomers. One main incognita in all living systems is the Actin filament length and the scaling of such length depending on the cell cycle phase and the developmental stage. In this work, we used single-molecule analysis to address this question.

We defined that the Actin filament average length can be calculated as following:

$$L = \frac{v}{\frac{1}{t_e} + \frac{1}{t_{dep}}}$$

with: L = average length of Actin filament (in µm)

v = Formin speed (in µm/s)

t_e = Formin elongation duration (in s)

t_{dep} = Actin time of depolymerization (in s)

Formin speed was collected previously. The lifetime was calculated for the total Formin population in AB cell and Formin population fraction, separated according to their lifetime, revealed that I had two populations of Formin tracks: a short one and a long one. We hypothesized that the short population corresponded to a mixture of tracks by sub- and superdiffusive Formins whereas the long one was the population composed exclusively of superdiffusive Formins. To exclude the population of subdiffusive Formin tracks, we operated a curve fitting of the lifetime data. Using a double-exponential curve fitting, we evaluated for each embryo what was the proportion of each fraction of Formin population. We fitted as two exponentials (one for each Formin population, see details in Method section).

Then, we evaluated what was the average lifetime duration for each population at interphase and during mitosis, in average of all embryos (Fig. 21E-H). Following our hypothesis that elongating Formins are the one actively polymerizing Actin filament, we used the average lifetime of the long-elongating population as t_e.

Then, we evaluated Actin time of depolymerization. We imaged Actin at single-molecule level using a strain carrying Actin fused with a GFP as an overexpression. We tracked

Actin molecules and as $k_{off} = \frac{1}{t_{dep}}$, we measured the unbinding rate at interphase and mitosis (Fig. 21D).

Putting this together, I could get an approximation of the Actin filament length. We calculated that in average an Actin filament measures ~1,79 µm at interphase and ~1,75 µm during mitosis.

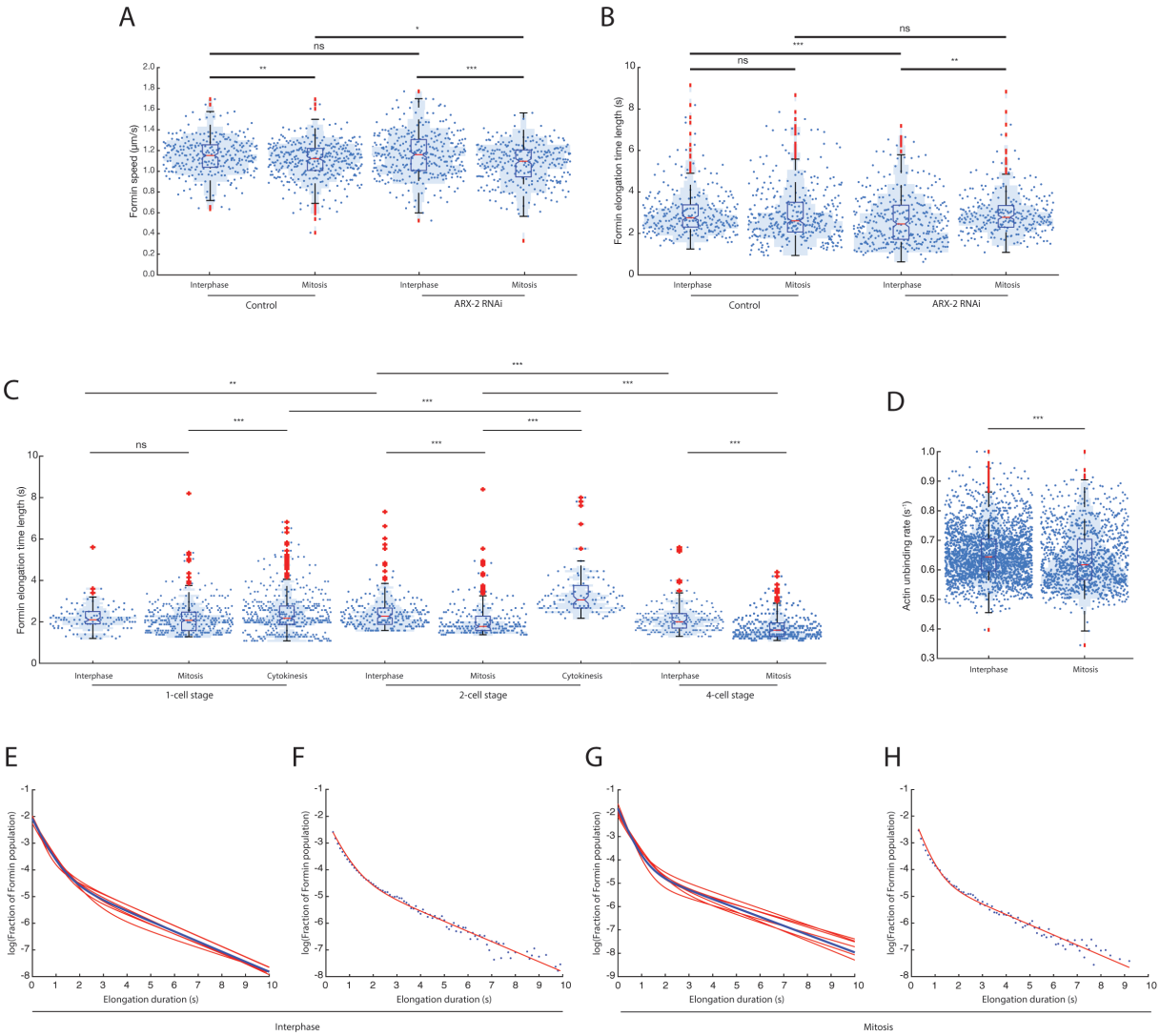

Figure 21. Complementary results. Formin speed (A) and elongation time length (B) in interphase and mitosis in wild-type context (left) and Arp2/3 depleted (RNAi against ARX-2) at 2-cell stage. (C) Formin elongation time length depending on the developmental stage and the cell cycle stage. (D) Actin unbinding rate (k_{off}) depending on the cell cycle stage. (E-H) Fraction of Formin population depending on the Formin elongation duration at interphase (E-F) and mitosis (G-H) at 2-cell stage. (E, G) Fitted curves of each embryo (red) and mean (blue). (F, H) Dispersion of the mean (blue dots) and fitted curve to this dispersion (red curve).

In conclusion, my result show that even though Formin speed significantly decreases between interphase and mitosis (~0,03 µm/s decrease) and Actin filament average length does not drastically change and is stable at a bit less than 1,8 µm.

Methods

Strains

SWG282 *gesIs008[Pcyk-1::CYK-1::GFP::cyk-1UTR, unc-119+]* and JH1541 *unc-119(ed4) III; pJH7.03[pie-1p::GFP::actin⁚⁚pie-1 3' UTR + unc-119(+)]* worms were used.

C. elegans culture

We cultured *C. elegans* at 20°C under standard conditions ((Brenner, 1974)).

RNAi assay

Worms carrying *cyk-1::gfp* in overexpression at L3-L4 stage were fed an RNAi against *arx-2* during 40 h at 25°C. To control the effectiveness of the RNAi worms carrying UTR::GFP (proxy for F-Actin) were placed in the same conditions and checked for typical phenotype of ARX-2 depletion at the moment of imaging.

Formin Speed measurement analysis

We performed single-molecule imaging as described previously. We mounted the embryos between glass slides with squares wells of 20 µm thick Epoxy and #1.5 coverslips (170 µm thick) in 2.5 µL of 0.22 µm filtered water with 15.4 µm polystyrene beads. We imaged single molecules using 50% of 90mW of 488 nm laser, 50 ms of exposure, no delay between frames, using Photometrics 95B prime 22 mm sCMOS camera. Laser angle was set to 65°. Room temperature maintained between 19 and 20.5 °C. After acquisition, we averaged two consecutive frames, in order to achieve 10 frames per second using ImageJ software (NIH Image, Bethesda, MD). We used Matlab implementation of the Crocker-Grier algorithm (Crocker and Grier, 1996) by the Kilfoil lab for single-particle tracking. We selected manually a ROI to exclude tracks from residual particles outside the cell for each stage: whole embryo for one-cell stage, anterior (AB) cell for two-cell stage, posterior AB daughter cell (ABp) for four-cell stage. Each stage was separated into three phases based on observed cortical dynamics: interphase (pulsed contractions at the cortex); mitosis (cortex "stable" with no identifiable pulsed contractions); and cytokinesis (visualized by cleavage furrow assembly).

Subsequent image analysis was performed in Matlab. We selected the trajectories based on their anomalous diffusion coefficient D and scaling exponents α. Tracks were classified as subdiffusive and superdiffusive, and we selected specifically superdiffusive

trajectories. In order to calculate the velocity only during elongation of actin filaments, we performed a second selection to exclude tracks displaying multiple behaviors during their lifetime (due to switches between subdiffusive and superdiffusive) and retained tracks displaying exclusively superdiffusive behavior. Finally, we screened individual trajectories manually to retain tracks that were closer to a line to avoid skewing our estimates of particle speed.

Statistical analysis

56 to 80 tracks per embryo were selected (see Table 3 in appendix for details). Normal distributions were verified. Two-sample Student tests (t-tests) were performed to measure the significance of the difference in speed between each stage and phase. *** means p<0.001, ** means p<0.01, ns: non-significant.

Actin length estimation

We tracked Formin molecules at AB cell scale similarly to what is described above at interphase and during mitosis. We used track duration as proxy for Formin elongation duration. We evaluated the fraction of Formin population regarding their lifetime. We proceeded the distribution in fraction of population as two exponentials, following this expression:

$$y = \log\left(\frac{a}{b}e^{-\frac{x}{b}} + \frac{1-a}{c}e^{-\frac{x}{c}}\right)$$

where: a is the fraction of the b population and b and c are the average Formin track duration. We collected the average lifetime for the 'long' fraction population.

We imaged 2-cell stage embryos carrying an overexpression of Actin fused with a GFP at single-molecule level at interphase and during mitosis and analyzed it similarly to what has been described above for Formin. We calculated Actin k_{off} by evaluating the molecules that have unbound from the embryonic cortex of the AB cell per second.

We estimated the Actin filament average length at interphase and during mitosis, following:

$$L = \frac{v}{\frac{1}{t_e} + \frac{1}{t_{dep}}}$$

with: L = average length of Actin filament (in µm)

v = Formin speed (in µm/s)

t_e = Formin elongation duration (in s)

t_{dep} = Actin time of depolymerization (in s)

Noting that Actin $k_{off} \sim \frac{1}{t_{dep}}$.

Author contributions:

François B. Robin and Serena Prigent Garcia planned the project. S. Prigent Garcia and Anaïs Djebara performed the experiments and analysis in Fig. 21A-B. S. Prigent Garcia performed the experiment and analysis in Fig. 21C, E-H. F.B. Robin performed the experiment and S. Prigent Garcia the analysis in Fig. 21D. S. Prigent Garcia and A. Djebara prepared the figure.

Discussion and Perspectives

The cortical Actomyosin network architecture has been of interest in morphogenesis for more than 25 years now. Repeatedly throughout development this network undergoes a variety of changes in its shape, but very little in its composition. It is mainly composed of two proteins: filament of Actin and minifilaments of Myosin molecular motors, the combination of these two molecules gives the ability to contract to this network. These contractile properties are essential during development and pulsed contractions have been shown to be the key player for several morphogenetic events in Vertebrates and in Invertebrates, at 1-cell stage as in late embryogenesis. Its universality makes it an important material to look at and to understand, its composition is so well preserved throughout evolution and yet the shapes emerging from morphogenesis are so diverse. Even if we know what are the elements composing the Actomyosin cortex, we fail to understand how its organization is regulated. Specifically, in this work, we tackled that we had yet to decipher the organization and the regulation of said organization of the pulsed contractions at the cortex at early stages of development. The control of this organization is key to drive the force generation across the cell and the tissue, which is crucial to achieve a successful morphogenesis.

On one hand, our work offers a better understanding on this versatile material. On the other hand, it shows that by its simplicity it can be of a great help in modeling and understanding more complex mechanism occurring during an organism development. To achieve this, I have used a simple model organism the *C. elegans* embryo and used cutting-edge techniques, including single molecule imaging with TIRF microscopy, numerical simulations and mathematical modeling to addressed fundamental questions about the biochemical control of the Actomyosin, and its interplay with the mechanical properties of the embryonic cell.

Actomyosin network dynamics is dependent on a biochemical input: the RhoA activation cascade at early stages of the development. It is characterized by a local pseudo-periodic activation at the cortex, which triggers recruitment and activation of downstream effectors. Delay in response has been previously reported in this activation cascade between RhoA activation and recruitment of ultimate effectors (Michaux et al., 2018).

1. <u>Formin elongating population arrives first and set a polar network at the pulse location</u>

On one side, the activation cascade consists on the recruitment and activation of the Formin, which is a processive elongator of Actin filaments, and attaches to the barbed-end of

the filament. We have shown in this study that Formins build a polar network by polymerizing with the (+)-end outwards of the pulsed contraction. This process occurs until all the local barbed-ends of the pulsed contraction are saturated by this elongating Formins and we could see the emergence of a new population appearing a few seconds after the elongating Formins and composed of Formins which are activated by RhoA but not effectively active, e.g. not elongating any filament as no barbed-ends are available anymore. In this work, I could show that actually the speed of elongation of the Actin filament by the Formin is reduced during cytokinesis, which we could explain by the densification of the network at the contractile ring, reducing the availability and diffusion of the Actin monomers. This availability might be explained by this 'crowding' of the network by long Actin bundles, or by the sequestration of Actin monomers by the Arp2/3 complex. To test this second hypothesis, I measured Formin speed or time of elongation in a Arp2/3 depleted context but did not observe a significant difference.

To confirm this, I propose several lines of experiments that could confirm this initial observation:

First, Arp2/3 requires NPFs to be activated, to be able nucleate a new Actin branch. I propose that depletion of such cofactors (WASP/WAVE) would lead to actually deplete the pool of monomers available to be taken by Arp2/3. Therefore, the pool of free monomers would be increased, in order to mimic a decrease in the competition for monomers. Therefore, we could repeat the measure of Formin speed and elongation duration using single-molecule imaging in a context where WSP-1 or WVE-1 are depleted by RNAi (both being expressed at early cell stages, their depletion not leading to significant phenotype in wild-type embryos during cytokinesis at 1-cell stage (Canman et al., 2008)). This depletion would lead to decrease in activity of the Arp2/3 complex, being less activated by WASP/WAVE, and we would expect this to lead to less sequestering of monomers in branched networks. Therefore, we would expect an increase in Formin speed or elongation duration in this context.

Formin do not use free monomers for Actin filament polymerization but Profilactin complex. If the system is robust against the depletion of WASP/WAVE, it might mean that the pool of free monomers is just being increased and the pool of monomers bound by Profilin is stable. Profilin is already pointed as the platform for monomer competition in cell (Suarez et al., 2015) and might, therefore, being implicated in regulating the pool of Actin monomers available to Formin-mediated filament polymerization. Experimentally increasing cellular

Profilin concentration might increase the pool of these Actin monomers. Following Formin speed and elongation duration at single-molecule level using TIRF microscopy, similarly to what has been done during my PhD, might give an answer as if Formin activity is actually regulated by Arp2/3 or synergistically regulated with Arp2/3 complex.

An alternative experiment to test our hypothesis would be to measure the impact of Formin on Arp2/3 activity. Previous work by Chan *et al.* has shown that Arp2/3 regulates the Formin activity during cytokinesis (Chan et al., 2019). We could hypothesize that the opposite is also true and that Formin might regulate the Arp2/3 activity. Therefore, depletion of Formin pool would make Actin subunits available to Arp2/3 complex and decrease the competition between these two proteins for monomers, resulting in an increase in Arp2/3 complex activity and an increase in filament branching. By experimentally depleting Formin (with an RNAi targeted against *cyk-1*) and using single-molecule imaging, we could evaluate the level of branching in the cell and compare, relatively, the context where Formin is depleted, or alternatively where Profilin is mildly depleted, with a wild-type context. Both total depletions of Formin and Profilin being lethal, this would need viability control in order to avoid artefactual variation in Actin filament branching. Increase in relative number of branching would indicates regulation of Arp2/3 activity by Formin and stability in this number of branching would indicate robustness in the system and a more global regulation of both proteins. These experiments would give us a better idea of the importance of the balance between monomers made available to Formin by Profilin and those made available to Arp2/3 by NPFs, this being key to the regulation of both proteins activity at each cell cycle step and show us if the co-regulation of these proteins is dependent on the stage of the cell cycle.

2. <u>Myosin dynamics explains its recruitment kinetic delay</u>

On the other side of the cascade, RhoA activates and recruits ROCK which phosphorylates the Regulatory Light-Chain of the Myosin. Myosin binds on the Actin filament and forms a mini-filament composed of several Myosin hexamers, several heads of the Myosin Heavy-Chains binding to the same filament. My results revealed that the different steps of this activation cascade occur with a kinetic delay of 4.5 s between RhoA activation and Myosin recruitment.

Importantly, I used a proxy to follow RhoA activation (RhoA-binding domain of Anilin that only binds to RhoA once activated). As it is a proxy, one could argue that it can affect the

delay measurement in my experiment. Real kinetic delay cannot be smaller as the proxy I used can only be tracked once RhoA is activated and the activated RhoA/proxy complex is recruited at the cortex. Therefore, real kinetic delay between the recruitment of the two proteins can only be equivalent or greater; in this work, I could be underestimating the delay between RhoA and Myosin. Importantly, my data strongly suggests that not all the steps in the activation cascade are equivalent in term of kinetic delay. Therefore, a delay between an early effector and the downstream effector cannot be sliced in equivalent kinetic delay of each step of the activation cascade.

Single-molecule observations of Myosin have shown in this thesis that most of this kinetic delay can be explained by the dynamic of the Myosin, its binding rate (K_{on}) and its unbinding rate (k_{off}), following:

$$\frac{dN}{dt} = K_{on} - k_{off} * N$$

with N: number of molecules at the cell surface

My results strongly support a model in which the pseudo-periodic activation of RhoA has a strong effect on Myosin k_{off} and a mild effect on Myosin K_{on}, leading to an out-of-equilibrium system always trying to keep up with the fluctuation of the dynamic parameters, to keep up with the target density (N*) defined by the K_{on} and k_{off} as: $N^* = \frac{K_{on}}{k_{off}}$. The kinetic delay between target density and actual variation in number of molecules is greater if the k_{off} is small, making the system much more robust to change and hence slower to react to variation. Biochemical perturbation in the binding and unbinding rate (as I did in this work by measuring Myosin dynamics in a context where the Myosin Phosphatase is mutated and not functional) of the Myosin actually do not affect the delay but put the system in a state where the variation in number of molecules is smaller, as it would always be 'at full regime', much closer to the high extreme value of the target density set up by the K_{on} and k_{off} compared to the control situation. Considering that the delay in this cascade can be almost completely explained solely by the observation of the dynamics of the Myosin, this simple model where the number of molecules at the cortex is only dependent of this two parameters, K_{on} and k_{off}, is valid to explain any kinetic delay that can be observed in any activation cascade where the ultimate effector is not limited in availability. Therefore, any activation cascade, would it be during morphogenesis or elsewhere (such as the kinetic delay observed when an activation cascade

is triggered thanks to an optogenetic tool for example) can see its kinetic delay explained by this model.

To go further with this model, we could try explain the temporal dynamic of another activation cascade in another context. HER2 is an epidermal growth factor tyrosine kinase and its amplification occurs in ~25% of all breast cancer, this causing aberrant constitutive activation of the signaling pathway and is correlated with a poor prognosis (reviewed in (Loibl and Gianni, 2017)). Temporal dynamic of activation cascade of HER2 is yet to be decipher. LET-23 is the only EGF receptor in *C. elegans* and is an ortholog of HER2. In physiological context, we could observe the dynamics of LET-23 and predict the temporal kinetics in this activation cascade. Using single-molecule imaging, we could follow the K_{on} and k_{off} of a LET-23 fused to a GFP. Such experiment would give us a better understanding on the difference in dynamic of LET-23 in wild-type versus in mutant context where LET-23 is overexpressed (mimicking the activation cascade dynamics when constitutively activated when HER2 is overexpressed). Such result would give us an insight in difference in dynamics of this protein and would give a strong tool to observe differences when using drugs to try rescue acute activation of LET-23 and HER2 cascade.

3. Myosin activation is globally regulated

Myosin activation is also dependent on the activity of its Phosphatase. ROCK, in addition to activate the Myosin by phosphorylation of the Light-Chain, inhibits the activity of the Myosin Phosphatase. The observation of Myosin Phosphatase Targeting subunit (MYPT) fused with a GFP at the cortex shows a pulsatile behavior of this protein. Trying to achieve a global overview of the Myosin biochemical dynamic, I tried to measure the delay at a pulse location between Myosin Heavy-Chain and the MYPT. Remarkably, the periodicity of the pulsed contraction of MYPT seems completely different compared to the one of the Myosin, making it impossible to calculate any kinetic delay between the two proteins. The frequency of MYPT activation and deactivation seems to be higher than the Myosin one. This result suggests that the unbinding of the Myosin is not dependent of the dephosphorylation of the Myosin by the Phosphatase at a local level. This observation points towards a global regulation of the Myosin by the Phosphatase rather than local.

In this work, I followed ROCK and Myosin recruitment at the cortex, measuring the kinetic delay between their local recruitment as we used lines where the endogenous gene

coding for these proteins were replaced, thanks to the CRISPR/Cas9, by a gene expressing the wild-type gene fused to a fluorescent marker, this giving us no information about the activation of these proteins. As a consequence, we can conclude that the **recruitment** of Myosin by ROCK is local.

These results taken together with the observation, in Prigent Garcia *et al.*, that there is no kinetic delay between Myosin Light-Chain and Heavy-Chain, suggest that the Myosin hexamer is assembled before its local recruitment at the cortex. I propose as a mechanism that the phosphorylation level of the Myosin (and therefore its activation status) is controlled before its recruitment at the cortex, before its binding to the Actin filament. Therefore, I propose that the hexamer assembly and its activation (or not) through phosphorylation occurs first, meaning that the action of ROCK or Myosin Phosphatase on the Myosin Regulatory Light-Chain occurs in the cytoplasm and before or after this, Myosin is assembled in mini-filaments. Then the whole hexamer is recruited at the pulsed contraction location, the Myosin heads directly binding to the Actin filament. This points towards a separation in time and space of recruitment and activation of the Myosin: a global regulation of its activation but a local regulation of its recruitment.

In order to test this hypothesis, we could observe Myosin dynamic in a context where Myosin Phosphatase is optogenetically addressed to the membrane, somehow forcing the deactivation to be local at the cortex. Precisely we could use the TULIPs method (Strickland et al., 2012), a strain would carry the LOVpep bound to the plasma membrane, the ePDZ fused to Nanobies that recognize the GFP and the MYPT fused with a GFP (*mel-11::gfp* strain used in Prigent Garcia *et al.*), shining light (blue laser <500 nm reported by Strickland *et al.*) to the embryo would address the MYPT to the membrane as long as the laser is shining. We could see if Myosin k_{off} is modified and, even, if the pulsed contraction structure is maintained in this context or is disrupted by the potential mislocalization of the Myosin activation. Additionally, we could use this reversible technique to bind and unbind MYPT to the membrane at a different periodicity to the one observed and measure Myosin dynamics all across the cortex to see if it is perturbed by the change in periodicity of the MYPT, or even if the Myosin pulse period is increased by this context. These experiments would give a better understanding of the biochemical regulation of the Myosin and how this molecular motor is assembled within the cell.

4. The model also explains Actin kinetic delay

Intuitively, an efficient Actomyosin contraction seems to depend on the efficient recruitment of Actin and Myosin at the pulsed contraction. Actin and Myosin being both recruited by the RhoA activation cascade, we hypothesized that recruitment of both proteins was synchronous. In this work, I do not have a direct measurement of the kinetic delay between RhoA activation and Actin recruitment but I have an indirect value. In addition to the delay of 4.5 s between RhoA activation and Myosin recruitment, I measured a significant delay of 0.5 s between Actin and Myosin recruitment. Again, as I used a proxy for Actin recruitment (Calponin homology domain of Utrophin which binds to F-Actin, with an unknown kinetic delay) I might be underestimating this delay. Nevertheless, these results show that Actin is being recruited before Myosin, which indicates that the Myosin might be directly recruited on the Actin filament and therefore points for a requirement for the presence of some cables of Actin prior to an effective Myosin recruitment. Hence, the delay between RhoA and Actin is in the range of the kinetic delay observed between RhoA and Myosin, most probably slightly smaller as Actin is recruited briefly before Myosin. Actin single-molecule analysis has shown that, remarkably, RhoA seems to have a much stronger effect on the Actin K_{on} (fluctuation of the K_{on} between basal level and peak is bigger than the one observed with Myosin, in addition to have a more elevated absolute value) than on its k_{off} compared to the effect of RhoA on Myosin. Nevertheless, again, the observed delay can be explained by the dynamic of Actin, underlying the robustness of the model even though the parameters are influenced differently. Remarkably, perturbation in Actin turnover by depletion of the Cofilin shows an increase in the pulse period, a flattening effect on Myosin k_{off} variation, little to no effect on Myosin K_{on} and yet the delay between target density and real variation in number of molecules is not affected or rather increased. This shows again tight connection between Actin and Myosin recruitments but robustness in the system against variation or disruption of the delay.

Capping Proteins (CP) bind to the filament barbed-ends, preventing them from being elongated by the Formins. Work by Shekhar *et al.* has shown competition for barbed-ends between CP and Formin, suggesting that CP and Formin regulate each other activity (Shekhar et al., 2015). During a pulsed contraction, the number of barbed-ends is limited, the recruited (but not elongating) Formins emerge from this limitation in barbed-end availability. Remarkably, CP are also locally recruited at the pulsed contraction in the *C. elegans* early embryo. Similar to what I have done before in this work, I measured the kinetic delay between

the recruitment of CP and Myosin. Interestingly, I measured a delay of 0.5 s, with no significant difference with the one I measured between Actin and Myosin, suggesting that Actin and CP are recruited simultaneously. Two possible explanations can be proposed. The first one is that Actin barbed-ends are capped when recruited and then decapped so that Formin can bind to it, either Formin directly competes with CP to decap Actin filament or a decapping process occurs prior to Formin binding. The second possibility is that, at first, Actin filaments are recruited bare, in bulk and are either quickly capped by Formin which will immediately start to polymerize and drive barbed-ends outside of the pulsed contraction location or capped by CP until eventually all barbed-ends are saturated by one or the other protein, leaving no bare barbed-end available to the rest of the recruited Formin, forming the subdiffusive population. This competition could be of help in the termination of the pulse contractions as it stops new Actin polymerization. This second model is supported by the fact that I measured the Formin recruitment appearing 4.5 s before the Myosin recruitment, pointing to a delay ~4 s between Formin and Actin recruitment and between Formin and CP at the pulse location. Formin elongating population starts Actin filament polymerization ~4 s before CP recruitment and is synchronous with the Actin K_{on} increase, k_{off} decrease and variation in target density. This result suggests that CP are responsible for the depletion of available barbed-ends, making a new population emerge of inactive barbed-ends and regulate the termination of new filament polymerization by Formin at the pulsed contraction location.

To test and confirm this hypothesis, we would need *in vivo* real-time observation of the barbed-ends during pulsed contractions. If Actin barbed-ends are recruited bare we should be able to see a significant amount of barbed-ends not bound by Formin nor CP, specifically in greater number in early pulses and decreasing with time in the pulses. If this population is significant, we would be able to see some bare barbed-ends. If none (or a very limited amount) is observed then Actin barbed-ends are probably recruited capped. Real-time *in vivo* imaging not giving a resolution high enough, we could image Actin in floxed embryos and have a count of barbed-ends, Formins, CP and other molecules that might be bound to the barbed-ends using super-resolution imaging in fixed embryos (similar to (Raz-Ben Aroush et al., 2017)). Such *in vivo* imaging would provide a new insight into Actin network composition during pulsed contractions.

5. *In vivo* Actin filament average length does not dramatically change during the cell cycle

Currently, we lack *in vivo* estimations of Actin filament length during cell cycle and during development. The average length of an Actin filament is dependent on the Formin speed and elongation duration and on the Actin k_{off}. We evaluated these parameters at different stages of the cell cycle at an early embryonic stage.

During my PhD, I tried to evaluate Formin elongation duration but this measurement has proven unreliable. To perform this measurement, a bias was introduced: to be able to classify the Formin trajectories, a minimal number of elongating steps is necessary, if the number of steps is too small, random walking cannot be distinguished from ballistic movement and therefore, sub- and superdiffusive behaviors cannot be distinguished. This means that tracks too short are excluded from the analysis, even though part of it (we do not know in which proportions) is actually superdiffusive. The calculated time of elongation mean is therefore lacking the sampling from short tracks and therefore I probably overestimated Formin elongation duration with this method.

Alternatively, we decided to take all together the tracks imaged in this analysis and measure the duration of all the tracks. Strikingly, when measuring the lifetime distribution, we observed two distinct populations of lifetimes, corresponding to a rapidly decaying, short-lived population and a long-lived population. We hypothesized that the short-lived population corresponded to the population of recruited but not elongating Formins (subdiffusive population fraction), whereas the long-lived population represented the elongating population of Formins (superdiffusive). In order to calculate the length of the Formin-mediated Actin filament, we decided to do a fitting of the curve, collecting average length of long tracks fraction population for a collection of embryos at interphase and during mitosis. This method gives a good approximation of the Actin filament average length (~1,79 µm and ~1,75 µm respectively) but is still flawed, bias being introduced by the curve fitting. The value extracted for the average elongating Formin lifetime is dependent on the quality of the curve fitting that we defined. Therefore, the Actin filament length calculation is an approximation, which quality is also dependent on this fitting.

To get a more precise value of Actin filament average length, Actin dynamic could be followed in a Arp2/3 depleted context. I could image Actin at single-molecular level similarly to what has been described previously and measure Actin k_{off} when ARX-2 is depleted and therefore Arp2/3 not functional. In this context, Formin only would be using Actin monomers

to polymerize filaments, therefore Formin would be the only protein affecting Actin k_{off}. This would increase the precision of the k_{off} estimation used for Actin filament length calculation.

6. Kinetic delay is of importance to drive efficient contraction through the cortex

Kinetic delay is observed throughout the whole activation cascade and comparison with control (Myosin vs Myosin in both red and green channels) has shown that actually the measured delay has more variation than the variation observed in the control. Variation in control reflects intrinsic variation observed in the measurements. This observation points toward the fact that there is not a strict delay in the system, but rather a range of delay at work in the activation cascade. I concluded that the system is actually flexible and can operate within a certain range of delay.

This observation taken together with the observed robustness in the conservation of the kinetic delay in the system against perturbation made us wonder what exactly was the physiological relevance of the kinetic delay within the activation cascade. Therefore, we decided to simulate the effect of absence or change in the kinetic delay and observe the effect of this perturbation on the efficiency of the contraction and the range of the transmission of the tension throughout the network in these conditions. The agent-based simulations showed, first, that increase in the delay reduces the Actomyosin contraction and second, that the delay actually has an impact on the long-range transmission of the force. Agent-based simulations show that an optimal delay exist for efficient force transmission throughout the network and this delay is around 5 s. We concluded that kinetic delay is important to drive a contraction which tension will efficiently propagate throughout the network, giving biological relevance of the robustness of the delay.

In order to decipher the importance of this range of kinetic delay in our system, we could hypothesize and test if indeed force propagation is optimal for a range of delay of for a specific kinetic delay value. We could repeat previous experiment but with simulations every second in order to have a better view of the force propagation relation with time delay. If a range of kinetic delay is equally efficient for force propagation we should observe the same behavior as observed for the 5 s delay simulation in a variety of kinetic delay and an abrupt change when this delay is no longer efficient for force transmission when it is too small or too big. If a specific time delay is still optimal then the variation in force transmission efficiency should be a normal distribution from 0 s to 10 s kinetic delay. In my thesis, we observed a

variability of the measured delay *in vivo*, so to support this experiment, we could also evaluate the contractility of the pulsed contraction area depending on the observed delay. To achieve this, we could measure the delay in a strain carrying UTR::mKate2 (or another red fluorophore) and NMY-2::GFP, same Myosin fusion as used for the single-molecule experiment in Prigent Garcia *et al.* (article 1 in this manuscript). By imaging NMY-2::GFP at single molecule level, we could measure the contraction of the area, similarly to what has been performed in Michaux, Robin *et al.* (Michaux et al., 2018).

To conclude, my PhD work has given a better understanding of the biochemical regulation of the Actomyosin network and its architecture at early stages of development. I have also shown that the organization of Actomyosin network can be dependent of phase of the cell cycle. This thesis has given evidence of a different regulation for activation and for recruitment of protein at the cell cortex and that kinetic delays in activation cascade have a physiological relevance. This work has actually measured *in vivo* kinetic delay in an activation cascade and provided simple mathematical tools to understand it in any activation cascade.

Appendix

List of figures

Introduction

Complementary results

List of tables

Table 1. Table of strains

Robin lab strain name	genotype	source
N2	Wild-type Bristol strain	CGC
EM264	*nmy-2(cp52[nmy-2::mKate2 + LoxP unc-119(+) LoxP]) I; xsSi5[cb-unc-119 (+) GFP::ANI-1(AH+PH)] II; unc-119(ed3) III*	Michaux et al., 2018
JH1541	*unc-119(ed4) III; pJH7.03[pie-1p::GFP::actin⁚pie-1 3′ UTR + unc-119(+)]*	Courtesy of G. Seydoux
LP229	*nmy-2(cp52[nmy-2::mKate2 + LoxP unc-119(+) LoxP]) I; unc-119 (ed3) III*	Dickinson et al, 2017
SWG282	*gesIs008[cyk-1p::cyk-1::GFP::cyk-1UTR, unc-119+]*	Costache, Prigent Garcia *et al.*
FBR175	*nmy-2(cp52[nmy-2::mKate2 + unc-119(+)]) I; cyk-1(jme14[cyk-1::eGFP]) unc-119(ed3) III*	Costache, Prigent Garcia *et al.*
FBR10	*nmy-2(cp52[nmy-2::mKate2 + unc-119(+)]) I; xsSi3[cb-unc-119(+) pie-1::GFP::utrophin::pie-1 3′ UTR] II; unc-119(ed3) III*	Tse et al., 2012
ML2508	*let-502(mc74[GFP::let-502]) I*	Bell et al., 2020
FBR28	*let-502(mc74[GFP::let-502]) nmy-2(cp52[nmy-2::mKate2 + LoxP unc-119(+) LoxP]) I; unc-119 (ed3) III*	Prigent Garcia *et al.*
JJ1473	*unc-119(ed3) III; zuIs45[nmy-2p::nmy-2::GFP + unc-119(+)] V*	Nance et al., 2003
FBR189	*nmy-2(cp52[nmy-2::mKate2 + LoxP unc-119(+) LoxP]) I; unc-119 (ed3) III; zuIs45 [nmy-2p::nmy-2::GFP + unc-119(+)] V*	Prigent Garcia *et al.*
FBR96	*mlc-4(jme4[mlc-4::eGFP + LoxP]) III*	Prigent Garcia *et al.*
FBR119	*nmy-2(cp52[nmy-2::mKate2 + LoxP unc-119(+) LoxP]) I; mlc-4(jme4[mlc-4::eGFP+loxP]) unc-119 (ed3) III*	Prigent Garcia *et al.*
FBR157	*mel-11(syb753[mel-11::GFP]) II*	Prigent Garcia *et al.*
FBR227	*nmy-2(cp52[nmy-2::mKate2 + LoxP unc-119(+) LoxP]) I; mel-11 (syb753[mel-11::GFP]) II; unc-119 (ed3) III*	Prigent Garcia *et al.*
ML2519	*cap-1(mc76[cap-1::GFP + unc-119(+)]) IV*	Courtesy of the Labouesse lab
FBR212	*nmy-2(cp52[nmy-2::mKate2 + LoxP unc-119(+) LoxP]) I; unc-119 (ed3) III; cap-1(mc76[cap-1::GFP + unc-119(+)]) IV*	Prigent Garcia *et al.*
SWG282	*gesIs008[Pcyk-1::CYK-1::GFP::cyk-1UTR, unc-119+]*	Costache, Prigent Garcia *et al.*
KK332	*mel-11(it26) unc-4(e120) sqt-1(sc13)/mnC1 [dpy-10(e128) unc-52(e444)] II*	CGC
FBR236	*mel-11(it26) unc-4(e120) sqt-1(sc13)/mnC1 [dpy-10(e128) unc-52(e444)] II; unc-119(ed3) III; zuIs45[nmy-2p::nmy-2::GFP + unc-119(+)] V*	Prigent Garcia *et al.*
FBR104	*cyk-1(jme06[cyk-1::mNeon])III*	Costache, Prigent Garcia *et al.*
FBR106	*cyk-1(jme06[cyk-1::mNeon])III; gesIs001[Pmex-5::Lifeact::mKate::nmy-2UTR, unc-119+]*	Costache, Prigent Garcia *et al.*
FBR160	*cyk-1(jme14[cyk-1::eGFP])III*	Costache, Prigent Garcia *et al.*
SWG001	*gesIs001[Pmex-5::Lifeact::mKate::nmy-2UTR, unc-119+]*	Reyman et al, 2016

Table 2. Table of experiment according to their cameras

experiment		camera
two-color imaging	RhoA vs Myosin	Andor
	ROCK vs Myosin	Andor
	Actin vs Myosin	Andor
	Formin vs Myosin	Andor
	Myosin light-chain vs heavy-chain	Andor
	Control: Myosin heavy-chain vs heavy-chain	Andor
	Capping Protein vs Myosin	Photometrics
	Myosin Phosphatase vs Myosin	Photometrics
single-molecule imaging	Myosin WT (GFP RNAi)	Andor
	Myosin WT + Myosin Phosphatase mutant (GFP RNAi)	Photometrics
	Myosin WT (UNC-60 + GFP RNAi)	Andor
	Actin	Robin et al., 2014
	Formin	Photometrics

Table 3. Table of statistical details for *arx-2* RNAi experiment

/	**formin_SPEED**		**track_LENGTH**		**nb_tracks**
	mean_pool	*median_pool*	*mean_pool_tr*	*median_pool_tr*	
CONTROL					
2c interphase	1.1496	1.1524	3.0155	2.7513	/
fov1	/	/	/	/	60
fov2	/	/	/	/	37
fov3	/	/	/	/	60
fov6	/	/	/	/	60
fov7	/	/	/	/	60
2c mitosis	1.1051	1.1218	2.9876	2.6112	/
fov1	/	/	/	/	51
fov2	/	/	/	/	55
fov3	/	/	/	/	60
fov4	/	/	/	/	60
fov6	/	/	/	/	60
fov7	/	/	/	/	60
RNAi ARX2					
2c interphase	1.1623	1.1606	2.6719	2.4559	/
fov1	/	/	/	/	80
fov2	/	/	/	/	79
fov3	/	/	/	/	80
fov4	/	/	/	/	80
2c mitosis	1.0733	1.0969	2.9682	2.7760	/
fov1	/	/	/	/	57
fov2	/	/	/	/	57
fov4	/	/	/	/	57
fov5	/	/	/	/	57
fov6	/	/	/	/	56

Table 4. Table of statistical t-tests for *arx-2* RNAi experiment

2 sample t-test			
CONTROL		*speed*	*length*
2c interphase	2c mitosis	p = 0.0019	p = 0.8002
RNAi ARX2		*speed*	*length*
2c interphase	2c mitosis	p = 1.2829e-07	p = 0.0017
2c mitosis	2c mitosis	p = 0.0315	p = 0.8559

Wilcoxon rank sum test			
CONTROL		*speed*	*length*
2c interphase	2c mitosis	p = 0.0038	p = 0.0719
RNAi ARX2		*speed*	*length*
2c interphase	2c mitosis	p = 3.3132e-06	p = 1.8419e-05
2c interphase	2c interphase	p = 0.6529	p = 9.2638e-06
2c mitosis	2c mitosis	p = 0.0617	p = 0.0695

Table 5. Table of detailed value extracted from fitting curves for Formin fraction of population

2c interphase fov number	a	b	c		up a	down a
1	0,5939	6,005	27,27		0,6724	0,5161
2	0,3998	4,977	25,63		0,5122	0,2873
3	0,478	4,747	24,53		0,5737	0,3824
4	0,7384	6,443	34,38		0,8011	0,6763
5	0,6074	4,904	28,19		0,6803	0,5345
7	0,3972	3,445	25,69		0,4738	0,3206
mean	0,5352	5,004	26,48		0,5734	0,4973
Actin filament length result:	1,7915					

2c mitosis fov number	a	b	c		up a	down a
1	0,611	4,539	34,41		0,6715	0,5505
4	0,4627	4,714	28,52		0,545	0,3805
5	0,5877	5,06	31,47	spec fit	0,6732	0,5021
6	0,7138	3,68	33,92		0,7569	0,6708
7	0,714	5,546	28,98		0,7813	0,6473
9	0,6235	4,671	24,23		0,7049	0,5423
mean	0,5897	3,94	26,3		0,6206	0,5591
Actin filament length result:	1,7531					

References

Achard, V., Martiel, J.-L., Michelot, A., Guérin, C., Reymann, A.-C., Blanchoin, L., and Boujemaa-Paterski, R. (2010). A “primer-”based mechanism underlies branched actin filament network formation and motility. Curr. Biol. *20*, 423–428.

Alberts, A.S. (2001). Identification of a carboxyl-terminal diaphanous-related formin homology protein autoregulatory domain. Journal of Biological Chemistry *276*, 2824–2830.

Alvarez, I.S., and Navascués, J. (1990). Shaping, invagination, and closure of the chick embryo otic vesicle: scanning electron microscopic and quantitative study. Anat Rec *228*, 315–326.

Amann, K.J., and Pollard, T.D. (2001). The Arp2/3 complex nucleates actin filament branches from the sides of pre-existing filaments. Nature Cell Biology *3*, 306–310.

Amano, M., Ito, M., Kimura, K., Fukata, Y., Chihara, K., Nakano, T., Matsuura, Y., and Kaibuchi, K. (1996). Phosphorylation and activation of myosin by Rho-associated kinase (Rho-kinase). Journal of Biological Chemistry *271*, 20246–20249.

Anderson, D.C., Gill, J.S., Cinalli, R.M., and Nance, J. (2008). Polarization of the C. elegans Embryo by RhoGAP-Mediated Exclusion of PAR-6 from Cell Contacts. Science *320*, 1771–1774.

Anyanful, A., Ono, K., Johnsen, R.C., Ly, H., Jensen, V., Baillie, D.L., and Ono, S. (2004). The RNA-binding protein SUP-12 controls muscle-specific splicing of the ADF/cofilin pre-mRNA in C. elegans. J Cell Biol *167*, 639–647.

Aydin, F., Courtemanche, N., Pollard, T.D., and Voth, G.A. (2018). Gating mechanisms during actin filament elongation by formins. eLife *7*.

Balzer, C.J., Wagner, A.R., Helgeson, L.A., and Nolen, B.J. (2018). Dip1 Co-opts Features of Branching Nucleation to Create Linear Actin Filaments that Activate WASP-Bound Arp2/3 Complex. Curr. Biol. *28*, 3886–3891.e4.

Balzer, C.J., Wagner, A.R., Helgeson, L.A., and Nolen, B.J. (2019). Single-Turnover Activation of Arp2/3 Complex by Dip1 May Balance Nucleation of Linear versus Branched Actin Filaments. Curr. Biol. *29*, 3331–3338.e3337.

Begg, D.A., Rodewald, R., and Rebhun, L.I. (1978). The visualization of actin filament polarity in thin sections. Evidence for the uniform polarity of membrane-associated filaments. J Cell Biol *79*, 846–852.

Behar, M., and Hoffmann, A. (2010). Understanding the temporal codes of intra-cellular signals. Current Opinion in Genetics & Development *20*, 684–693.

Behar, M., Hao, N., Dohlman, H.G., and Elston, T.C. (2008). Dose-to-duration encoding and signaling beyond saturation in intracellular signaling networks. PLoS Comput Biol *4*, e1000197.

Bement, W.M., Miller, A.L., and Dassow, von, G. (2006). Rho GTPase activity zones and transient contractile arrays. Bioessays *28*, 983–993.

Benoit Bouvrette, L.P., Cody, N.A.L., Bergalet, J., Lefebvre, F.A., Diot, C., Wang, X., Blanchette, M., and Lécuyer, E. (2018). CeFra-seq reveals broad asymmetric mRNA and noncoding RNA distribution profiles in Drosophila and human cells. Rna *24*, 98–113.

Blanchoin, L., and Pollard, T.D. (1999). Mechanism of interaction of Acanthamoeba actophorin (ADF/Cofilin) with actin filaments. J. Biol. Chem. *274*, 15538–15546.

Blanchoin, L., Amann, K.J., Higgs, H.N., Marchand, J.B., Kaiser, D.A., and Pollard, T.D. (2000). Direct observation of dendritic actin filament networks nucleated by Arp2/3 complex and WASP/Scar proteins. Nature *404*, 1007–1011.

Blanchoin, L., Boujemaa-Paterski, R., Sykes, C., and Plastino, J. (2014). Actin dynamics, architecture, and mechanics in cell motility. Physiological Reviews *94*, 235–263.

Bombardier, J.P., Eskin, J.A., Jaiswal, R., Corrêa, I.R., Xu, M.-Q., Goode, B.L., and Gelles, J. (2015). Single-molecule visualization of a formin-capping protein "decision complex" at the actin filament barbed end. Nature Communications *6*, 8707–8709.

Brenner, S. (1974). The genetics of Caenorhabditis elegans. Genetics *77*, 71–94.

Bresnick, A.R., Warren, V., and Condeelis, J. (1990). Identification of a short sequence essential for actin binding by Dictyostelium ABP-120. Journal of Biological Chemistry *265*, 9236–9240.

Broderick, M.J.F., and Winder, S.J. (2005). Spectrin, alpha-actinin, and dystrophin. Adv Protein Chem *70*, 203–246.

Brotschi, E.A., Hartwig, J.H., and Stossel, T.P. (1978). The gelation of actin by actin-binding protein. Journal of Biological Chemistry *253*, 8988–8993.

Buracco, S., Claydon, S., and Insall, R. (2019). Control of actin dynamics during cell motility. F1000Res *8*, 1977.

Burgess, D.R. (2005). Cytokinesis: new roles for myosin. Curr. Biol. *15*, R310–R311.

Burke, T.A., Christensen, J.R., Barone, E., Suarez, C., Sirotkin, V., and Kovar, D.R. (2014). Homeostatic actin cytoskeleton networks are regulated by assembly factor competition for monomers. Curr. Biol. *24*, 579–585.

Burnette, D.T., Manley, S., Sengupta, P., Sougrat, R., Davidson, M.W., Kachar, B., and Lippincott-Schwartz, J. (2011). A role for actin arcs in the leading-edge advance of migrating cells. Nature Publishing Group *13*, 371–381.

Canman, J.C., Lewellyn, L., Laband, K., Smerdon, S.J., Desai, A., Bowerman, B., and Oegema, K. (2008). Inhibition of Rac by the GAP activity of centralspindlin is essential for cytokinesis. Science *322*, 1543–1546.

Cao, L., Kerleau, M., Suzuki, E.L., Wioland, H., Jouet, S., Guichard, B., Lenz, M., Romet-Lemonne, G., and Jégou, A. (2018). Modulation of formin processivity by profilin and mechanical tension. eLife *7*.

Carlsson, L., Nyström, L.E., Sundkvist, I., Markey, F., and Lindberg, U. (1977). Actin polymerizability is influenced by profilin, a low molecular weight protein in non-muscle cells. Journal of Molecular Biology *115*, 465–483.

Castrillon, D.H., and Wasserman, S.A. (1994). Diaphanous is required for cytokinesis in Drosophila and shares domains of similarity with the products of the limb deformity gene. Development *120*, 3367–3377.

Cavanaugh, K.E., Staddon, M.F., Munro, E., Banerjee, S., and Gardel, M.L. (2020). RhoA Mediates Epithelial Cell Shape Changes via Mechanosensitive Endocytosis. Developmental Cell *52*, 152–166.e155.

Chan, F.-Y., Silva, A.M., Saramago, J., Pereira-Sousa, J., Brighton, H.E., Pereira, M., Oegema, K., Gassmann, R., and Carvalho, A.X. (2019). The ARP2/3 complex prevents excessive formin activity during cytokinesis. Molecular Biology of the Cell *30*, 96–107.

Chang, F., Drubin, D., and Nurse, P. (1997). cdc12p, a protein required for cytokinesis in fission yeast, is a component of the cell division ring and interacts with profilin. J Cell Biol *137*, 169–182.

Charras, G.T., Hu, C.-K., Coughlin, M., and Mitchison, T.J. (2006). Reassembly of contractile actin cortex in cell blebs. The Journal of Cell Biology *175*, 477–490.

Chesarone, M.A., DuPage, A.G., and Goode, B.L. (2010). Unleashing formins to remodel the actin and microtubule cytoskeletons. Nat Rev Mol Cell Biol *11*, 62–74.

Chew, T.G., Huang, J., Palani, S., Sommese, R., Kamnev, A., Hatano, T., Gu, Y., Oliferenko, S., Sivaramakrishnan, S., and Balasubramanian, M.K. (2017). Actin turnover maintains actin filament homeostasis during cytokinetic ring contraction. J Cell Biol *216*, 2657–2667.

Courson, D.S., and Rock, R.S. (2010). Actin cross-link assembly and disassembly mechanics for alpha-Actinin and fascin. J. Biol. Chem. *285*, 26350–26357.

Courtemanche, N., Lee, J.Y., Pollard, T.D., and Greene, E.C. (2013). Tension modulates actin filament polymerization mediated by formin and profilin. Proc. Natl. Acad. Sci. U.S.a. *110*, 9752–9757.

Craig, R., Smith, R., and Kendrick-Jones, J. (1983). Light-chain phosphorylation controls the conformation of vertebrate non-muscle and smooth muscle myosin molecules. Nature *302*, 436–439.

Crocker, J.C., and Grier, D.G. (1996). Methods of digital video microscopy for colloidal studies. Journal of Colloid and Interface Science *179*, 298–310.

Danuser, G., and Waterman-Storer, C.M. (2006). Quantitative fluorescent speckle microscopy of cytoskeleton dynamics. Annu Rev Biophys Biomol Struct *35*, 361–387.

Davies, P.J., Wallach, D., Willingham, M., Pastan, I., and Lewis, M.S. (1980). Self-association of chicken gizzard filamin and heavy merofilamin. Biochemistry *19*, 1366–1372.

Davies, T., Jordan, S.N., Chand, V., Sees, J.A., Laband, K., Carvalho, A.X., Shirasu-Hiza, M., Kovar, D.R., Dumont, J., and Canman, J.C. (2014). High-resolution temporal analysis reveals a functional timeline for the molecular regulation of cytokinesis. Developmental Cell *30*, 209–223.

Delanote, V., Vandekerckhove, J., and Gettemans, J. (2005). Plastins: versatile modulators of actin organization in (patho)physiological cellular processes. Acta Pharmacol Sin *26*, 769–779.

DeMaso, C.R., Kovacevic, I., Uzun, A., and Cram, E.J. (2011). Structural and Functional Evaluation of C. elegans Filamins FLN-1 and FLN-2. PLoS ONE *6*, e22428.

Ding, S.S., and Woollard, A. (2017). Non-muscle myosin II is required for correct fate specification in the Caenorhabditis elegans seam cell divisions. Sci Rep *7*, 3524–13.

Ding, W.Y., Ong, H.T., Hara, Y., Wongsantichon, J., Toyama, Y., Robinson, R.C., Nédélec, F., and Zaidel-Bar, R. (2017). Plastin increases cortical connectivity to facilitate robust polarization and timely cytokinesis. J Cell Biol *216*, 1371–1386.

Djinović-Carugo, K., Young, P., Gautel, M., and Saraste, M. (1999). Structure of the alpha-actinin rod: molecular basis for cross-linking of actin filaments. Cell *98*, 537–546.

Dominguez, R. (2009). Actin filament nucleation and elongation factors--structure-function relationships. Crit Rev Biochem Mol Biol *44*, 351–366.

Dulyaninova, N.G., and Bresnick, A.R. (2013). The heavy chain has its day: regulation of myosin-II assembly. Bioarchitecture *3*, 77–85.

Dulyaninova, N.G., Malashkevich, V.N., Almo, S.C., and Bresnick, A.R. (2005). Regulation of myosin-IIA assembly and Mts1 binding by heavy chain phosphorylation. Biochemistry *44*, 6867–6876.

Egelhoff, T.T., Lee, R.J., and Spudich, J.A. (1993). Dictyostelium myosin heavy chain phosphorylation sites regulate myosin filament assembly and localization in vivo. Cell *75*, 363–371.

Egile, C., Rouiller, I., Xu, X.-P., Volkmann, N., Li, R., and Hanein, D. (2005). Mechanism of filament nucleation and branch stability revealed by the structure of the Arp2/3 complex at actin branch junctions. Plos Biol *3*, e383.

Evangelista, M., Pruyne, D., Amberg, D.C., Boone, C., and Bretscher, A. (2002). Formins direct Arp2/3-independent actin filament assembly to polarize cell growth in yeast. Nature Cell Biology *4*, 260–269.

Falzone, T.T., Lenz, M., Kovar, D.R., and Gardel, M.L. (2012). Assembly kinetics determine the architecture of α-actinin crosslinked F-actin networks. Nature Communications *3*, 861–869.

Ferrell, J.E. (2013). Feedback loops and reciprocal regulation: recurring motifs in the systems biology of the cell cycle. Current Opinion in Cell Biology *25*, 676–686.

Files, J.G., Carr, S., and Hirsh, D. (1983). Actin gene family of Caenorhabditis elegans. Journal of Molecular Biology *164*, 355–375.

Foth, B.J., Goedecke, M.C., and Soldati, D. (2006). New insights into myosin evolution and classification. Proceedings of the National Academy of Sciences *103*, 3681–3686.

Freedman, S.L., Suarez, C., Winkelman, J.D., Kovar, D.R., Voth, G.A., Dinner, A.R., and Hocky, G.M. (2019). Mechanical and kinetic factors drive sorting of F-actin cross-linkers on bundles. Proc. Natl. Acad. Sci. U.S.a. *116*, 16192–16197.

Fritzsche, M., Lewalle, A., Duke, T., Kruse, K., and Charras, G. (2013). Analysis of turnover dynamics of the submembranous actin cortex. Molecular Biology of the Cell *24*, 757–767.

Fuller, B.G., Lampson, M.A., Foley, E.A., Rosasco-Nitcher, S., Le, K.V., Tobelmann, P., Brautigan, D.L., Stukenberg, P.T., and Kapoor, T.M. (2008). Midzone activation of aurora B in anaphase produces an intracellular phosphorylation gradient. Nature *453*, 1132–1136.

Funk, J., Merino, F., Venkova, L., Heydenreich, L., Kierfeld, J., Vargas, P., Raunser, S., Piel, M., and Bieling, P. (2019). Profilin and formin constitute a pacemaker system for robust actin filament growth. eLife *8*.

Gally, C., Wissler, F., Zahreddine, H., Quintin, S., Landmann, F., and Labouesse, M. (2009). Myosin II regulation during C. elegans embryonic elongation: LET-502/ROCK, MRCK-1 and PAK-1, three kinases with different roles. Development *136*, 3109–3119.

Gierer, A., and Meinhardt, H. (1972). A theory of biological pattern formation. Kybernetik *12*, 30–39.

Goehring, N.W., Hoege, C., Grill, S.W., and Hyman, A.A. (2011). PAR proteins diffuse freely across the anterior–posterior boundary in polarized C. elegans embryos. J Cell Biol *193*, 583–594.

Gould, C.J., Maiti, S., Michelot, A., Graziano, B.R., Blanchoin, L., and Goode, B.L. (2011). The Formin DAD Domain Plays Dual Roles in Autoinhibition and Actin Nucleation. Current Biology *21*, 384–390.

Gressin, L., Guillotin, A., Guérin, C., Blanchoin, L., and Michelot, A. (2015). Architecture dependence of actin filament network disassembly. Curr. Biol. *25*, 1437–1447.

Griffith, J.S. (1968). Mathematics of cellular control processes. I. Negative feedback to one gene. Journal of Theoretical Biology *20*, 202–208.

Guha, M., Zhou, M., and Wang, Y.-L. (2005). Cortical actin turnover during cytokinesis requires myosin II. Curr. Biol. *15*, 732–736.

Gunning, P.W., Ghoshdastider, U., Whitaker, S., Popp, D., and Robinson, R.C. (2015). The evolution of compositionally and functionally distinct actin filaments. Journal of Cell Science *128*, 2009–2019.

Gunsalus, K.C., Bonaccorsi, S., Williams, E., Verni, F., Gatti, M., and Goldberg, M.L. (1995).

Mutations in twinstar, a Drosophila gene encoding a cofilin/ADF homologue, result in defects in centrosome migration and cytokinesis. J Cell Biol *131*, 1243–1259.

Guo, S., and Kemphues, K.J. (1996). A non-muscle myosin required for embryonic polarity in Caenorhabditis elegans. Nature *382*, 455–458.

Halatek, J., Brauns, F., and Frey, E. (2018). Self-organization principles of intracellular pattern formation. Philos. Trans. R. Soc. Lond., B, Biol. Sci. *373*.

Hartman, M.A., and Spudich, J.A. (2012). The myosin superfamily at a glance. Journal of Cell Science *125*, 1627–1632.

Hartshorne, D.J., Ito, M., and Erdödi, F. (1998). Myosin light chain phosphatase: subunit composition, interactions and regulation. J Muscle Res Cell Motil *19*, 325–341.

Haviv, L., Gillo, D., Backouche, F., and Bernheim-Groswasser, A. (2008). A cytoskeletal demolition worker: myosin II acts as an actin depolymerization agent. Journal of Molecular Biology *375*, 325–330.

Hayden, S.M., Miller, P.S., Brauweiler, A., and Bamburg, J.R. (1993). Analysis of the interactions of actin depolymerizing factor with G- and F-actin. Biochemistry *32*, 9994–10004.

He, L., Wang, X., Tang, H.L., and Montell, D.J. (2010). Tissue elongation requires oscillating contractions of a basal actomyosin network. Nature Cell Biology *12*, 1133–1142.

Heissler, S.M., and Manstein, D.J. (2013). Nonmuscle myosin-2: mix and match. Cell. Mol. Life Sci. *70*, 1–21.

Heissler, S.M., and Sellers, J.R. (2016). Various Themes of Myosin Regulation. Journal of Molecular Biology *428*, 1927–1946.

Higashida, C. (2004). Actin Polymerization-Driven Molecular Movement of mDia1 in Living Cells. Science *303*, 2007–2010.

Higgs, H.N., and Peterson, K.J. (2005). Phylogenetic analysis of the formin homology 2 domain. Molecular Biology of the Cell *16*, 1–13.

Himmel, M., Van Der Ven, P.F.M., Stöcklein, W., and Fürst, D.O. (2003). The limits of promiscuity: isoform-specific dimerization of filamins. Biochemistry *42*, 430–439.

Huang, Y., Yi, X., Kang, C., and Wu, C. (2019). Arp2/3-Branched Actin Maintains an Active Pool of GTP-RhoA and Controls RhoA Abundance. Cells *8*, 1264.

Huxley, A.F. (1957). Muscle structure and theories of contraction. Prog Biophys Biophys Chem *7*, 255–318.

Inoue, Y., Suzuki, M., Watanabe, T., Yasue, N., Tateo, I., Adachi, T., and Ueno, N. (2016). Mechanical roles of apical constriction, cell elongation, and cell migration during neural tube formation in Xenopus. Biomech Model Mechanobiol *15*, 1733–1746.

Jégou, A., Carlier, M.-F., and Romet-Lemonne, G. (2013). Formin mDia1 senses and generates mechanical forces on actin filaments. Nature Communications *4*, 1883–1887.

Jung, H.S., Komatsu, S., Ikebe, M., and Craig, R. (2008). Head-head and head-tail interaction: a general mechanism for switching off myosin II activity in cells. Molecular Biology of the Cell *19*, 3234–3242.

Kaiser, D.A., Vinson, V.K., Murphy, D.B., and Pollard, T.D. (1999). Profilin is predominantly associated with monomeric actin in Acanthamoeba. Journal of Cell Science *112 (Pt 21)*, 3779–3790.

Kamps, D., Koch, J., Juma, V.O., Campillo-Funollet, E., Graessl, M., Banerjee, S., Mazel, T., Chen, X., Wu, Y.-W., Portet, S., et al. (2020). Optogenetic Tuning Reveals Rho Amplification-Dependent Dynamics of a Cell Contraction Signal Network. Cell Rep *33*, 108467.

Karess, R.E., Chang, X.J., Edwards, K.A., Kulkarni, S., Aguilera, I., and Kiehart, D.P. (1991). The regulatory light chain of nonmuscle myosin is encoded by spaghetti-squash, a gene required for cytokinesis in Drosophila. Cell *65*, 1177–1189.

Kay, A.J., and Hunter, C.P. (2001). CDC-42 regulates PAR protein localization and function to control cellular and embryonic polarity in C. elegans. Curr. Biol. *11*, 474–481.

Kemphues, K.J., Priess, J.R., Morton, D.G., and Cheng, N.S. (1988). Identification of genes required for cytoplasmic localization in early C. elegans embryos. Cell *52*, 311–320.

Kendrick-Jones, J., Smith, R.C., Craig, R., and Citi, S. (1987). Polymerization of vertebrate non-muscle and smooth muscle myosins. Journal of Molecular Biology *198*, 241–252.

Kholodenko, B.N. (2006). Cell-signalling dynamics in time and space. Nat Rev Mol Cell Biol *7*, 165–176.

Kholodenko, B.N., and Birtwistle, M.R. (2009). Four-dimensional dynamics of MAPK information processing systems. Wiley Interdiscip Rev Syst Biol Med *1*, 28–44.

Kimura, K., Ito, M., Amano, M., Chihara, K., Fukata, Y., Nakafuku, M., Yamamori, B., Feng, J., Nakano, T., Okawa, K., et al. (1996). Regulation of myosin phosphatase by Rho and Rho-associated kinase (Rho-kinase). Science *273*, 245–248.

Kiuchi, T., Nagai, T., Ohashi, K., and Mizuno, K. (2011). Measurements of spatiotemporal changes in G-actin concentration reveal its effect on stimulus-induced actin assembly and lamellipodium extension. J Cell Biol *193*, 365–380.

Klinkert, K., Levernier, N., Gross, P., Gentili, C., Tobel, von, L., Pierron, M., Busso, C., Herrman, S., Grill, S.W., Kruse, K., et al. (2019). Aurora A depletion reveals centrosome-independent polarization mechanism in Caenorhabditis elegans. eLife *8*.

Koestler, S.A., Rottner, K., Lai, F., Block, J., Vinzenz, M., and Small, J.V. (2009). F- and G-actin concentrations in lamellipodia of moving cells. PLoS ONE *4*, e4810.

Kovar, D.R., Harris, E.S., Mahaffy, R., Higgs, H.N., and Pollard, T.D. (2006). Control of the

assembly of ATP- and ADP-actin by formins and profilin. Cell *124*, 423–435.

Kubota, H., Miyazaki, M., Ogawa, T., Shimozawa, T., Kinosita, K., and Ishiwata, S. (2017). Biphasic Effect of Profilin Impacts the Formin mDia1 Force-Sensing Mechanism in Actin Polymerization. Biophysical Journal *113*, 461–471.

Kuczmarski, E.R., and Spudich, J.A. (1980). Regulation of myosin self-assembly: phosphorylation of Dictyostelium heavy chain inhibits formation of thick filaments. Proceedings of the National Academy of Sciences *77*, 7292–7296.

Kühn, S., and Geyer, M. (2014). Formins as effector proteins of Rho GTPases. Small GTPases *5*, e29513.

La Cruz, De, E.M. (2005). Cofilin binding to muscle and non-muscle actin filaments: isoform-dependent cooperative interactions. Journal of Molecular Biology *346*, 557–564.

Lammers, M., Rose, R., Scrima, A., and Wittinghofer, A. (2005). The regulation of mDia1 by autoinhibition and its release by Rho*GTP. The EMBO Journal *24*, 4176–4187.

Lappalainen, P., and Drubin, D.G. (1997). Cofilin promotes rapid actin filament turnover in vivo. Nature *388*, 78–82.

Lecuit, T., Lenne, P.-F., and Munro, E. (2011). Force generation, transmission, and integration during cell and tissue morphogenesis. Annu. Rev. Cell Dev. Biol. *27*, 157–184.

Lee, J.-Y., and Goldstein, B. (2003). Mechanisms of cell positioning during C. elegans gastrulation. Development *130*, 307–320.

Lee, K.H., Sulbarán, G., Yang, S., Mun, J.Y., Alamo, L., Pinto, A., Sato, O., Ikebe, M., Liu, X., Korn, E.D., et al. (2018). Interacting-heads motif has been conserved as a mechanism of myosin II inhibition since before the origin of animals. Proc. Natl. Acad. Sci. U.S.a. *115*, E1991–E2000.

Leite, J., Chan, F.-Y., Osório, D.S., Saramago, J., Sobral, A.F., Silva, A.M., Gassmann, R., and Carvalho, A.X. (2020). Equatorial Non-muscle Myosin II and Plastin Cooperate to Align and Compact F-actin Bundles in the Cytokinetic Ring. Front Cell Dev Biol *8*, 573393.

Leptin, M. (1999). Gastrulation in Drosophila: the logic and the cellular mechanisms. The EMBO Journal *18*, 3187–3192.

Lécuyer, E., Yoshida, H., Parthasarathy, N., Alm, C., Babak, T., Cerovina, T., Hughes, T.R., Tomancak, P., and Krause, H.M. (2007). Global analysis of mRNA localization reveals a prominent role in organizing cellular architecture and function. Cell *131*, 174–187.

Li, H.-Y., and Zheng, Y. (2004). Phosphorylation of RCC1 in mitosis is essential for producing a high RanGTP concentration on chromosomes and for spindle assembly in mammalian cells. Genes Dev. *18*, 512–527.

Li, Z., Lee, H., Eskin, S.G., Ono, S., Zhu, C., and McIntire, L.V. (2020). Mechanochemical coupling of formin-induced actin interaction at the level of single molecular complex.

Biomech Model Mechanobiol 1–13.

Liang, W., Warrick, H.M., and Spudich, J.A. (1999). A structural model for phosphorylation control of Dictyostelium myosin II thick filament assembly. J Cell Biol *147*, 1039–1048.

Lieleg, O., Schmoller, K.M., Claessens, M.M.A.E., and Bausch, A.R. (2009a). Cytoskeletal polymer networks: viscoelastic properties are determined by the microscopic interaction potential of cross-links. Biophysical Journal *96*, 4725–4732.

Lieleg, O., Claessens, M.M.A.E., and Bausch, A.R. (2009b). Structure and dynamics of cross-linked actin networks. Soft Matter 218–225.

Lieleg, O., Schmoller, K.M., Cyron, C.J., Luan, Y., Wall, W.A., and Bausch, A.R. (2009c). Structural polymorphism in heterogeneous cystoskeletal networks. Soft Matter *5*, 1796–1803.

Little, S.C., Tkačik, G., Kneeland, T.B., Wieschaus, E.F., and Gregor, T. (2011). The formation of the Bicoid morphogen gradient requires protein movement from anteriorly localized mRNA. Plos Biol *9*, e1000596.

Liu, X., Billington, N., Shu, S., Yu, S.-H., Piszczek, G., Sellers, J.R., and Korn, E.D. (2017). Effect of ATP and regulatory light-chain phosphorylation on the polymerization of mammalian nonmuscle myosin II. Proc. Natl. Acad. Sci. U.S.a. *114*, E6516–E6525.

Liu, X., Hong, M.-S., Shu, S., Yu, S., and Korn, E.D. (2013). Regulation of the filament structure and assembly of Acanthamoeba myosin II by phosphorylation of serines in the heavy-chain nonhelical tailpiece. Proc. Natl. Acad. Sci. U.S.a. *110*, E33–E40.

Liu, X., Shu, S., and Korn, E.D. (2018). Polymerization pathway of mammalian nonmuscle myosin 2s. Proc. Natl. Acad. Sci. U.S.a. *115*, E7101–E7108.

Loibl, S., and Gianni, L. (2017). HER2-positive breast cancer. Lancet *389*, 2415–2429.

Lutkenhaus, J. (2007). Assembly dynamics of the bacterial MinCDE system and spatial regulation of the Z ring. Annu. Rev. Biochem. *76*, 539–562.

Ma, W., Trusina, A., El-Samad, H., Lim, W.A., and Tang, C. (2009). Defining network topologies that can achieve biochemical adaptation. Cell *138*, 760–773.

Machesky, L.M., Mullins, R.D., Higgs, H.N., Kaiser, D.A., Blanchoin, L., May, R.C., Hall, M.E., and Pollard, T.D. (1999). Scar, a WASp-related protein, activates nucleation of actin filaments by the Arp2/3 complex. Proceedings of the National Academy of Sciences *96*, 3739–3744.

MacLean-Fletcher, S., and Pollard, T.D. (1980). Mechanism of action of cytochalasin B on actin. Cell *20*, 329–341.

MacQueen, A.J., Baggett, J.J., Perumov, N., Bauer, R.A., Januszewski, T., Schriefer, L., and Waddle, J.A. (2005). ACT-5 is an essential Caenorhabditis elegans actin required for intestinal microvilli formation. Molecular Biology of the Cell *16*, 3247–3259.

Maduro, M.F., and Rothman, J.H. (2002). Making worm guts: the gene regulatory network of the Caenorhabditis elegans endoderm. Developmental Biology *246*, 68–85.

Mahajan, R.K., and Pardee, J.D. (1996). Assembly mechanism of Dictyostelium myosin II: regulation by K+, Mg2+, and actin filaments. Biochemistry *35*, 15504–15514.

Mahajan, R.K., Vaughan, K.T., Johns, J.A., and Pardee, J.D. (1989). Actin filaments mediate Dictyostelium myosin assembly in vitro. Proceedings of the National Academy of Sciences *86*, 6161–6165.

Marshall, C.J. (1995). Specificity of receptor tyrosine kinase signaling: transient versus sustained extracellular signal-regulated kinase activation. Cell *80*, 179–185.

Marston, D.J., Higgins, C.D., Peters, K.A., Cupp, T.D., Dickinson, D.J., Pani, A.M., Moore, R.P., Cox, A.H., Kiehart, D.P., and Goldstein, B. (2016). MRCK-1 Drives Apical Constriction in C. elegans by Linking Developmental Patterning to Force Generation. Curr. Biol. *26*, 2079–2089.

Martin, A.C. (2010). Developmental Biology. Developmental Biology *341*, 114–125.

Martin, A.C., and Goldstein, B. (2014). Apical constriction: themes and variations on a cellular mechanism driving morphogenesis. Development *141*, 1987–1998.

Matsumura, F., and Hartshorne, D.J. (2008). Myosin phosphatase target subunit: Many roles in cell function. Biochemical and Biophysical Research Communications *369*, 149–156.

Maupin, P., and Pollard, T.D. (1986). Arrangement of actin filaments and myosin-like filaments in the contractile ring and of actin-like filaments in the mitotic spindle of dividing HeLa cells. J Ultrastruct Mol Struct Res *94*, 92–103.

McCall, P.M., MacKintosh, F.C., Kovar, D.R., and Gardel, M.L. (2019). Cofilin drives rapid turnover and fluidization of entangled F-actin. Proc. Natl. Acad. Sci. U.S.a. *116*, 12629–12637.

McCullough, B.R., Blanchoin, L., Martiel, J.-L., and La Cruz, De, E.M. (2008). Cofilin increases the bending flexibility of actin filaments: implications for severing and cell mechanics. Journal of Molecular Biology *381*, 550–558.

McGough, A., Pope, B., Chiu, W., and Weeds, A. (1997). Cofilin changes the twist of F-actin: implications for actin filament dynamics and cellular function. J Cell Biol *138*, 771–781.

McKim, K.S., Matheson, C., Marra, M.A., Wakarchuk, M.F., and Baillie, D.L. (1994). The Caenorhabditis elegans unc-60 gene encodes proteins homologous to a family of actin-binding proteins. Mol Gen Genet *242*, 346–357.

Meinhardt, H. (2008). Models of biological pattern formation: from elementary steps to the organization of embryonic axes. Curr. Top. Dev. Biol. *81*, 1–63.

Melli, L., Billington, N., Sun, S.A., Bird, J.E., Nagy, A., Friedman, T.B., Takagi, Y., and Sellers, J.R. (2018). Bipolar filaments of human nonmuscle myosin 2-A and 2-B have distinct motile

and mechanical properties. eLife *7*.

Miao, H., and Blankenship, J.T. (2020). The pulse of morphogenesis: actomyosin dynamics and regulation in epithelia. Development *147*.

Michaux, J.B., Robin, F.B., McFadden, W.M., and Munro, E.M. (2018). Excitable RhoA dynamics drive pulsed contractions in the early C. elegans embryo. J Cell Biol *217*, 4230–4252.

Mishra, M., Kashiwazaki, J., Takagi, T., Srinivasan, R., Huang, Y., Balasubramanian, M.K., and Mabuchi, I. (2013). In vitro contraction of cytokinetic ring depends on myosin II but not on actin dynamics. Nature Cell Biology *15*, 853–859.

Miyoshi, T., and Watanabe, N. (2013). Can filament treadmilling alone account for the F-actin turnover in lamellipodia? Cytoskeleton (Hoboken) *70*, 179–190.

Moon, A., and Drubin, D.G. (1995). The ADF/cofilin proteins: stimulus-responsive modulators of actin dynamics. Molecular Biology of the Cell *6*, 1423–1431.

Moon, A.L., Janmey, P.A., Louie, K.A., and Drubin, D.G. (1993). Cofilin is an essential component of the yeast cortical cytoskeleton. J Cell Biol *120*, 421–435.

Moriyama, K., and Yahara, I. (1999). Two activities of cofilin, severing and accelerating directional depolymerization of actin filaments, are affected differentially by mutations around the actin-binding helix. The EMBO Journal *18*, 6752–6761.

Morone, N., Fujiwara, T., Murase, K., Kasai, R.S., Ike, H., Yuasa, S., Usukura, J., and Kusumi, A. (2006). Three-dimensional reconstruction of the membrane skeleton at the plasma membrane interface by electron tomography. J Cell Biol *174*, 851–862.

Moser, S.C., Elsner, von, S., Büssing, I., Alpi, A., Schnabel, R., and Gartner, A. (2009). Functional dissection of Caenorhabditis elegans CLK-2/TEL2 cell cycle defects during embryogenesis and germline development. PLoS Genet *5*, e1000451.

Motegi, F., and Sugimoto, A. (2006). Sequential functioning of the ECT-2 RhoGEF, RHO-1 and CDC-42 establishes cell polarity in Caenorhabditis elegans embryos. Nature Cell Biology *8*, 978–985.

Muller, J., Oma, Y., Vallar, L., Friederich, E., Poch, O., and Winsor, B. (2005). Sequence and comparative genomic analysis of actin-related proteins. Molecular Biology of the Cell *16*, 5736–5748.

Mullins, R.D., Heuser, J.A., and Pollard, T.D. (1998). The interaction of Arp2/3 complex with actin: nucleation, high affinity pointed end capping, and formation of branching networks of filaments. Proceedings of the National Academy of Sciences *95*, 6181–6186.

Munjal, A., Philippe, J.-M., Munro, E., and Lecuit, T. (2015). A self-organized biomechanical network drives shape changes during tissue morphogenesis. Nature *524*, 351–355.

Munro, E., Nance, J., and Priess, J.R. (2004). Cortical Flows Powered by Asymmetrical

Contraction Transport PAR Proteins to Establish and Maintain Anterior-Posterior Polarity in the Early C. elegans Embryo. Developmental Cell *7*, 413–424.

Murakami, N., Kotula, L., and Hwang, Y.W. (2000). Two distinct mechanisms for regulation of nonmuscle myosin assembly via the heavy chain: phosphorylation for MIIB and mts 1 binding for MIIA. Biochemistry *39*, 11441–11451.

Murrell, M., Oakes, P.W., Lenz, M., and Gardel, M.L. (2015). Forcing cells into shape: the mechanics of actomyosin contractility. Nat Rev Mol Cell Biol *16*, 486–498.

Murthy, K., and Wadsworth, P. (2005). Myosin-II-dependent localization and dynamics of F-actin during cytokinesis. Curr. Biol. *15*, 724–731.

Nance, J. (2005). PAR proteins and the establishment of cell polarity during C. elegans development. Bioessays *27*, 126–135.

Nance, J., and Priess, J.R. (2002). Cell polarity and gastrulation in C. elegans. Development *129*, 387–397.

Nance, J., Lee, J.-Y., and Goldstein, B. (2005). Gastrulation in C. elegans. WormBook 1–13.

Niederman, R., and Pollard, T.D. (1975). Human platelet myosin. II. In vitro assembly and structure of myosin filaments. J Cell Biol *67*, 72–92.

Nishikawa, M., Naganathan, S.R., Jülicher, F., and Grill, S.W. (2017). Controlling contractile instabilities in the actomyosin cortex. eLife *6*.

Novak, B., and Tyson, J.J. (1993a). Numerical analysis of a comprehensive model of M-phase control in Xenopus oocyte extracts and intact embryos. Journal of Cell Science *106 (Pt 4)*, 1153–1168.

Novak, B., and Tyson, J.J. (1993b). Modeling the Cell Division Cycle: M-phase Trigger, Oscillations, and Size Control. Journal of Theoretical Biology *165*, 101–134.

Nunns, H., and Goentoro, L. (2018). Signaling pathways as linear transmitters. eLife *7*.

Ono, K. (2003). Specific requirement for two ADF/cofilin isoforms in distinct actin-dependent processes in Caenorhabditis elegans. Journal of Cell Science *116*, 2073–2085.

Osório, D.S., Chan, F.-Y., Saramago, J., Leite, J., Silva, A.M., Sobral, A.F., Gassmann, R., and Carvalho, A.X. (2019). Crosslinking activity of non-muscle myosin II is not sufficient for embryonic cytokinesis in C. elegans. Development *146*.

Otomo, T., Tomchick, D.R., Otomo, C., Panchal, S.C., Machius, M., and Rosen, M.K. (2005). Structural basis of actin filament nucleation and processive capping by a formin homology 2 domain. Nature *433*, 488–494.

Pandey, D.K., and Chaudhary, B. (2017). Evolutionary expansion and structural functionalism of the ancient family of profilin proteins. Gene *626*, 70–86.

Pantaloni, D., and Carlier, M.F. (1993). How profilin promotes actin filament assembly in the presence of thymosin beta 4. Cell *75*, 1007–1014.

Paul, A.S., and Pollard, T.D. (2009). Review of the mechanism of processive actin filament elongation by formins. Cell Motil. Cytoskeleton *66*, 606–617.

Paul, A.S., Paul, A., Pollard, T.D., and Pollard, T. (2008). The role of the FH1 domain and profilin in formin-mediated actin-filament elongation and nucleation. Curr. Biol. *18*, 9–19.

Pelham, R.J., and Chang, F. (2002). Actin dynamics in the contractile ring during cytokinesis in fission yeast. Nature *419*, 82–86.

Piano, F., Schetter, A.J., Mangone, M., Stein, L., and Kemphues, K.J. (2000). RNAi analysis of genes expressed in the ovary of Caenorhabditis elegans. Curr. Biol. *10*, 1619–1622.

Piekny, A.J., and Mains, P.E. (2002). Rho-binding kinase (LET-502) and myosin phosphatase (MEL-11) regulate cytokinesis in the early Caenorhabditis elegans embryo. Journal of Cell Science *115*, 2271–2282.

Piekny, A.J., Johnson, J.-L.F., Cham, G.D., and Mains, P.E. (2003). The Caenorhabditis elegans nonmuscle myosin genes nmy-1 and nmy-2 function as redundant components of the let-502/Rho-binding kinase and mel-11/myosin phosphatase pathway during embryonic morphogenesis. Development *130*, 5695–5704.

Plastino, J., and Blanchoin, L. (2018). Dynamic stability of the actin ecosystem. Journal of Cell Science *132*.

Polet, D., Lambrechts, A., Ono, K., Mah, A., Peelman, F., Vandekerckhove, J., Baillie, D.L., AMPE, C., and Ono, S. (2006). Caenorhabditis elegans expresses three functional profilins in a tissue-specific manner. Cell Motil. Cytoskeleton *63*, 14–28.

Pollard, T.D. (1982). Structure and polymerization of Acanthamoeba myosin-II filaments. J Cell Biol *95*, 816–825.

Pollard, T.D., Blanchoin, L., and Mullins, R.D. (2000). Molecular mechanisms controlling actin filament dynamics in nonmuscle cells. Annu Rev Biophys Biomol Struct *29*, 545–576.

Pollard, T.D. (2007). Regulation of actin filament assembly by Arp2/3 complex and formins. Annu Rev Biophys Biomol Struct *36*, 451–477.

Pollard, T.D. (2010). Mechanics of cytokinesis in eukaryotes. Current Opinion in Cell Biology *22*, 50–56.

Pollard, T.D., and Borisy, G.G. (2003). Cellular motility driven by assembly and disassembly of actin filaments. Cell *112*, 453–465.

Pollard, T.D., and Cooper, J.A. (2009). Actin, a central player in cell shape and movement. Science *326*, 1208–1212.

Pomerening, J.R., Sontag, E.D., and Ferrell, J.E. (2003). Building a cell cycle oscillator:

hysteresis and bistability in the activation of Cdc2. Nature Cell Biology *5*, 346–351.

Ponti, A. (2004). Two Distinct Actin Networks Drive the Protrusion of Migrating Cells. Science *305*, 1782–1786.

Pring, M., Evangelista, M., Boone, C., Yang, C., and Zigmond, S.H. (2003). Mechanism of formin-induced nucleation of actin filaments. Biochemistry *42*, 486–496.

Pruyne, D. (2016). Revisiting the Phylogeny of the Animal Formins: Two New Subtypes, Relationships with Multiple Wing Hairs Proteins, and a Lost Human Formin. PLoS ONE *11*, e0164067.

Pruyne, D. (2017). Probing the origins of metazoan formin diversity: Evidence for evolutionary relationships between metazoan and non-metazoan formin subtypes. PLoS ONE *12*, e0186081.

Pruyne, D., Evangelista, M., Yang, C., Bi, E., Zigmond, S., Bretscher, A., and Boone, C. (2002). Role of formins in actin assembly: nucleation and barbed-end association. Science *297*, 612–615.

Pujol, T., Roure, du, O., Fermigier, M., and Heuvingh, J. (2012). Impact of branching on the elasticity of actin networks. Proceedings of the National Academy of Sciences *109*, 10364–10369.

Qin, X., Hannezo, E., Mangeat, T., Liu, C., Majumder, P., Liu, J., Choesmel-Cadamuro, V., McDonald, J.A., Liu, Y., Yi, B., et al. (2018). A biochemical network controlling basal myosin oscillation. Nature Communications *9*, 1210–1215.

Ramm, B., Heermann, T., and Schwille, P. (2019). The E. coli MinCDE system in the regulation of protein patterns and gradients. Cell. Mol. Life Sci. *76*, 4245–4273.

Raz-Ben Aroush, D., Ofer, N., Abu-Shah, E., Allard, J., Krichevsky, O., Mogilner, A., and Keren, K. (2017). Actin Turnover in Lamellipodial Fragments. Curr. Biol. *27*, 2963–2973.e14.

Robin, F.B., McFadden, W.M., Yao, B., and Munro, E.M. (2014). Single-molecule analysis of cell surface dynamics in Caenorhabditis elegans embryos. Nat Meth *11*, 677–682.

Roh-Johnson, M., and Goldstein, B. (2009). In vivo roles for Arp2/3 in cortical actin organization during C. elegans gastrulation. Journal of Cell Science *122*, 3983–3993.

Roh-Johnson, M., Shemer, G., Higgins, C.D., McClellan, J.H., Werts, A.D., Tulu, U.S., Gao, L., Betzig, E., Kiehart, D.P., and Goldstein, B. (2012). Triggering a cell shape change by exploiting preexisting actomyosin contractions. Science *335*, 1232–1235.

Rose, L., and Gönczy, P. (2014). Polarity establishment, asymmetric division and segregation of fate determinants in early C. elegans embryos. WormBook 1–43.

Rotty, J.D., Wu, C., Haynes, E.M., Suarez, C., Winkelman, J.D., Johnson, H.E., Haugh, J.M., Kovar, D.R., and Bear, J.E. (2015). Profilin-1 Serves as a Gatekeeper for Actin Assembly by Arp2/3-Dependent and -Independent Pathways. Developmental Cell *32*, 54–67.

Sagot, I., Rodal, A.A., Moseley, J., Goode, B.L., and Pellman, D. (2002). An actin nucleation mechanism mediated by Bni1 and profilin. Nature Cell Biology *4*, 626–631.

Salbreux, G., Charras, G., and Paluch, E. (2012). Actin cortex mechanics and cellular morphogenesis. Trends in Cell Biology *22*, 536–545.

Sato, M., Leimbach, G., Schwarz, W.H., and Pollard, T.D. (1985). Mechanical properties of actin. Journal of Biological Chemistry *260*, 8585–8592.

Sawa, M., Suetsugu, S., Sugimoto, A., Miki, H., Yamamoto, M., and Takenawa, T. (2003). Essential role of the C. elegans Arp2/3 complex in cell migration during ventral enclosure. Journal of Cell Science *116*, 1505–1518.

Schonegg, S., Constantinescu, A.T., Hoege, C., and Hyman, A.A. (2007). The Rho GTPase-activating proteins RGA-3 and RGA-4 are required to set the initial size of PAR domains in Caenorhabditis elegans one-cell embryos. Proc. Natl. Acad. Sci. U.S.a. *104*, 14976–14981.

Schutt, C.E., Myslik, J.C., Rozycki, M.D., Goonesekere, N.C., and Lindberg, U. (1993). The structure of crystalline profilin-beta-actin. Nature *365*, 810–816.

Sellers, J.R. (2000). Myosins: a diverse superfamily. Biochim. Biophys. Acta *1496*, 3–22.

Severson, A.F., Baillie, D.L., and Bowerman, B. (2002). A Formin Homology protein and a profilin are required for cytokinesis and Arp2/3-independent assembly of cortical microfilaments in C. elegans. Curr. Biol. *12*, 2066–2075.

Sha, W., Moore, J., Chen, K., Lassaletta, A.D., Yi, C.-S., Tyson, J.J., and Sible, J.C. (2003). Hysteresis drives cell-cycle transitions in Xenopus laevis egg extracts. Proceedings of the National Academy of Sciences *100*, 975–980.

Shekhar, S., Kerleau, M., Kühn, S., Pernier, J., Romet-Lemonne, G., Jégou, A., and Carlier, M.-F. (2015). Formin and capping protein together embrace the actin filament in a ménage à trois. Nature Communications *6*, 8730–12.

Shelton, C.A., Carter, J.C., Ellis, G.C., and Bowerman, B. (1999). The nonmuscle myosin regulatory light chain gene mlc-4 is required for cytokinesis, anterior-posterior polarity, and body morphology during Caenorhabditis elegans embryogenesis. J Cell Biol *146*, 439–451.

Shukla, V.K., Kabra, A., Maheshwari, D., Yadav, R., Jain, A., Tripathi, S., Ono, S., Kumar, D., and Arora, A. (2015). Solution structures and dynamics of ADF/cofilins UNC-60A and UNC-60B from Caenorhabditis elegans. Biochem. J. *465*, 63–78.

Silva, A.M., Osório, D.S., Pereira, A.J., Maiato, H., Pinto, I.M., Rubinstein, B., Gassmann, R., Telley, I.A., and Carvalho, A.X. (2016). Robust gap repair in the contractile ring ensures timely completion of cytokinesis. J Cell Biol *215*, 789–799.

Simões, S. de M., Mainieri, A., and Zallen, J.A. (2014). Rho GTPase and Shroom direct planar polarized actomyosin contractility during convergent extension. J Cell Biol *204*, 575–589.

Sjöblom, B., Salmazo, A., and Djinović-Carugo, K. (2008). α-Actinin structure and regulation.

Cell. Mol. Life Sci. *65*, 2688–2701.

Skau, C.T., Courson, D.S., Bestul, A.J., Winkelman, J.D., Rock, R.S., Sirotkin, V., and Kovar, D.R. (2011). Actin filament bundling by fimbrin is important for endocytosis, cytokinesis, and polarization in fission yeast. J. Biol. Chem. *286*, 26964–26977.

Skop, A.R., Liu, H., Yates, J., Meyer, B.J., and Heald, R. (2004). Dissection of the mammalian midbody proteome reveals conserved cytokinesis mechanisms. Science *305*, 61–66.

Skruber, K., Read, T.-A., and Vitriol, E.A. (2018). Reconsidering an active role for G-actin in cytoskeletal regulation. Journal of Cell Science *131*.

Skubiszak, L., and Kowalczyk, L. (2002). Myosin molecule packing within the vertebrate skeletal muscle thick filaments. A complete bipolar model. Acta Biochim Pol *49*, 829–840.

Sobieszek, A. (1972). Cross-bridges on self-assembled smooth muscle myosin filaments. Journal of Molecular Biology *70*, 741–744.

Sönnichsen, B., Koski, L.B., Walsh, A., Marschall, P., Neumann, B., Brehm, M., Alleaume, A.-M., Artelt, J., Bettencourt, P., Cassin, E., et al. (2005). Full-genome RNAi profiling of early embryogenesis in Caenorhabditis elegans. Nature *434*, 462–469.

Staddon, M.F., Cavanaugh, K.E., Munro, E.M., Gardel, M.L., and Banerjee, S. (2019). Mechanosensitive Junction Remodeling Promotes Robust Epithelial Morphogenesis. Biophysical Journal *117*, 1739–1750.

Stone, S., and Shaw, J.E. (1993). A Caenorhabditis elegans act-4::lacZ fusion: use as a transformation marker and analysis of tissue-specific expression. Gene *131*, 167–173.

Stossel, T.P., Condeelis, J., Cooley, L., Hartwig, J.H., Noegel, A., Schleicher, M., and Shapiro, S.S. (2001). Filamins as integrators of cell mechanics and signalling. Nat Rev Mol Cell Biol *2*, 138–145.

Strickland, D., Lin, Y., Wagner, E., Hope, C.M., Zayner, J., Antoniou, C., Sosnick, T.R., Weiss, E.L., and Glotzer, M. (2012). TULIPs: tunable, light-controlled interacting protein tags for cell biology. Nat Meth *9*, 379–384.

Su, Z., and Kiehart, D.P. (2001). Protein kinase C phosphorylates nonmuscle myosin-II heavy chain from Drosophila but regulation of myosin function by this enzyme is not required for viability in flies. Biochemistry *40*, 3606–3614.

Suarez, C., and Kovar, D.R. (2016). Internetwork competition for monomers governs actin cytoskeleton organization. Nat Rev Mol Cell Biol *17*, 799–810.

Suarez, C., Carroll, R.T., Burke, T.A., Christensen, J.R., Bestul, A.J., Sees, J.A., James, M.L., Sirotkin, V., and Kovar, D.R. (2015). Profilin Regulates F-Actin Network Homeostasis by Favoring Formin over Arp2/3 Complex. Developmental Cell *32*, 43–53.

Suarez, C., Roland, J., Boujemaa-Paterski, R., Kang, H., McCullough, B.R., Reymann, A.-C., Guérin, C., Martiel, J.-L., La Cruz, De, E.M., and Blanchoin, L. (2011). Cofilin Tunes the

Nucleotide Stateof Actin Filaments and Severs at Bare and Decorated Segment Boundaries. Current Biology *21*, 862–868.

Sulston, J.E., Schierenberg, E., White, J.G., and Thomson, J.N. (1983). The embryonic cell lineage of the nematode Caenorhabditis elegans. Developmental Biology *100*, 64–119.

Svitkina, T.M., and Borisy, G.G. (1999). Arp2/3 complex and actin depolymerizing factor/cofilin in dendritic organization and treadmilling of actin filament array in lamellipodia. J Cell Biol *145*, 1009–1026.

Swan, K.A., Severson, A.F., Carter, J.C., Martin, P.R., Schnabel, H., Schnabel, R., and Bowerman, B. (1998). cyk-1: a C. elegans FH gene required for a late step in embryonic cytokinesis. Journal of Cell Science *111 (Pt 14)*, 2017–2027.

Sweeton, D., Parks, S., Costa, M., and Wieschaus, E. (1991). Gastrulation in Drosophila: the formation of the ventral furrow and posterior midgut invaginations. Development *112*, 775–789.

Szent-Györgyi, A.G. (2004). The early history of the biochemistry of muscle contraction. J Gen Physiol *123*, 631–641.

Tan, I., Yong, J., Dong, J.M., Lim, L., and Leung, T. (2008). A tripartite complex containing MRCK modulates lamellar actomyosin retrograde flow. Cell *135*, 123–136.

Tinevez, J.-Y., Schulze, U., Salbreux, G., Roensch, J., Joanny, J.-F., and Paluch, E. (2009). Role of cortical tension in bleb growth. Proc. Natl. Acad. Sci. U.S.a. *106*, 18581–18586.

Toettcher, J.E., Weiner, O.D., and Lim, W.A. (2013). Using optogenetics to interrogate the dynamic control of signal transmission by the Ras/Erk module. Cell *155*, 1422–1434.

Tonino, P., Simon, M., and Craig, R. (2002). Mass determination of native smooth muscle myosin filaments by scanning transmission electron microscopy. Journal of Molecular Biology *318*, 999–1007.

Totsukawa, G., Yamakita, Y., Yamashiro, S., Hartshorne, D.J., Sasaki, Y., and Matsumura, F. (2000). Distinct roles of ROCK (Rho-kinase) and MLCK in spatial regulation of MLC phosphorylation for assembly of stress fibers and focal adhesions in 3T3 fibroblasts. J Cell Biol *150*, 797–806.

Trybus, K.M. (1991). Assembly of cytoplasmic and smooth muscle myosins. Current Opinion in Cell Biology *3*, 105–111.

Tse, Y.C., Werner, M., Longhini, K.M., Labbé, J.-C., Goldstein, B., and Glotzer, M. (2012). RhoA activation during polarization and cytokinesis of the early Caenorhabditis elegans embryo is differentially dependent on NOP-1 and CYK-4. Molecular Biology of the Cell *23*, 4020–4031.

Turing, A.M. (1952). THE CHEMICAL BASIS OF MORPHOGENESIS. Philos. Trans. R. Soc. Lond., B, Biol. Sci. *237*, 37–72.

Tyson, J.J., Chen, K.C., and Novák, B. (2003). Sniffers, buzzers, toggles and blinkers: dynamics of regulatory and signaling pathways in the cell. Current Opinion in Cell Biology *15*, 221–231.

Vale, R.D. (2003). The molecular motor toolbox for intracellular transport. Cell *112*, 467–480.

Valencia-Expósito, A., Grosheva, I., Míguez, D.G., González-Reyes, A., and Martín-Bermudo, M.D. (2016). Myosin light-chain phosphatase regulates basal actomyosin oscillations during morphogenesis. Nature Communications *7*, 10746–11.

Valon, L., Etoc, F., Remorino, A., di Pietro, F., Morin, X., Dahan, M., and Coppey, M. (2015). Predictive Spatiotemporal Manipulation of Signaling Perturbations Using Optogenetics. Biophysical Journal *109*, 1785–1797.

Velarde, N., Gunsalus, K.C., and Piano, F. (2007). Diverse roles of actin in C. elegans early embryogenesis. BMC Dev. Biol. *7*, 142–16.

Vicente-Manzanares, M., Ma, X., Adelstein, R.S., and Horwitz, A.R. (2009). Non-muscle myosin II takes centre stage in cell adhesion and migration. Nat Rev Mol Cell Biol *10*, 778–790.

Virel, A., and Backman, L. (2004). Molecular evolution and structure of alpha-actinin. Mol Biol Evol *21*, 1024–1031.

Vizcarra, C.L., Bor, B., and Quinlan, M.E. (2014). The role of formin tails in actin nucleation, processive elongation, and filament bundling. J. Biol. Chem. *289*, 30602–30613.

Wagner, A.R., Luan, Q., Liu, S.-L., and Nolen, B.J. (2013). Dip1 defines a class of Arp2/3 complex activators that function without preformed actin filaments. Curr. Biol. *23*, 1990–1998.

Warrick, H.M., and Spudich, J.A. (1987). Myosin structure and function in cell motility. Annu Rev Cell Biol *3*, 379–421.

Watanabe, N. (2002). Single-Molecule Speckle Analysis of Actin Filament Turnover in Lamellipodia. Science *295*, 1083–1086.

Watanabe, N., Kato, T., Fujita, A., Ishizaki, T., and Narumiya, S. (1999). Cooperation between mDia1 and ROCK in Rho-induced actin reorganization. Nature Cell Biology *1*, 136–143.

Watanabe, S., Ando, Y., Yasuda, S., Hosoya, H., Watanabe, N., Ishizaki, T., and Narumiya, S. (2008). mDia2 induces the actin scaffold for the contractile ring and stabilizes its position during cytokinesis in NIH 3T3 cells. Molecular Biology of the Cell *19*, 2328–2338.

Watanabe, S., Okawa, K., Miki, T., Sakamoto, S., Morinaga, T., Segawa, K., Arakawa, T., Kinoshita, M., Ishizaki, T., and Narumiya, S. (2010). Rho and anillin-dependent control of mDia2 localization and function in cytokinesis. Molecular Biology of the Cell *21*, 3193–3204.

Waterman-Storer, C.M., Desai, A., Bulinski, J.C., and Salmon, E.D. (1998). Fluorescent speckle microscopy, a method to visualize the dynamics of protein assemblies in living cells. Curr. Biol. *8*, 1227–1230.

Waterman-Storer, C.M., and Danuser, G. (2002). New directions for fluorescent speckle microscopy. Curr. Biol. *12*, R633–R640.

Wear, M.A., and Cooper, J.A. (2004). Capping protein: new insights into mechanism and regulation. Trends Biochem Sci *29*, 418–428.

Wei, X., Zhang, Y., Li, C., Ai, K., Li, K., Li, H., and Yang, J. (2020). The evolutionarily conserved MAPK/Erk signaling promotes ancestral T-cell immunity in fish via c-Myc-mediated glycolysis. J. Biol. Chem. *295*, 3000–3016.

Willis, J.H., Munro, E., Lyczak, R., and Bowerman, B. (2006). Conditional dominant mutations in the Caenorhabditis elegans gene act-2 identify cytoplasmic and muscle roles for a redundant actin isoform. Molecular Biology of the Cell *17*, 1051–1064.

Wilson, C.A., Tsuchida, M.A., Allen, G.M., Barnhart, E.L., Applegate, K.T., Yam, P.T., Ji, L., Keren, K., Danuser, G., and Theriot, J.A. (2010). Myosin II contributes to cell-scale actin network treadmilling through network disassembly. Nature *465*, 373–377.

Winkelman, J.D., Suarez, C., Hocky, G.M., Harker, A.J., Morganthaler, A.N., Christensen, J.R., Voth, G.A., Bartles, J.R., and Kovar, D.R. (2016). Fascin- and α-Actinin-Bundled Networks Contain Intrinsic Structural Features that Drive Protein Sorting. Curr. Biol. *26*, 2697–2706.

Wioland, H., Guichard, B., Senju, Y., Myram, S., Lappalainen, P., Jégou, A., and Romet-Lemonne, G. (2017). ADF/Cofilin Accelerates Actin Dynamics by Severing Filaments and Promoting Their Depolymerization at Both Ends. Curr. Biol. *27*, 1956–1967.e1957.

Wurzenberger, C., Held, M., Lampson, M.A., Poser, I., Hyman, A.A., and Gerlich, D.W. (2012). Sds22 and Repo-Man stabilize chromosome segregation by counteracting Aurora B on anaphase kinetochores. J Cell Biol *198*, 173–183.

Xu, J., Schwarz, W.H., Käs, J.A., Stossel, T.P., Janmey, P.A., and Pollard, T.D. (1998). Mechanical properties of actin filament networks depend on preparation, polymerization conditions, and storage of actin monomers. Biophysical Journal *74*, 2731–2740.

Xu, Y., Moseley, J.B., Sagot, I., Poy, F., Pellman, D., Goode, B.L., and Eck, M.J. (2004). Crystal structures of a Formin Homology-2 domain reveal a tethered dimer architecture. Cell *116*, 711–723.

Yamashiro, S., Mohri, K., and Ono, S. (2005). The two Caenorhabditis elegans actin-depolymerizing factor/cofilin proteins differently enhance actin filament severing and depolymerization. Biochemistry *44*, 14238–14247.

Yamashiro, S., Tanaka, S., McMillen, L.M., Taniguchi, D., Vavylonis, D., and Watanabe, N. (2018). Myosin-dependent actin stabilization as revealed by single-molecule imaging of actin turnover. Molecular Biology of the Cell *29*, 1941–1947.

Yu, M., Yuan, X., Lu, C., Le, S., Kawamura, R., Efremov, A.K., Zhao, Z., Kozlov, M.M., Sheetz, M., Bershadsky, A., et al. (2017). mDia1 senses both force and torque during F-actin filament polymerization. Nature Communications *8*, 1650–1659.

Zaner, K.S., and Stossel, T.P. (1983). Physical basis of the rheologic properties of F-actin. Journal of Biological Chemistry *258*, 11004–11009.

Zhang, R., Chang, M., Zhang, M., Wu, Y., Qu, X., and Huang, S. (2016). The Structurally Plastic CH2 Domain Is Linked to Distinct Functions of Fimbrins/Plastins. J. Biol. Chem. *291*, 17881–17896.

Zhao, P., Teng, X., Tantirimudalige, S.N., Nishikawa, M., Wohland, T., Toyama, Y., and Motegi, F. (2019). Aurora-A Breaks Symmetry in Contractile Actomyosin Networks Independently of Its Role in Centrosome Maturation. Developmental Cell *49*, 651–653.

Zigmond, S.H., Evangelista, M., Boone, C., Yang, C., Dar, A.C., Sicheri, F., Forkey, J., and Pring, M. (2003). Formin leaky cap allows elongation in the presence of tight capping proteins. Curr. Biol. *13*, 1820–1823.

Zimmermann, D., Homa, K.E., Hocky, G.M., Pollard, L.W., La Cruz, De, E.M., Voth, G.A., Trybus, K.M., and Kovar, D.R. (2017). Mechanoregulated inhibition of formin facilitates contractile actomyosin ring assembly. Nature Communications *8*, 703–713.

Zweifel, M.E., and Courtemanche, N. (2020a). Profilin's Affinity for Formin Regulates the Availability of Filament Ends for Actin Monomer Binding. Journal of Molecular Biology *432*, 166688.

Zweifel, M.E., and Courtemanche, N. (2020b). Competition for delivery of profilin-actin to barbed ends limits the rate of formin-mediated actin filament elongation. J. Biol. Chem. *295*, 4513–4525.